

UNIVERSITY OF BIRMINGHAM

Theoretical and Experimental Advances in Two-port Injection Matched Antennas

By

Peter Mgaya Kihogo

A thesis submitted to the University of Birmingham for the degree of
Doctor of Philosophy

Department of Electronic, Electrical and Systems Engineering
School of Engineering
College of Engineering and Physical Sciences
University of Birmingham
August 2021

UNIVERSITY OF
BIRMINGHAM

University of Birmingham Research Archive

e-theses repository

This unpublished thesis/dissertation is copyright of the author and/or third parties. The intellectual property rights of the author or third parties in respect of this work are as defined by The Copyright Designs and Patents Act 1988 or as modified by any successor legislation.

Any use made of information contained in this thesis/dissertation must be in accordance with that legislation and must be properly acknowledged. Further distribution or reproduction in any format is prohibited without the permission of the copyright holder.

Abstract

The bandwidth enhancement of two-port single radiator patch antennas for wireless communications is studied through single resonance and frequency tunability using the injection matching technique. The approach uses the variations of the relative amplitude γ and phase shift φ between the two coherent excitation signals at port two of the antenna to modulate the terminal impedances at the two ports, which simultaneously matches the two ports of the antenna to the 50 Ω coherent sources. Particular focus is paid to the active modulation of the electrical length of the patch antenna to enhance the bandwidth of an electrically small antenna.

Wide bandwidth greater than 64% is attained from the two-port proximity-fed patch antenna with approximately stable omnidirectional H-plane radiation patterns, radiation efficiency higher than 99% and total efficiency higher than 89% across the antenna passband through excitation of two characteristic modes of the antenna with $\gamma = 1$ and $\varphi = 180°$ applied to the antenna. Also, the fractional bandwidths of 67% and 19% with radiation efficiency higher than 98% and total efficiency higher than 84% across the antenna passband are attained from a patch antenna through a non-progressive frequency tuning of the antenna modes with $\gamma = 1$ and $\varphi = 180°$, and $\gamma = 1$ and $\varphi = 0°$, respectively. It is further shown that other γ and φ combinations apart from $\gamma = 1$ and $\varphi = 180°$ or

$\gamma = 1$ and $\varphi = 0°$ can only affect the matching of the attained differential or common mode resonances.

Besides, an electrically small operation with electrical length $ka = 0.81$, radiation and total efficiencies of 93%, and a -10 dB fractional bandwidth of 2.7% at a 1.423 Gigahertz (GHz) centre frequency has been attained on a patch antenna which is incorporated with a slow-wave structure, through the application of the injection matching technique. It is further shown that the use of lumped elements for tuning the two-port injection matched antennas to an electrically small frequency of operation is not feasible because of the narrowband matching behaviour of the lumped elements, which causes significant variations in the applied γ and φ.

Also, the reciprocity analysis of the two-port injection matched antennas shows that the same feeding network arrangement used by the antenna in transmit mode can be fed by an injection matched antenna in the receive mode. Besides, the two-port injection matched antennas can work reciprocally with any other antenna with similar radiation characteristics.

The high bandwidths attained by the two-port injection matched antennas are attributed to the excitation of the multiple characteristic modes of the antenna through the application of the injection matching technique. However, all these features are attained at the expense of complex driving circuitry, which is not always advantageous to realise.

To my wife and children for their fervent love, patience, encouragement, and support.

Acknowledgement

My sincere gratitude and praises—the sweet aroma of my lips, go to the Holy Spirit of the Living God for the inspiration during the whole period of this study. It was not easy to accomplish this work considering the situation at hand—the coronavirus disease of 2019 (COVID-19) lockdown now and then.

Many thanks to my supervisors, Prof. Costas Constantinou and Prof. Peter Gardner, for their moral and scientific guidance in achieving this work.

I want to thank my wife, Ms Anna E. Kihogo, and my children Paul, Joanna, Herrycrista and Herrycristiana for their patience, support, and encouragement during this busiest moment in my life.

Special thanks to Mr Alan Yates and Aleksandr Bystrov for their support during experiments. Many gratitude to Long Shen for his cooperation from the beginning to the end of this work. Last but not least, my thanks to all my colleagues whose efforts brought this work into completion. Your contributions are unforgettable.

Contents

Abstract **ii**

Acknowledgement **v**

List of Figures **xi**

List of Tables **xxxv**

List of acronyms and abbreviations **xxxvii**

1 Introduction **1**

1.1 Background 1

1.2 Objectives and hypothesis 4

1.3 Thesis organisation 6

2 Review of multiport antennas **9**

2.1 Background 9

2.2 Single radiator multiport antennas 10

2.3 Characteristic modes vs multiport antennas 14

2.4 The two-port antennas 16

2.4.1 Two-port wideband antennas 16
2.4.2 Two-port electrically small antennas 20
2.4.3 Two-port frequency tunable antennas 22
2.4.4 Two-port multiband antennas 25
2.5 Measurement challenges in multiport antennas 27
2.6 Towards the research of this thesis 30
2.6.1 Strategy for bandwidth enhancement 32

3 Theory for the two-port injection matched antennas 36
3.1 Background 36
3.2 Injection matching theory 37
3.3 Reflection and transmission coefficients for injection matched antennas . . 40
3.3.1 Total active reflection coefficient 41
3.3.2 Reflection and transmission coefficients at the individual ports . . . 43
3.3.3 Efficiency of injection matched antennas 45
3.4 Characterisation of the radiation patterns for injection matched antennas . 47
3.5 Reciprocity of injection matched antennas 49
3.5.1 Theory and derivation 50
3.5.2 Circuit implementation of two-port antenna reciprocity 55
3.6 Summary 59

4 Design methodology, application and validation 60
4.1 Background 60
4.2 Design methodology for injection matched patch antennas 61
4.3 Application of the design methodology 63

4.3.1 Design of one-port antenna 63
4.3.2 Positioning the feed lines 66
4.3.3 The two-port injection matched antenna 72
4.3.4 Simulated TARC 87
4.3.5 Injection matching operation 93
4.3.6 Simulated surface current 97
4.3.7 Injection matched antenna reciprocity 100
4.4 Validation of injection matching technique 105
4.4.1 Measurement of TARC, terminal impedances and currents 105
4.4.2 Measurement of radiation patterns 112
4.5 Results and discussion 116
4.6 Summary 120

5 Broadband injection matched antennas **121**
5.1 Background 121
5.2 Design, simulation and validation 122
5.3 Results and discussion 139
5.4 Summary 151

6 Tunable injection matched antennas **153**
6.1 Background 153
6.2 Design, simulation and validation 154
6.2.1 Feeding on two opposite corners of the patch 173
6.2.2 Antenna validation 180
6.3 Results and discussion 181

6.4 Summary 197

7 Electrically small injection matched antennas 199

7.1 Background 199

7.2 Design and simulation 200

7.2.1 Tuning with LC network 213

7.2.2 Slow-wave structure 218

7.3 Results and discussion 222

7.4 Summary 228

8 Conclusions and future work 230

8.1 Conclusions 230

8.2 Contributions to the research 232

8.2.1 Theory for the two-port injection matched antennas 232

8.2.2 Design methodology for injection matched antennas 232

8.2.3 Injection matched antenna reciprocity 232

8.2.4 Bandwidth enhancement in patch antennas 233

8.2.5 Validation of injection matched antenna operation 233

8.2.6 Wideband, frequency tunability and electrically small operations . . 233

8.3 Future work 234

8.3.1 Bandwidth enhancement 234

8.3.2 Leakage currents on partial grounds 234

8.3.3 Modulating and demodulating a carrier signal 235

8.3.4 Analysis of two-port monopole patch antennas 235

8.3.5 Experimental validation of reciprocity analysis of injection matched antennas . . . 235

Appendices **236**

A List of publications . . . 237

B Further design information . . . 238

B.1 Simulation of injection matched antennas . . . 238

B.2 CMA of planar antennas in CST MWS . . . 245

B.3 Further results . . . 246

B.4 Antenna bandwidth calculations . . . 249

B.5 Design equations for electrically small antenna . . . 249

C Measurements with **R&S** ZVA67 VNA . . . 250

D Reference antenna . . . 251

References **255**

List of Figures

Figure 1.1 Organisation of the thesis chapters. 7

Figure 2.1 (a) An integrated multiport driven antenna architecture (b) radiation pattern for the multiport driven antenna [21]. 11

Figure 2.2 (a) Front view of the multiband antenna (b) back view of the multiband antenna (c) simulated and measured reflection coefficients (d) simulated and measured isolation between the multiple ports [21]. 12

Figure 2.3 (a) An SRMP antenna with $w = 44.6$ mm, $d = 9.4$ mm and $h = 1.6$ mm printed on FR4 substrate with $\varepsilon_r = 4.5$ (b) Isolation between multiple ports of an SRMP antenna [13]. 13

Figure 2.4 (a) An ultra-wideband antenna (b) CPW to CPS transition (c) rectangular loop slot antenna (d) tapered slot antenna (e) simulated transmission and reflection coefficients for the wide-narrowband antenna [29]. . . 17

Figure 2.5 (a) Doherty amplifier operational diagram (b) active load modulation with Doherty amplifier (c) simulated currents for the carrier and peaking amplifiers (d) simulated impedances for the carrier and peaking amplifiers [39]. 19

Figure 2.6 (a) Two-port antenna active matching with NICs (b) variation of reactance with frequency [30, 53]. 21

Figure 2.7 (a) Front view (b) back view (c) reflection coefficient on narrow-band port (d) reflection coefficient on wideband port for the disc monopole antenna [56]. 23

Figure 2.8 Structure of a dual-port frequency reconfigurable antenna proposed in [57]. 24

Figure 2.9 (a) Front (b) back view of the two-port dual-band duplexing antenna (c) reflection coefficients and isolation between the two ports of the dual-band duplexing antenna [58]. 26

Figure 2.10 Illustration of beam squinting on antenna pattern [64]. 29

Figure 2.11 A traditional rectangular planar monopole antenna. 33

Figure 2.12 Proposed multiport rectangular planar monopole antenna. 34

Figure 3.1 The impedance model for the two-port network. 37

Figure 3.2 The reflection and transmission coefficient model for the two-port network. 40

Figure 3.3 An experimental setup for measuring the far-field characteristics of the two-port injection matched antennas in the anechoic chamber. 48

Figure 3.4 The two N-port antennas under reciprocity. 51

Figure 3.5 Two-port antennas under reciprocity. 56

Figure 3.6 Equivalent circuit for the two-port antenna in the receive mode. . . 58

Figure 4.1 A flow chart summarising the design procedure for the two-port injection matched antennas. 62

Figure 4.2 Proximity-fed patch antenna with single feed line. The black colour indicates the layers of copper. 64

Figure 4.3 S-parameter for the one-port proximity-fed patch antenna under investigation. 65

Figure 4.4 Proximity-fed patch antenna with two partial grounds and without feed lines. The black colour indicates the layers of copper. 66

Figure 4.5 The modal significance for the first four characteristic modes of the proximity-fed patch antenna under investigation. 67

Figure 4.6 Characteristic surface current for (a) mode J_{01} at 3.848 GHz (b) mode J_1 at 4.275 GHz and (c) mode J_2 at 4.282 GHz frequency for the antenna under investigation. 68

Figure 4.7 Characteristic directive radiation patterns for (a) mode J_{01} at 3.848 GHz (b) mode J_1 at 4.275 GHz and (c) mode J_2 at 4.282 GHz frequency for the antenna under investigation. 70

Figure 4.8 Presentation of the two-port antenna in the Cartesian coordinate system in CST MWS, showing the ϕ and θ directions. 71

Figure 4.9 Proximity-fed patch antenna with two feed lines. The black colour indicates the layers of copper. 73

Figure 4.10 The block diagram for implementing the two-port injection matching technique in CST DS. 74

Figure 4.11 TARC for the differentially and common mode excited two-port antenna under investigation when $\gamma = 1$ at different φ, w and g values. . . 74

Figure 4.12 Simulated surface current at (a) 2.822 GHz (b) 3.049 GHz (c) 3.562 GHz and (d) 3.961 GHz frequencies resulting from the differential excitation of the antenna under investigation when $g = 0.1$ mm and $w = 0.8$ mm. The modal significance for this antenna is shown in Figure 4.5. 75

Figure 4.13 Simulated radiation patterns at (a) 2.822 GHz (b) 3.049 GHz (c) 3.562 GHz and (d) 3.961 GHz frequencies resulting from the differential excitation of the antenna under investigation when $g = 0.1$ mm and $w = 0.8$ mm. The modal significance of this antenna is shown in Figure 4.5. . . 77

Figure 4.14 Typical results for the optimised TARC resonances for the differentially excited two-port antenna. 80

Figure 4.15 Typical results of the fine-tuned TARC resonances for the differentially excited two-port antenna whose dimensions are depicted in Table B.3 in Appendix B.3. 81

Figure 4.16 Simulated TARC, individual port reflection coefficients, and transmission coefficients between the two ports for the differentially excited two-port injection matched antenna compared to S_{11} for the corresponding one-port antenna. The dimensions for the two antennas are depicted by TARC7 resonance in Table B.3 in Appendix B.3. 81

Figure 4.17 The modal significance for the first three resonant characteristic modes of the proximity-fed patch antenna whose TARC resonance is depicted in Figure 4.16. 82

Figure 4.18 Characteristic surface current for (a) mode J_{01} at 3.640 GHz (b) mode J_1 at 3.770 GHz (c) mode J_2 at 3.895 GHz for the antenna depicted in Figure 4.16, whose modal significance is shown in Figure 4.17. 83

Figure 4.19 Variation of the theoretical (a) phase shift φ of Equation (3.8) with frequency (b) relative amplitude γ of Equation (3.9) with frequency on the two-port injection matched antenna whose TARC is shown in Figure 4.16. 85

Figure 4.20 The common mode TARC in comparison to the differential mode TARC for the two-port injection matched antenna under investigation. . . 86

Figure 4.21 Typical TARC resonances for the two-port injection matched antenna at different γ and φ values. 88

Figure 4.22 (a) Variation of γ on the two-port injection matched antenna when $\varphi = 180°$ (b) Variation of φ on the two-port injection matched antenna when $\gamma = 1$. 89

Figure 4.23 Typical differential mode TARC resonances when γ and φ are varied in ranges of $0.6 \leq \gamma \leq 1.4$ and $173° \leq \varphi \leq 187°$. 90

Figure 4.24 Transmission coefficient (a) S_{12} for $\gamma \leq 1$ (b) S_{21} for $\gamma \leq 1$ on the two-port injection matched antenna when $\varphi = 180°$. 91

Figure 4.25 Transmission coefficient (a) S_{12} for $\gamma \geq 1$ (b) S_{21} for $\gamma \geq 1$ on the two-port injection matched antenna when $\varphi = 180°$. 92

Figure 4.26 Simulated active impedances on the differentially excited two-port injection matched antenna whose TARC resonance is depicted in Figure 4.16 at (a) 2.175 GHz (b) 2.447 GHz (c) 3.881 GHz and (d) 4.221 GHz frequencies. 94

Figure 4.27 Simulated passive impedances on the two-port antenna at (a) 2.175 GHz (b) 2.447 GHz (c) 3.881 GHz and (d) 4.221 GHz frequencies, before injection matching operation is applied to the antenna whose TARC resonance is depicted in Figure 4.16. 96

Figure 4.28 Surface current on the differentially excited two-port injection matched patch antenna (including partial grounding planes) at (a) 2.175 GHz (b) 2.447 GHz (c) 3.881 GHz and (d) 4.221 GHz frequencies. The simulated TARC for this antenna is shown in Figure 4.16. 98

Figure 4.29 Simulated surface current on the corresponding one-port patch antenna (including partial grounding plane) in the (a) 2.647 GHz (b) 3.150 GHz and (c) 3.843 GHz frequencies. The simulated S_{11} for this antenna is shown in Figure 4.16. 99

Figure 4.30 Circuit implementation of the two-port injection matched antenna reciprocity in CST DS. 101

Figure 4.31 (a) Simulated reciprocity of the two two-port injection matched antennas (b) simulated receive mode of the two-port injection matched antenna. 102

Figure 4.32 An experimental setup for simulating the receive mode of the two-port injection matched antenna in AWR® Microwave Office. 103

Figure 4.33 (a) Simulated relative amplitude γ (b) simulated phase shift φ between the currents I_1^R and I_2^R when the two-port injection matched antenna is configured to work in the receive mode. 104

Figure 4.34 (a) Front view of the printed two-port antenna (b) back view of the printed two-port antenna (c) front view of the printed corresponding one-port antenna (d) back view of the printed corresponding one-port antenna. The two antennas have dimensions corresponding to the TARC7 resonance shown in Table B.3. 106

Figure 4.35 Picture showing (a) the use of ferrite beads in measuring the radiation patterns of a two-port antenna (b) the use of ferrite beads in measuring the radiation patterns of a one-port antenna (c) the RS ZVA67 VNA. The same ferrite beads were used in the experiment for characterising TARC for the two-port antenna and S_{11} for the corresponding one-port antenna using techniques outlined in [89]. 107

Figure 4.36 Measured and simulated TARC for the differentially excited two-port injection matched antenna compared to S_{11} for the corresponding one-port antenna. The simulated and printed antennas are shown in Figure 4.16 and 4.34, respectively. 108

Figure 4.37 Measured and simulated response of the applied (a) relative amplitude γ between the currents I_1 and I_2 (b) phase shift φ between the currents I_1 and I_2 (c) relative amplitude γ between the waves a_1 and a_2 (d) phase shift φ between the waves a_1 and a_2 when the patch antenna was injection matched at $\gamma = 1$ and $\varphi = 180°$. The simulated and printed antennas are shown in Figure 4.16 and 4.34, respectively. 109

Figure 4.38 Simulated and measured terminal impedances for the differentially excited two-port antenna. The simulated and printed antennas are shown in Figure 4.16 and 4.34, respectively. 110

Figure 4.39 Simulated efficiency for the differentially excited two-port injection matched antenna in comparison with the simulated efficiency for the corresponding one-port antenna. The simulated and printed antennas are shown in Figure 4.16 and 4.34, respectively. 111

Figure 4.40 Simulated and measured co-polar patterns for the differentially excited two-port injection matched antenna in the (a) 2.175 and 2.353 GHz (b) 2.447 and 2.638 GHz (c) 3.881 and 3.635 GHz (d) 4.221 and 4.015 GHz frequencies, respectively. The simulated and printed antennas are shown in Figure 4.16 and 4.34, respectively. 114

Figure 4.41 Simulated and measured co-polar radiation patterns for the corresponding one-port antenna in the (a) 2.647 and 2.733 GHz (b) 3.150 and 3.065 GHz and (c) 3.843 and 3.730 GHz frequencies. The simulated and printed antennas are shown in Figure 4.16 and 4.34, respectively. 115

Figure 4.42 Simulated (a) H-plane ($\phi = 90°$) realised gain for the two-port injection matched patch antenna (b) H-plane ($\phi = 90°$) realised gain for the one-port patch antenna (c) H-plane ($\phi = 90°$) maximum realised gain for the two-port injection matched patch antenna and for the corresponding one-port antenna. The simulated TARC and S_{11} for the two antennas are shown in Figure 4.16. 118

Figure 5.1 (a) Proximity-fed patch antenna with single feed line (b) proximity-fed patch antenna with two feed lines. The black colour indicates the layers of copper. 123

Figure 5.2 S-parameter for the one-port proximity-fed patch antenna under investigation. 123

Figure 5.3 TARC for the differentially excited ($\gamma = 1$, $\varphi = 180°$) two-port proximity-fed patch antenna, which corresponds to the one-port antenna whose resonance is depicted in Figure 5.2. 124

Figure 5.4 Typical results for the optimised TARC resonances for the differentially excited two-port proximity-fed patch antenna under investigation. . . 126

Figure 5.5 Typical results for the fine-tuned TARC resonances for the differentially excited two-port proximity-fed patch antenna under investigation. . 126

Figure 5.6 Optimum TARC (TARC1) resonance, individual port reflection coefficients, and transmission coefficients between the two ports for the differentially excited two-port proximity-fed patch antenna under investigation in comparison to the S-parameter for the corresponding one-port antenna. The dimensions for the two antennas are depicted by TARC1 resonance in Table 5.2. 127

Figure 5.7 The modal significance for the first four characteristic modes of the proximity-fed patch antenna whose TARC is depicted in Figure 5.6. 128

Figure 5.8 Characteristic surface current for (a) mode J_{01} at a 2.315 GHz frequency (b) mode J_2 at a 3.826 GHz frequency (c) mode J_1 at a 4.871 GHz frequency for the antenna depicted in Figure 5.6, whose modal significant is shown in Figure 5.7. 129

Figure 5.9 TARC resulting from excitation of modes J_{01} and J_1 of the patch antenna under investigation through two pairs of differential excitations delivered at the opposite short patch edges at the current maxima positions 5 and 6, and 7 and 8 of mode J_1, as shown in Figure 5.8, with $w = 0.7$ mm and $g = 1.5$ mm for each pair of the feed lines, while $L_p = 22.8$, $W_p = 20$, $L_s = 41.8$, $W_s = 32.2$, and $Lg = 7.6$ mm. The modified antenna layer two is shown in Figure 5.10. 131

Figure 5.10 Layer two for the four-port proximity-fed patch antenna whose TARC resonance is depicted in Figure 5.9. The discrete face ports 1 through 4 are created on the outer end-faces of the feed lines at positions 1 through 4, respectively. Ports 1 and 2, as well as ports 3 and 4 excitations are differentially driven. The black colour indicates the copper layer, while the white colour indicates the substrate layer. Other antenna dimensions are $w = 0.7$ mm, $L_p = 22.8$, $W_p = 20$, $L_s = 41.8$, $W_s = 32.2$, and $Lg = 7.6$ mm. 132

Figure 5.11 Simulated (a) efficiency (b) H-plane ($\phi = 90°$) co-polar patterns (c) H-plane ($\phi = 90°$) cross-polar patterns for the four-port proximity-fed injection matched patch antenna whose TARC resonance is depicted in Figure 5.9. 133

Figure 5.12 TARC resonances obtained by changing substrate heights h_1 and h_2, feed lines width w and the gap g between the two feed lines as shown in Table 5.3. 135

Figure 5.13 Typical differential mode TARC4 resonances when $\gamma = 1$ and φ are varied in the range of $175° \leq \varphi \leq 185°$. 135

Figure 5.14 Typical differential mode TARC1 resonances when γ and φ are varied in the ranges of $0.6 \leq \gamma \leq 1.4$ and $173° \leq \varphi \leq 187°$. 136

Figure 5.15 Variation of the theoretical (a) phase shift φ (b) relative amplitude γ with frequency across the two-port antenna whose TARC resonance is depicted in Figure 5.6. 138

Figure 5.16 (a) Front view of the printed two-port patch antenna (b) back view of the printed two-port patch antenna (c) front view of the printed corresponding one-port patch antenna (d) back view of the printed corresponding one-port patch antenna. The two antennas have dimensions depicted by TARC1 resonance in Table 5.2. 140

Figure 5.17 Measured and simulated reflection coefficients for the differentially excited two-port injection matched patch antenna in comparison to the S-parameters for the corresponding one-port antenna. The simulated and printed antennas are shown in Figure 5.6 and 5.16, respectively. 141

Figure 5.18 Measured and simulated response of the applied (a) relative amplitude γ between the currents I_1 and I_2 (b) phase shift φ between the currents I_1 and I_2 when the patch antenna was injection matched at $\gamma = 1$ and $\varphi = 180°$. The simulated and printed antennas are shown in Figure 5.6 and 5.16, respectively. 142

Figure 5.19 Simulated and measured terminal impedances for the differentially excited two-port patch antenna under investigation. The simulated and printed antennas are shown in Figure 5.6 and 5.16, respectively. 143

Figure 5.20 Simulated efficiency for the two-port injection matched patch antenna in comparison to the simulated efficiency for the corresponding one-port antenna. The simulated and printed antennas are shown in Figure 5.6 and 5.16, respectively. 143

Figure 5.21 Simulated surface current on the two-port patch antenna at around (a) 2.414 GHz (b) 2.775 GHz (c) 4.215 GHz and (d) 4.956 GHz frequencies. The simulated TARC for this antenna is shown in Figure 5.6. 145

Figure 5.22 Simulated surface current on the single-port antenna in the (a) 3.150 GHz (b) 3.781 GHz and (c) 4.359 GHz frequencies. The simulated S_{11} for this antenna is shown in Figure 5.6. 146

Figure 5.23 Simulated (a) H-plane ($\phi = 90°$) realised gain for the two-port injection matched patch antenna (b) H-plane ($\phi = 90°$) realised gain for the corresponding one-port patch antenna (c) H-plane ($\phi = 90°$) maximum realised gain for the two-port injection matched patch antenna and for the corresponding one-port patch antenna. The simulated TARC and S_{11} for the two antennas are shown in Figure 5.6. 147

Figure 5.24 Simulated and measured co-polar patterns for the differentially excited two-port injection matched antenna in the (a) 2.414 and 2.353 GHz (b) 2.775 and 2.638 GHz (c) 4.215 and 3.635 GHz (d) 4.956 and 4.015 GHz frequencies, respectively. The simulated and printed antennas are shown in Figure 5.6 and 5.16, respectively. 149

Figure 5.25 Simulated and measured co-polar patterns for the one-port antenna in the (a) 3.150 and 2.733 GHz (b) 3.781 and 3.065 GHz (c) 4.359 and 3.73 GHz frequencies, respectively. The simulated and printed antennas are shown in Figure 5.6 and 5.16, respectively. 150

Figure 6.1 (a) Proximity-fed patch antenna with single feed line (b) proximity-fed patch antenna with two feed lines. The black colour indicates the layers of copper. 155

Figure 6.2 S-parameter for the one-port proximity-fed patch antenna under investigation. 155

Figure 6.3 TARC resonances for the tunable two-port proximity-fed patch antenna derived from the one-port antenna with S-parameter resonance in Figure 6.2. The dimensions of this antenna are depicted by TARC0 in Table 6.1. 156

Figure 6.4 (a) Modal significance and (b) mode J_{02} surface current for the antenna whose TARC is shown in Figure 6.3. The surface currents for modes J_{01} and J_1 are similar to the ones shown in Figure 4.6. The CMA was conducted in CST MWS using a Multilayer Solver with solver and mesh settings provided in Appendix B.2. 157

Figure 6.5 Simulated surface current at (a) 1.963 GHz (b) 2.639 GHz (c) 3.134 GHz and (d) 5.427 GHz frequencies resulting from the differential and common mode excitations of the antenna under investigation whose modal significance is shown in Figure 6.4a. 158

Figure 6.6 Optimised common mode TARC for the two-port proximity-fed injection matched patch antenna under investigation at different antenna dimensions depicted in Table 6.1. 160

Figure 6.7 Differential and common mode TARC resonances for the tunable two-port proximity-fed patch antenna under investigation at different antenna dimensions depicted in Table 6.1. 161

Figure 6.8 The TARC (TARC5) resonances, individual port reflection coefficients, and transmission coefficients between the two ports for the tunable two-port injection matched antenna in comparison to the S-parameter for the corresponding one-port antenna. The dimensions for the two antennas are depicted by TARC5 resonance in Table 6.1. 162

Figure 6.9 The modal significance for the first six resonant characteristic modes of the proximity-fed patch antenna whose TARC resonances are depicted in Figure 6.8 and 6.12. 164

Figure 6.10 Characteristic surface current for (a) mode one at 2.660 GHz frequency (b) mode two at 3.176 GHz frequency (c) mode three at 3.938 GHz frequency (d) mode four at 5.786 GHz frequency (e) mode five at 7.052 GHz frequency (f) mode six at 7.934 GHz frequency for the patch antenna whose TARC resonances are depicted in Figure 6.8 and 6.12, and modal significance shown in Figure 6.9. 165

Figure 6.11 Characteristic directive radiation patterns for (a) mode four at 5.786 GHz (b) mode five at 7.052 GHz and (c) mode six at 7.934 GHz frequency for the patch antenna whose TARC resonance is depicted in Figure 6.8, and modal significance shown in Figure 6.9. The eigenpatterns for modes J_{01}, J_1, and J_2 of this antenna are similar to the patterns shown in Figure 4.7. 166

Figure 6.12 TARC resulting from excitation of mode J_{01} and J_1 of the patch antenna under investigation through two pairs of differential excitations delivered at the opposite short patch edges at the current maxima positions 5 and 6, and 7 and 8 of mode J_1, as shown in Figure 6.10c with $w = 0.7$ mm and $g = 4.29$ mm for each pair of the feed lines, while $L_p = 23.9$, $W_p = 18.1$, $L_s = 42.3$, $W_s = 41.1$, and $Lg = 8.0$ mm. The modified antenna layer two is shown in Figure 6.13. 167

Figure 6.13 Layer two of the four-port proximity-fed patch antenna whose TARC resonance is depicted in Figure 6.12. The discrete face ports 1 through 4 are created at the outer ends of the feed lines at positions 1 through 4, respectively. Ports 1 and 2, as well as ports 3 and 4 excitations, are differentially driven. The black colour indicates the copper layer, while the white colour indicates the substrate layer. Other antenna dimensions are $w = 0.7$ mm, $L_p = 23.9$, $W_p = 18.1$, $L_s = 42.3$, $W_s = 41.1$, and $Lg = 8.0$ mm. 168

Figure 6.14 Simulated (a) efficiency (b) H-plane ($\phi = 90°$) co-polar patterns (c) H-plane ($\phi = 90°$) cross-polar patterns for the four-port proximity-fed injection matched patch antenna whose TARC resonance is depicted in Figure 6.12. 169

Figure 6.15 Variation of the theoretical (a) phase shift φ (b) relative amplitude γ with frequency across the two-port antenna with TARC5 resonances depicted in Figure 6.8. 171

Figure 6.16 Typical common mode TARC resonances when γ and φ are varied in ranges of $0.8 \leq \gamma \leq 1.2$ and $-3° \leq \varphi \leq 3°$. 172

Figure 6.17 Typical differential mode TARC resonances when γ and φ are varied in ranges of $0.7 \leq \gamma \leq 1.3$ and $175° \leq \varphi \leq 185°$. 173

Figure 6.18 (a) Grounding planes (b) feed lines (c) patch for the square microstrip-fed patch antenna. The black colour indicates the layers of copper, while the white colour indicates the substrate layers. The antenna dimensions are $w = 3.6$, $L_p = W_p = 23.9$, $L_s = W_s = 42.3$, $g = 7.4$ and $L_g = 8$ mm, giving rise to the TARC resonances in Figure 6.23. The width, w and the gap, g at the attained TARC resonances were obtained through optimisation of w and g through parameter sweep in CST DS between 0.7 and 10 mm, and 0.1 and 33 mm, respectively. 175

Figure 6.19 The modal significance for the first five resonant modes of the proximity-fed patch antenna whose dimensions are depicted in Figure 6.18. 176

Figure 6.20 Characteristic surface current for (a) mode one at 2.630 GHz (b) mode two at 3.092 GHz (c) mode three at 3.854 GHz (d) mode four at 7.424 GHz (e) mode five at 7.460 GHz frequency for the antenna depicted in Figure 6.18, whose modal significant is shown in Figure 6.19. 177

Figure 6.21 Characteristic directive radiation patterns for (a) mode four at 7.424 GHz and (b) mode five at 7.460 GHz frequency for the patch antenna whose TARC resonance is depicted in Figure 6.23, and modal significance shown in Figure 6.19. The patterns for mode J_{01}, J_1, and J_2 for this antenna are similar to the patterns shown in Figure 4.7. 178

Figure 6.22 Simulated 3D radiation patterns at (a) 2.946 GHz (b) 3.856 GHz and (c) 5.732 GHz frequencies, for the square microstrip-fed patch antenna whose TARC resonances are shown in Figure 6.23. 179

Figure 6.23 Simulated TARC for the tunable multiband antenna resulting from feeding on the opposite corners of the square proximity-fed patch antenna whose dimensions are depicted in Figure 6.18. 180

Figure 6.24 (a) Front view of the printed two-port patch antenna (b) back view of the printed two-port patch antenna (c) front view of the printed corresponding one-port patch antenna (d) back view of the printed corresponding one-port patch antenna. The two antennas have dimensions depicted by TARC5 resonance in Table 6.1. 181

Figure 6.25 Simulated and measured TARC for the two-port injection matched patch antenna in comparison to the simulated and measured S-parameter for the corresponding one-port antenna. The simulated and printed antennas are shown in Figure 6.8 and 6.24, respectively. 182

Figure 6.26 Measured and simulated response of the applied (a) relative amplitude γ between the currents I_1 and I_2 (b) phase shift φ between the currents I_1 and I_2 when the two-port patch antenna was injection matched at $\gamma = 1$ and $\varphi = 180°$. The simulated and printed antennas are shown in Figure 6.8 and 6.24, respectively. 183

Figure 6.27 Simulated and measured terminal impedances for the differentially excited two-port injection matched patch antenna under investigation. The simulated and printed antennas are shown in Figure 6.8 and 6.24, respectively. 184

Figure 6.28 Measured and simulated response of the applied (a) relative amplitude γ between the currents I_1 and I_2 (b) phase shift φ between the currents I_1 and I_2 when the two-port patch antenna was injection matched at $\gamma = 1$ and $\varphi = 0°$. The simulated and printed antennas are shown in Figure 6.8 and 6.24, respectively. 185

Figure 6.29 Simulated and measured terminal impedances for the common mode excited two-port injection matched patch antenna under investigation. The simulated and printed antennas are shown in Figure 6.8 and 6.24, respectively.186

Figure 6.30 Simulated efficiency for the injection matched patch antenna in comparison to the simulated efficiency for the corresponding one-port antenna whose TARC and S_{11} resonances are shown in Figure 6.8. 187

Figure 6.31 Simulated surface current on the two-port patch antenna at (a) 6.190 GHz (b) 6.644 GHz and (c) 7.607 GHz frequencies, when the antenna was injection matched at $\gamma = 1$ and $\varphi = 0°$ as shown in Figure 6.8. 188

Figure 6.32 Simulated surface current on the two-port patch antenna at (a) 2.260 GHz (b) 2.546 GHz (c) 4.060 GHz and (d) 4.585 GHz frequencies, when the antenna was injection matched at $\gamma = 1$ and $\varphi = 180°$ as shown in Figure 6.8. 189

Figure 6.33 Simulated surface current on the one-port patch antenna at (a) 2.916 GHz (b) 3.713 GHz and (c) 4.515 GHz frequencies. The simulated S_{11} for this antenna is shown in Figure 6.8. 190

Figure 6.34 Simulated and measured co-polar patterns for the differentially excited two-port injection matched patch antenna in the (a) 2.260 and 2.590 GHz (b) 2.546 and 2.780 GHz (c) 4.060 and 4.063 GHz (d) 4.585 and 4.348 GHz frequencies, respectively. The simulated and printed antennas are shown in Figure 6.8 and 6.24, respectively. 193

Figure 6.35 Simulated and measured co-polar patterns for the common mode excited two-port injection matched patch antenna in the (a) 6.190 and 6.105 GHz (b) 6.644 and 7.863 GHz (c) 7.607 and 8.290 GHz frequencies, respectively. The simulated and printed antennas are shown in Figure 6.8 and 6.24, respectively. 194

Figure 6.36 Simulated and measured co-polar patterns for the one-port patch antenna in the (a) 2.916 and 3.018 GHz (b) 3.713 and 3.92 GHz (c) 4.515 and 4.728 GHz frequencies, respectively. The simulated and printed antennas are shown in Figure 6.8 and 6.24, respectively. 195

Figure 6.37 Simulated (a) H-plane ($\phi = 90°$) realised gain for the differentially excited two-port injection matched patch antenna (b) H-plane ($\phi = 90°$) realised gain for the one-port patch antenna (c) H-plane ($\phi = 90°$) realised gain for the common mode excited two-port injection matched patch antenna (d) H-plane ($\phi = 90°$) maximum realised gain for the two-port injection matched antenna and for the corresponding one-port antenna. The simulated TARC and S_{11} for the two antennas are shown in Figure 6.8. . . 196

Figure 7.1 (a) Proximity-fed patch antenna with single feed line (b) proximity-fed patch antenna with two feed lines. The black colour indicates the layers of copper. 201

Figure 7.2 S-parameter for the one-port proximity-fed patch antenna under investigation. 202

Figure 7.3 TARC resonance for the differentially excited ($\gamma = 1$, $\varphi = 180°$) two-port proximity-fed patch antenna derived from the one-port antenna with S-parameter resonance in Figure 7.2. The dimensions of this antenna are depicted by TARC0 in Table 7.1. 203

Figure 7.4 Optimised (a) TARC responses that correspond to the γ and φ variations in Figure 7.5a and 7.5b (b) electrical length corresponding to the TARC resonances in (a). 204

Figure 7.5 Optimised (a) theoretical γ variations with frequency of Equation (3.9) (b) theoretical φ variations with frequency of Equation (3.8) on the two-port antenna. These variations correspond to the TARC resonances depicted in Figure 7.4a. 205

Figure 7.6 Refined (a) TARC resonances corresponding to the γ and φ variations in Figure 7.5a and 7.5b (b) electrical length corresponding to the TARC resonances in (a). 207

Figure 7.7 Refined results for (a) theoretical γ variations with frequency (b) theoretical φ variations with frequency on the two-port antenna. These variations correspond to the TARC resonances depicted in Figure 7.6a. . . 208

Figure 7.8 Variation of the theoretical (a) phase shift φ (b) relative amplitude γ with frequency across the two-port antenna with TARC4 resonance depicted in Figure 7.6a. 210

Figure 7.9 Optimum TARC for the differentially excited two-port electrically large antenna in comparison to the common mode TARC, and S-parameter for the corresponding one-port antenna. 211

Figure 7.10 Response of the applied (a) relative amplitude γ (b) phase shift φ to the two-port electrically large antenna whose TARC resonance is depicted in Figure 7.9. 212

Figure 7.11 Architecture for an L-section of lumped elements matching of an injection matched antenna in CST DS. 213

Figure 7.12 Typical optimisation results for total active reflection coefficient (TARC) when the two-port patch antenna whose TARC resonance is depicted in Figure 7.9 was matched with inductor-capacitor (LC) networks at its two ports. 214

Figure 7.13 Typical optimised (a) S_{12} for an LC matched two-port injection matched patch antenna (b) S_{21} for the LC matched injection matched patch antenna. 216

Figure 7.14 Simulated response of the applied (a) relative amplitude γ between the currents I_1 and I_2 when the LC matched two-port patch antenna was injection matched at $\gamma = 1$ and $\varphi = 180°$ (b) phase shift φ between the currents I_1 and I_2 when the LC matched two-port patch antenna was injection matched at $\gamma = 1$ and $\varphi = 180°$. 217

Figure 7.15 Modified layer 3 of the two-port patch antenna under investigation. Other dimensions of the antenna remained unchanged. 219
Figure 7.16 Optimised TARC values for the two-port ESA. 220
Figure 7.17 Modal significance for the first six characteristic modes of the ESA under investigation sorted at around 1.386 GHz. The CMA was conducted in CST MWS using a Multilayer Solver with solver and mesh settings provided in Appendix B.2. 220
Figure 7.18 Characteristic mode one current on the ESA whose modal significance is shown in Figure 7.17. 221
Figure 7.19 Typical optimisation results for the TARC when the two-port ESA was matched by varying the gap between two coupled lines and the width of the coupled lines. 222
Figure 7.20 Simulated TARC, individual port reflection coefficients, and transmission coefficients between the two ports for the two-port injection matched ESA, and the S-parameter for the corresponding one-port ESA. . 223
Figure 7.21 Simulated efficiencies for the two-port ESA and for the corresponding one-port antenna. 224
Figure 7.22 Simulated response of the applied (a) relative amplitude γ between the currents I_1 and I_2 (b) phase shift φ between the currents I_1 and I_2 when the two-port ESA was injection matched at $\gamma = 1$ and $\varphi = 180°$. . . . 225
Figure 7.23 Surface current on the (a) two-port injection matched ESA at around 1.423 GHz frequency (b) corresponding one-port ESA at around 1.514 GHz frequency. 226

Figure 7.24 Simulated directive (a) radiation patterns for the two-port ESA at 1.423 GHz frequency (b) radiation patterns for the corresponding one-port ESA at 1.514 GHz frequency. 227

Figure 7.25 Simulated realised gain in the H-plane ($\phi = 90°$) for the two ESAs at their resonant frequencies. 227

Figure B.1 The Time Domain Solver settings used in simulating the one-port antennas, and two-port injection matched patch antennas in CST MWS. . 239

Figure B.2 Mesh settings used in simulating one-port antennas, and two-port injection matched patch antennas in CST MWS. 240

Figure B.3 The schematic for exciting the two-port injection matched patch antennas in CST DS. 241

Figure B.4 Setting the signal source for exciting the two-port injection matched patch antennas in CST DS. 242

Figure B.5 Post-processing of the simulated TARC from the simulated current and voltage signals in CST DS. 243

Figure B.6 Defining the field monitors for the simulation of the radiation patterns and efficiency of two-port injection matched antenna using the AC result combining tool in CST DS. 244

Figure B.7 Variation of (a) g on the two-port injection matched antenna when $L_p = 25$, $W_p = 18$, $L_s = 35$, $W_s = 28$, $L_g = 5$, and $w = 1.6$ mm (b) L_g on the two-port injection matched antenna when $L_p = 25$, $W_p = 18$, $L_s = 35$, $W_s = 28$, $w = 1.6$ and $g = 1.5$ mm. 246

Figure B.8 Variation of w on the two-port injection matched antenna when $L_p = 25$, $W_p = 18$, $L_s = 35$, $W_s = 28$, $L_g = 5$, and $g = 1.5$ mm. 247

Figure B.9 Variation of (a) L_p on the two-port injection matched antenna when $W_p = 18$, $L_s = 35$, $W_s = 28$, $L_g = 5$, $w = 1.6$ and $g = 1.5$ mm (b) W_p on the two-port injection matched antenna when $L_p = 25$, $L_s = 35$, $W_s = 28$, $L_g = 5$, $w = 1.6$ and $g = 1.5$ mm. 247

List of Tables

Table 2.1 A summary of most significant works related to this thesis. 31

Table 4.1 Lower and upper bounds of the antenna dimensions used in the optimisation of TARC in CST DS. 79

Table 4.2 Dimensions for the optimised TARC resonances shown in Figure 4.14. 80

Table 4.3 Lower and upper bounds of the antenna dimensions used in the fine-tuning of TARC through parameter sweep in CST DS. 80

Table 5.1 Antenna dimensions and −10 dB FBW for the optimised TARC resonances shown in Figure 5.4. 125

Table 5.2 Antenna dimensions and −10 dB FBW for the fine-tuned TARC resonances shown in Figure 5.5. 127

Table 5.3 Antenna dimensions and −10 dB FBW corresponding to the TARC resonances shown in Figure 5.12. 136

Table 6.1 Dimensions for the optimised TARC resonances shown in Figure 6.6. 161

Table 6.2 Calculated FBW for the tunable injection matched patch antennas with resonances depicted in Figure 6.7, where f_{LB}, f_{UB} and f_c are the −10 dB lower boundary, upper boundary, and centre frequencies, respectively. . . . 162

Table 7.1 Dimensions for the optimised TARC resonances shown in Figure 7.4a and for TARC0 in Figure 7.3, and their corresponding ka values calculated at resonant frequencies, f_r. 206

Table 7.2 Dimensions for the fine-tuned TARC resonances shown in Figure 7.6a, and the corresponding ka values calculated at resonant frequencies, f_r. 206

Table B.1 Multilayer mesh settings used in the CMA of proposed patch antennas in this thesis. 245

Table B.2 Multilayer Solver parameter settings used in the CMA of the proposed patch antennas in this thesis. 245

Table B.3 Dimensions for the fine-tuned TARC resonances shown in Figure 4.15.248

List of acronyms and abbreviations

3D three-dimensional 174

1G first generation 1

2G second generation 2

3G third generation 2

3GPP Third Generation Partnership Project 2

4G fourth generation 2

5G fifth generation 3

6G sixth generation 3

AUT antenna under test 47

BW bandwidth 198

CMA characteristic mode analysis 66

COVID-19 coronavirus disease of 2019 v

CPS coplanar stripline 16

CPW coplanar waveguide 16

CST DS CST Design Studio™ 39

CST MWS CST Microwave Studio® 61

CST SS CST Studio Suite® 124

dB decibel 11

dBi decibel relative to isotropic 69

dBm decibel milliwatt 113

DoA direction of arrival 3

ELA electrically large antenna 211

EM electromagnetic 32

ESA electrically small antenna 20

FBW fractional bandwidth 64

FDMA Frequency Division Multiple Access 1

FGP full ground plane 61

GHz Gigahertz 2

GPS global positioning satellite 2

HSPA High Speed Packet Access 2

IMT services International Mobile Telecommunication services 154

IoT Internet of Things 3

ISM Industrial, Scientific and Medical 154

ITU International Telecommunications Union 1

kHz kilohertz 1

LC inductor-capacitor 22

LHS left hand side 53

LTE Long Term Evolution 2

LTE-A LTE - Advanced 2

MEMS microelectromechanical system 22

MHz Megahertz 1

mMIMO massive multiple input multiple output 3

MNOs mobile network operators 1

MRMP multiple radiator multiport 2

MPD multiport driven 10

nH nanohenry 213

NICs negative impedance converters 21

PA power amplifier 18

PEC perfect electric conductor 66

pF picofarad 213

PGP partial ground plane 34

PIN positive-intrinsic–negative 22

RF radio frequency 2

RHS right hand side 52

R&S Rohde and Schwarz 47

SMA Sub-Miniature Version A 27

SNR signal-to-noise ratio 28

SRMP single radiator multiport 3

TACS Total Access Communication System 1

TARC total active reflection coefficient 5

TDS Time Domain Solver 238

TOSM Through, Open, Short and Match 48

UK United Kingdom 1

VNA vector network analyser 47

Wi-Fi Wireless Fidelity 2

Chapter 1

Introduction

1.1 Background

The antenna is an essential component of the wireless system for transforming energy between electrical and electromagnetic energy. Apart from other antenna parameters [1], antenna bandwidth is necessary for capacity enhancements of the wireless system [2]. However, the need for antenna bandwidth is driven by technological advancements.

In the earliest analogue wireless systems such as the first generation (1G) of mobile networks, which used a purely Frequency Division Multiple Access (FDMA) technique [3], the antenna bandwidth of around 15 to 25 Megahertz (MHz) was sufficient to meet the capacity requirements in the access layer for voice communications. For example, in some International Telecommunications Union (ITU) Region 1 countries, such as the United Kingdom (UK), the deployment of Total Access Communication System (TACS) network, which supported between 600 to 1,320 equally spaced 25 kilohertz (kHz) radio channels in the 900 MHz band allowed each of the end-user terminals integrated with a 25 MHz bandwidth antenna to access the network services from any of the authorised mobile

network operators (MNOs) [3]. While the desired capacity was attained, portability of the user equipment was another critical requirement. However, the two conditions were easily met as the desired low antenna bandwidth simplified the antenna design [4].

The increase in capacity needs, being influenced by the introduction of multimedia services such as text, data, video streaming and video on demand, caused the 1G wireless systems to progressively evolve towards the second generation (2G), third generation (3G) and fourth generation (4G) of mobile networks [5]. This evolution caused a progressive rise in the need for large antenna bandwidths, except the 2G systems which use the same radio frequency (RF) spectrum that was allocated for 1G systems, to meet the capacity requirements [6]. Other techniques such as advanced modulation schemes, advanced access techniques, and multiple antenna technology, which utilises multiple radiator multiport (MRMP) configuration, were introduced in the 3G and 4G systems to enhance the capacity requirements, which also complicated the antenna designs [5]. The high mutual coupling effects and bulkiness presented by the MRMP antennas in 3G and 4G systems, such as High Speed Packet Access (HSPA), Long Term Evolution (LTE) and LTE - Advanced (LTE-A), are the main challenges [7–9]. Also, the introduction of carrier aggregation by the Third Generation Partnership Project (3GPP) release 10 influenced the need for realising multiband antennas and even ultra-wideband antennas [10, 11].

Besides, the introduction of secondary systems, such as Bluetooth, global positioning satellite (GPS) transceivers, and Wireless Fidelity (Wi-Fi) systems in mobile phones opened new challenges in antenna designs. As these services are operating in different frequency bands (2.4 Gigahertz (GHz) for Bluetooth, 2.4 and 5.8 GHz for Wi-Fi, and L-band for GPS), the need for multiband, ultra-wideband or multiple antennas is unavoidable. Though multiple antennas have been widely adopted to address this requirement,

multiband or ultra-wideband antennas are cost-effective and enhance user equipment's miniaturisation.

The new technological advancements, such as the fifth generation (5G) and forthcoming sixth generation (6G) systems, take the antenna bandwidth challenge in a new sphere. The capacity needs are so high to foster multimedia services, which include the Internet of Things (IoT). Though advanced modulation schemes, advanced access techniques and multiple antenna technologies such as massive multiple input multiple output (mMIMO) are still employed, a prominent radio spectrum has been allocated by ITU for the gig capacity. For example, the 5G operation in the Sub-6 GHz band (600 MHz to 6 GHz) requires antennas with large bandwidth to cover the whole band or at least part of the band, such as the Sub-6 GHz low-band or Sub-6 GHz high-band (2.3 to 4.7 GHz) depending on the operational mode. To have an antenna covering such massive bandwidths is challenging.

Microstrip patch antennas are proposed in this thesis for addressing the bandwidth requirements of the 5G wireless systems and other dynamically shared services in the Sub-6 GHz high-band because of their planar geometry, being lightweight, easy and inexpensive to fabricate [1]. Though the realisable bandwidths on patch antennas under conventional feeding techniques are limited to around 13% [1], mechanisms are devised in this thesis to achieve high operational bandwidths to cater for the bandwidth requirements of the 5G wireless systems in the Sub-6 GHz high-band. The realised antennas use a single radiator, being excited through two ports forming single radiator multiport (SRMP) patch antennas with the advantage of utilising either of the ports for signal transmission and reception because of the high correlation between the two ports. Features of the MRMP antennas, such as direction of arrival (DoA) estimation [12], diversity transmission and reception,

and electronic beam steering [13], which are not part of this investigation, can also be attained through an SRMP patch antenna.

1.2 Objectives and hypothesis

Two-port SRMP patch antennas have been investigated in [14–16] using the injection matching technique. However, the high bandwidth attained in [16] is also attributed to the lateral displacement of the feed lines from the magnetic symmetry line of the patch, which distorts the antenna cross-polar patterns [17]. The theory for the reflection coefficients, transmission coefficients and the matching efficiency for the two-port injection matched antennas has not been provided [14–16]. Also, the systematic design and validation procedures and the receive mode operation for the two-port injection matched antennas are yet to be characterised. Besides, the wideband, frequency tunability and electrically small operations have not been distinguished from each other in how they can be attained by an injection matched antenna. These knowledge gaps need to be filled to establish a complete characterisation of the injection matched antennas.

This thesis uses the injection matching technique to investigate bandwidth enhancement of two-port single radiator microstrip patch antennas through single resonance and frequency tunability. Particular focus is paid on bandwidth improvement for electrically small patch antennas. Besides, the theoretical and experimental characterisation of the reflection and transmission coefficients, efficiency (radiation, matching and total efficiency), radiation patterns, and the receive mode operation for the two-port injection matched antennas are explored. The main objectives of this study can be summarised as,

(1) Investigating the bandwidth enhancement of patch antennas through single resonance and frequency tunability using the injection matching technique.

(2) Developing a rigorous theory for the two-port injection matched antennas to characterise the reflection and transmission coefficients, antenna efficiency (radiation, matching and total efficiency) and radiation patterns.

(3) Performing the reciprocity analysis of the two-port injection matched antennas to verify an intuitive arrangement of the feeding network around the antenna to be fed by an injection matched antenna in the receive mode.

(4) Formulating the design methodology for the two-port injection matched patch antennas, including the placement of the feed lines.

(5) Formulating the validation procedure for the two-port injection matched antennas to experimentally characterise the total active reflection coefficient (TARC) and radiation patterns for the antennas.

(6) Carrying out an investigation to distinguish between wideband, frequency tunability and electrically small operations attained by the two-port injection matched antennas.

It is assumed that modulating the relative amplitude and phase shift between the two excitation signals that are simultaneously applied to a two-port patch antenna will actively modulate the driving terminal impedances of the antenna. This action will alter the surface current distribution on the antenna to change the frequency of operation and radiation patterns. Also, the bandwidth enhancement of the patch antenna can be attained through the same action. However, the attainability of these features requires

integrating active devices such as the amplifier in the antenna driving circuitry. Though the realised antenna is reciprocal, a rigorous reciprocity analysis is needed to establish how the driving circuitry (feeding network) around the antenna can be arranged to be fed by a multiport antenna in the receive mode. However, the realisation of the driving circuitry for the two-port injection matched antennas lies outside the scope of this study.

1.3 Thesis organisation

The thesis is organised into eight chapters as shown in Figure 1.1. Chapter 2 reviews the various techniques for the implementation of SRMP antennas to achieve wide bandwidth on microstrip patch antennas through single resonance, multiple bands operation, or frequency tunability. The chapter synthesises the valuable concepts that can be merged with the idea of this thesis to enhance the bandwidth of multiport patch antennas.

Chapters 3 to 7 are the main contributions of this thesis. In Chapter 3, the theory that characterises the two-port injection matched antennas to operate in both the transmitting and receiving modes is outlined. Special attention is paid to the reciprocity analysis of the two-port injection matched antennas to verify an intuitive arrangement of the feeding network around the antenna to be fed by an injection matched antenna in the receive mode.

Chapter 4 establishes the design and validation procedures for the two-port injection matched antennas. Also, the theory of characteristic modes is linked with the injection matching technique to determine the position for the placement of the feed lines on the two-port injection matched antennas. Besides, the design and validation procedures are applied to realise and test a two-port injection matched antenna.

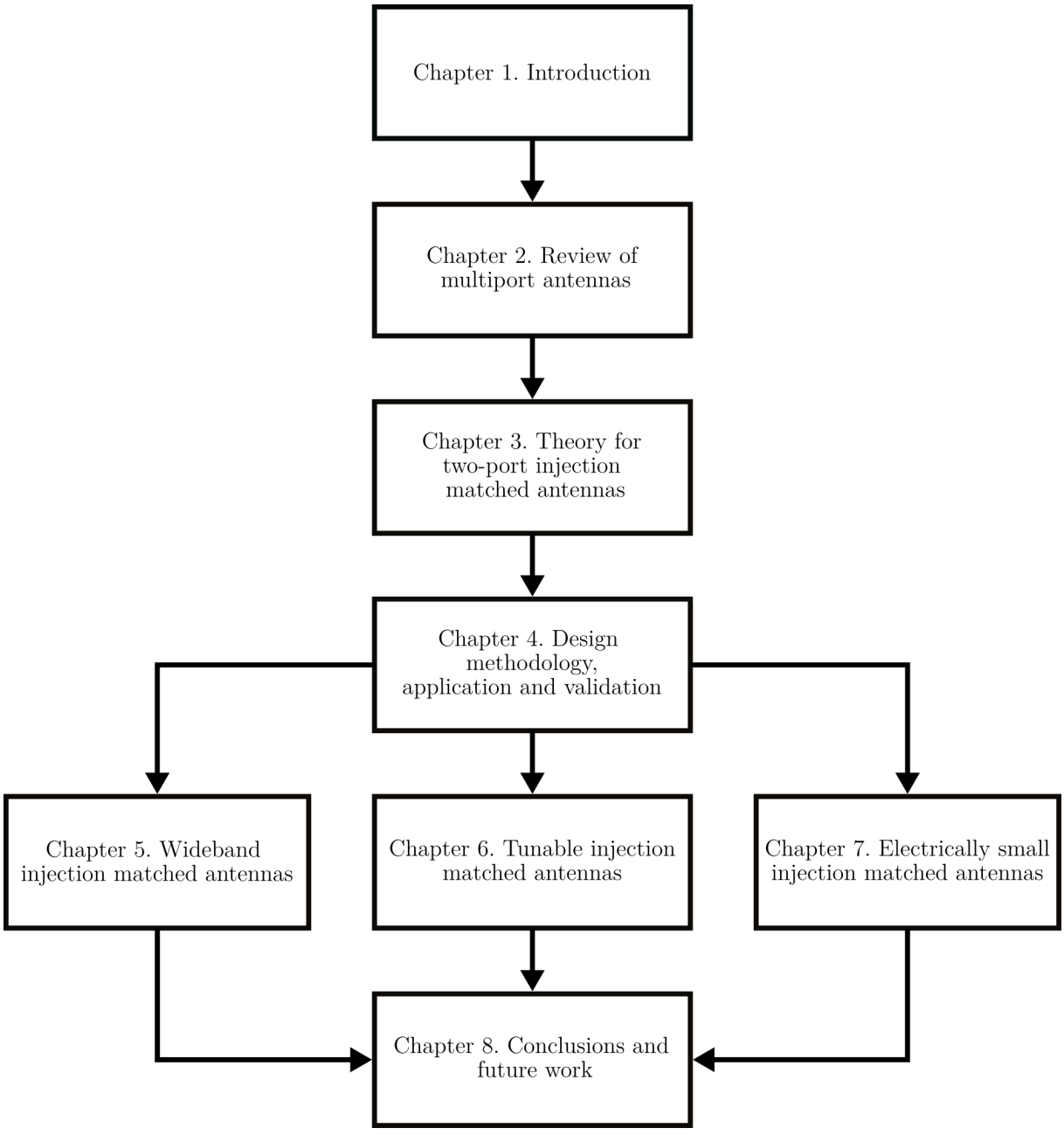


Figure 1.1. Organisation of the thesis chapters.

Particular focus on applying the injection matching technique to achieve wide bandwidth, frequency tunability, and electrically small operation is paid in Chapter 5, 6 and 7. In these chapters, the three operating modes are distinguished from each other in how they can be attained from an injection matched antenna. Other feeding techniques, such as feeding on the opposite corners of the patch and the use of four feed lines, are also discussed in Chapter 5 and 6 to investigate bandwidth enhancements on the patch antenna.

Chapter 8 summarises the main contributions of this thesis, identifies the gaps which are not addressed by this thesis, and suggests future work to be done to improve the study.

Chapter 2

Review of multiport antennas

2.1 Background

In recent years, SRMP antennas [13, 18] are widely being investigated for use in diversity transmission and reception, and in electronic beam steering [13] because of their compact size [12] and low mutual coupling between the multiple ports, though at the expense of low gain and low spectrum efficiency [12], compared to the MRMP antennas [7, 8, 19]. Despite the attractive features of the SRMP antennas, the use of such antennas in higher data rate applications is limited by their operational bandwidth [2].

In this chapter, the various techniques for implementing SRMP antennas are outlined to investigate the possibility of improving the bandwidth of microstrip patch antennas through single resonance, frequency tunability, or multiband resonances. The review is extended to look at the similarities between multiport antennas and characteristic modes of the antenna. Particular focus is paid to the two-port antennas, which are the main concern of this study, finishing with a review on measurement challenges for multiport antennas.

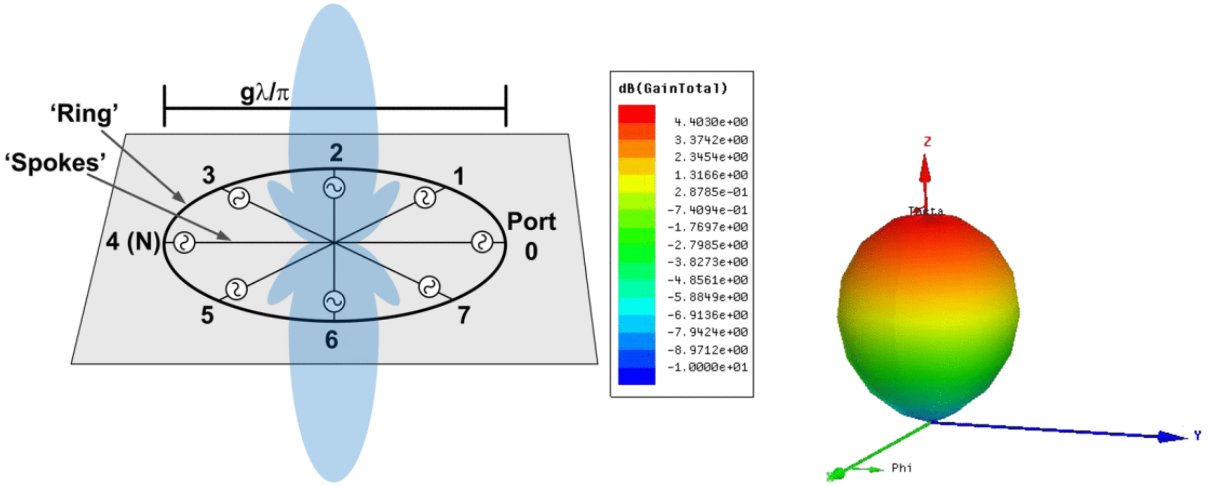
2.2 Single radiator multiport antennas

An SRMP antenna consists of a single radiating element and multiple ports connected to the radiator to allow excitation of the desired feature [12]. In the literature, typical features of power combining [20], directive patterns [21], multi-band resonances [22], and adaptive beamforming capabilities [13] have been reported from SRMP antennas. Though these features do not form the basis of investigations in this thesis, they are being reviewed here to synthesize valuable concepts that can be merged with the proposed idea of this thesis to enhance the bandwidth of multiport patch antennas.

In [20], an SRMP patch antenna for power combining applications was realised by combining different excitation signals with different amplitudes from each of the multiple ports inside the antenna. The amplitude of each excitation signal was attained by the use of an amplifier positioned externally to the antenna. The idea utilises a similar approach proposed in this thesis though it lacks some features of controlling the phases of the excitation signals. However, there is no improvement in bandwidth by the SRMP antenna of this configuration when compared to the corresponding single-port antenna. The antenna dimensions are also large to support miniaturisation.

An integrated multiport driven (MPD) radiator is reported in [21]. The radiator is formed by a ring designed similarly to a bicycle ring with spokes, where the spokes represent the grounding lines, which provide a path for routing the return currents from the circumference of the ring to the centre of the ring as depicted in Figure 2.1a. The antenna is excited through multiple integrated driving circuits realised from amplifiers and oscillators. The desired pattern from the antenna is attained by altering the surface current distribution on the antenna by controlling the injected currents through a mechanism

described in [21]. The approach uses a similar feature, to the proposed antenna of this thesis, of changing the surface current distribution on the antenna to achieve the desired pattern. However, the challenge with this configuration lies in its complexity in realising the driving circuitry, which requires the driving currents to be well controlled to avoid the reflected currents from cancelling out the input signal currents. In particular, the realised pattern is circularly polarised with a maximum directive gain of around 4.4 dBi as shown in Figure 2.1b.



(a) **(b)**

Figure 2.1. (a) An integrated multiport driven antenna architecture (b) radiation pattern for the multiport driven antenna [21].

A passive and compact SRMP multiband antenna has been proposed in [22]. The antenna has three ports sharing the same radiator composed of two Sierpinski fractal triangles, where the two ports are the main ports, and the third port is an auxiliary port. Wideband operation is attained between 1 and 4 GHz at each of the two main ports, while multiband operations are attained at the auxiliary port around 2.4, 3.4, and 5.2 GHz frequencies. The minimum port isolation is around 5 decibel (dB) as shown in Figure 2.2. The technique used in this configuration to achieve good isolation between

the multiple ports can be utilised in the antennas of [14, 15], which also form the basis of investigations in this thesis.

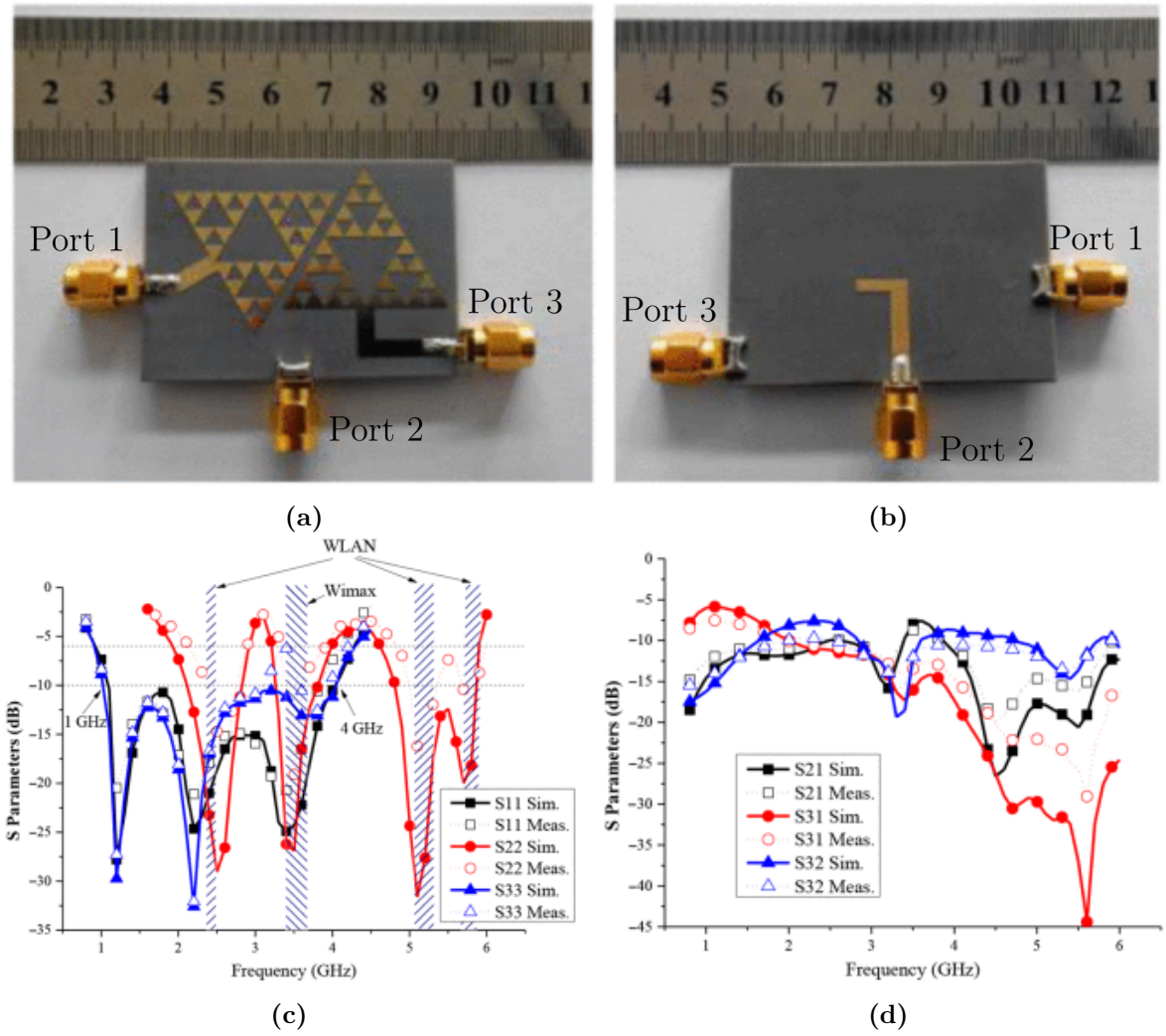


Figure 2.2. (a) Front view of the multiband antenna (b) back view of the multiband antenna (c) simulated and measured reflection coefficients (d) simulated and measured isolation between the multiple ports [21].

Another SRMP patch antenna is reported in [13]. The antenna was excited through four ports, which were probe fed from the ground plane below the substrate as shown in Figure 2.3a. Good port isolation shown in Figure 2.3b was attained, which showed good performance in beam steering, interference mitigation and DoA estimation compared to the corresponding 2×2 MRMP antenna, according to the tests performed in [13]. However,

the SRMP antenna is more complex to design than the corresponding MRMP antennas because of the small spacing between the multiple ports. A similar approach in [13] can be utilised in the proposed antennas of this thesis to achieve good port isolation and to investigate other functionalities such as beamforming applications.

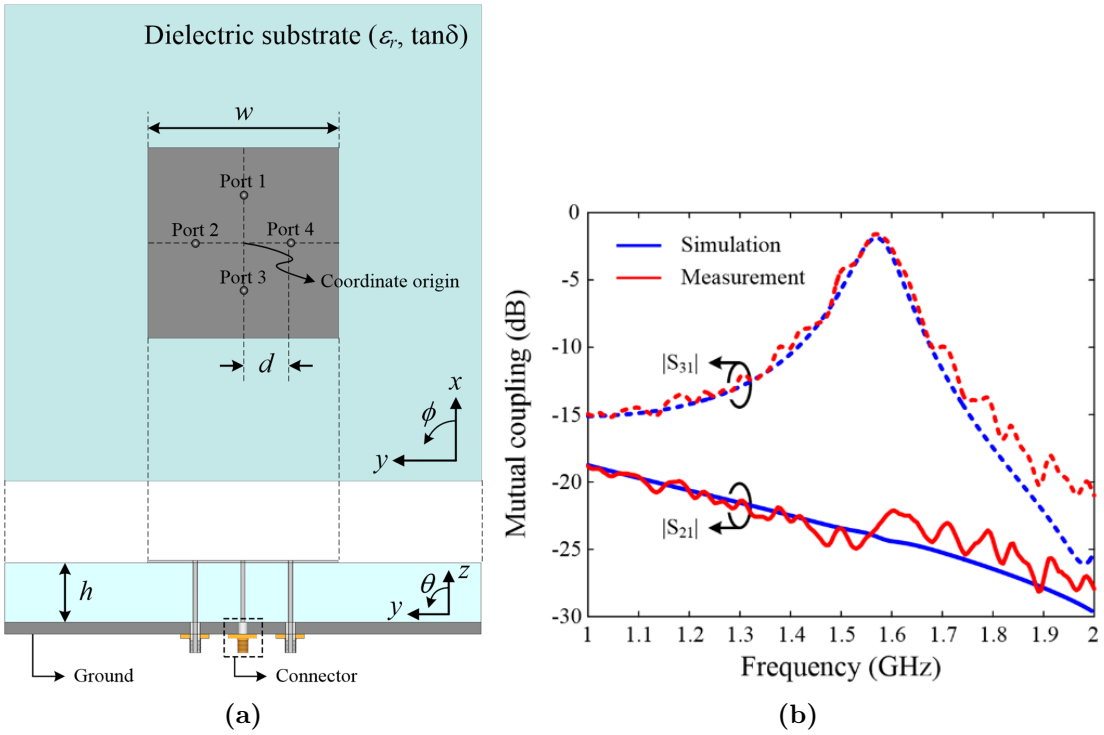


Figure 2.3. (a) An SRMP antenna with $w = 44.6$ mm, $d = 9.4$ mm and $h = 1.6$ mm printed on FR4 substrate with $\varepsilon_r = 4.5$ (b) Isolation between multiple ports of an SRMP antenna [13].

In [23], a modified approach to the one in [20] was used to attain power combining inside the antenna by introducing a phase shifter at each of the multiple ports. The phase shifters were essentially for changing the antenna polarisation by simply altering the phase at each port to achieve power combining in different polarisation states. Though the idea in this configuration looks similar to the proposed antennas in this thesis, the structure is bulky because of the incorporated multiple phase shifters and amplifiers. Also, the polarisation of the antenna in [23] is circularly changed in different states by combining the phase shifts for the different excitation signals at the multiple ports, contrary to the

proposed technique in this thesis, which does not alter the antenna polarisation by simply changing the phase shift at the multiple ports. In this thesis, the antenna polarisation can only be altered by changing the feeding arrangement and the antenna configuration during the design process.

According to the presented literature in this section, the challenge in designing the SRMP antennas lies in the small spacing between the multiple ports, which makes it difficult to attain high port isolation, limiting the number of the supported multiple ports. As a result, most SRMP antennas are considerably large, making them not a better choice for miniaturisation.

2.3 Characteristic modes vs multiport antennas

The theory of characteristic modes is widely being used in the realisation of multiport antennas. In SRMP antennas, this is achieved by exciting multiple modes on the surface of the radiator by use of multiple ports or multiple feeds [24, 25]. The excitation of multiple modes is attained by grouping similar significant modes at each port, which are jointly excited either differentially or in common mode by the use of multiple voltage sources [24]. Because the modes belonging to the same group are correlated to each other, they are jointly excited by the same applied excitation. As a result of simultaneous excitation of the multiple similar modes from each of the orthogonal ports, broadband operation with high port isolation can easily be obtained [25].

In [25], a planar four-port multimode SRMP antenna was investigated for beamforming applications. Different radiation characteristics were obtained from each port, allowing the ports to be independently utilised in the beam scanning. The antenna showed the gain

enhancement of up to around 3 dB in various scan angles as measured from the different antenna ports. This observation indicates that good port isolation can be attained from multimode SRMP antennas. Another similar four-port antenna was realised in [26] for the DoA estimation with low mutual coupling between the multiple ports. Because of the orthogonal behaviour of the radiated signals from the different ports and the low mutual coupling between the multiple ports, an N-port multimode antenna can mimic an N-element antenna array. Besides, though the investigations were based on the parameter which is not part of this thesis, it is generally shown that good port isolation can be achieved on an SRMP antenna.

In contrast to the injection matching technique reported in [14], the multimode SRMP antennas use a similar feeding mechanism when the differential excitation mode is employed [27]. This observation shows that the injection matching technique is also based on the excitation of multiple characteristic modes through differential feeding. However, because of the methods used in locating the feeding points for each port [24, 27], the resulted antenna ports are already matched to the 50 Ω impedance, making the frequency tuning by altering the phases and amplitudes of the excitation signals impossible as it disturbs the port matching. That is because only a phase shift of 180° is allowed in the differential excitation mode [27, p. 3909].

However, some challenges arise from multimode SRMP antennas, one of them being the realisation of multiple voltage sources for each port configuration, which requires the use of multiple signal splitters, and multiple 180° hybrid couplers when differential feeding is needed, to deliver the excitations at the multiple feed points for each port that need to be simultaneously driven [27, p. 3909]. This requirement makes the driving circuitry for each port bulky and complex to realise, which may compromise the number of feasible

ports on the multiport antenna. Also, the arrangement of ports requires a consideration of the symmetry of the modes while at the same time ensuring that the number of ports is minimised to minimise the coupling between them [24]. Besides, the excitation of specific modes from a group of correlated modes is restricted because of the high correlation between the modal currents, which limits the number of uncorrelated antenna ports [24].

2.4 The two-port antennas

There are quite a several techniques that give a two-port antenna configuration the ability to either provide bandwidth enhancements [28, 29], electrically small operations [30–32], multiband operations [33], or frequency tunability [34].

2.4.1 Two-port wideband antennas

In [29], an integrated ultra-wideband antenna has been proposed. The antenna was realised by integrating a coplanar waveguide (CPW) to coplanar stripline (CPS) transition, a tapered slot antenna with elliptical tapering, and a rectangular loop slot antenna in a composite structure shown in Figure 2.4 by following the design procedure outlined in [28, 29, 35–38]. An ultra-wideband operation was attained by integrating an elliptically tapered slot antenna of Figure 2.4d onto the ports P_a and P_b of the CPW to CPS transition. Also, integration of the rectangular loop slot antenna onto the gap between the two tapered slots of the ultra-wideband antenna produced a narrowband operation at port P2 without affecting the ultra-bandwidth at port P1. Besides, a minimum port isolation of 45 dB shown in Figure 2.4e was achieved. Though the antenna has potential ultra-wide

bandwidth and good port isolation, it is difficult to realise because of the complexity in modelling the coupling losses between the three elements.

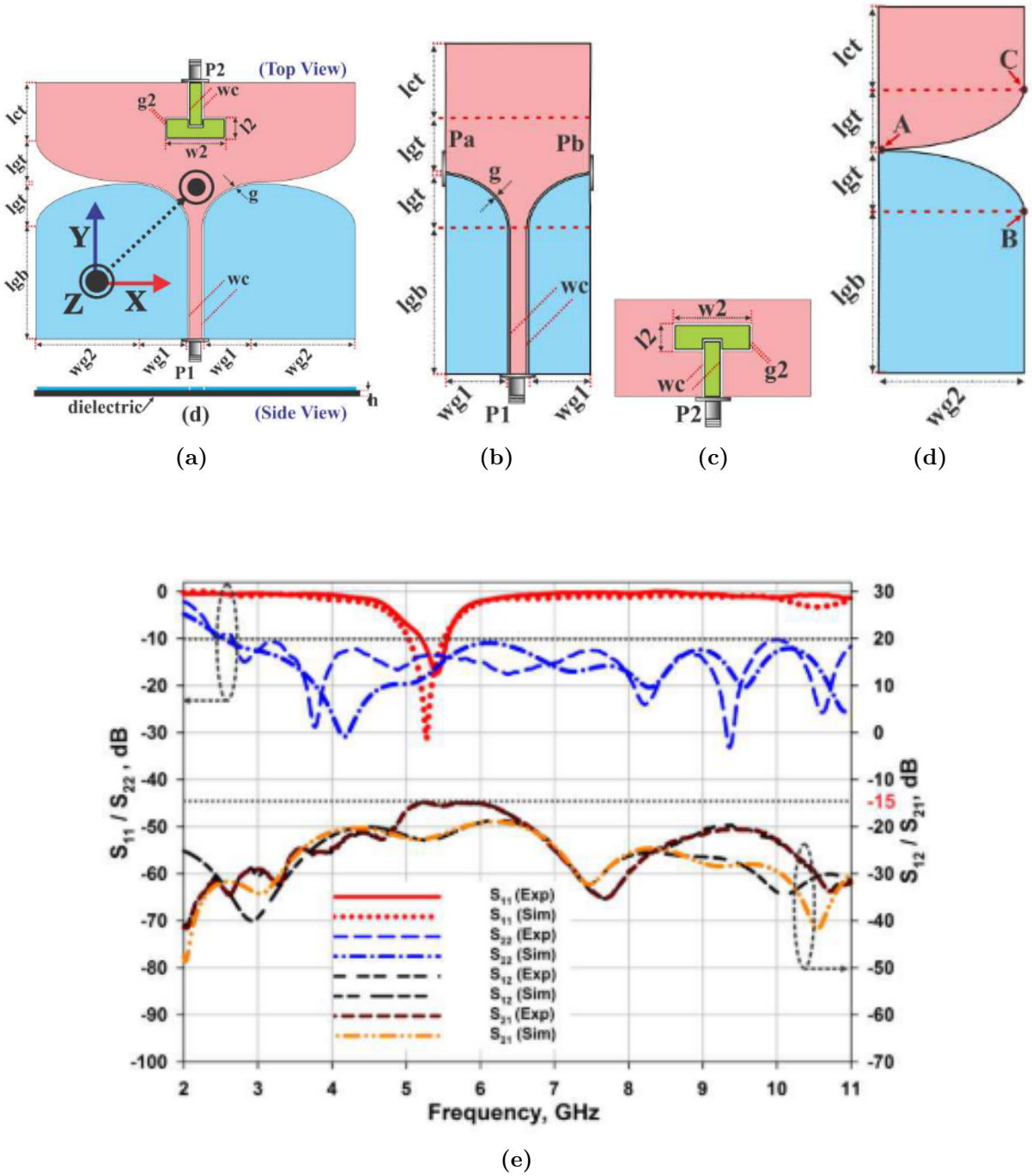


Figure 2.4. (a) An ultra-wideband antenna (b) CPW to CPS transition (c) rectangular loop slot antenna (d) tapered slot antenna (e) simulated transmission and reflection coefficients for the wide-narrowband antenna [29].

Another two-port based approach for realising wideband antennas is outlined in [28]. In this case, a monopole antenna with a CPW feeding architecture was integrated with a shorted microstrip patch antenna excited through a tapered microstrip feed line. The antenna was configured to allow the monopole antenna to provide the grounding plane for the shorted patch antenna. The monopole antenna offers wideband operation at frequencies between 3 and 11 GHz, whereas the shorted microstrip antenna provides a narrowband operation between 5.15 and 5.35 GHz, with minimum isolation of around 5 dB across its bandwidth [28]. However, the antenna is complex to realise because of the difficulty in modelling the coupling between the two radiators. The realised antenna finds applications in cognitive radio operations.

A wideband antenna can also be realised from the Doherty amplification technique [39, 40]. The main concept of Doherty Amplification is based on utilising the active load modulation attained through an impedance transforming quarter wavelength, $\lambda/4$ transformer shown in Figure 2.5a to match the two elements of an antenna array connected at the carrier power amplifier (PA) and peaking PA branches. In this case, the self and mutual impedance of the connected antennas and the currents flowing through the two amplifiers are used to efficiently match the two antenna elements to the 50 Ω source. The transmission line (shown in Figure 2.5a) or phase delay (shown in Figure 2.5b) in the peaking PA is used to optimise the load impedance for the carrier PA when the system is in saturation. This action alters the load impedance of the carrier PA to operate at a low power level such that it only depends on the self impedance of the antenna element, which drives the PA into saturation earlier for efficiency enhancement in the back-off region. However, the load impedance is decreased at a high power level so that more output power is delivered. A typically designed active array in [39] showed that

by adjusting the ratio I_2/I_1, Z_{in1} could be modulated between around 30 Ω and 52 Ω as shown in Figure 2.5c and 2.5d.

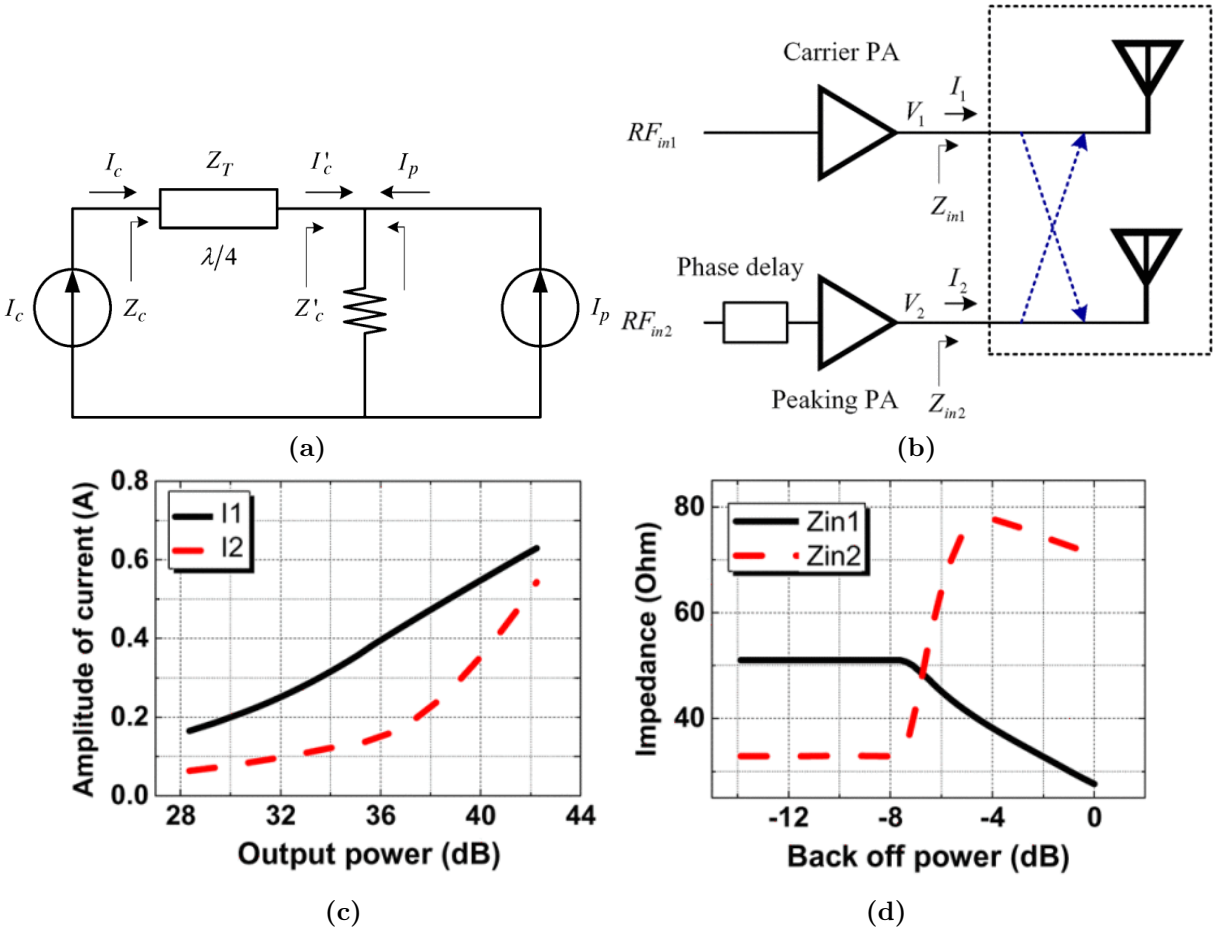


Figure 2.5. (a) Doherty amplifier operational diagram (b) active load modulation with Doherty amplifier (c) simulated currents for the carrier and peaking amplifiers (d) simulated impedances for the carrier and peaking amplifiers [39].

Although in saturation, Z_{in1} was affected by the phase delay of the current at the peaking PA, by maintaining the current ratio I_2/I_1 and a 90° phase delay, it was possible to realise Z_{in1} of 52 Ω in the power back-off region. Because of the analogy between the two-element antenna array and two-port antenna, the concept of Doherty amplification can be deducted for a two-port antenna, which is the main focus of this thesis.

Typically, an injection matching technique was derived from the operational principle of the Doherty amplifier [14]. The technique was then applied in the realisation of a

two-port wideband antenna [16]. Through adjustment of the phase shift and relative amplitude between the two excitation signals at the two ports of the two-port proximity-fed microstrip patch antenna, a -10 dB impedance matched bandwidth of around $2.4:1$ was achieved. Comparing this method with a traditional approach for realising patch antennas where a fractional bandwidth of up to around 13% is possible [1], this is a great achievement in patch antennas. However, some drawbacks arise from the bulkiness of the driving circuitry, which includes phase shifter, signal splitter and amplifier, that are essentially needed to perform the injection matching. Also, the feed lines were laterally displaced from the magnetic symmetry line of the patch, which distorts the antenna cross-polar patterns [17].

2.4.2 Two-port electrically small antennas

Electrically small antennas are one whose electrical length satisfies the condition $ka < 1$, where a is the radius of the hypothetical Chu sphere circumscribing the maximum dimension of the antenna, $k = 2\pi/\lambda$ is the free space wavenumber, and λ is the free space wavelength [41, 42]. Because an electrically small antenna (ESA) occupies a small volume in the Chu sphere, its radiation resistance, R_r, becomes very low while its capacitive reactance, X_a is very high [43, 44]. Since $X_a \gg R_r$ for an ESA, the quality factor $Q = X_a/R_r$ becomes very high [45]. The low value of radiation resistance for electrically small antennas is translated to low radiation efficiency and, consequently, low total efficiency. In contrast, the high value of Q factor is translated to the narrow bandwidth exhibited by ESAs [46].

The design of an electrically small antenna involves finding trade-offs between Q, bandwidth and efficiency. However, the lowest possible Q attained by an ESA is limited by the Chu limit $Q_{Chu} \geq (1/(ka)^3 + 1/ka)$ [47]. Therefore, making Q close to the Chu limit may attain an ESA with enhanced performance.

The most efficient and wideband ESA is obtained by maximising the volume utilised by the antenna in the hypothetical Chu sphere [48]. However, this method is limited in shape as planar antennas are often highly preferred in a range of applications. Other techniques which are less efficient are based on tuning with Foster or non-Foster elements [31, 49–51], and on the incorporation of slow-wave structures on the antenna [52].

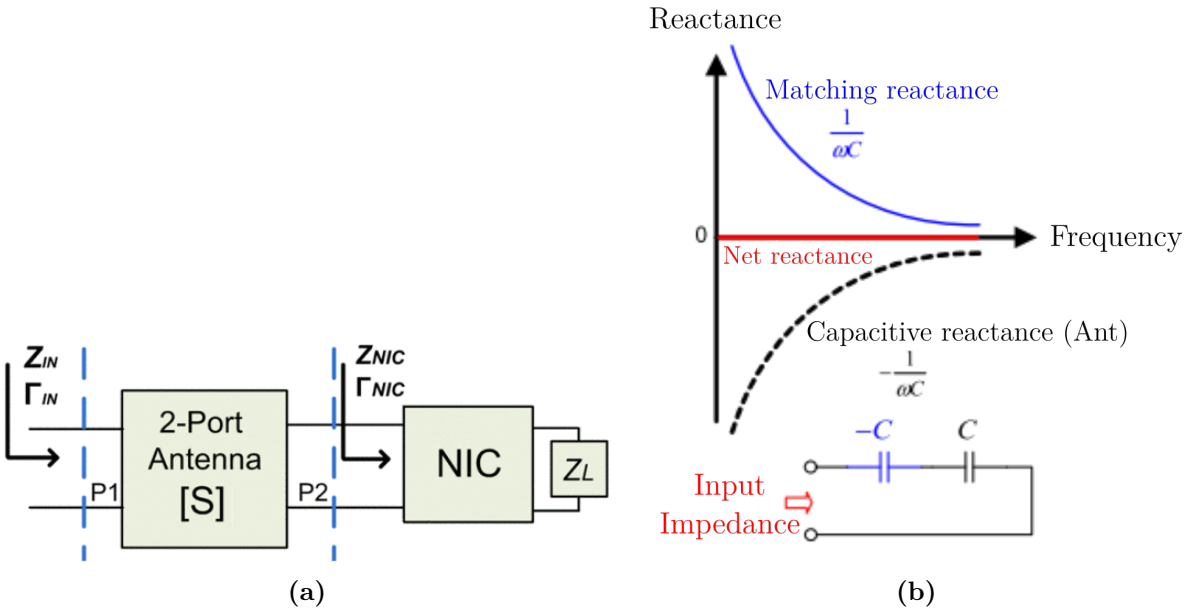


Figure 2.6. (a) Two-port antenna active matching with NICs (b) variation of reactance with frequency [30, 53].

In a two-port configuration, a wideband ESA can be realised through tuning with non-Foster elements [30] as shown in Figure 2.6a. The scheme utilises the decrease in reactance with the increase in frequency feature of the negative impedance converters (NICs) to cancel the capacitive reactance of the antenna in a broad frequency range as shown in

Figure 2.6b. As applied to a semi-loop antenna [30], the electrical length ka ranging between 0.04 and 0.17 was achieved, though at the expense of stability, losses, and antenna efficiency.

An electrically small mode of a two-port antenna is also reported in [14, 15, 54] through injection matching technique. The approach uses the variation of relative amplitude and phase shift between the two coherent excitation signals to match the antenna to the source. However, the reflection coefficient at port two of the antenna and the coupling between the two ports were not reported [14, 15]. Though the reflection coefficient in [54] was derived from the two ports and was characterised by the TARC, there was an inductor-capacitor (LC) matching network introduced to the antenna. The use of an LC matching network in [54] does not provide a clue on whether the electrically small operation was attained by the LC matching network or by the injection matching technique. Because of these two factors, the applicability of the injection matching technique to ESAs needs to be further investigated.

2.4.3 Two-port frequency tunable antennas

Frequency tunable (or reconfigurable) antennas are mainly realised by the use of microelectromechanical system (MEMS) switches and semiconductor switches (positive-intrinsic–negative (PIN) diodes and varactor diodes) [55]. Despite being slow in response, MEMS have the advantages of low insertion losses and low power consumption. PIN diodes are advantageous for being fast in response, having a high power handling capability and being small in size. However, their stability is problematic when biased, which degrades the antenna efficiency [55]. On the other hand, the variation of capacitance

of the varactor diodes is very sensitive to the bias voltage, making them unsuitable in handling high-power signals [55].

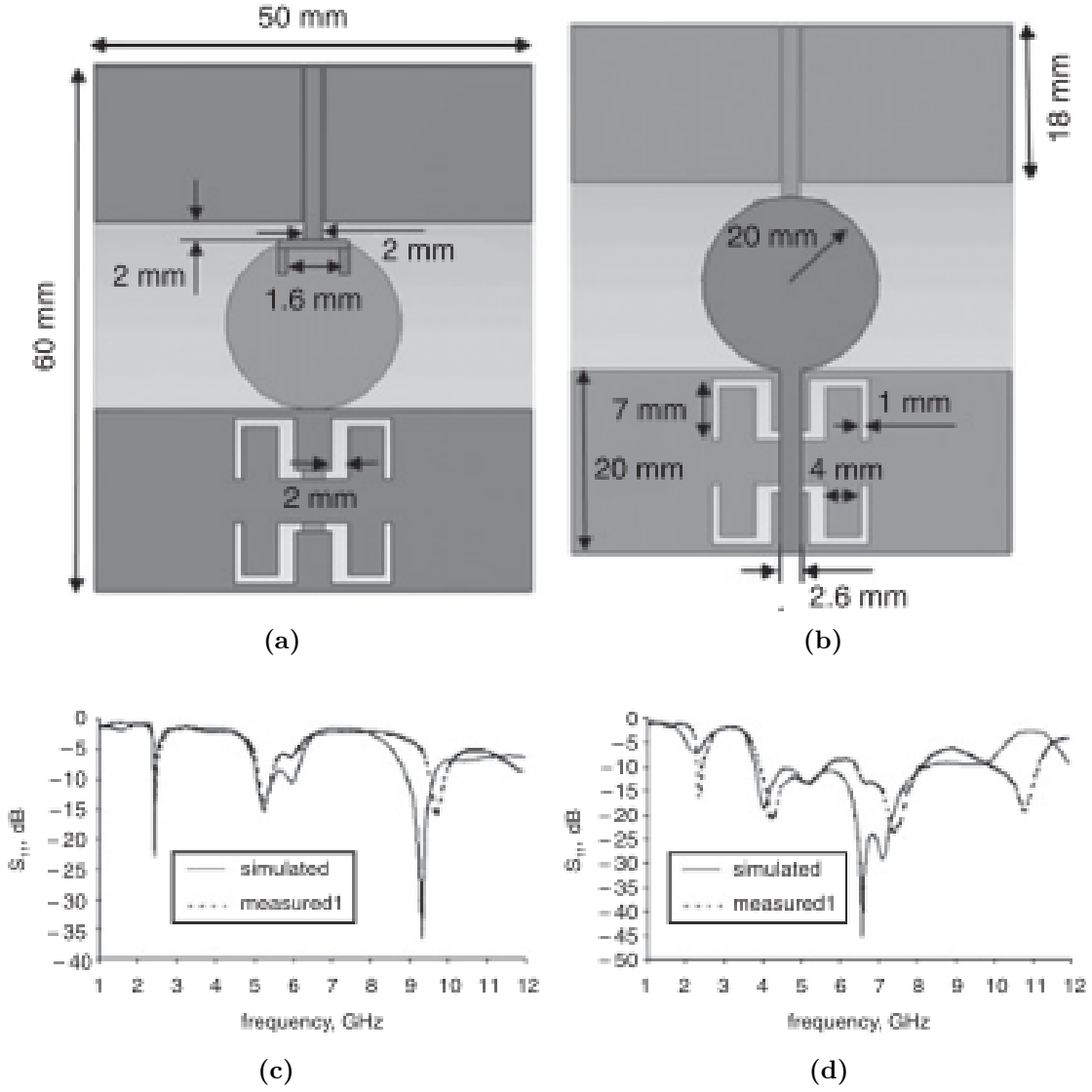


Figure 2.7. (a) Front view (b) back view (c) reflection coefficient on narrowband port (d) reflection coefficient on wideband port for the disc monopole antenna [56].

In [56], a two-port frequency reconfigurable antenna has been realised by exciting a disc monopole from its two ends as shown in Figure 2.7 by use of coplanar and microstrip feed lines. The defect slots were created on the ground plane of the microstrip feed line to suppress the undesired out of band frequencies. The tuning of this antenna was achieved by varying the length of the slots. A wideband operation was attained from the coplanar

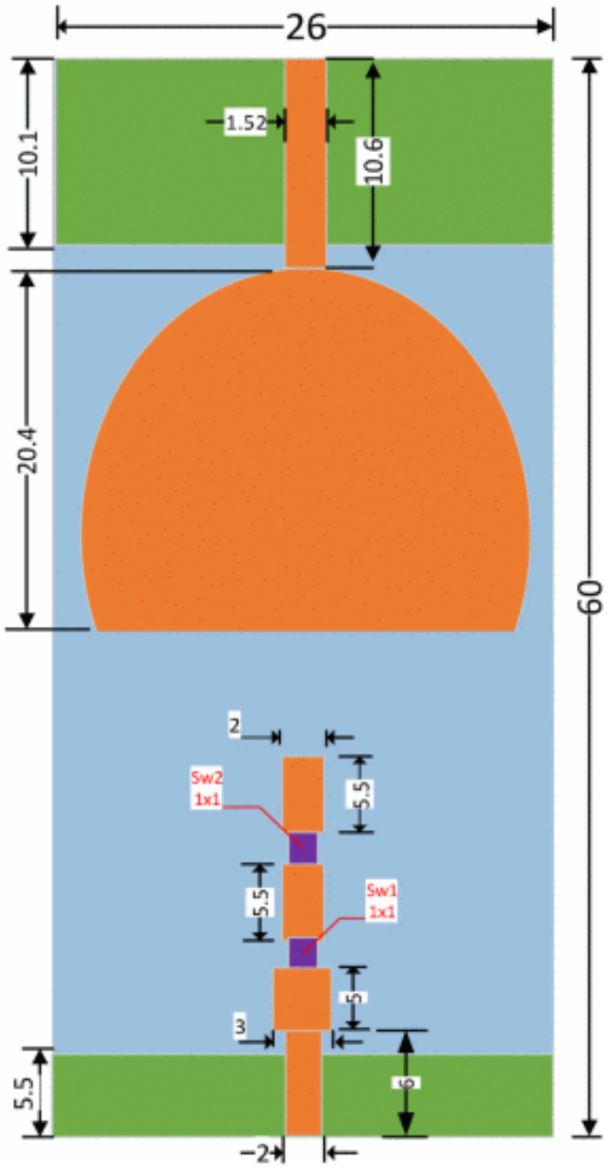


Figure 2.8. Structure of a dual-port frequency reconfigurable antenna proposed in [57].

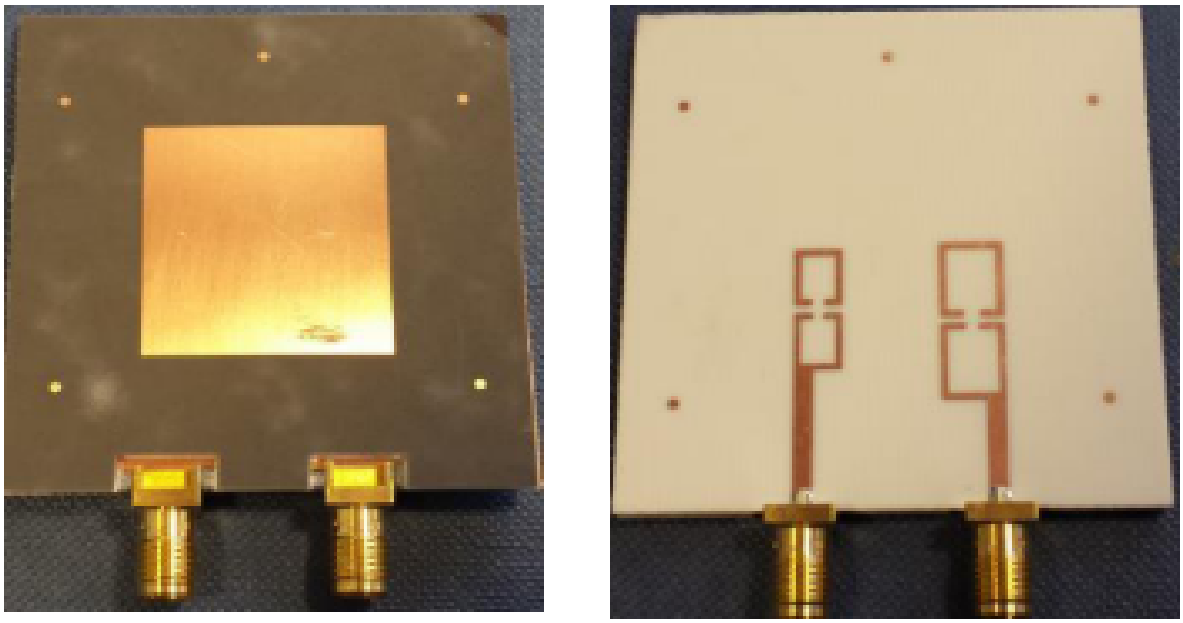
feed line port and a narrowband resonance at the microstrip feed line port. The minimum isolation between the two ports was around 10 dB. However, the antenna does not provide a tuning flexibility [56].

A modified version of the disc monopole antenna (shown in Figure 2.8) has been studied in [57] for cognitive radio applications. The radiator was sliced on one end, and the feeding arrangement on the narrowband port was modified to incorporate two electronic switches for the narrowband tuning. A wideband resonance at one of the ports is used for beam scanning, and the tunable narrowband resonance is used for communication [57]. The attained isolation between the two ports is greater than 10 dB. However, because the narrowband feeding arrangement forms the second radiator, it is difficult to control the mutual coupling between the two radiators.

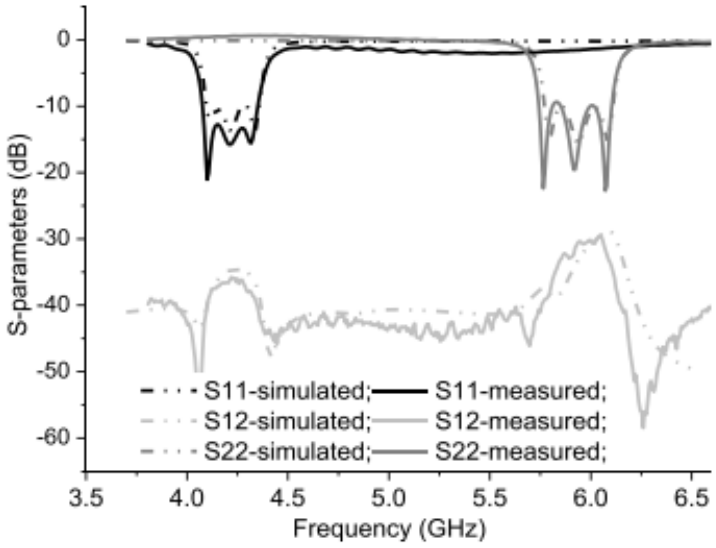
In [14, 15], wideband frequency tuning of a microstrip patch antenna has been achieved by varying the phase shift and relative amplitude between the two excitation signals from two coherent sources through the injection matching technique. However, the reflection coefficient at port two of the antenna and isolation between the two ports were not reported. Because of these factors, there is no evidence of whether the injection matching technique can achieve frequency tunability. The main drawback of this approach is the bulkiness of the antenna driving circuitry, which includes phase shifter, signal splitter and amplifier, that are needed to perform the injection matching.

2.4.4 Two-port multiband antennas

Multiband antennas provide another alternative for addressing the bandwidth requirements in wireless communications [59]. They are realised by introducing meandered sec-



(a) **(b)**



(c)

Figure 2.9. (a) Front (b) back view of the two-port dual-band duplexing antenna (c) reflection coefficients and isolation between the two ports of the dual-band duplexing antenna [58].

tions on the antenna radiating element through the creation of slits and or slots [59–61], or by use of multiport excitations where the reflection coefficient from each port is utilised for resonance on a separate frequency band. When these slits and slots are introduced on a single radiator two-port antenna, the antenna is converted to a multiband two-port antenna.

A typical example of a two-port multiband antenna is given in [58], where a dual-port dual-band dual-polarised antenna with duplexing and filtering functionality has been proposed. The antenna consists of the printed patch on the upper substrate and feeding arrangements printed below the lower substrate, where the two printed layers share the same slotted ground in the middle layer as shown in Figure 2.9. To allow excitation of orthogonal polarisations of the patch, the two slots in the ground plane were created perpendicular to each other. Each of the feeding networks consists of the hairpin resonator and stub-loaded resonator, shown in Figure 2.9b, which provide the design flexibility in adjusting the frequency ratio of the two bands. The two ports are working in two separate frequency bands with high isolation between them, as shown in Figure 2.9c. The attained fractional bandwidths from the two resonances were around 4.8% and 5.1% with minimum port isolation of around 30 dB. However, it is difficult to control the coupling between resonators in the feeding networks, complicating the design process.

2.5 Measurement challenges in multiport antennas

Measurement challenges in multiport antennas range from the inflexibility of the required testing tools, the stray inductance of the Sub-Miniature Version A (SMA) connectors [20], mutual coupling between multiple ports and feeding networks [62, 63], beam squinting

with frequency [64], and variations of the relative phases and amplitudes of the signal components in the far-field of the antennas [65].

Most of the tools in anechoic chambers are designated for single-port antennas, lacking multiport functionality. Therefore, some modifications may be required to allow the characterisation of multiport antennas.

A study carried in [20] on a multiport patch antenna has revealed that the inductance of SMA connectors influences the resonance of the antenna, which changes the corresponding radiation pattern.

The mutual coupling between multiple ports in SRMP antennas or between array elements in MRMP antennas predominantly affects the multiport antenna radiation patterns as low mutual coupling losses are desired for optimal patterns [62, 63]. In antenna arrays, the high mutual coupling between array elements will decrease the power level radiated by the antenna array and therefore reduces the range of the antenna or system capacity due to a reduction in signal-to-noise ratio (SNR) [62]. Also, the high mutual coupling between the multiple ports reduces the active reflection coefficient of the SRMP antenna, which reduces the radiation efficiency of the antenna [13]. However, the effect of mutual coupling in multiport antennas can be minimised by increasing the distance of separation between the antenna ports or array elements. However, in MRMP antennas, the increase in separation between array elements increases the antenna size, which is then translated to high side-lobes in the far-field of the antenna that may lead to adjacent channel interference [62]. Also, increasing the separation between the multiple ports in SRMP antennas results in large antenna sizes, making them unsuitable for miniaturisation.

In active multiport antennas, beam squinting with frequency is a common notable problem caused by the usage of time delay circuits in the antenna driving circuitry [64].

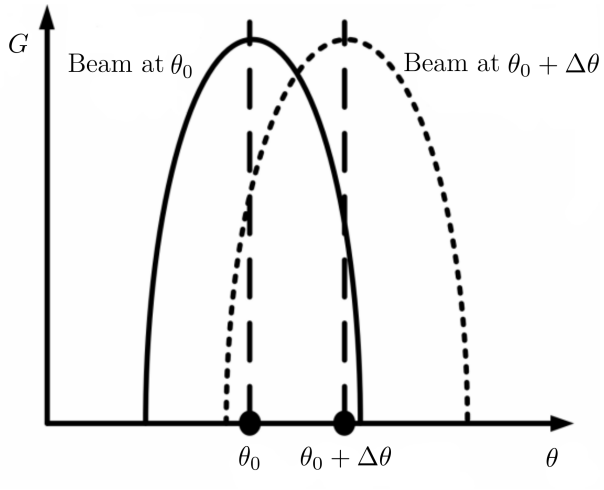


Figure 2.10. Illustration of beam squinting on antenna pattern [64].

Such use of time delay circuits gives rise to a non-linear variation of the phase with frequency in the far-field of the antenna. The variation of phase in the antenna far-field directs the antenna pattern towards $\theta_0 + \Delta\theta$ at frequency $f_0 + \Delta f$ instead of θ_0, which was the pointing direction at frequency f_0 as shown in Figure 2.10 [64], resulting to the deformation of the antenna beam pattern [66]. The effect is translated to a reduction of antenna gain, G in the direction θ_0, while at the same time limiting the usable bandwidth of the antenna [64].

In antenna arrays, the variation in amplitudes of the signal components caused by thermal effects on the active circuit elements such as power amplifiers affects the peak gain and sidelobe levels [67]. On the other hand, the distribution of the relative phase error affects the orientation of the radiation pattern [65]. When the phase error is uniformly distributed over the array elements, the main beam direction is unaffected, but the nulls suffer from severe degradation of around 10 to 20 dB [65]. However, when the phase error is non-uniformly distributed, the main beam will be changed to a different direction, resulting in the beam squint [65, 68]. Phase error variation in antenna arrays is caused by

thermal effects arising from active components and manufacturing tolerances in the RF feeding networks [64, 69].

2.6 Towards the research of this thesis

Based on the reviewed literature and the summary established in Table 2.1, active multiport antennas with Doherty amplifier integration have shown an attractive feature of efficient matching in a broad frequency range [39]. This feature inspired the construction of a two-port antenna, which functions by utilising the variations of the phase shift and relative amplitude of the signal at port two of the antenna to match the two ports to the 50 Ω coherent sources [54]. The broadband operation [16], frequency tunability [14, 15], and an electrically small operation mode [14, 15] have been reported through the injection matching technique.

However, the reflection coefficient at port two of the antenna and isolation between the two ports were not reported in [14, 15]. Though the reflection coefficient in [54] was derived from the two ports and characterised by the TARC, the antenna was also matched with an LC network. These two issues pose a question on whether the injection matching technique works as it has been reported.

Besides, the theory for characterising the reflection and transmission coefficients and total efficiency for the injection matched antennas has not been provided. It is also not known how the injection matched antennas can be made to work in receive mode. On the other hand, the systematic design procedure for the two-port injection matched antennas has not been formulated. The experimental procedure for characterising the far-field patterns is also yet to be established.

It is also reported in [70] that the position of the feed lines and port locations could affect the performance of the injection matched antennas, but there is no guideline for positioning the feeds and ports. The conditions under which the injection matched antenna can work in broadband, frequency tunability or electrically small modes were not distinguished. These are the knowledge gaps that need to be filled before a complete characterisation of the injection matched antennas is established.

Table 2.1. A summary of most significant works related to this thesis.

Features	**Literature/Technique**				
	Multimode antenna [24, 27]	Integrated ultra-wideband antenna [29]	Power combining antenna [20, 23]	Doherty amplification [39, 40]	Injection matching technique [14–16, 54]
Operational bandwidth	High	4.2:1	<30%	50%	Not clear
Radiation efficiency	High	>70%	Unreported	High	High
Total efficiency	High	Unreported	70%	>50%	>80%
Port isolation (dB)	Unreported	>45	Unreported	>12	Not clear
Frequency reconfigurability	Unreported	No	No	Unreported	Not clear
Multiband operations	Yes	Yes	Unreported	Unreported	Unreported
Miniaturisation support	No	Yes	No	Yes, but requires bulky driving circuitry	Yes, but requires bulky driving circuitry
ESA mode attainability	Unreported	Unreported	Unreported	Unreported	Not clear
Design complexity	Simple	Very complex	Difficulty	Simple	Simple

This thesis aims to investigate the bandwidth enhancement of microstrip patch antennas using injection matching technique while characterising the reflection and transmission coefficients, efficiency (radiation, matching and total efficiency), and radiation patterns of the injection matched antennas from a theoretical and an experimental point of view. Also, the reciprocity analysis of the two-port injection matched antennas to verify an intuitive arrangement of the feeding network around the antenna to be fed by an injection matched antenna in receive mode is discussed. A linkage between the injection matching theory and theory of characteristic modes is used to precisely determine the feeding positions for the injection matched antennas' optimum performance. The theoretical and experimental investigation of injection matched antennas to distinguish between broadband mode, electrically small mode and frequency tunability is also discussed.

2.6.1 Strategy for bandwidth enhancement

Attaining wide bandwidths from microstrip patch antennas under conventional feeding mechanisms is infeasible because of the stored electromagnetic (EM) at the metal-substrate boundaries. However, through modifications of the patch antenna's radiating element [71, 72] and or ground plane [73], one can achieve ultra-wide bandwidth. In the literature, truncating the grounding plane of a patch antenna to form a planar monopole antenna is advantageous in terms of high bandwidth and good antenna performance, attaining omnidirectional radiation patterns. Rectangular, circular, and elliptical patch antennas are preferred in implementing planar monopole antennas because they provide broad bandwidth among the microstrip patch antenna configurations [74].

Though the circular and elliptical patch monopole antennas attain higher bandwidths than the rectangular patch antenna, their radiation characteristics are less stable [74]. This reason promotes the rectangular monopole antenna for bandwidth enhancements. The omnidirectivity of the rectangular planar monopole antenna can be utilised for the surrounding transmission and reception of signals, a feature needed by wireless systems that use multi-path propagation. Also, the monopole antenna is miniaturised to operate at considerably low frequencies compared to the traditional patch antenna of the same size. However, all these potentials are achieved when the symmetry property of the dipole antenna is satisfied during excitation.

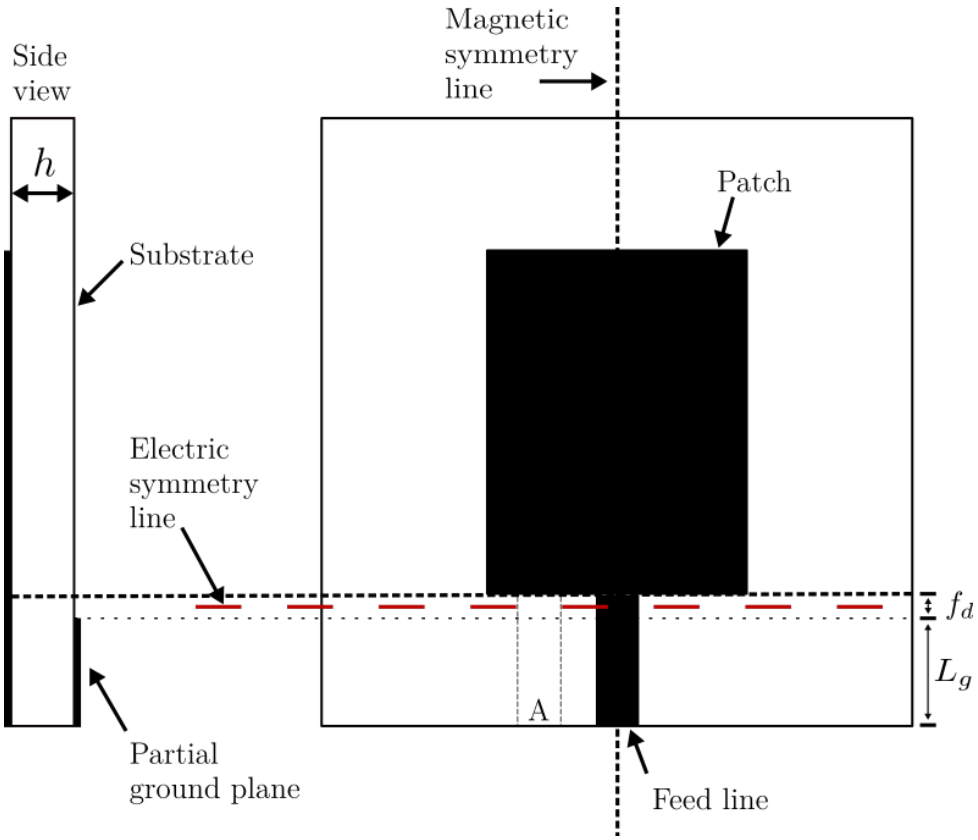


Figure 2.11. A traditional rectangular planar monopole antenna.

In a traditional planar monopole antenna shown in Figure 2.11, the enhanced performance is achieved by exciting the antenna from the patch edge along the antenna's

magnetic symmetry line. Also, a small feeding discontinuity, f_d is created between the partial ground plane (PGP) and the lower patch edge so that there is an electric symmetry line between the two. However, offsetting the feed line from the magnetic symmetry line, such as to some position "A" shown in Figure 2.11, results in the antenna's reduced performance due to cross-polarisation of the fields. On the other hand, extending the PGP above the electric symmetry line of the monopole reduces the antenna's bandwidth, and alters the omnidirectivity of the antenna patterns. These are the things requiring attention in the design process.

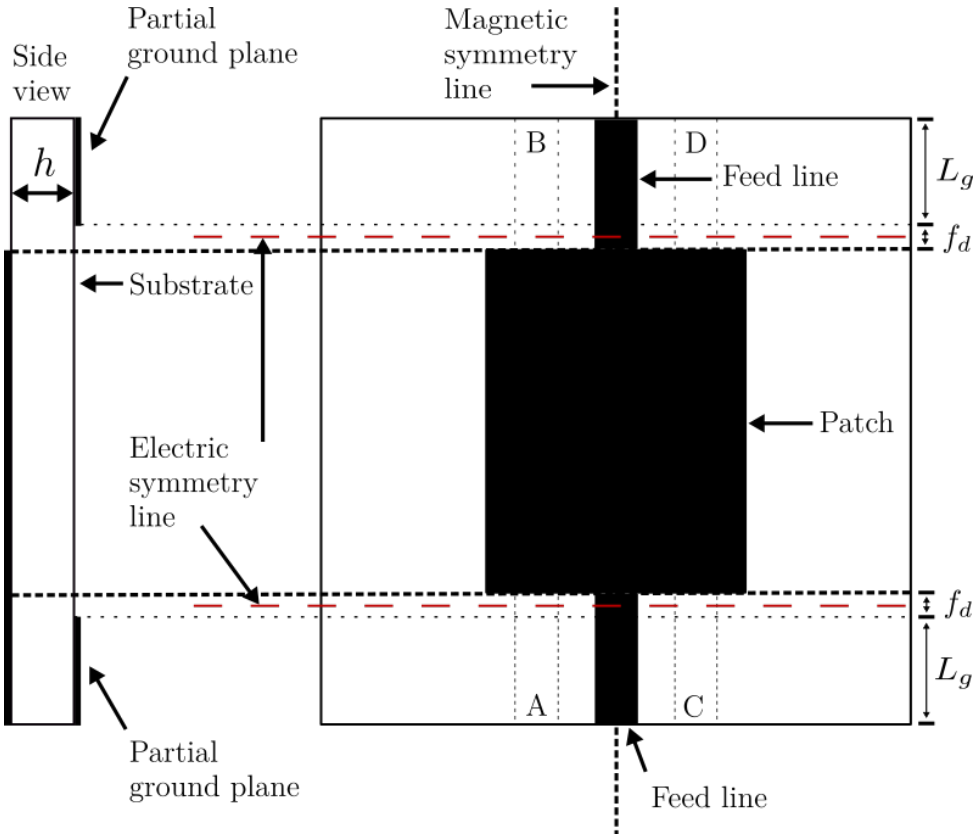


Figure 2.12. Proposed multiport rectangular planar monopole antenna.

In this thesis, apart from utilising the symmetry property of the planar monopole antenna, the PGP is mirrored to the other end of the patch to allow excitations from the two ends of the antenna as shown in Figure 2.12. With this scheme, more operational

bandwidth can be attained from the resulting two-port rectangular planar monopole antenna than what could be achieved from a single-port monopole of the same size. Also, the radiation patterns are more stabilised than the patterns attained by the corresponding single-port antenna because of driving the antenna from the two ends. The antenna can also be excited through four ports, where the effect of displacing the two feed lines on one side of the magnetic symmetry line (such as to positions A and B) is compensated by the next two feed lines, which are equally displaced on the other side of the symmetry line (at positions C and D). As such, investigations for bandwidth enhancements of patch antennas in this thesis rely on obeying the symmetry property of the planar monopole antenna, which also allows the performance enhancements of the realised antennas.

Chapter 3

Theory for the two-port injection matched antennas

3.1 Background

The Doherty amplifier consists of a carrier amplifier and peaking amplifier. The function of the peaking amplifier is to actively load-pull the carrier amplifier by injecting a current to the load when the carrier amplifier has approached its saturation point. Through this action, the impedance seen by the carrier amplifier from the load is constantly maintained at 50 Ω, thereby increasing the amplifier efficiency [75].

The theory of operation of the Doherty amplifier inspired the construction of an injection matched antenna, hereafter referred to as injection matching technique. In this configuration, a two-port antenna was constructed, and the port one terminal impedance of the antenna was matched to the 50 Ω source by using variations of the relative amplitude γ and phase shift φ between the currents I_1 and I_2 at ports one and two [75]. The

theory was then expanded to allow the simultaneous matching of both ports one and two of the antenna to the 50 Ω coherent sources [54].

In this chapter, the theory for two-port injection matched antennas is presented in outline. The reflection coefficients, transmission coefficients, and (radiation, matching and total) efficiencies for injection matched antennas are theoretically characterised. Also, the procedure for experimental characterisation of the radiation patterns is discussed. Besides, the reciprocity analysis of injection matched antennas to verify an intuitive arrangement of the feeding network around the antenna to be fed by an injection matched antenna in receive mode is explored.

3.2 Injection matching theory

Neglecting the radiation port, a two-port injection matched antenna is treated as a two-port network as shown in Figure 3.1. The two injected current signals I_1 and I_2 depicted in Figure 3.1 are related to γ and φ by,

$$\frac{I_2}{I_1} = \gamma e^{j\varphi} \tag{3.1}$$

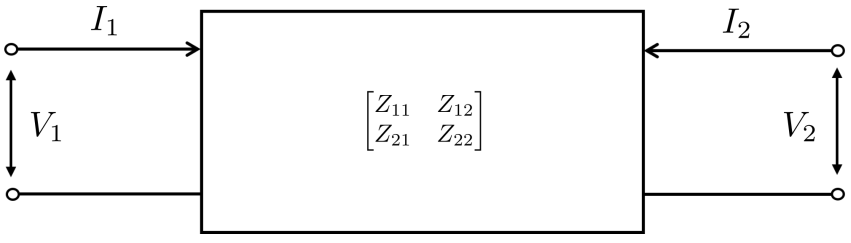


Figure 3.1. The impedance model for the two-port network.

Applying circuit theory to the two-port network in Figure 3.1, the terminal impedances at ports one and two of the antenna are given by [75],

$$Z_1 = Z_{11} + Z_{12}\gamma e^{j\varphi} \tag{3.2}$$

and

$$Z_2 = Z_{22} + \frac{Z_{21}}{\gamma e^{j\varphi}} \tag{3.3}$$

where Z_{ij} is the ij element of the Z-matrix. The terminal impedance at port one, Z_1 can be expressed in terms of its real and imaginary parts R_1 and X_1, respectively by [75],

$$R_1 = |Z_{11}| \cos\theta_{11} + \gamma\,|Z_{12}| \cos(\varphi + \theta_{12}) \tag{3.4}$$

and

$$X_1 = |Z_{11}| \sin\theta_{11} + \gamma\,|Z_{12}| \sin(\varphi + \theta_{12}) \tag{3.5}$$

where θ_{ij} is the phase angle for Z_{ij}. Similarly, the real and imaginary parts R_2 and X_2 respectively, of the terminal impedance Z_2 at port two of the antenna are given by [75],

$$R_2 = |Z_{22}| \cos\theta_{22} + \frac{|Z_{21}|}{\gamma} \cos(\theta_{21} - \varphi) \tag{3.6}$$

and

$$X_2 = |Z_{22}| \sin\theta_{22} + \frac{|Z_{21}|}{\gamma} \sin(\varphi + \theta_{21}) \tag{3.7}$$

Under simultaneous matched conditions of an injection matched antenna, both the real impedances R_1 and R_2 tend to 50 Ω and the imaginary impedances X_1 and X_2 tend to zero. Using this matched condition, Equations (3.4) and (3.5) can be simplified to give [75],

$$\varphi = \arctan\left(\frac{|Z_{11}| \sin\theta_{11}}{|Z_{11}| \cos(\theta_{11} - R_1)}\right) - \theta_{12} \tag{3.8}$$

and

$$\gamma = \frac{-|Z_{11}|\sin\theta_{11}}{|Z_{12}|\sin(\varphi+\theta_{12})} \tag{3.9}$$

To initialise the simultaneous two-port injection matching on a given antenna, the two conditions $\mathrm{Re}(Z_1) > 0$ and $\mathrm{Re}(Z_2) > 0$ must be satisfied. These conditions are decided by analysing the graphs of $\mathrm{Re}(Z_1)$ and $\mathrm{Re}(Z_2)$ against frequency before the two ports are locked. The two graphs can be plotted using Equations (3.2) and (3.3), or (3.4) and (3.6). Alternatively, the graphs of theoretical φ and γ variations against frequency (on the antenna) plotted from Equations (3.8) and (3.9) can be investigated to determine where φ and γ are at the same time approximately constant, have minima or combinations of flat regions and minima across the frequency range of interest, which are the regions where the injection matching operation can be initialised. If any of the above conditions is not satisfied, the antenna geometry may require a modification. An outlined investigation of the theoretical φ and γ plots is given in Section 4.3.3, 5.2 and 6.2.

Depending on the flatness (or coexistence of the minima or combinations of flat regions and minima) of the theoretical γ and φ variations against frequency at a given frequency range where the injection matching can be initialised, there exist a numerical set of (γ, φ) at which the antenna is injection matched to the source. This is obtained by optimising the values of γ and φ in the ranges $\gamma \in (0.1, 20)$ and $\varphi \in (-180°, 180°)$, respectively, in CST Design Studio™ (CST DS). This range of values of γ is arbitrary and is chosen for practical convenience [15].

3.3 Reflection and transmission coefficients for injection matched antennas

Consider a two-port network that is being simultaneously driven by injecting the two currents I_1 and I_2 at ports one and two, respectively. Because of the complexity in measuring the currents and voltages at high frequencies, the reflection and transmission coefficients measurement becomes easier when dealing with the waves than with the terminal currents and voltages [76]. The terminal currents and voltages at the i^{th} port of a two-port antenna are related to the incident and reflected waves, a_i and b_i respectively, from the i^{th} port of the antenna shown in Figure 3.2 by,

$$a_i = \frac{V_i + I_i Z_0}{2\sqrt{Z_0}} \tag{3.10}$$

and

$$b_i = \frac{V_i - I_i Z_0}{2\sqrt{Z_0}} \tag{3.11}$$

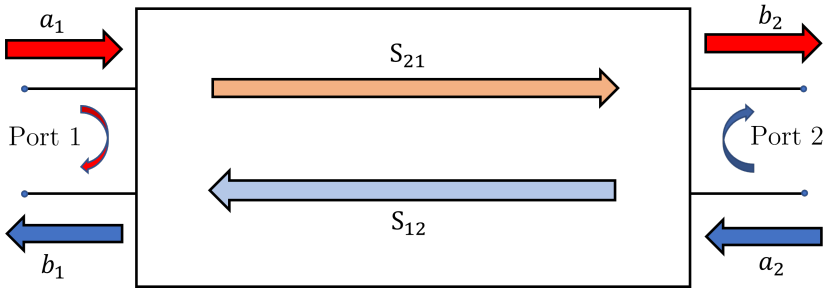


Figure 3.2. The reflection and transmission coefficient model for the two-port network.

Therefore, the reflection and transmission coefficients for the two-port antenna can be derived from the input and reflected waves, which are also expressed in terms of the terminal voltages and currents at the two ports of the antenna.

3.3.1 Total active reflection coefficient

The reflection coefficient for the two-port injection matched antennas is characterised by the total active reflection coefficient (TARC), which is the square root of the ratio of the total reflected power by the antenna to the total delivered power to the antenna [77].

$$\text{TARC} = \sqrt{\frac{\text{total reflected power from all ports}}{\text{total incident power at all ports}}} \tag{3.12}$$

If a_i and b_i are the incident and reflected waves, respectively, at the i^{th} port of an N-port antenna, Equation (3.12) can be written as [77],

$$\text{TARC} = \frac{\mathbf{b}^{\text{H}}\mathbf{b}}{\mathbf{a}^{\text{H}}\mathbf{a}} = \sqrt{\frac{\sum_{i=1}^{\text{N}} |b_i|^2}{\sum_{i=1}^{N} |a_i|^2}} \tag{3.13}$$

where $\mathbf{a}^{\text{H}}$ and $\mathbf{b}^{\text{H}}$ are the conjugate transpose for the vectors $\mathbf{a}$ and $\mathbf{b}$, respectively. For the two-port antenna, Equation (3.13) can be simplified to give [77],

$$\text{TARC} = \sqrt{\frac{|b_1|^2 + |b_2|^2}{|a_1|^2 + |a_2|^2}} \tag{3.14}$$

Substituting Equations (3.10) and (3.11) into Equation (3.14) one can relate the terminal voltages and currents V_i and I_i, respectively, with TARC by,

$$\text{TARC} = \sqrt{\frac{|V_1 - I_1 Z_0|^2 + |V_2 - I_2 Z_0|^2}{|V_1 + I_1 Z_0|^2 + |V_2 + I_2 Z_0|^2}} \tag{3.15}$$

where Z_0 is the characteristic impedance of the source which is 50 Ω. From the Z-matrix of the two-port network [75], the following equations can also be written,

$$V_1 = Z_{11}I_1 + Z_{12}I_2 \tag{3.16}$$

and

$$V_2 = Z_{21}I_1 + Z_{22}I_2 \tag{3.17}$$

Substituting Equations (3.16) and (3.17) into Equation (3.15) gives,

$$\text{TARC} = \sqrt{\frac{|Z_{11}I_1 + Z_{12}I_2 - I_1Z_0|^2 + |Z_{21}I_1 + Z_{22}I_2 - I_2Z_0|^2}{|Z_{11}I_1 + Z_{12}I_2 + I_1Z_0|^2 + |Z_{21}I_1 + Z_{22}I_2 + I_2Z_0|^2}} \tag{3.18}$$

Dividing each term under the square root in Equation (3.18) by $|I_1|^2$ gives,

$$\begin{aligned}\text{TARC} &= \sqrt{\frac{|Z_{11}I_1 + Z_{12}I_2 - I_1Z_0|^2/|I_1|^2 + |Z_{21}I_1 + Z_{22}I_2 - I_2Z_0|^2/|I_1|^2}{|Z_{11}I_1 + Z_{12}I_2 + I_1Z_0|^2/|I_1|^2 + |Z_{21}I_1 + Z_{22}I_2 + I_2Z_0|^2/|I_1|^2}} \\ &= \sqrt{\frac{\left|(Z_{11}I_1 + Z_{12}I_2 - I_1Z_0)/I_1\right|^2 + \left|(Z_{21}I_1 + Z_{22}I_2 - I_2Z_0)/I_1\right|^2}{\left|(Z_{11}I_1 + Z_{12}I_2 + I_1Z_0)/I_1\right|^2 + \left|(Z_{21}I_1 + Z_{22}I_2 + I_2Z_0)/I_1\right|^2}}\end{aligned} \tag{3.19}$$

Equation (3.19) is simplified to,

$$\text{TARC} = \sqrt{\frac{\left|Z_{11} + Z_{12}I_2/I_1 - Z_0\right|^2 + \left|Z_{21} + Z_{22}I_2/I_1 - Z_0I_2/I_1\right|^2}{\left|Z_{11} + Z_{12}I_2/I_1 + Z_0\right|^2 + \left|Z_{21} + Z_{22}I_2/I_1 + Z_0I_2/I_1\right|^2}} \tag{3.20}$$

Substituting Equation (3.1) into (3.20) gives,

$$\text{TARC} = \sqrt{\frac{|Z_{11} + Z_{12}\gamma e^{j\varphi} - Z_0|^2 + |Z_{21} + Z_{22}\gamma e^{j\varphi} - Z_0\gamma e^{j\varphi}|^2}{|Z_{11} + Z_{12}\gamma e^{j\varphi} + Z_0|^2 + |Z_{21} + Z_{22}\gamma e^{j\varphi} + Z_0\gamma e^{j\varphi}|^2}} \tag{3.21}$$

From Equation (3.3), the following equation can also be written,

$$Z_2\gamma e^{j\varphi} = Z_{21} + Z_{22}\gamma e^{j\varphi} \tag{3.22}$$

Substituting Equations (3.2) and (3.22) into Equation (3.21) gives,

$$\text{TARC} = \sqrt{\frac{|Z_1 - Z_0|^2 + |Z_2\gamma e^{j\varphi} - Z_0\gamma e^{j\varphi}|^2}{|Z_1 + Z_0|^2 + |Z_2\gamma e^{j\varphi} + Z_0\gamma e^{j\varphi}|^2}} \tag{3.23}$$

Therefore, Equations (3.21) and (3.23) can be used to characterise the TARC for the two-port injection matched antennas in terms of their respective Z-matrix and terminal impedances at the two ports.

3.3.2 Reflection and transmission coefficients at the individual ports

From the scattering matrix of the two-port network, the following equations are written,

$$b_1 = S_{11}a_1 + S_{12}a_2 \tag{3.24}$$

and

$$b_2 = S_{21}a_1 + S_{22}a_2 \tag{3.25}$$

Port two is terminated to the system impedance, and the maximum power theory is applied to obtain the S-parameters at port one. If the incident and reflected waves at port i are denoted by a_i and b_i, respectively, the following equations are written [78],

$$S_{11} = \frac{\text{reflected wave from port 1}}{\text{incident wave on port 1}} = \frac{b_1}{a_1} = \frac{V_1 - I_1Z_0}{V_1 + I_1Z_0} \tag{3.26}$$

and

$$S_{21} = \frac{\text{reflected wave from port 2}}{\text{incident wave on port 1}} = \frac{b_2}{a_1} = \frac{V_2 - I_2Z_0}{V_1 + I_1Z_0} \tag{3.27}$$

Similarly, if port one is terminated to the system impedance, the following equations are obtained,

$$S_{22} = \frac{\text{reflected wave from port 2}}{\text{incident wave on port 2}} = \frac{b_2}{a_2} = \frac{V_2 - I_2 Z_0}{V_2 + I_2 Z_0} \tag{3.28}$$

and

$$S_{12} = \frac{\text{reflected wave from port 1}}{\text{incident wave on port 2}} = \frac{b_1}{a_2} = \frac{V_1 - I_1 Z_0}{V_2 + I_2 Z_0} \tag{3.29}$$

The S-parameters defined in Equation (3.26) through (3.29) are the input port reflection coefficients and transmission coefficients between the two ports [79]. The amplitudes and phases for the terminal currents, voltages, and waves are unchanged in ideal matching conditions, allowing the following equations to be written,

$$S_1 = S_{11a} = S_{11} + S_{12}\gamma e^{j\varphi} \tag{3.30}$$

$$S_2 = S_{22a} = S_{22} + \frac{S_{21}}{\gamma e^{j\varphi}} \tag{3.31}$$

$$S_{12a} = S_{12} + \frac{S_{11}}{\gamma e^{j\varphi}} \tag{3.32}$$

and

$$S_{21a} = S_{21} + S_{22}\gamma e^{j\varphi} \tag{3.33}$$

where,

$$\frac{a_2}{a_1} = \gamma e^{j\varphi} \tag{3.34}$$

Using Equations (3.30) and (3.33), the TARC in Equation (3.14) can be expressed in terms of the passive S-parameters as,

$$\text{TARC} = \sqrt{\frac{|S_{11} + S_{12}\gamma e^{j\varphi}|^2 + |S_{21} + S_{22}\gamma e^{j\varphi}|^2}{1 + |\gamma e^{j\varphi}|^2}} \tag{3.35}$$

From Equation (3.31), the following equation can also be written,

$$S_2\gamma e^{j\varphi} = S_{21} + S_{22}\gamma e^{j\varphi} \tag{3.36}$$

Substituting Equation (3.36) into Equation (3.35) gives the following equation for the total active reflection coefficient for the two-port injection matched antennas,

$$\text{TARC} = \sqrt{\frac{|S_1|^2 + |S_2\gamma e^{j\varphi}|^2}{1 + |\gamma e^{j\varphi}|^2}} \tag{3.37}$$

where, S_1 and S_2 are the active reflection coefficients at ports one and two of the antenna, and S_{12a} and S_{21a} are the active transmission coefficients between the two ports.

3.3.3 Efficiency of injection matched antennas

For a lossless multiport antenna, the matching efficiency is given by the ratio of the accepted power to the available power at the antenna ports [1, 80]. If P_{accepted} and $P_{\text{available}}$ are the accepted and available power at the two-ports of the antenna, then the matching efficiency η_m can be written as,

$$\eta_m = \frac{P_{\text{accepted}}}{P_{\text{available}}} = \frac{P_{\text{available}} - P_{\text{reflected}}}{P_{\text{available}}} \tag{3.38}$$

where $P_{\text{reflected}}$ is the reflected power at the antenna ports. Equation (3.38) can be expressed in terms of the incident and reflected waves a_i and b_i, respectively, at the antenna i^{th} port to give [80],

$$\eta_m = \frac{\mathbf{a}^{\text{H}}\mathbf{a} - \mathbf{b}^{\text{H}}\mathbf{b}}{\mathbf{a}^{\text{H}}\mathbf{a}} = \frac{\sum_{i=1}^{\text{N}} |\mathbf{a}_i|^2 - \sum_{i=1}^{\text{N}} |\mathbf{b}_i|^2}{\sum_{i=1}^{N} |\mathbf{a}_i|^2} \tag{3.39}$$

Equation (3.39) can be simplified to give [80],

$$\eta_m = 1 - |\text{TARC}|^2 \tag{3.40}$$

Equation (3.40) gives the matching efficiency for a lossless two-port antenna. Suppose η_d and η_c stand for the dielectric efficiency and conduction efficiency, respectively. In that case, the total efficiency η_T for the two-port antenna becomes [1, p. 65],

$$\eta_T = \Big(1 - |\text{TARC}|^2\Big)\eta_d\eta_c \tag{3.41}$$

where $\eta_d\eta_c = \eta_r$ is the radiation efficiency of the antenna. Equation 3.41 provides a mathematical model for characterising the total efficiency for the two-port injection matched antennas.

3.4 Characterisation of the radiation patterns for injection matched antennas

The theoretical radiation patterns for the two-port injection matched antennas are obtained from simulations. However, getting the experimental patterns for these antennas is challenging as the available automated tool for measuring the far-field characteristics of antennas in anechoic chambers does not support multiport functionality. As such, modifications in the measuring system are required to allow measurements of the far-field characteristics of two-port antennas, and a total of three ports are needed, as shown in Figure 3.3. The experimental setup is configured by disconnecting the interface between the vector network analyser (VNA) and the automated software. Though the turntable rotation is manually controlled from the software in an azimuth angle step which depends on the selected resolution, the corresponding transmitted and received power at ports 1, 2 and 3 should be manually recorded for each azimuth angle between 0° and 360°.

Ports 1 and 2 of the Rohde and Schwarz (R&S) ZVA67 VNA generate coherent signals for exciting the two-port antenna. The relative amplitude γ and phase shift φ at port 2 are predefined in the VNA. Port 3 of the VNA is connected to the reference antenna. The antenna under test (AUT) is in the transmit mode with the transmit power $P_t = |a_1|^2 + |a_2|^2$, while the reference antenna is in the receive mode with the receive power $P_r = |b_3|^2$, where a_i and b_i are the incident and reflected waves, respectively, at the i^{th} port of the antenna [78]. From Friis equation [1], the gain G_t of the transmit antenna is given by,

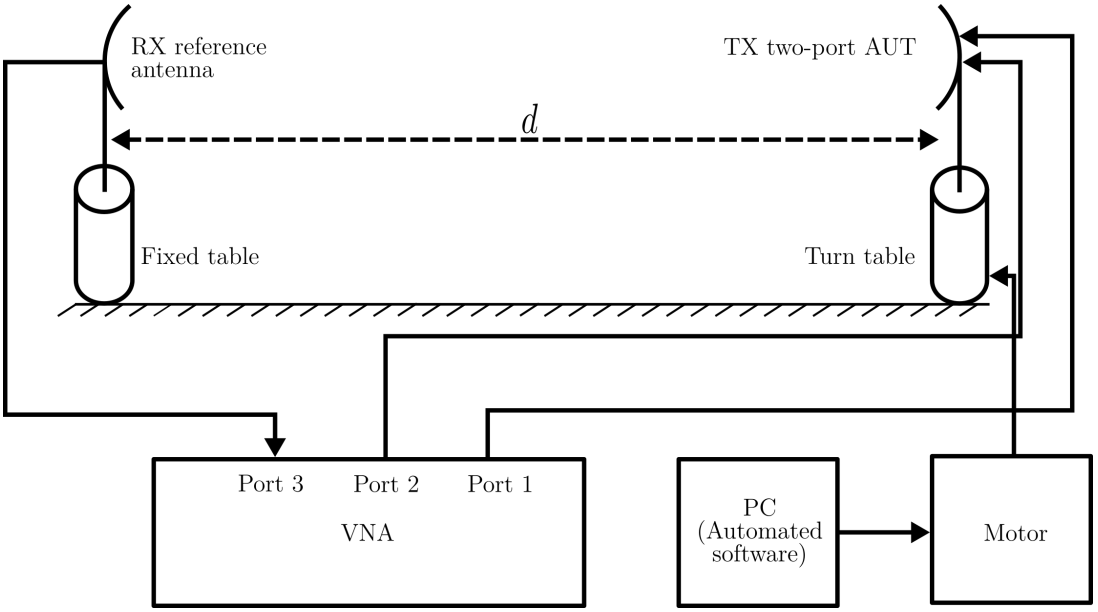


Figure 3.3. An experimental setup for measuring the far-field characteristics of the two-port injection matched antennas in the anechoic chamber.

$$G_t = \frac{P_r}{P_t G_r}\left(\frac{4\pi df}{c}\right)^2 \tag{3.42}$$

But $G_t = \eta_r D_t$ and $\eta_r = 1 - |\text{TARC}|^2$, where η_r is the radiation efficiency, D_t is the directivity of the transmit antenna, TARC is the total active reflection coefficient for the two-port antenna under test, d is the line of sight distance between the two antennas, P_t is the power transmitted by the two-port antenna, P_r is the power received by the reference antenna whose gain is G_r, c is the velocity of EM waves in free space and f is the frequency in Hz. Therefore, the directivity of the transmit antenna is given by,

$$D_t = \frac{P_r}{P_t G_r\left(1 - |\text{TARC}|^2\right)}\left(\frac{4\pi df}{c}\right)^2 \tag{3.43}$$

The VNA is assumed to be calibrated using a Through, Open, Short and Match (TOSM) calibration technique with the plane of calibration taken at the points where the feeding

coaxial cables interface the antennas so that the cable losses become part of the VNA sensitivity. These losses are therefore ignored during the link budgeting. Equation (3.43) is expressed in dB to give,

$$D_t{}^{\mathrm{dB}} = P_r{}^{\mathrm{dBm}} - P_t{}^{\mathrm{dBm}} - G_r{}^{\mathrm{dB}} - 10\log\left(1 - |\mathrm{TARC}|^2\right) + 20\log\left(\frac{4\pi df}{c}\right) \tag{3.44}$$

Expressing Equation (3.44) in terms of the waves a_i and b_i at the i^{th} port of the antenna gives,

$$\begin{aligned} D_t{}^{\mathrm{dB}} = 20\log|b_3| - 10\log(|a_1|^2 + |a_2|^2) - G_r{}^{\mathrm{dB}} - 10\log\left(1 - |\mathrm{TARC}|^2\right) \\ +20\log\left(\frac{4\pi df}{c}\right) \end{aligned} \tag{3.45}$$

where $|a_1|$, $|a_2|$, and $|b_3|$ are the linear power magnitudes in mW.

Therefore, using Equation (3.45), the directivity of the two-port AUT as a function of the azimuth and elevation angles can be determined in both the E and H-plane. Typical results for the E and H-plane radiation patterns obtained using this approach are given in Section 4.4.2.

3.5 Reciprocity of injection matched antennas

Previous investigations of two-port injection matched antennas were focused on the transmitting operation only. Intuitively, it might be expected that the same feeding arrangement used by the antenna in the transmit mode can be fed by the two-port injection

matched antenna in the receive mode. In this section, the Lorentz reciprocity theorem is used to perform a rigorous reciprocity analysis of the two-port injection matched antenna to verify that this intuitive arrangement of the feeding network will indeed enable an injection matched antenna to operate in receive mode. The experimental exploration of this analysis is discussed in Section 4.3.7.

3.5.1 Theory and derivation

Consider two N-port antennas placed in an isotropic medium of permittivity ε and permeability μ as depicted in Figure 3.4. The two antennas are assumed to work in both the transmit and receive mode in order to consider reciprocity. If P_1 and P_{21} denote the power transmitted by antenna 1 and power received by antenna 2, respectively, then the following Maxwell Equations can be written [81],

$$\vec{\nabla} \times \vec{E_1} = -j\omega\mu\vec{H_1} \tag{3.46}$$

and

$$\vec{\nabla} \times \vec{H_1} = \vec{j_1} + j\omega\varepsilon\vec{E_1} \tag{3.47}$$

where $\vec{E_1}$ and $\vec{H_1}$ are the electric and magnetic field vectors at any observation point, and $\vec{j_1}$ is the impressed source current associated with antenna 1.

Similarly, when antenna 2 is transmitting power P_2 and antenna 1 is receiving power P_{12}, the fields $\vec{E_2}$ and $\vec{H_2}$ at any observation point are given by [81],

$$\vec{\nabla} \times \vec{E_2} = -j\omega\mu\vec{H_2} \tag{3.48}$$

and

$$\vec{\nabla} \times \vec{H_2} = \vec{j_2} + j\omega\varepsilon\vec{E_2} \tag{3.49}$$

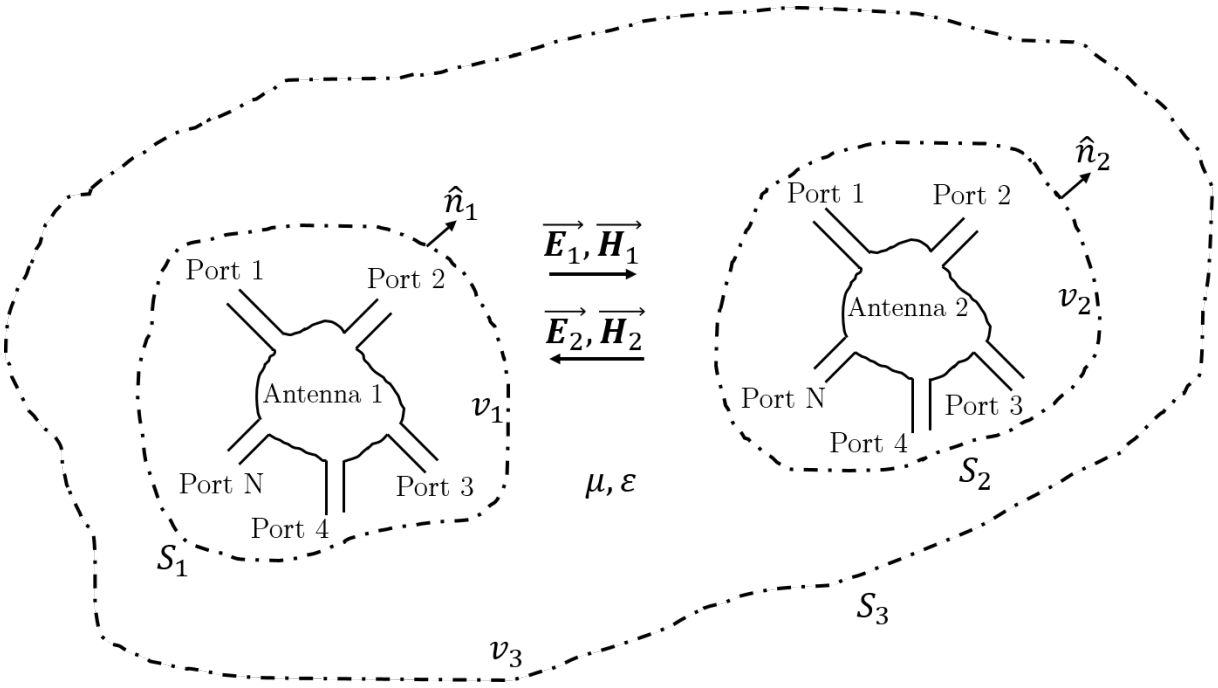


Figure 3.4. The two N-port antennas under reciprocity.

where $\vec{j_2}$ is the impressed source current associated with antenna 2.

Subtracting the scalar product of Equation (3.48) and $\vec{H}_1$ from the scalar product of Equation (3.47) and $\vec{E}_2$, and rearranging it in the form $\vec{\nabla} \cdot (\vec{a} \times \vec{b}) = \vec{b} \cdot \vec{\nabla} \times \vec{a} - \vec{a} \cdot \vec{\nabla} \times \vec{b}$ gives [81],

$$-\vec{\nabla} \cdot \left(\vec{E}_2 \times \vec{H}_1\right) = \vec{E}_2 \cdot \vec{j_1} + j\omega\varepsilon\vec{E}_1 \cdot \vec{E}_2 + j\omega\mu\vec{H}_1 \cdot \vec{H}_2 \tag{3.50}$$

Similarly, subtracting the scalar product of Equation (3.49) and $\vec{E}_1$ from the scalar product of Equation (3.46) and $\vec{H}_2$, and after rearrangement gives [81],

$$\vec{\nabla} \cdot \left(\vec{E}_1 \times \vec{H}_2\right) = -\vec{E}_1 \cdot \vec{j_2} - j\omega\varepsilon\vec{E}_1 \cdot \vec{E}_2 - j\omega\mu\vec{H}_1 \cdot \vec{H}_2 \tag{3.51}$$

Adding Equation (3.50) and (3.51) gives [81],

$$\vec{\nabla} \cdot \left(\vec{E}_1 \times \vec{H}_2\right) - \vec{\nabla} \cdot \left(\vec{E}_2 \times \vec{H}_1\right) = \vec{E}_2 \cdot \vec{j_1} - \vec{E}_1 \cdot \vec{j_2} \tag{3.52}$$

Considering the case when antenna 1 radiates power P_1. Integrating Equation (3.52) over the surface S_1 that encloses this antenna gives,

$$\oiint_{S_1} \left(\vec{E_1} \times \vec{H_2} - \vec{E_2} \times \vec{H_1}\right) \cdot \hat{n}_1 d\vec{S} = \iiint_{v_1} \left(\vec{E_2} \cdot \vec{j_1}\right) dv \tag{3.53}$$

On the other hand, when antenna 2 is transmitting power P_2, integrating Equation (3.52) over the surface S_2 enclosing this antenna gives [81],

$$\oiint_{S_2} \left(\vec{E_1} \times \vec{H_2} - \vec{E_2} \times \vec{H_1}\right) \cdot \hat{n}_2 d\vec{S} = -\iiint_{v_2} \left(\vec{E_1} \cdot \vec{j_2}\right) dv \tag{3.54}$$

Lastly, taking any closed surface, S_3 which encloses both sources [81, 82], the following equation is written,

$$\begin{aligned} \oiint_{S_3} \left(\vec{E_1} \times \vec{H_2} - \vec{E_2} \times \vec{H_1}\right) \cdot d\vec{S} = & \iiint_{v_3} \left(\vec{E_2} \cdot \vec{j_1}\right) dv \\ & - \iiint_{v_3} \left(\vec{E_1} \cdot \vec{j_2}\right) dv \end{aligned} \tag{3.55}$$

According to the usual Lorentz reciprocity derivation, for the sources $\vec{j_1}$ and $\vec{j_2}$ contained in a bounded region, the asymptotic radiation fields vary as $1/r$ and have the form $\mu\vec{H_1} = \hat{r} \times \vec{E_1}$ and $\mu\vec{H_2} = \hat{r} \times \vec{E_2}$, so that the surface integral on the right hand side (RHS) of Equation (3.55) vanishes over a sufficiently large volume v_3 due to the fact that the fields obey the radiation boundary condition at infinity, and remains,

$$\iiint_{v_3} \left(\vec{E_2} \cdot \vec{j_1}\right) dv = \iiint_{v_3} \left(\vec{E_1} \cdot \vec{j_2}\right) dv \tag{3.56}$$

For the two antennas 1 and 2 bounded in volumes v_1 and v_2 shown in Figure 3.4, Equation (3.56) can be written as,

$$\begin{aligned} &\iiint_{v_1} \left(\vec{E}_{2,\text{antenna1}} \cdot \vec{j}_{1,\text{antenna1}}\right) dv + \iiint_{v_2} \left(\vec{E}_{2,\text{antenna2}} \cdot \vec{j}_{1,\text{antenna2}}\right) dv \\ &= \iiint_{v_1} \left(\vec{E}_{1,\text{antenna1}} \cdot \vec{j}_{2,\text{antenna1}}\right) dv + \iiint_{v_2} \left(\vec{E}_{1,\text{antenna2}} \cdot \vec{j}_{2,\text{antenna2}}\right) dv \end{aligned} \tag{3.57}$$

The impressed current distributions $\vec{j_1}$ and $\vec{j_2}$ are spatially disjoint, and are non-zero in the contiguous volumes v_1 and v_2, respectively. Therefore, the current densities $\vec{j}_{1,\text{antenna2}}$ and $\vec{j}_{2,\text{antenna1}}$ do not exist in the gaps between the terminals of antenna 2 and antenna 1, respectively. This makes,

$$\vec{E}_{2,\text{antenna2}} \cdot \vec{j}_{1,\text{antenna2}} = 0 = \vec{E}_{1,\text{antenna1}} \cdot \vec{j}_{2,\text{antenna1}} \tag{3.58}$$

Substituting Equation (3.58) into Equation (3.57) gives,

$$\iiint_{v_1} \left(\vec{E}_{2,\text{antenna1}} \cdot \vec{j}_{1,\text{antenna1}}\right) dv = \iiint_{v_2} \left(\vec{E}_{1,\text{antenna2}} \cdot \vec{j}_{2,\text{antenna2}}\right) dv \tag{3.59}$$

The left hand side (LHS) of Equation (3.59) is the reaction of source 1 on the fields from source 2, while the RHS of this equation is the reaction of source 2 on the fields from source 1. This means that, in order for energy to keep flowing between the two antennas, the sources must react to the fields in their vicinity by supplying or absorbing energy [83]. Suppose the gap between the terminals of each port i for the two antennas in Figure 3.4 is dl. Considering antenna 1, when the field $\vec{E_2}$ interacts with this antenna, each port of the antenna will react by supplying or absorbing energy. It is also assumed that both

the feed line and ground plane for each port are on the same layer, so that the received field $\vec{E}_2$ and the source current density $\vec{j_1}$ are oriented on the same plane of the ports. Therefore, the reaction of antenna 1 to the field $\vec{E}_2$ is given by,

$$\begin{aligned}\iiint_{v_1} \left(\vec{E}_{2,\text{antenna1}} \cdot \vec{j}_{1,\text{antenna1}}\right) dv &= \iiint_{\text{antenna 1}} \left(\vec{E}_{2,\text{antenna1}} \cdot \vec{j}_{1,\text{antenna1}}\right) dv \\ &= \sum_{i=1}^{N} \left(I^{+}_{i,\text{antenna1}} \int_{\text{port i}} \vec{E}_{2,\text{antenna 1}} \cdot \vec{dl} \right) = -\sum_{i=1}^{N} I^{+}_{i,\text{antenna1}} V^{-}_{i,\text{antenna1}}\end{aligned} \tag{3.60}$$

where, $V^{-}_{i,\text{antenna1}}$ and $I^{+}_{i,\text{antenna1}}$ are the received terminal voltage, and transmitted current at the i^{th} port of antenna 1.

Similarly, when the field $\vec{E_1}$ interacts with antenna 2 in Figure 3.4, each port of this antenna will react by supplying or absorbing energy. The reaction of antenna 2 to the field $\vec{E_1}$ is given by,

$$\begin{aligned}\iiint_{v_2} \left(\vec{E}_{1,\text{antenna2}} \cdot \vec{j}_{2,\text{antenna2}}\right) dv &= \iiint_{\text{antenna 2}} \left(\vec{E}_{1,\text{antenna2}} \cdot \vec{j}_{2,\text{antenna2}}\right) dv \\ &= \sum_{i=1}^{N} \left(I^{+}_{i,\text{antenna2}} \int_{\text{port i}} \vec{E}_{1,\text{antenna 2}} \cdot \vec{dl} \right) = -\sum_{i=1}^{N} I^{+}_{i,\text{antenna2}} V^{-}_{i,\text{antenna2}}\end{aligned} \tag{3.61}$$

where, $V^{-}_{i,\text{antenna2}}$ and $I^{+}_{i,\text{antenna2}}$ are the received terminal voltage, and transmitted current at the i^{th} port of antenna 2. Substituting Equations (3.60) and (3.61) into Equation (3.59) gives [81, 82, 84],

$$\sum_{i=1}^{N} V^{-}_{i,\text{antenna1}} I^{+}_{i,\text{antenna1}} = \sum_{i=1}^{N} V^{-}_{i,\text{antenna2}} I^{+}_{i,\text{antenna2}} \tag{3.62}$$

where $V^{-}_{i,\text{antenna1}}$, $V^{-}_{i,\text{antenna2}}$ and $I^{+}_{i,\text{antenna1}}$, $I^{+}_{i,\text{antenna2}}$ are the received terminal voltages and transmitted currents at the i^{th} port of the N-port antennas. For the two-port antennas Equation (3.62) can be simplified to,

$$V^{-}_{1,\text{antenna1}} I^{+}_{1,\text{antenna1}} + V^{-}_{2,\text{antenna1}} I^{+}_{2,\text{antenna1}} = V^{-}_{1,\text{antenna2}} I^{+}_{1,\text{antenna2}} + V^{-}_{2,\text{antenna2}} I^{+}_{2,\text{antenna2}} \tag{3.63}$$

Equation (3.63) is the power reciprocity theorem (antenna power conservation) for injection matched antennas, and it is valid for linear and time-invariant reciprocal antennas having the same transmitting and receiving patterns.

However, Equation (3.63) is under-determined. It does not provide enough information, such as the terminal currents or voltages, to show whether it is possible to have an injection matched receive operation. It only tells that the two-port antenna can only transmit and receive when under reciprocity with another similar antenna. In this regard, an extra equation is needed to provide additional information required to determine the voltages and currents for the injection matched receive operation. Therefore, a further investigation on the receiving mode for the two-port injection matched antenna is provided in the next section.

3.5.2 Circuit implementation of two-port antenna reciprocity

Consider the reciprocal operation of two two-port injection-matched antennas shown in Figure 3.5. The source $\vec{j_1}$ is an impressed current distribution on antenna 1 when driven

by impressed currents I_1 and I_2, $\vec{j_2}$ is an impressed current distribution on antenna 2 when driven by impressed currents I_3 and I_4, $\vec{E}_2$ is the incident electric field on antenna 1 when antenna 2 is transmitting, and $\vec{E}_1$ is the incident electric field on antenna 2 when antenna 1 is transmitting. The two antennas are driven by voltage sources V_{Si} with the characteristic impedance of Z_{Si} at each i^{th} port as shown in Figure 3.5. The voltages V_i and currents I_i are the terminal voltages and currents at port i of the antennas. Applying Equations (3.59) and (3.60) into the circuit configuration of Figure 3.5 gives,

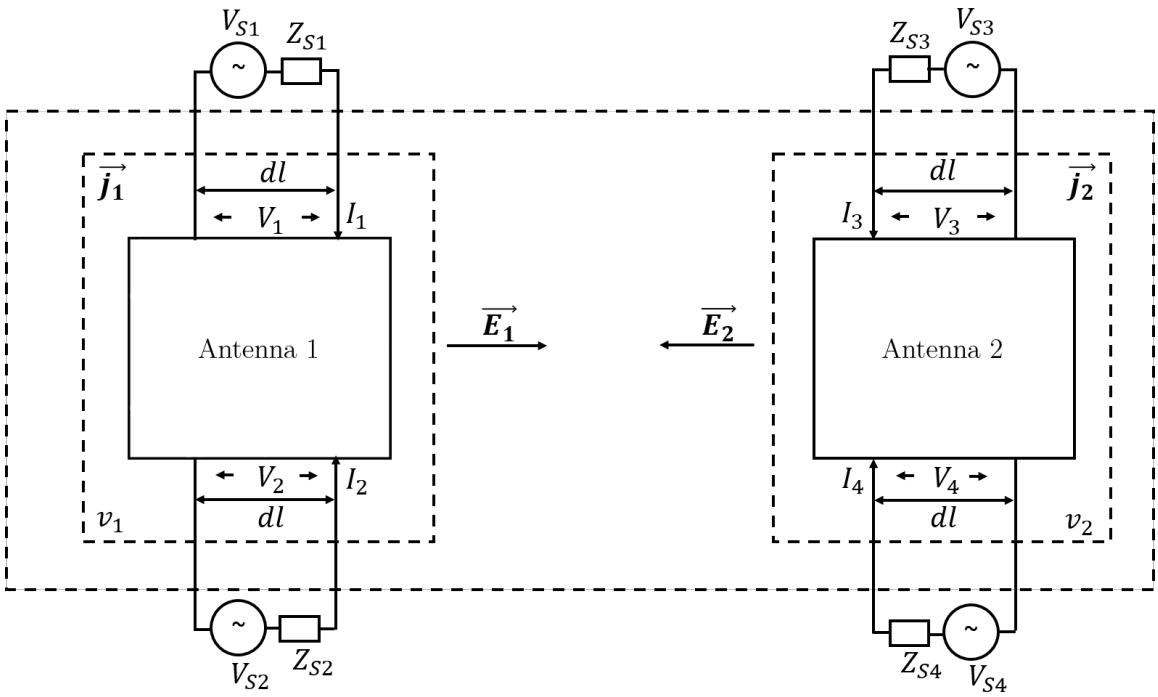


Figure 3.5. Two-port antennas under reciprocity.

$$\begin{aligned}\iiint_{v_1}\left(\vec{E}_2\cdot\vec{j_1}\right)dv=\sum_{i=1}^{2}\left(I_i^+\int_{\text{port i}}\vec{E}_2\cdot\vec{dl}\right)=I_1^+\int_{\text{port 1}}\vec{E}_2\cdot\vec{dl}\\ +I_2^+\int_{\text{port 2}}\vec{E}_2\cdot\vec{dl}=-V_1^-I_1^+-V_2^-I_2^+\end{aligned}\tag{3.64}$$

and

$$\iiint_{v_2} \left(\vec{E}_1 \cdot \vec{j_2}\right) dv = \sum_{i=3}^{4} \left(I_i^+ \int_{\text{port i}} \vec{E}_1 \cdot \vec{dl} \right) = I_3^+ \int_{\text{port 3}} \vec{E}_1 \cdot \vec{dl} + I_4^+ \int_{\text{port 4}} \vec{E}_1 \cdot \vec{dl} = -V_3^- I_3^+ - V_4^- I_4^+ \tag{3.65}$$

Substituting Equations (3.64) and (3.65) into Equation (3.59) gives,

$$V_1^- I_1^+ + V_2^- I_2^+ = V_3^- I_3^+ + V_4^- I_4^+ \tag{3.66}$$

where $V_i^- = b_i\sqrt{Z_0} = V_{Si} - I_i Z_0 - a_i\sqrt{Z_0}$, and $I_i^+ = {}^{a_i}/_{\sqrt{Z_0}}$ are the received voltages and transmitted currents, a_i and b_i are the incident and reflected waves, respectively, and Z_{Si} is the characteristic impedance at the i^{th} port of the antenna which, under ideal conditions, is equal to Z_0 [78].

Receive state

When antenna 1 of Figure 3.5 is in the receive mode, the excitation source is removed, and it becomes source-less. The antenna can therefore be represented by an equivalent circuit in Figure 3.6, where Z_A^R is the effective impedance of the receiving antenna, and V_{eff}^R is the effective received voltage by the antenna. Z_i^R and I_i^R are the terminal impedances and terminal currents at the i^{th} port of the antenna, respectively, when the antenna is in the receive mode. Applying Kirchhoff's voltage law on loops 1 and 2 in Figure 3.6, the following equations can be written,

$$V_1^R - V_{eff}^R = -I_{eff}^R Z_A^R - I_1^R Z_1^R \tag{3.67}$$

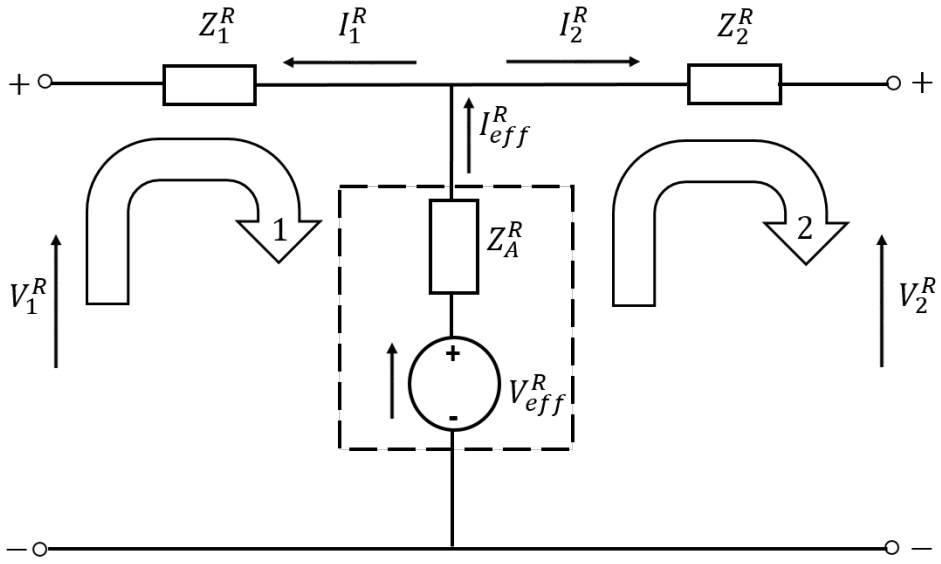


Figure 3.6. Equivalent circuit for the two-port antenna in the receive mode.

and

$$V_{eff}^R - V_2^R = I_{eff}^R Z_A^R + I_2^R Z_2^R \tag{3.68}$$

Combining Equations (3.67) and (3.68) gives,

$$V_1^R - V_2^R = I_2^R Z_2^R - I_1^R Z_1^R \tag{3.69}$$

which upon rearrangement becomes,

$$V_1^R + I_1^R Z_1^R = V_2^R + I_2^R Z_2^R \tag{3.70}$$

where $V_i^R = V_i^+ + V_i^-$ and $I_i^R = I_i^+ - I_i^-$ are the terminal voltage and current at the i^{th} port of the antenna when it is in the receive mode. Also, $Z_1^R = Z_{11}^R + Z_{12}^R \gamma e^{j\varphi}$ and $Z_2^R = Z_{22}^R + Z_{21}^R / \gamma e^{j\varphi}$, where Z_{ij}^R is the ij element of the Z-matrix of the antenna in receive mode.

Equation (3.70) shows that voltage is conserved at the ports when the two-port injection matched antenna is in the receive mode, indicating that the injection matched

antenna can work independently as a receiving antenna. The variables I_1^R, I_2^R, V_1^R and V_2^R in Equation (3.70) together with the reciprocity Equation (3.66) provide a fully determined problem from which the antenna reciprocity can be validated. These two equations fix the relationships between the terminal currents and voltages in the receive mode of the antenna, indicating that the same feeding arrangement used by the injection matched antenna in the transmit mode can be fed by an injection matched antenna in the receive mode.

3.6 Summary

It has been shown in this chapter that the TARC for the two-port injection matched antennas is a function of the individual port reflection coefficients and isolation between the two ports. As such, characterising the antenna's reflection coefficient by TARC guarantees good port isolation at the -10 dB operational bandwidth of the antenna. Also, the radiation patterns for the two-port injection matched antennas can be experimentally characterised from Equation (3.45) derived from Friis equation.

Besides, the reciprocity analysis of the two-port injection matched antennas reveals that the same feeding network arrangement used by the injection matched antenna in transmit mode can be fed by an injection matched antenna in the receive mode. However, this observation requires validation, which is discussed in Section 4.3.7.

The next chapter discusses, applies and validates the design methodology for the injection matched antennas through simulations and experiments. An intuitive arrangement of the feeding network around the injection matched antenna verified in this chapter is also validated through simulation.

Chapter 4

Design methodology, application and validation

4.1 Background

In the previous chapter, the theory for the two-port injection matched antennas was formulated and discussed. The terminal impedances, reflection and transmission coefficients, and efficiencies (radiation, matching and total efficiency) for the simultaneously excited two-port antennas were theoretically characterised. Theoretical procedures for describing the radiation patterns and reciprocity analysis of the two-port antennas were also outlined.

This chapter presents an outline design methodology for the two-port injection matched antennas. The methodology is then applied in the realisation of a two-port injection matched antenna. The TARC and radiation patterns for the two-port injection matched antennas are studied through simulation and experiments. Also, the radiation, matching and total efficiency of the injection matched antennas are explored through sim-

ulation. Besides, the reciprocity analysis of the two-port injection matched antennas to verify an intuitive arrangement of the feeding network around the antenna to be fed by an injection matched antenna in the receive mode is explored through simulation.

4.2 Design methodology for injection matched patch antennas

The design of injection matched patch antennas is achieved through the following procedure, which is also summarised in Figure 4.1:

(1) The desired frequency of operation f_0, dielectric constants ε_{r1} and ε_{r2}, and substrate thicknesses h_1 and h_2 for the proximity-fed patch antenna are specified based on application and desired bandwidth.

(2) The antenna dimensions for the one-port proximity-fed patch antenna with the full ground plane (FGP) are calculated using the design equations outlined in [85]. The antenna is excited through a discrete face port created on the outer end-face of the feed line, simulated and optimised in CST Microwave Studio® (CST MWS).

(3) The one-port antenna in (2) is transformed into a planar monopole antenna by truncating the ground plane such that the length of the resulting PGP is $Lg = (L_s - L_p)/2$, as shown in Figure 4.2. The antenna is simulated in CST MWS and its S_{11} is plotted.

(4) The one-port antenna in (3) is converted to a two-port antenna by adding another excitation at the opposite patch edge with respect to the first excitation, and the

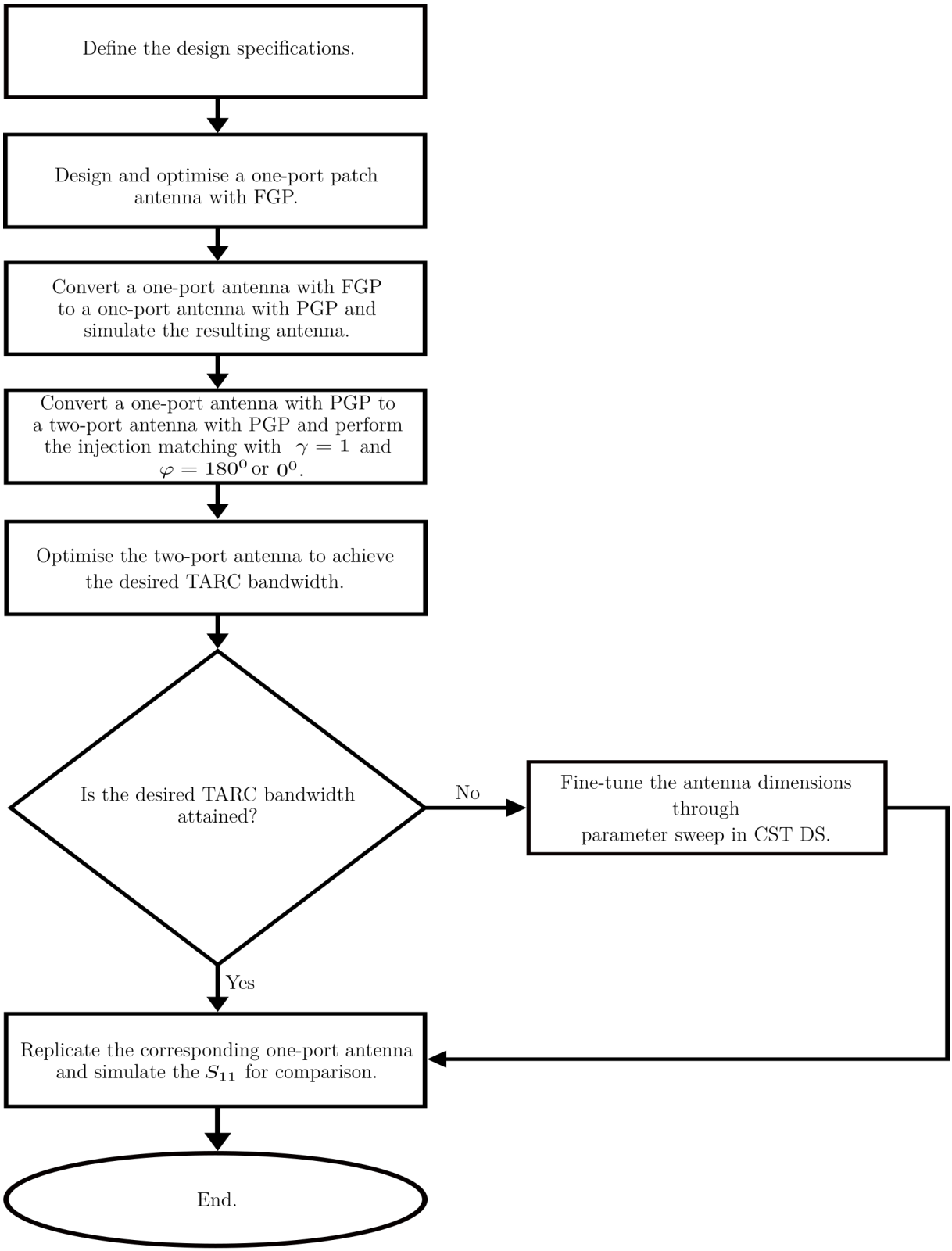


Figure 4.1. A flow chart summarising the design procedure for the two-port injection matched antennas.

second PGP for the second excitation as described in Section 4.3.2. The antenna is simulated to obtain the passive S-parameters, which are used for calculating the TARC resonance when $\gamma = 1$ and $\varphi = 0°$ or $\varphi = 180°$.

(5) Depending on the desired bandwidth and resonant frequency, the antenna dimensions are optimised while TARC is being monitored.

(6) Depending on the TARC convergence in (5), the optimum TARC may be obtained by sweeping the dimensions of the antenna in a narrow range, near the dimensions of the best TARC in (5).

(7) After the desired TARC is obtained, the resulting two-port injection matched antenna dimensions are used to create the corresponding one-port antenna. Finally, the one-port antenna is simulated and the obtained results are used for comparison with the two-port antenna.

4.3 Application of the design methodology

The main objective of this section is to illustrate the design of two-port injection matched antennas by applying the methodology established in Section 4.2. So a two-port injection matched antenna is designed at around 3.9 GHz to investigate bandwidth enhancement, frequency tunability and electrically small operation of the antenna. Any other frequency of operation could be selected to illustrate the injection matching technique.

4.3.1 Design of one-port antenna

A one-port proximity-fed patch antenna with FGP is designed in CST MWS to operate at around 3.9 GHz by following the procedure outlined in [85] and Appendix B.1. The

antenna is realised on two layers of Rogers Duroid RT 5880 substrate with relative permittivity ε_r of 2.2, loss tangent of 0.0009, lower substrate height of 1.575 mm, upper substrate height of 0.787 mm, and copper cladding thickness of 0.035 mm. The antenna has a patch length $L_p = 25$ mm, patch width $W_p = 18$ mm, substrate length $L_s = 35$ mm, substrate width $W_s = 28$ mm, width of the feed line $w = 1.6$ mm and the distance of the coupled line from the centre of the patch $d = 0.0$ mm. The antenna is excited through a discrete face port created on the outer end-face of the feed line.

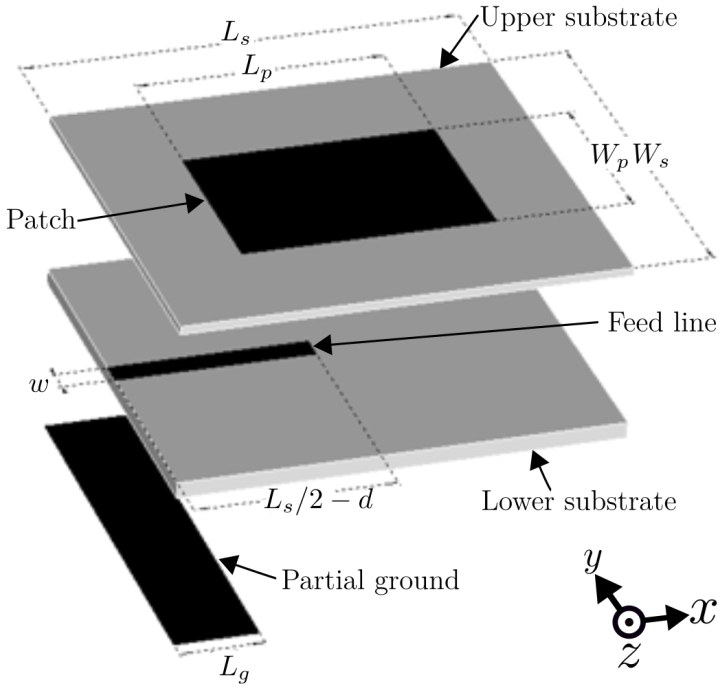


Figure 4.2. Proximity-fed patch antenna with single feed line. The black colour indicates the layers of copper.

The impedance of the excitation signal is maintained at 50 Ω. The S_{11} for the one-port antenna with FGP resulting from these antenna dimensions is depicted in Figure 4.3. The −6 dB fractional bandwidth (FBW) for this antenna is around 5.7% (calculated using Equation (B.1) in Appendix B.4) at a 3.853 GHz centre frequency. The bandwidth is enhanced by converting the antenna to a monopole patch antenna through truncation

of the grounding plane, as shown in Figure 4.2. The length of the PGP is $L_g = 5$ mm, which is the maximum length of the ground plane for which a patch antenna is converted to a planar monopole antenna, is calculated from $L_g = (L_s - L_p)/2$.

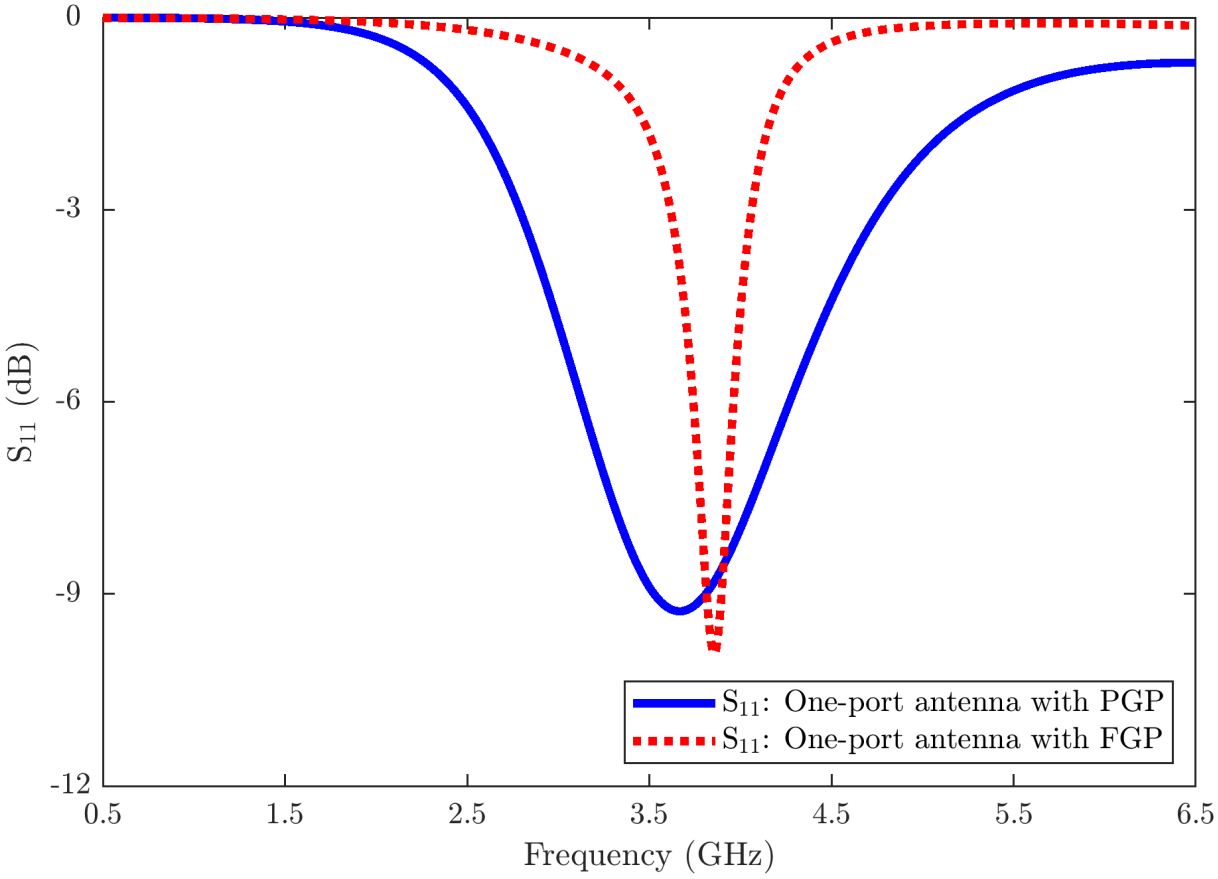


Figure 4.3. S-parameter for the one-port proximity-fed patch antenna under investigation.

The S_{11} for the one-port antenna with PGP is depicted in Figure 4.3. The -6 dB FBW of this antenna is around 30.5% at a 3.699 GHz centre frequency, and the main resonance is at around 3.666 GHz frequency. This observation is an indication that the bandwidth of a conventional patch antenna can be increased by truncating the ground plane of the antenna. The impedance matching for the one-port antenna with PGP will be improved through injection matching after the positions for the placement of the feed lines for the corresponding two-port antenna are determined in Section 4.3.2.

4.3.2 Positioning the feed lines

In this section, the one-port antenna shown in Figure 4.2 is modified by removing the feed line as depicted in Figure 4.4. Also, a second PGP is added as shown in Figure 4.4 so that symmetry is created where the two ports are likely to be positioned. The characteristic currents on the patch antenna are studied to determine the position for placing the two feed lines (feeding points) to obtain a two-port antenna that can be injection matched. This is achieved through characteristic mode analysis (CMA) in CST MWS using the Multilayer Solver with the mesh and solver settings provided in Table B.1 and B.2 in Appendix B.2. The lossless Rogers Duroid RT 5880 substrate and perfect electric conductor (PEC) are used in the CMA. The dimensions of the resulting antenna are the same as the dimensions of the one-port antenna shown in Section 4.3.1 and are summarised in Table 4.2 by TARC0 resonance. The adoption of the PGPs also allows the initialisation of stable values of the Z-matrix elements and reduces the stored EM energy in the field as well as the antenna Q to enhance bandwidth.

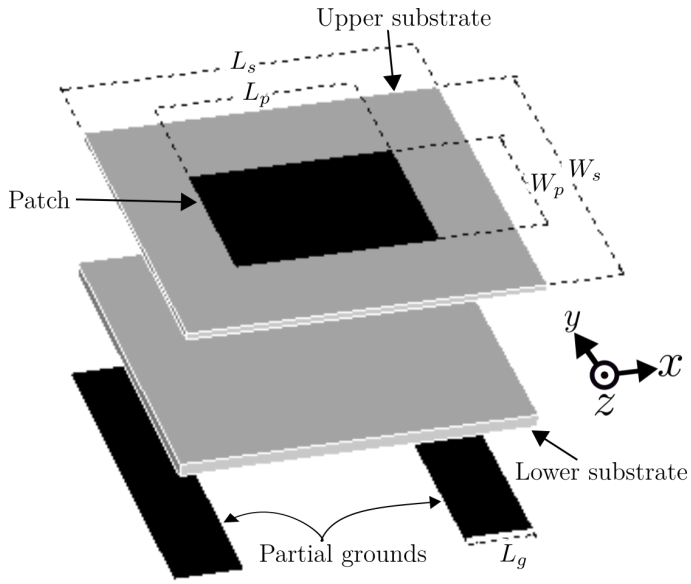


Figure 4.4. Proximity-fed patch antenna with two partial grounds and without feed lines. The black colour indicates the layers of copper.

The modal significance obtained from the CMA of the antenna prototype in Figure 4.4 in CST MWS is provided in Figure 4.5. It is shown in Figure 4.5 that only the first three modes are resonant and have a modal significance greater than $1/\sqrt{2}$ [27] in wide frequency ranges, which is sufficient to contribute to the radiation of the antenna in those frequencies. The remaining mode is less significant, so it has a minor contribution to the antenna radiation characteristics in the design frequency. Based on this observation, the characteristic currents and patterns for the first three modes are plotted in Figure 4.6 and 4.7, respectively, for analysis.

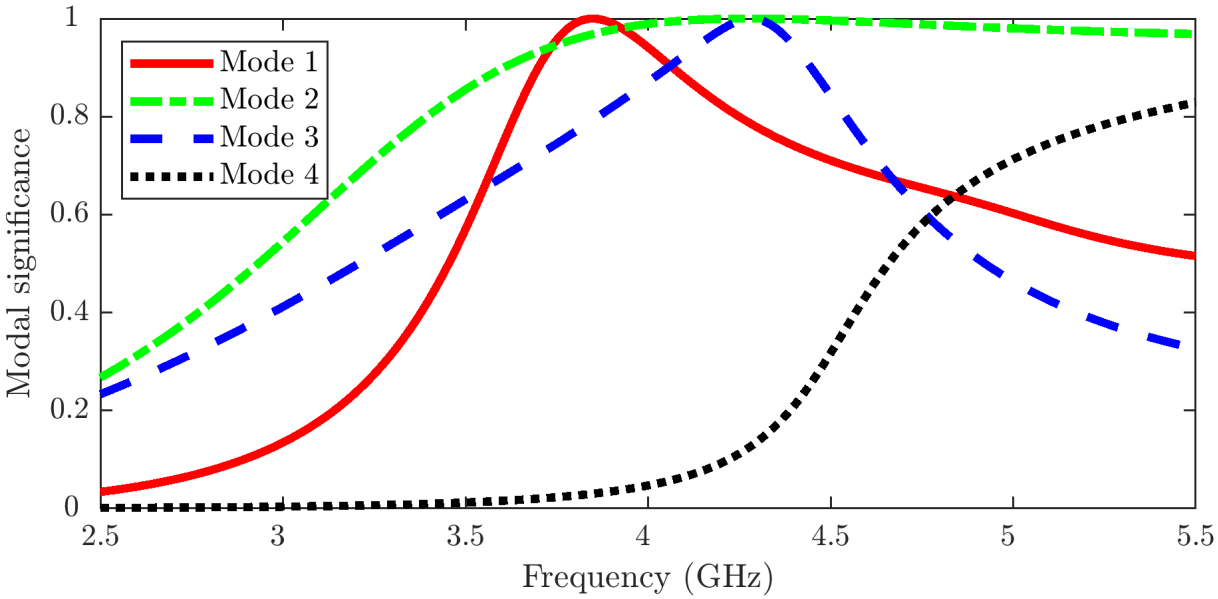


Figure 4.5. The modal significance for the first four characteristic modes of the proximity-fed patch antenna under investigation.

The maximum mode currents for a rectangular patch are at the patch edges [24]. Because of this behaviour, the orientation of the principal modal currents at the patch edges is investigated to identify pairs of symmetrical points, where excitations can be placed to excite particular modes as desired by the symmetry property of characteristic modes [27]. For example, the first mode shown in Figure 4.6a is an inductive fundamental

mode J_{01}, having the principal current forming a single horizontally directed loop, which requires horizontally arranged excitations (in the case of dual feeding) to be excited [86–88]. Also, at the two opposite short edges of the patch, the two current maxima have the principal currents oriented in opposite directions, which means they are out of phase by 180°. The opposite orientation of the principal current at the two edges signifies that mode J_{01} can be excited by differentially driving the two excitations delivered at the current maxima positions 1 and 2 at the two opposite short patch edges.

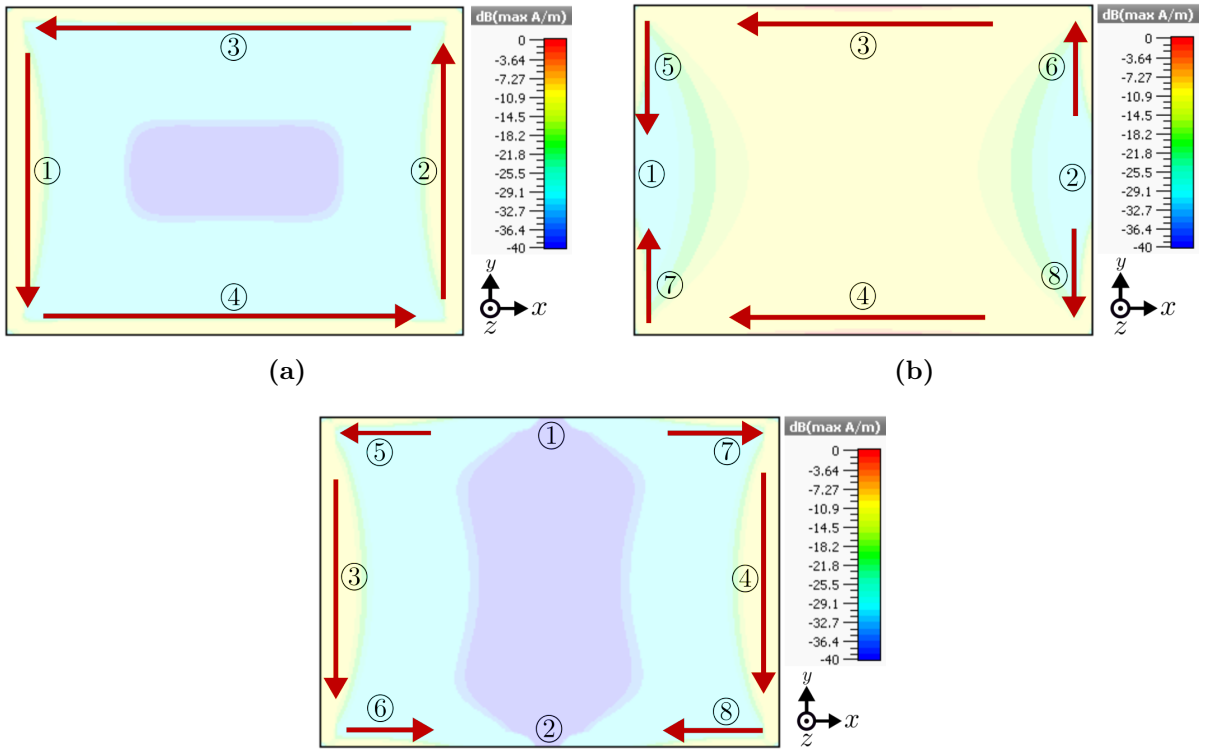


Figure 4.6. Characteristic surface current for (a) mode J_{01} at 3.848 GHz (b) mode J_1 at 4.275 GHz and (c) mode J_2 at 4.282 GHz frequency for the antenna under investigation.

The E and H-plane directive patterns for mode J_{01} are shown in Figure 4.7a. Considering the E-plane ($\phi = 0°$) directive pattern for mode J_{01}, simultaneously feeding the antenna at $\theta = 90°$ and $\theta = 270°$ (shown in Figure 4.8) or at positions 1 and 2 (shown in Figure 4.6a) suppresses the mode so that it radiates along $\theta = 0°$ and $\theta = 180°$ (in the E-plane). Also,

because of the mode suppression, the E-plane main lobe directive gain is reduced from 5.72 decibel relative to isotropic (dBi) to around 2.3 dBi as shown in Figure 4.7a and later in Figure 4.13a. On the other hand, the nulls for the H-plane ($\phi = 90°$) directive pattern are reduced while the H-plane directive gain is enhanced to form an approximately omnidirectional pattern.

Mode two is a horizontal mode J_1 [87, 88], having two branches of the principal current originating at point 2 and joining at point 1, as shown in Figure 4.6b. Because of its polarisation, and the differential orientation of the principal current at the two opposite short patch edges, excitation of mode J_1 requires two pairs of differential excitations to be placed at the current maxima positions 5 and 6, and 7 and 8 at the opposite short edges, as shown in Figure 4.6b. This setup requires four feeding points, which is outside the scope of the injection matching technique at this stage. The use of four feeding points to excite this particular mode is discussed in Section 5.2. However, because of the wide distribution of strong mode J_1 currents on the patch, as shown in Figure 4.6b, feeding at positions 1 and 2 of the short patch edges for this mode will jointly excite modes J_1 and J_{01} to enable wide operational bandwidth.

The E and H-plane directive patterns for mode J_1 are shown in Figure 4.7b. Simultaneously feeding the antenna at $\theta = 90°$ and $\theta = 270°$ (considering the E-plane pattern shown in Figure 4.8) or at positions 1 and 2 (shown in Figure 4.6b) for mode J_1, suppresses the mode so that its E-plane directive gain is reduced from a maximum value of 6 dBi to some values of around 2 dBi as shown in Figure 4.7a and later in Figure 4.13d. Because of the suppression of mode J_1 as a result of feeding at the two E-plane nulls, the nulls for the H-plane directive pattern are reduced to form an approximately omnidirectional pattern.

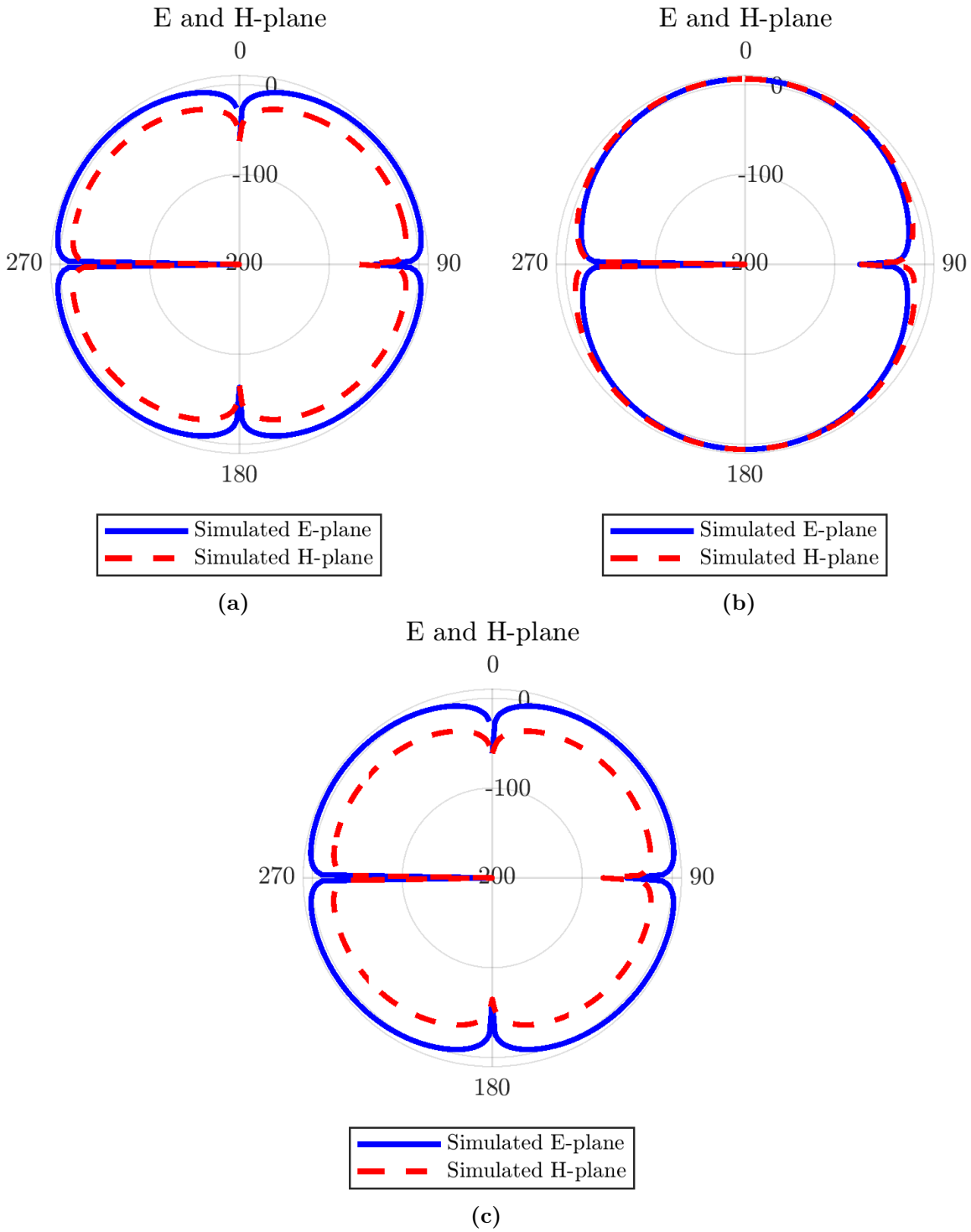


Figure 4.7. Characteristic directive radiation patterns for (a) mode J_{01} at 3.848 GHz (b) mode J_1 at 4.275 GHz and (c) mode J_2 at 4.282 GHz frequency for the antenna under investigation.

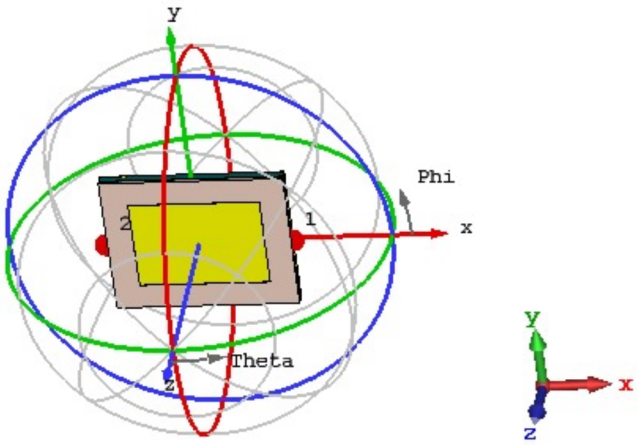


Figure 4.8. Presentation of the two-port antenna in the Cartesian coordinate system in CST MWS, showing the ϕ and θ directions.

On the other hand, mode three is a vertical mode J_2, having two branches of the principal current originating at point 1 and joining at point 2 along the opposite long patch edges as shown in Figure 4.6c. The principal currents are out of phase by 180° at the opposite two long patch edges. Excitation of mode J_2 requires two pairs of differential excitations to be delivered at the maxima positions 5 and 6, and 7 and 8 at the two long patch edges as shown in Figure 4.6c, which is, however, not feasible because of the absence of the grounding planes at these locations as shown in Figure 4.4. Introducing the PGPs below the long patch edges of this antenna or replacing the PGPs with the FGP alters the electrical symmetry of the monopole antenna, which is utilised in this thesis for bandwidth and performance enhancements of patch antennas, as discussed in Section 2.6.1. As such, the antenna structure is maintained throughout this thesis. However, the excitation of this kind of mode on a two-port planar monopole antenna is discussed in Section 6.2.1. The vertical mode J_2 has the E and H-plane directive patterns shown in Figure 4.7c, which also predict approximately omnidirectional patterns if excitations could be placed at the E-plane vertical nulls of this mode.

The joint excitation of modes J_{01} and J_1 of the proposed antenna is discussed in Section 4.3.3 by feeding the antenna at locations 1 and 2, shown in Figure 4.6a and 4.6b, using two EM coupled feed lines to enable wideband operation.

4.3.3 The two-port injection matched antenna

To excite modes J_{01} and J_1, the two feed lines are etched on top of the lower substrate along the magnetic symmetry line of the patch as shown in Figure 4.9, and two discrete face ports are created on the outer end-faces of the feed lines. The dissipation loss for the two Rogers RT Duroid 5880 substrates in Figure 4.9 is changed to 0.0009, and copper cladding is used instead of the PEC. The gap between the feed lines is initially chosen to be $g = 1.5$ mm, but any value of g between 0.1 and 2.0 mm can be selected, which can later be adjusted by sweeping the parameter g in CST DS through the procedure outlined in Appendix B.1, between 0.1 and 2.0 mm. The width of the feed lines is initially chosen to be $w = 1.6$ mm.

The two-port antenna is then injection matched in CST DS using the setup in Figure 4.10. The role of the signal splitter is to generate the two coherent signals required for driving the two-port antenna. The signal at port two is amplified by a linear factor γ and phase-shifted by φ relatively to the port one signal after passing through the amplifier and phase shifter. The TARC for the injection matched antenna under investigation at $\gamma = 1$ and $\varphi = 0°$, as well as $\gamma = 1$ and $\varphi = 180°$, is shown in Figure 4.11. It is shown in Figure 4.11 that, at $w = 1.6$ mm and $g = 1.5$ mm, the differential TARC (i.e. TARC at $\gamma = 1$ and $\varphi = 180°$) has good impedance matching than the corresponding common mode TARC (i.e. TARC at $\gamma = 1$ and $\varphi = 0°$) because there is no mode in Figure 4.6

which requires common mode excitation. The FBW for the differential mode TARC attained at $g = 1.5$ mm and $w = 1.6$ mm is around 43.1% (calculated using Equation (B.1) in Appendix B.4) at a 3.637 GHz centre frequency. The high FBW has been attained by exciting correlated modes J_{01} and J_1 of the antenna [27]. The excited two modes are indicated by the differential TARC resonances obtained when g is fixed at 0.1 mm and w varied between 0.6 and 2.5 mm, as shown in Figure 4.11.

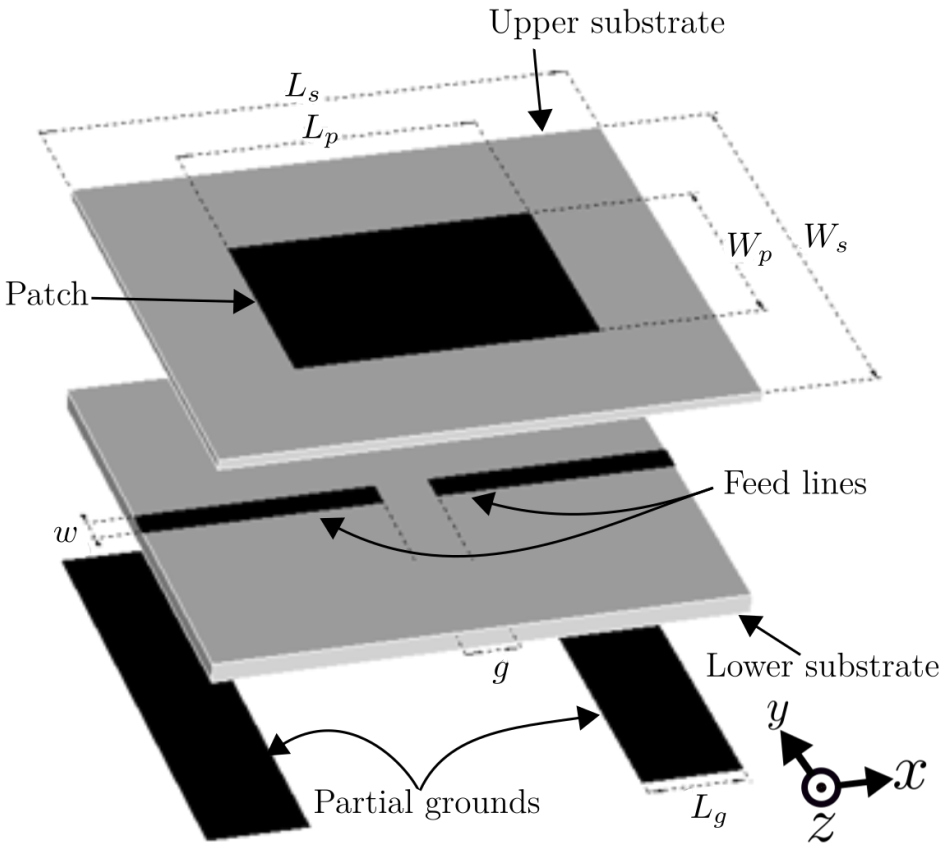


Figure 4.9. Proximity-fed patch antenna with two feed lines. The black colour indicates the layers of copper.

Typically, the TARC resonance attained when $g = 0.1$ mm and $w = 0.8$ mm shows that there are two modes at around 3.049 and 3.562 GHz frequencies resulting from excitation of modes J_{01} and J_1 of the antenna. Considering the surface currents resulting from the differentially excited two-port antenna when $g = 0.1$ mm and $w = 0.8$ mm,

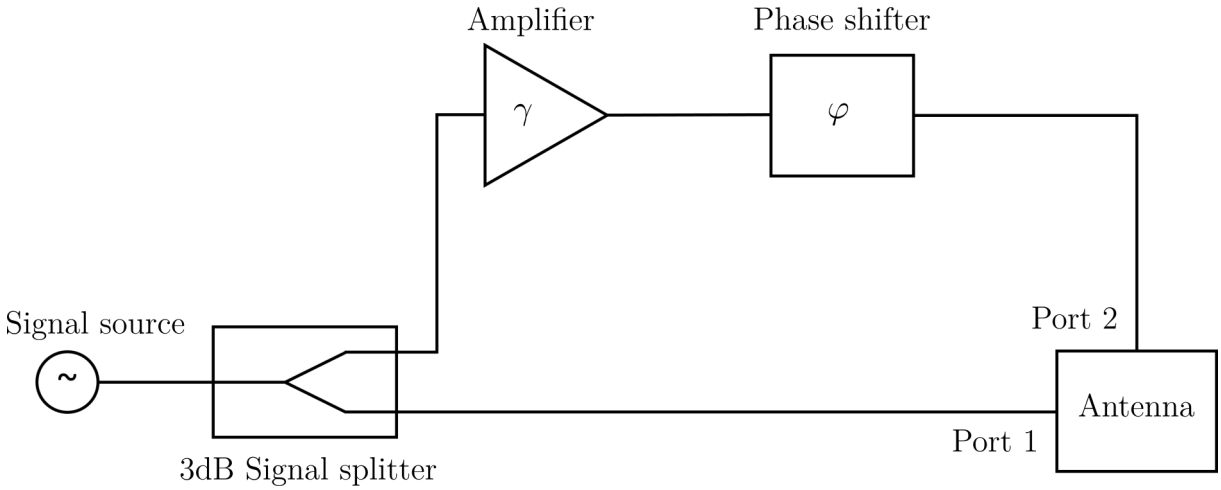


Figure 4.10. The block diagram for implementing the two-port injection matching technique in CST DS.

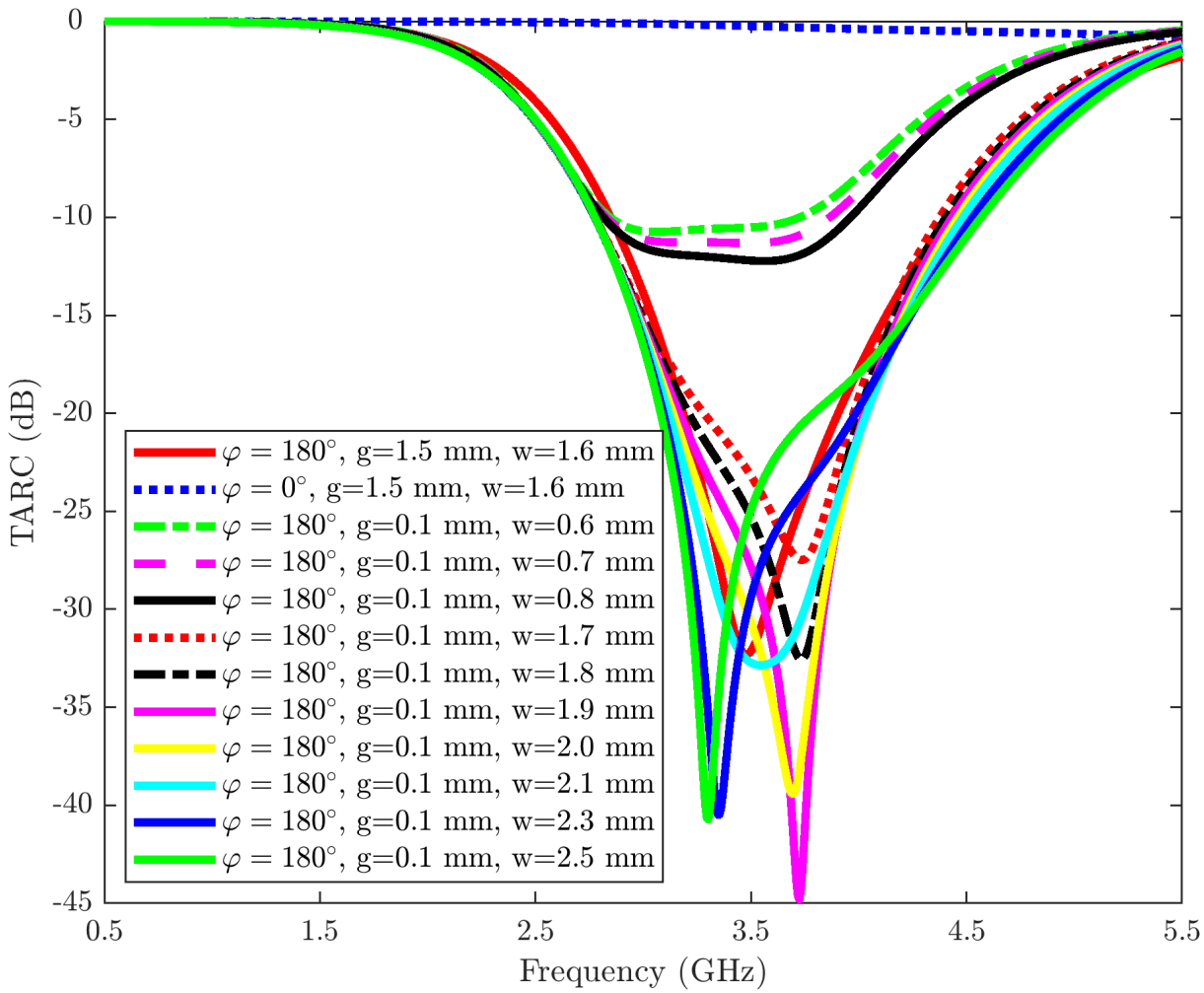


Figure 4.11. TARC for the differentially and common mode excited two-port antenna under investigation when $\gamma = 1$ at different φ, w and g values.

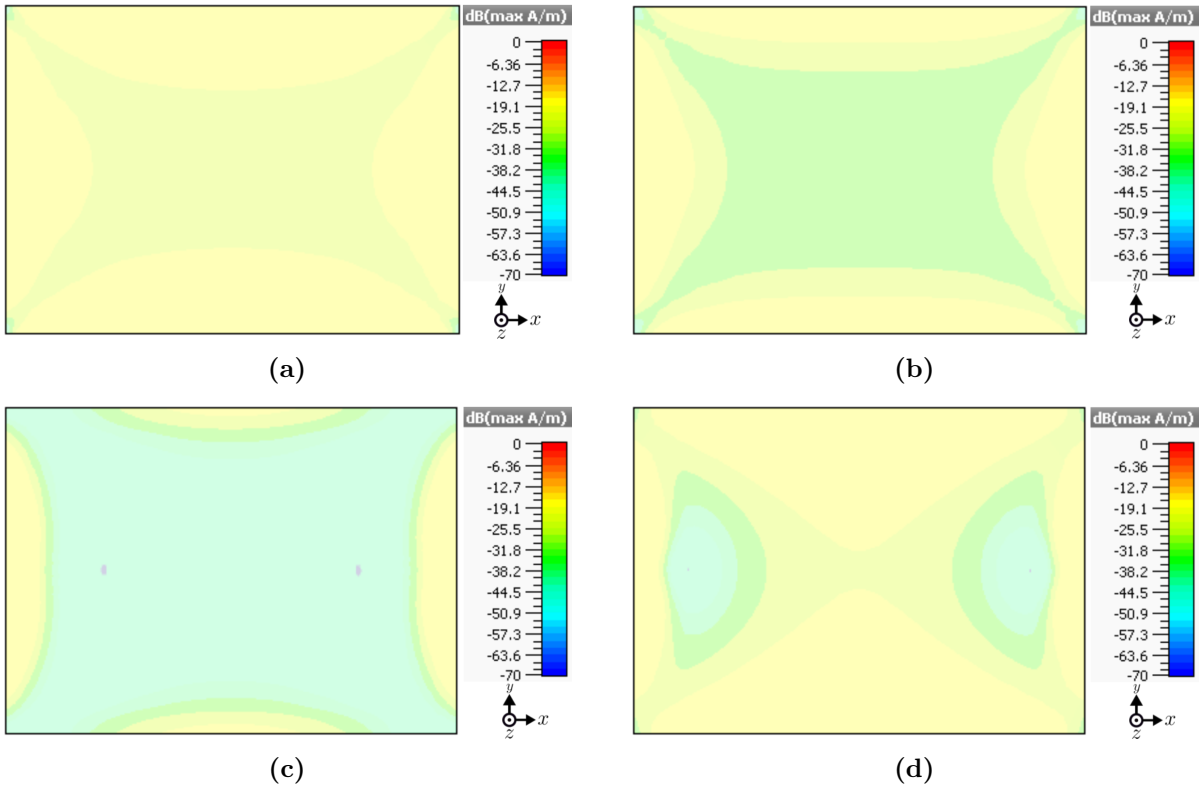


Figure 4.12. Simulated surface current at (a) 2.822 GHz (b) 3.049 GHz (c) 3.562 GHz and (d) 3.961 GHz frequencies resulting from the differential excitation of the antenna under investigation when $g = 0.1$ mm and $w = 0.8$ mm. The modal significance for this antenna is shown in Figure 4.5.

depicted in Figure 4.12, it is shown that the surface currents at 2.822 and 3.049 GHz frequencies (shown in Figure 4.12a and 4.12a) are similar to the mode J_{01} current shown in Figure 4.6a. This observation indicates that mode J_{01} of the antenna has been excited at 2.822 and 3.049 GHz frequencies. However, features of modes J_{01} and J_1 are seen at 3.562 GHz frequency, as shown in Figure 4.12c, where mode J_{01} current dominates over mode J_1 current (shown in Figure 4.6a and 4.6b), indicating the excitation of both modes J_{01} and J_1 at this frequency. Also, the surface current at 3.961 GHz shown in Figure 4.12d has both features of modes J_{01} and J_1 currents shown in Figure 4.6a and 4.6b, indicating the excitation of modes J_{01} and J_1 at this frequency. However, at this frequency (3.961 GHz), mode J_1 is dominant over mode J_{01}. These observations indicate the high correlation between the surface currents for modes J_{01} and J_1 of the antenna under investigation.

The H-plane ($\phi = 90°$) directive radiation patterns resulting from excitation of modes J_{01} and J_1 are approximately omnidirectional as shown in Figure 4.13 as predicted by the eigenpatterns in Figure 4.7. However, the E-plane ($\phi = 0°$) patterns have two nulls in the directions $\theta = 90°$ and $\theta = 270°$ because of feeding the antenna at these locations.

On the other hand, there is an improvement in the impedance matching of modes J_{01} and J_1 shown by the differential TARC resonances attained at $g = 0.1$ mm and $w = 2.5$ mm, and $g = 0.1$ mm and $w = 1.9$ mm, respectively. A maximum FBW of around 46.6% at a 3.672 GHz centre frequency is attained by the differential TARC resonance when $g = 0.1$ mm and $w = 2.5$ mm, as shown in Figure 4.11, due to the excitation of modes J_{01} and J_1 of the antenna.

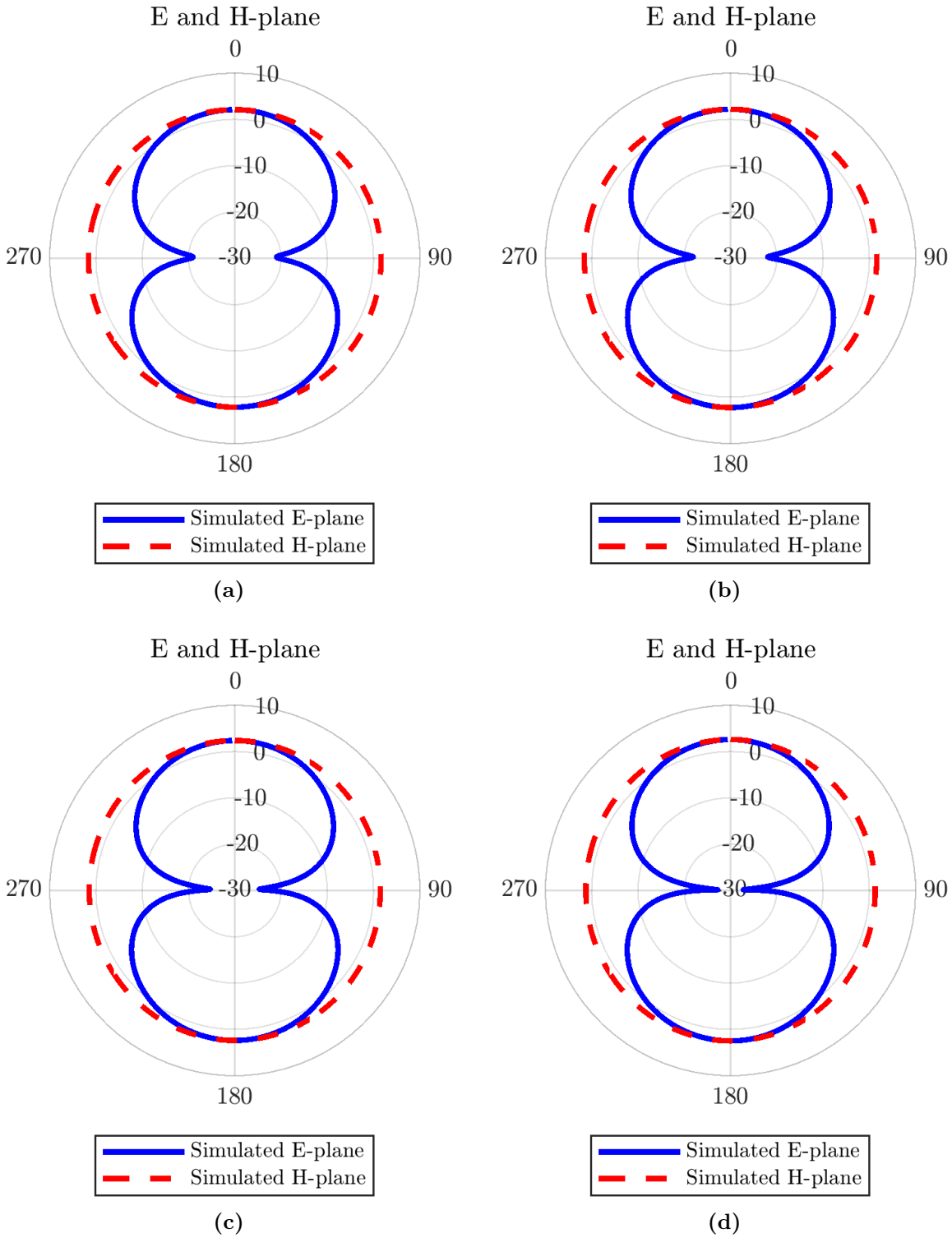


Figure 4.13. Simulated radiation patterns at (a) 2.822 GHz (b) 3.049 GHz (c) 3.562 GHz and (d) 3.961 GHz frequencies resulting from the differential excitation of the antenna under investigation when $g = 0.1$ mm and $w = 0.8$ mm. The modal significance of this antenna is shown in Figure 4.5.

The bandwidth attained from the patch antenna in Figure 4.11 can be enhanced by changing the resonance behaviour of the modes on the patch. This change is achieved by altering the antenna dimensions through optimisation. However, before the antenna dimensions are optimised, the effect of changing each (antenna) dimension to the two-port injection matched antenna is studied in Figure B.7 through B.9 in Appendix B.3 while other antenna dimensions are fixed.

In Figure B.7a in Appendix B.3 the gap g between the two feed lines was varied from 0.1 to L_p mm, and it can be seen that TARC < -10 dB is obtained when g is between 0.1 and 10 mm. However, good -10 dB impedance matched bandwidth is maintained when g is between 0.1 and 2.2 mm or 0.1 and $0.09L_p$ mm. Also, the variation of the feed line width w in Figure B.8, which was varied between $0.9w$ and $2.6w$ shows that small w feed lines provide good impedance matching. However, the -10 dB impedance matched bandwidth is maintained by adopting the feed line width of up to $2.3w$. So, for a good trade-off between bandwidth, input impedance, and easy of soldering, w ranging between $0.9w$ and $2.3w$ is sufficient for realisation of the two-port injection matched antenna under investigation. Besides, decreasing the length of PGP to some values below $(L_s - L_p)/2$, as shown in Figure B.7b in Appendix B.3, widens the -10 dB impedance matched bandwidth by allowing the multiple modes of the antenna to resonate. The minimum PGP length of 4.2 mm or $0.84L_g$ mm for this antenna can be sufficient to allow the excitation of multiple modes. Smaller ground planes with L_g less than 4.2 mm, for this antenna, are avoided as they are more problematic in providing sufficient grounding during measurements.

The patch length L_p and patch width W_p were varied between $0.8L_p$ and $1.2L_p$, and $0.8W_p$ and $1.2W_p$, respectively. It is shown in Figure B.9a and B.9b in Appendix B.3

that changing L_p or W_p affects both the bandwidth and input impedance of the two-port injection matched antenna. The choice of the lower and upper bounds for L_p and W_p can therefore be done through trial and error method until the desired results are obtained. Also, the changes in L_p and W_p will equally lead to the changes in L_s and W_s.

Therefore, the bandwidth for the TARC resonance in Figure 4.11 can be enhanced by allowing the multiple differential modes to resonate on the patch through adjustment of the antenna dimensions. Based on the previous investigation in this section, the patch length L_p, patch width W_p, substrate length L_s, substrate width W_s, length of partial grounds L_g, width of the coupled lines w and the gap between the two coupled lines g are optimised in CST DS between the established bounds shown in Table 4.1. At the same time, the TARC is monitored and plotted in Figure 4.14.

Table 4.1. Lower and upper bounds of the antenna dimensions used in the optimisation of TARC in CST DS.

Optimisation Bounds	Antenna dimensions (mm)						
	L_p	W_p	L_s	W_s	L_g	w	g
Lower bound	23	17	34	24	4.2	1.44	0.1
Upper bound	31	22	46	32	8	3.7	2.25

The TARC3 resonance is well-matched and has the widest bandwidth among the resonances depicted in Figure 4.14, as shown in Table 4.2. The dimensions of the antenna at this resonance are depicted in Table 4.2. The bandwidth and impedance matching for this resonance are improved by fine-tuning the antenna dimensions through parameter sweep in CST DS, in the bounds shown in Table 4.3. The typical optimum results derived from this parameter sweep are provided in Figure 4.15.

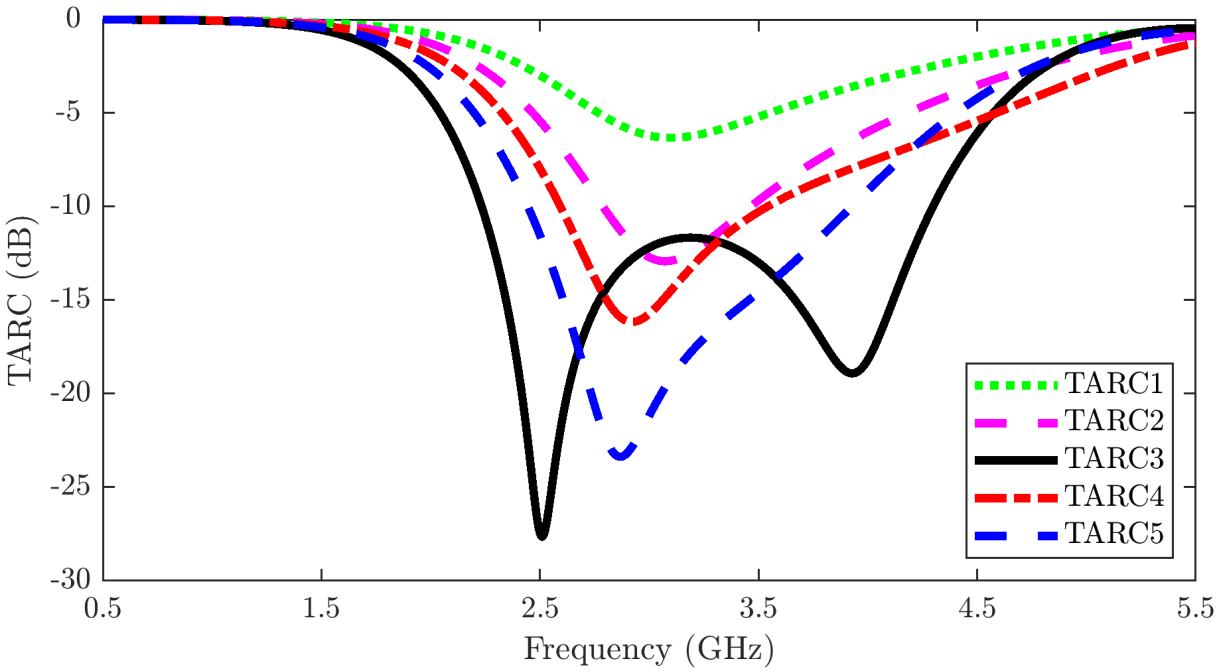


Figure 4.14. Typical results for the optimised TARC resonances for the differentially excited two-port antenna.

Table 4.2. Dimensions for the optimised TARC resonances shown in Figure 4.14.

Simulation ID	Antenna dimensions (mm)							FBW
	L_p	W_p	L_s	W_s	L_g	w	g	
TARC0	25.0	18.0	35.0	28.0	5.0	1.6	1.5	0.431
TARC1	29.5	19.32	37.0	27.51	7.1	2.9	1.2	-
TARC2	27.0	16.73	38.0	28.3	8.0	2.6	0.4	0.213
TARC3	29.3	18.88	43.0	29.82	5.2	2.2	0.2	0.631
TARC4	27.0	17.57	40.0	28.02	7.5	3.2	0.27	0.307
TARC5	28.7	20.86	42.0	29.4	6.3	2.5	0.38	0.465

Table 4.3. Lower and upper bounds of the antenna dimensions used in the fine-tuning of TARC through parameter sweep in CST DS.

Optimisation Bounds	Antenna dimensions (mm)						
	L_p	W_p	L_s	W_s	L_g	w	g
Lower bound	29	17.9	43	28.8	5.2	2.1	0.1
Upper bound	31	20.9	46	30.8	5.4	2.5	0.5

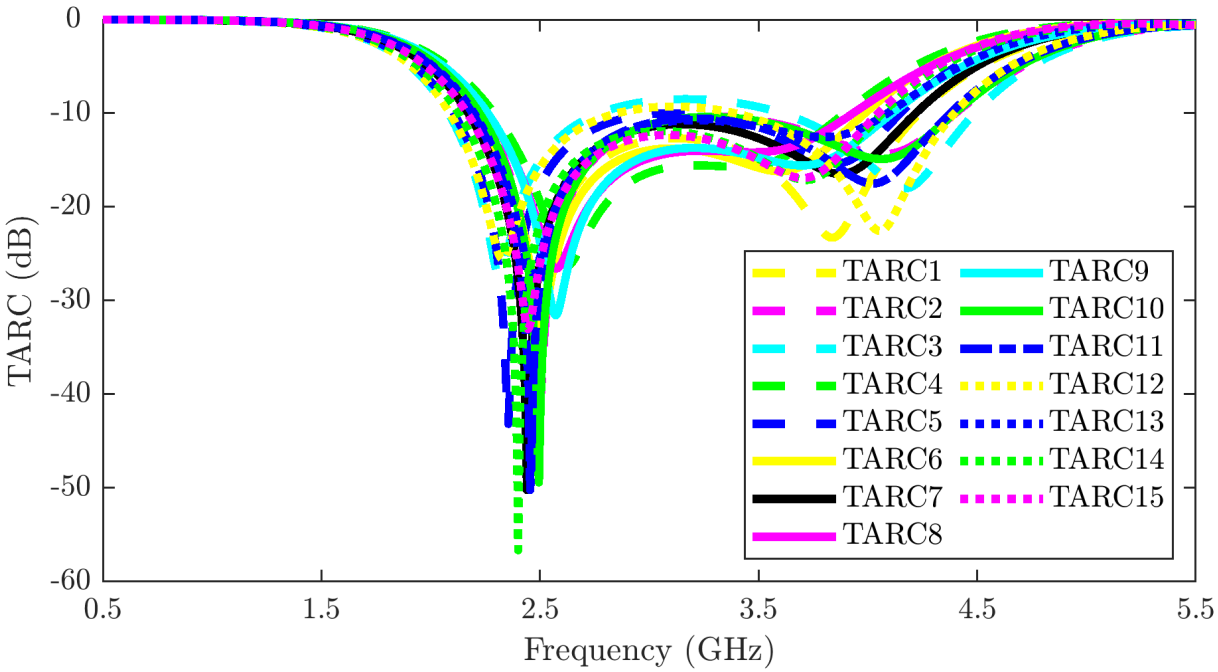


Figure 4.15. Typical results of the fine-tuned TARC resonances for the differentially excited two-port antenna whose dimensions are depicted in Table B.3 in Appendix B.3.

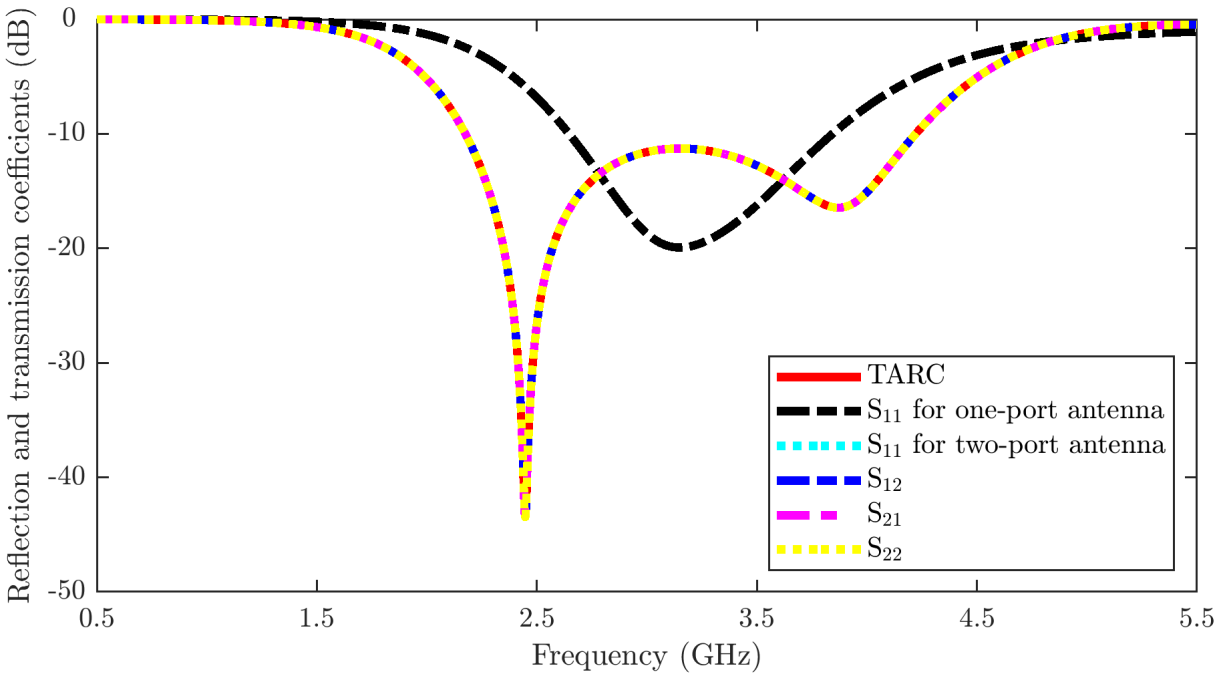


Figure 4.16. Simulated TARC, individual port reflection coefficients, and transmission coefficients between the two ports for the differentially excited two-port injection matched antenna compared to S_{11} for the corresponding one-port antenna. The dimensions for the two antennas are depicted by TARC7 resonance in Table B.3 in Appendix B.3.

Considering wide bandwidth and good impedance matching criteria at −10 dB for the fine-tuned TARC resonances in Figure 4.15, TARC7 met the criteria, and is depicted in Figure 4.16 together with the corresponding S_{11}, S_{21}, S_{12}, and S_{22} for the realised two-port antenna. It is shown in Figure 4.16 that the S_{11}, S_{21}, S_{12}, and S_{22} for the two-port antenna are equal to the TARC resonance because of the symmetry between the two feed points.

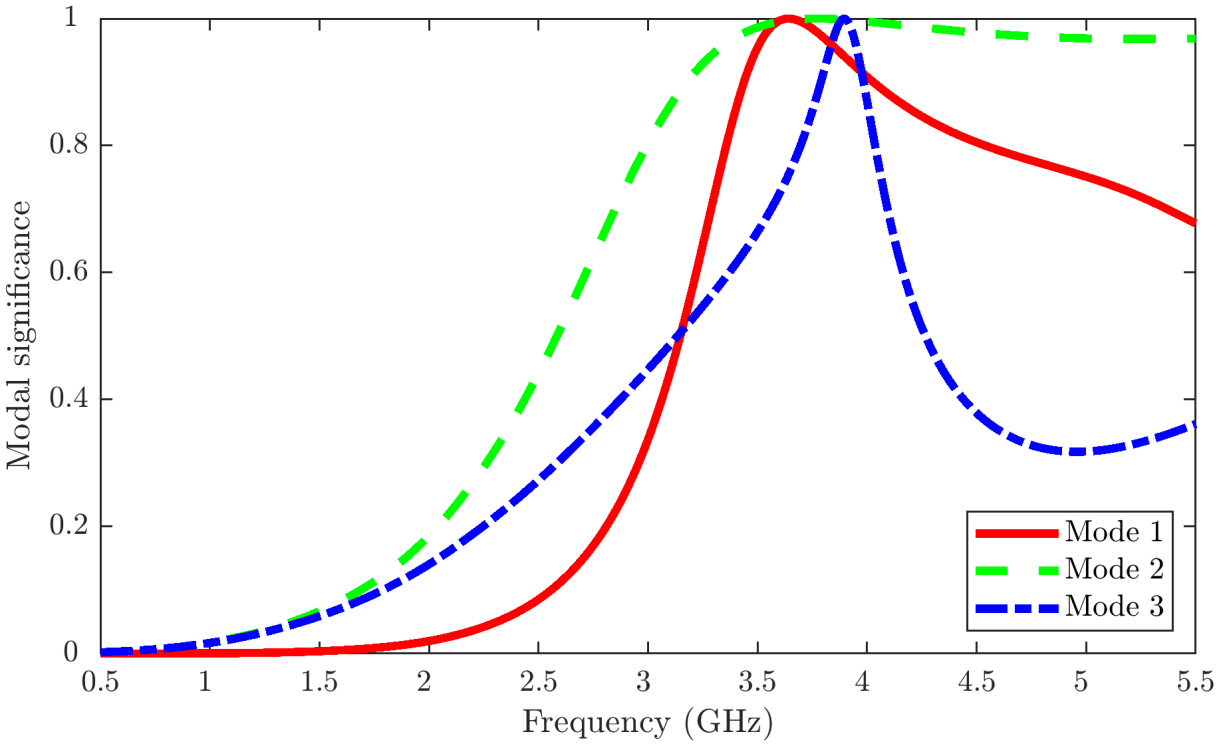


Figure 4.17. The modal significance for the first three resonant characteristic modes of the proximity-fed patch antenna whose TARC resonance is depicted in Figure 4.16.

The CMA of the antenna whose TARC resonance is depicted in Figure 4.16 is provided in Figure 4.17 and 4.18. It is shown in Figure 4.17 and 4.18a that mode one is an inductive mode J_{01}, having a characteristic current that forms a horizontally directed closed loop on the patch. Also, the principal current for mode J_{01} is differentially oriented along the two opposite short patch edges, allowing the mode to be differentially excited from the centre of these edges at positions 1 and 2, as shown in Figure 4.18a. The H-plane ($\phi = 90°$)

radiation patterns resulting from excitation of mode J_{01}, shown in Figure 4.40b and 4.42a at a 2.447 GHz resonant frequency, are approximately omnidirectional as predicted by mode J_{01} patterns in Figure 4.7a and 4.13a. However, at the same frequency, the E-plane ($\phi = 0°$) patterns have two deep nulls in the directions $\theta = 90°$ and $\theta = 270°$ (shown in Figure 4.40b) as a result of feeding the antenna at these locations.

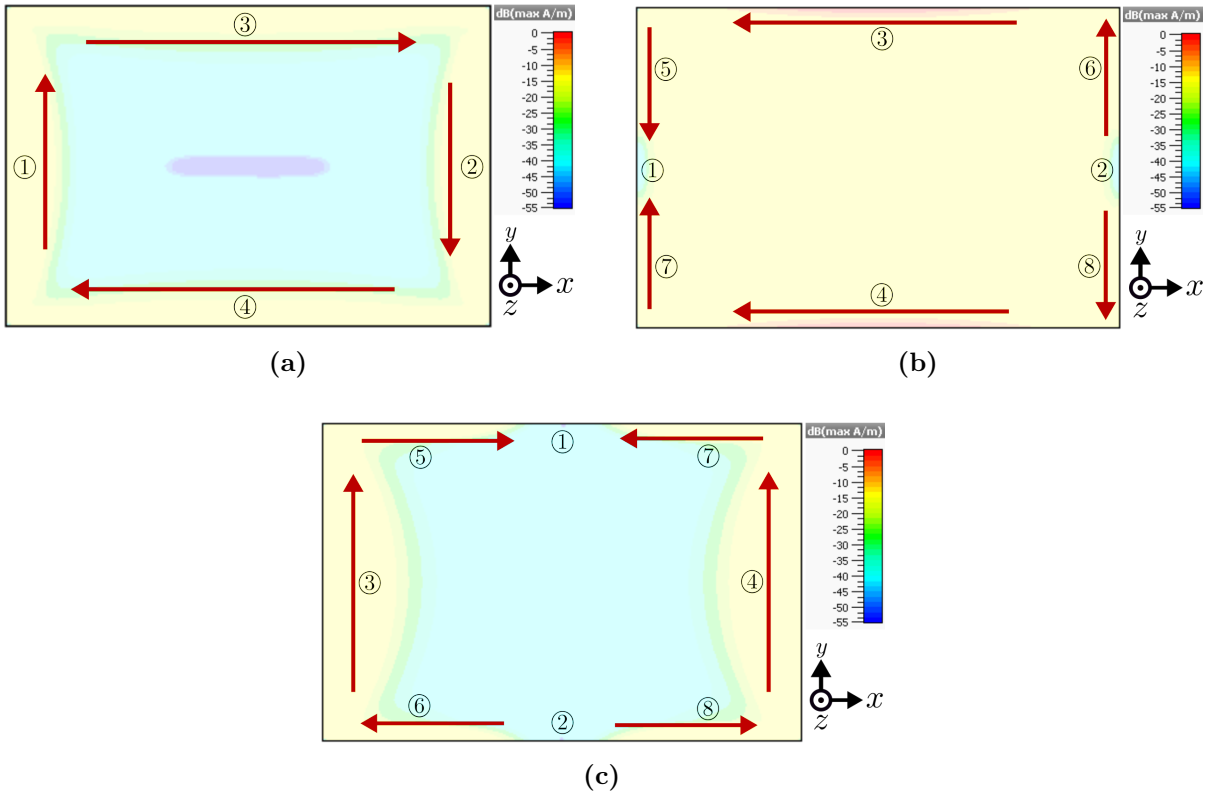


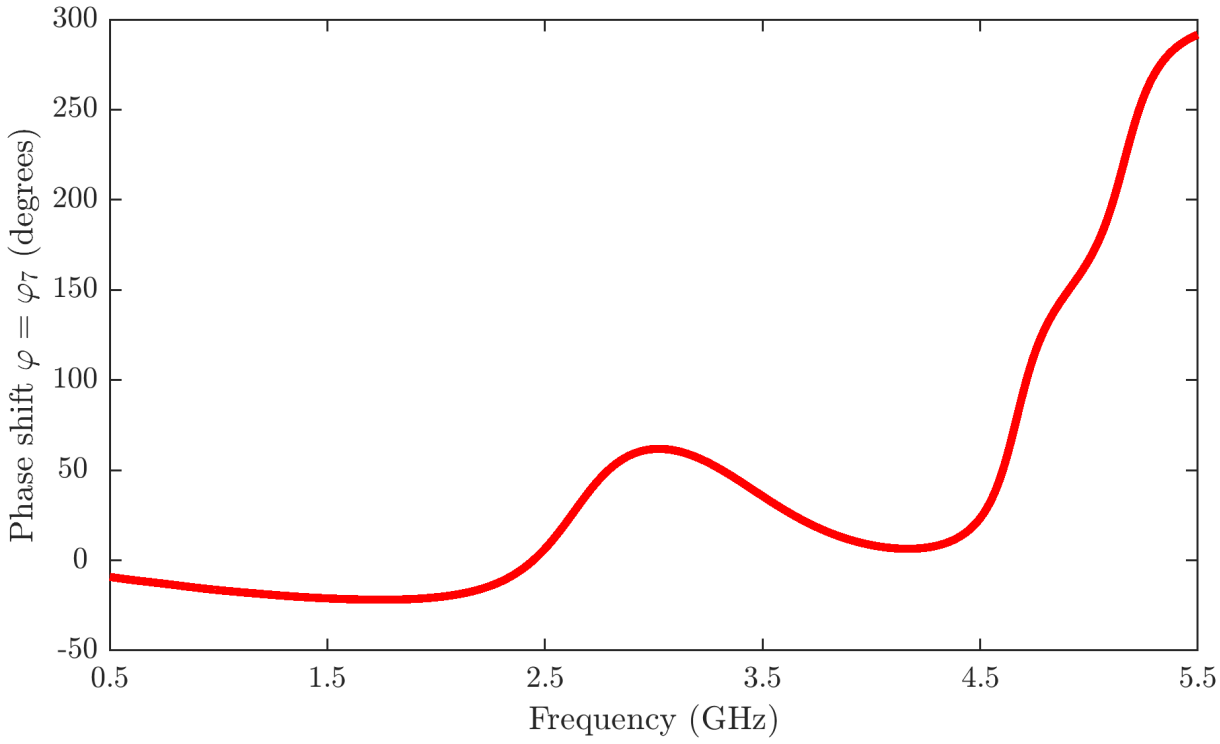
Figure 4.18. Characteristic surface current for (a) mode J_{01} at 3.640 GHz (b) mode J_1 at 3.770 GHz (c) mode J_2 at 3.895 GHz for the antenna depicted in Figure 4.16, whose modal significance is shown in Figure 4.17.

Mode two is horizontal J_1 mode, having two branches of the principal characteristic current originating from position 2, attaining maximum value at different positions along the patch periphery such as at the maxima positions 3 through 8 and joining at position 1 in the short patch edge as shown in Figure 4.17 and 4.18b. Because of its polarisation and distribution of the strong current on the patch, as shown in Figure 4.18b, mode J_1

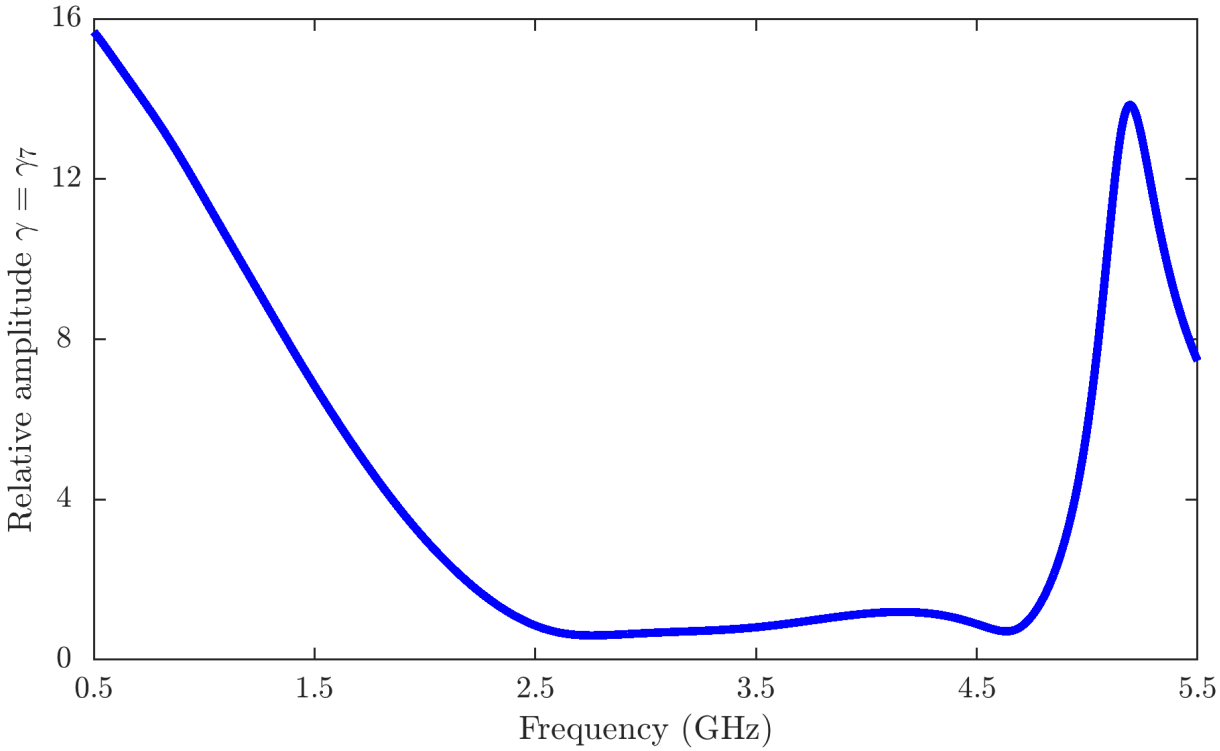
is jointly excited with mode J_{01} by differentially feeding at the patch edge positions 1 and 2, shown in Figure 4.18b. The H-plane ($\phi = 90°$) radiation patterns resulting from excitation of mode J_1, shown in Figure 4.40c and 4.42a at a 3.881 GHz resonant frequency, are approximately omnidirectional as predicted by mode J_1 patterns in Figure 4.7b and 4.13d. However, at the same frequency, the E-plane ($\phi = 0°$) patterns have two deep nulls in the directions $\theta = 90°$ and $\theta = 270°$ (shown in Figure 4.40c) as a result of feeding the antenna at these locations.

On the other hand, mode three is a vertical mode J_2, having two branches of the principal current originating from position 2 and joining at positions 1, as shown in Figure 4.17 and 4.18c. Because of its polarisation and a differential orientation of the principal current at the long patch edges, excitation of mode J_2 requires two pairs of differential excitations arranged at the maxima positions 5 and 6, and 7 and 8 as shown in Figure 4.18c. However, feeding at these positions is not feasible because of the absence of grounding planes below the two long patch edges of this antenna. Excitation of this particular mode is discussed in Section 6.2.1. Hence, the wideband operation of the realised two-port injection matched patch antenna depicted in Figure 4.16 is attributed to the excitation of correlated modes J_{01} and J_1 of the antenna, which are shown in Figure 4.17 and 4.18.

The theoretical φ and γ variations with frequency, which correspond to TARC7 resonance, are also shown in Figure 4.19. It is shown in Figure 4.19 that the theoretical φ variation with frequency has two minima at around 2 and 4 GHz. The 2 GHz minimum for φ coincides with a fairly flat region in the theoretical γ variation slightly below 2.5 GHz, which form resonances near these frequencies. Also, the 4 GHz minimum for φ coincides with a fairly flat region in the γ variation at the same frequency, which enables



(a)



(b)

Figure 4.19. Variation of the theoretical (a) phase shift φ of Equation (3.8) with frequency (b) relative amplitude γ of Equation (3.9) with frequency on the two-port injection matched antenna whose TARC is shown in Figure 4.16.

another resonance at 4 GHz. Because the two resonances (resonant modes) are correlated to each other [24], they merge to enable a wideband resonance through differential excitation. The antenna dimensions for the TARC resonance in Figure 4.16 are depicted in Figure 4.9 and Table B.3 in Appendix B.3.

The electrical length attained by the differential TARC is around $ka = 1.4$ and $ka = 1.2$ at a 2.448 GHz resonance and -10 dB lower boundary frequency of 2.175 GHz, respectively. However, because of the non-constant behaviour of the theoretical γ variation below this frequency, shown in Figure 4.19b, it is impossible to reduce ka below these values. An outline study of an ESA mode of the injection matched antennas is discussed in Section 7.2 through 7.4.

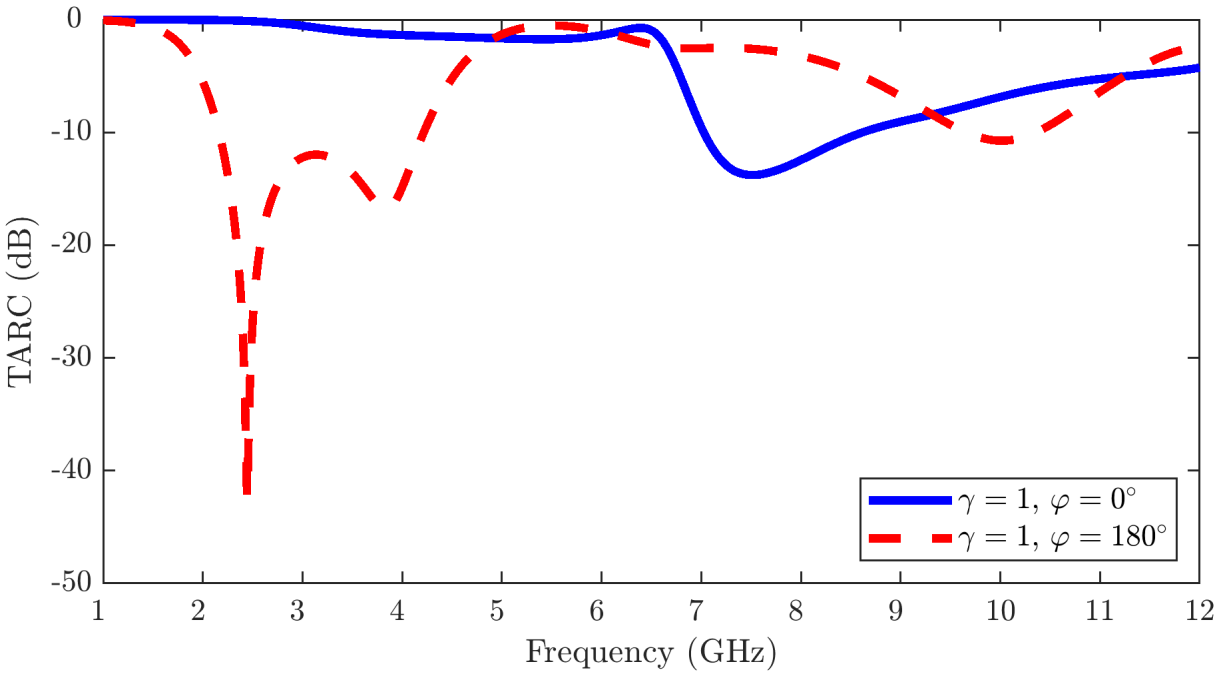


Figure 4.20. The common mode TARC in comparison to the differential mode TARC for the two-port injection matched antenna under investigation.

Extending the frequency range of investigation to 12 GHz, there is a common mode resonance at around 7.5 GHz frequency shown in Figure 4.20. This resonance results from

the excitation of a higher mode of the antenna through the application of the injection matching technique at $\gamma = 1$ and $\varphi = 0°$. However, the bandwidth of this resonance cannot be controlled because the mode was excited by the same feeding arrangement used for exciting the differential mode TARC. Because of the limited number of the feeding points supported by the injection matching technique the two TARC resonances (the differential mode TARC and the common mode TARC) cannot be widened at the same time. Changing the feeding position or the antenna dimensions to improve the common mode TARC will distort the differential TARC. Therefore, this investigation will focus on improving the bandwidth of the differential mode TARC only. The common mode excitations on the patch antenna are particularly studied in depth in Section 6.2.

The S-parameter for the corresponding one-port antenna, depicted in Figure 4.16, was derived from the two-port antenna dimensions depicted by TARC7 resonance in Table B.3 in Appendix B.3. The two reflection coefficient plots in Figure 4.16 are discussed in Section 4.3.4 and 4.4.1.

4.3.4 Simulated TARC

A further investigation of TARC for the differentially excited two-port antenna shown in Figure 4.16 is carried out by varying the applied relative amplitude γ and phase shift φ at port two of the antenna in the ranges $\gamma \in (0.1, 3)$ and $\varphi \in (0°, 180°)$ in CST DS. Typical results for the TARC resonances derived from the whole (γ, φ) optimisation space domain are shown in Figure 4.21.

It is shown in Figure 4.21 that the change in relative amplitude γ and phase shift φ decreases the matching depth of the TARC resonance obtained at $\gamma = 1$ and $\varphi = 180°$.

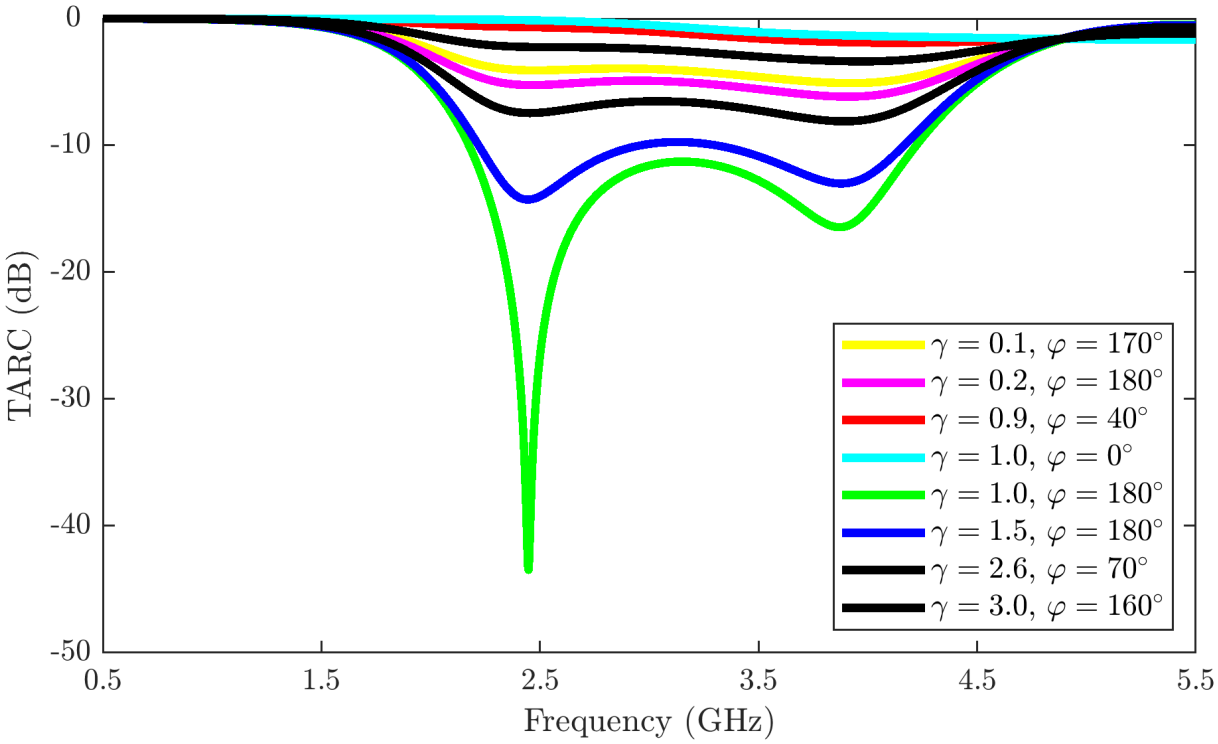
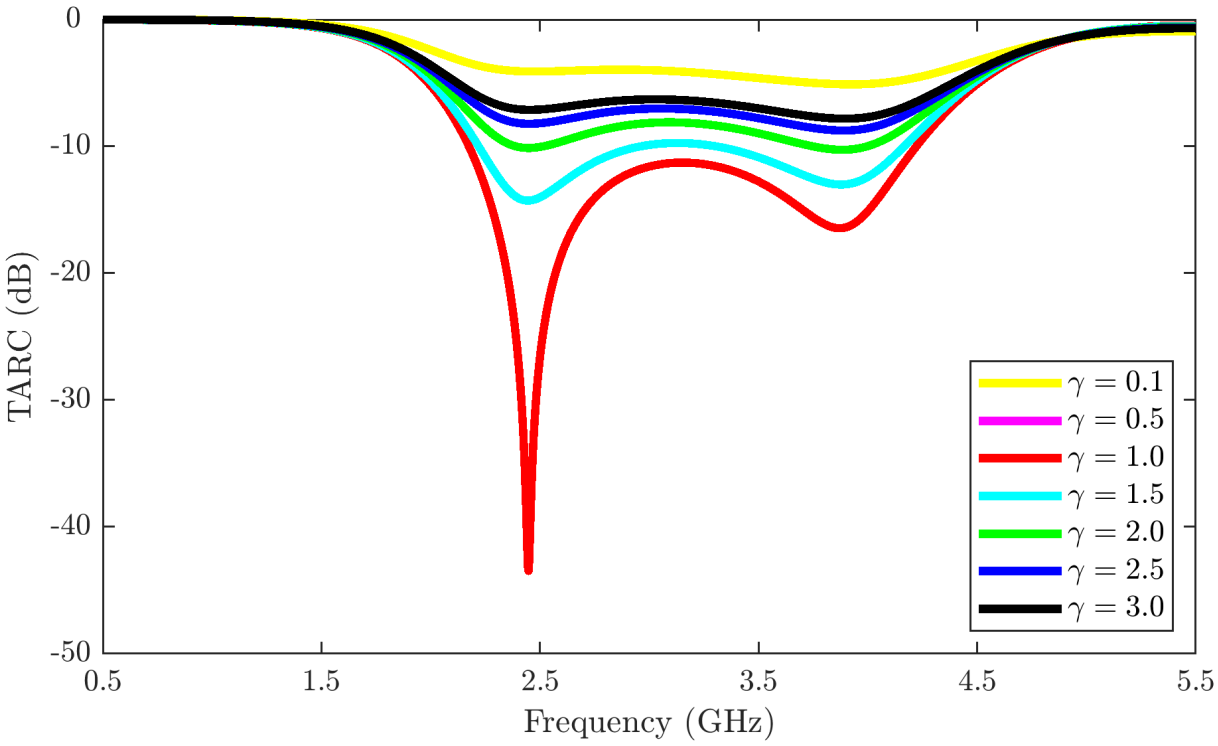


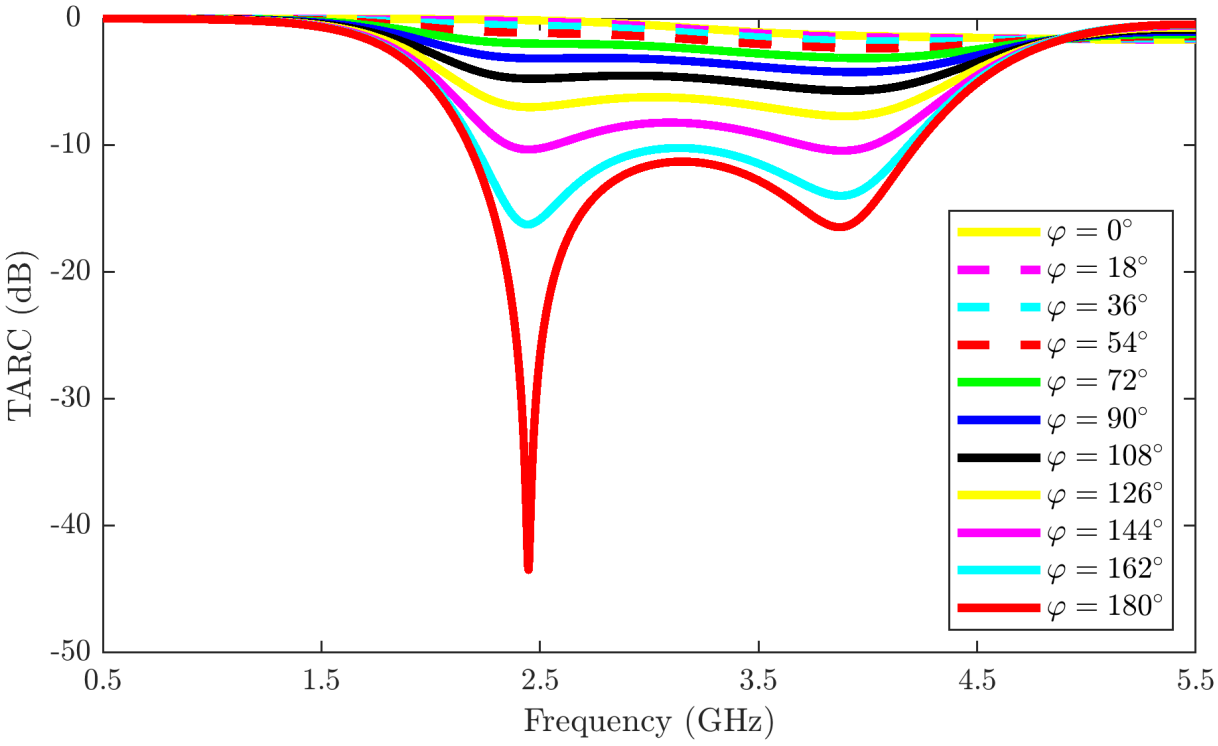
Figure 4.21. Typical TARC resonances for the two-port injection matched antenna at different γ and φ values.

This behaviour is depicted by fixing the phase shift at port two at $\varphi = 180°$, and varying the relative amplitude γ between 0.1 and 3.0. This investigation is also repeated by fixing the relative amplitude at port two at $\gamma = 1$, and varying the phase shift φ between 0° and 180°. The results for this investigation are shown in Figure 4.22a and 4.22b.

The deterioration of TARC resonance is caused by the flow of energy between the two ports when $\gamma < 1$, $\gamma > 1$ or $\varphi \neq 180°$ is applied at port two of the antenna, as shown in Figure 4.21 and 4.22. However, the -10 dB bandwidth is fairly maintained by the combinations of γ and φ values in ranges $0.7 \leq \gamma \leq 1.4$ and $173° \leq \varphi \leq 187°$, which is shown in Figure 4.23 by the typical values of γ and φ derived from this optimisation domain. For $\gamma = 0.6$ the TARC resonance is at around -9.1 dB at all φ in $173° \leq \varphi \leq 187°$ domain. These observations are an indication that the fairly operation of the realised two-



(a)



(b)

Figure 4.22. (a) Variation of γ on the two-port injection matched antenna when $\varphi = 180°$ (b) Variation of φ on the two-port injection matched antenna when $\gamma = 1$.

port injection matched antenna through differential excitation is attained at $\gamma = 1 \pm 0.4$ and $\varphi = 180° \pm 7°$.

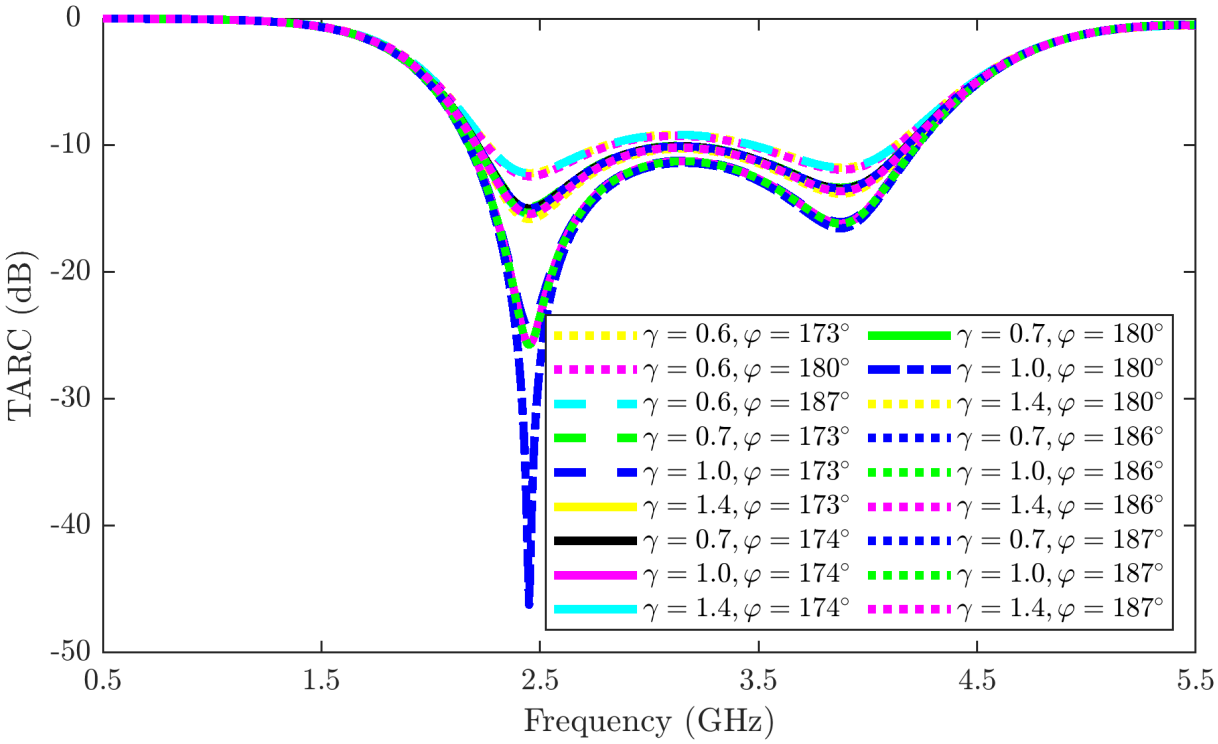
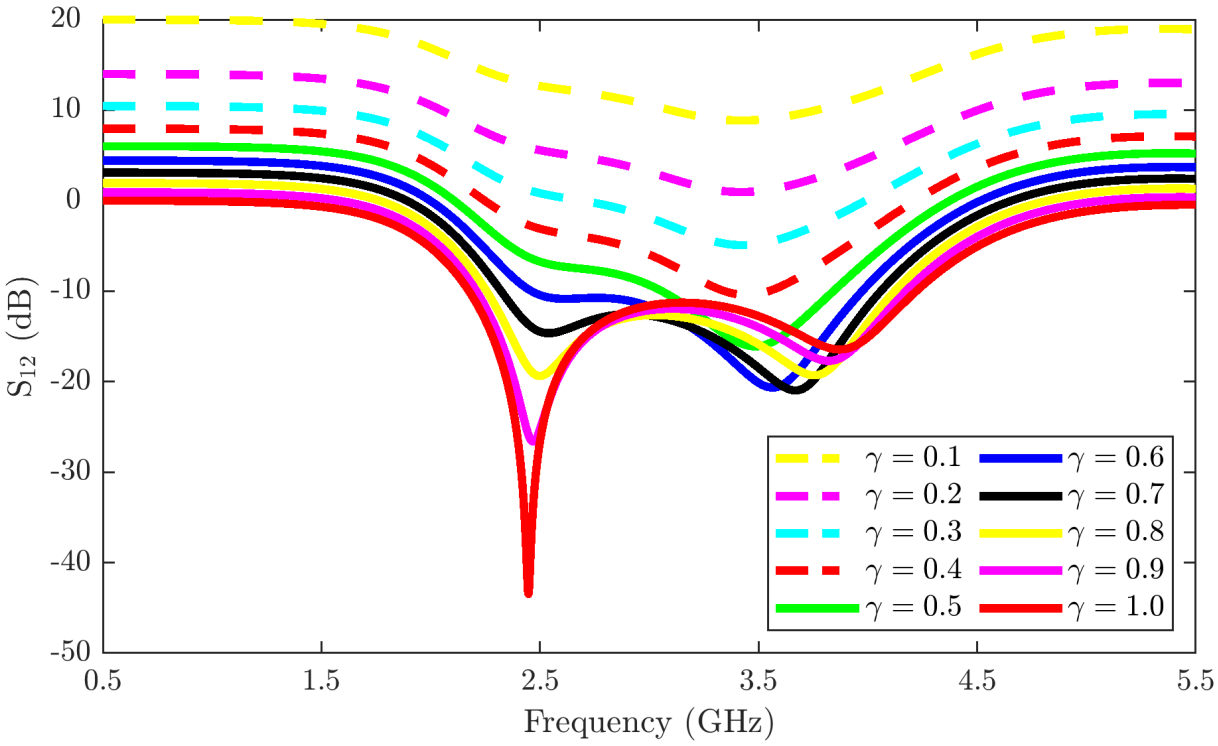
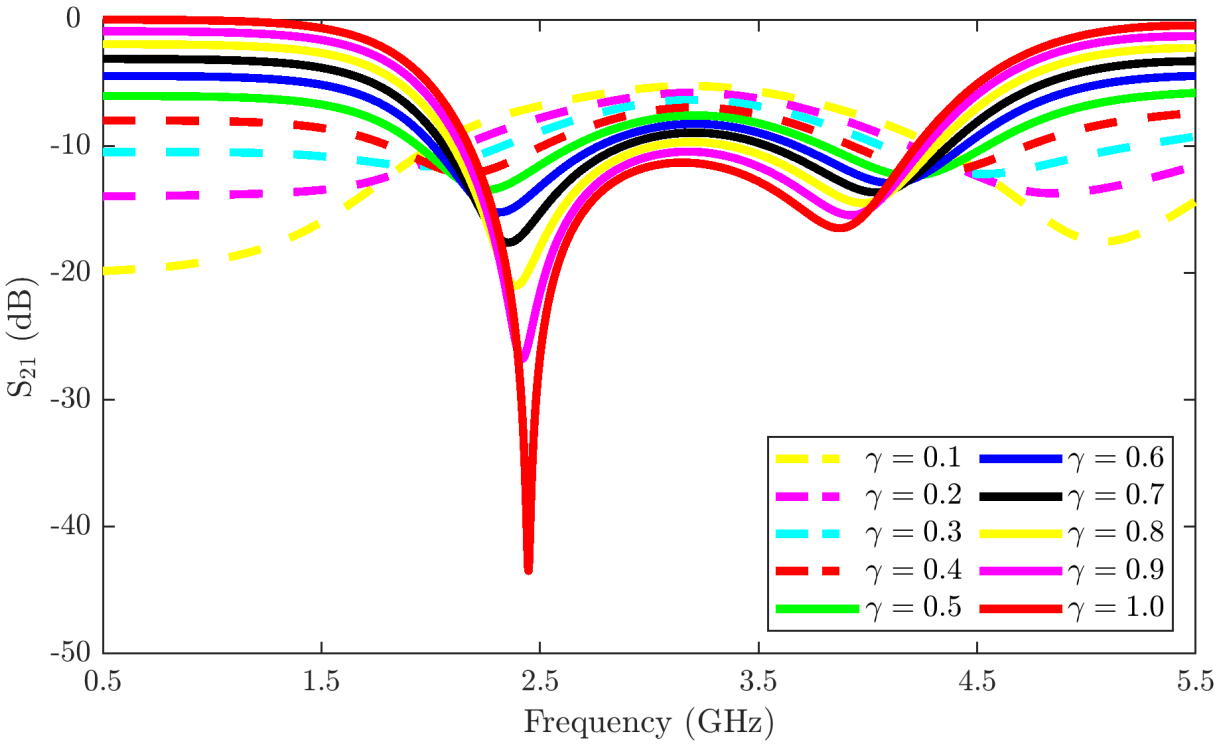


Figure 4.23. Typical differential mode TARC resonances when γ and φ are varied in ranges of $0.6 \leq \gamma \leq 1.4$ and $173° \leq \varphi \leq 187°$.

In particular, the phenomenon in Figure 4.22a is studied by monitoring the transmission coefficients S_{12} and S_{21} at the two ports as shown in Figure 4.24 and 4.25. It is shown in Figure 4.24a and 4.24b that for $\gamma < 1$, there is a flow of energy from port two to port one. On the other hand, it is shown in Figure 4.25a and 4.25b that, when $\gamma > 1$ energy flows from port one to port two. Because of these phenomena happening at the two ports when the relative amplitude γ is below or above $\gamma = 1$, it is impossible to have an effective injection matched operation on the two-port patch antenna with any other γ apart from $\gamma = 1$. Therefore, the optimum TARC for this investigation remains at $\gamma = 1$ and $\varphi = 180°$.

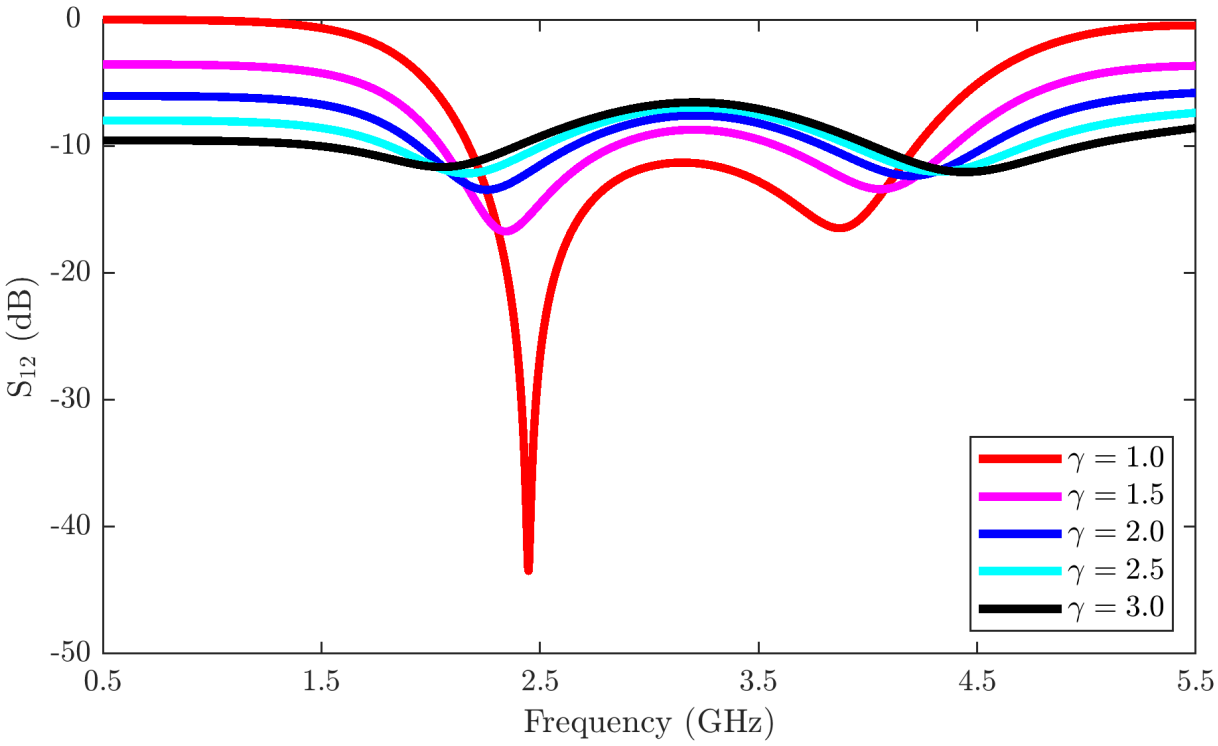


(a)

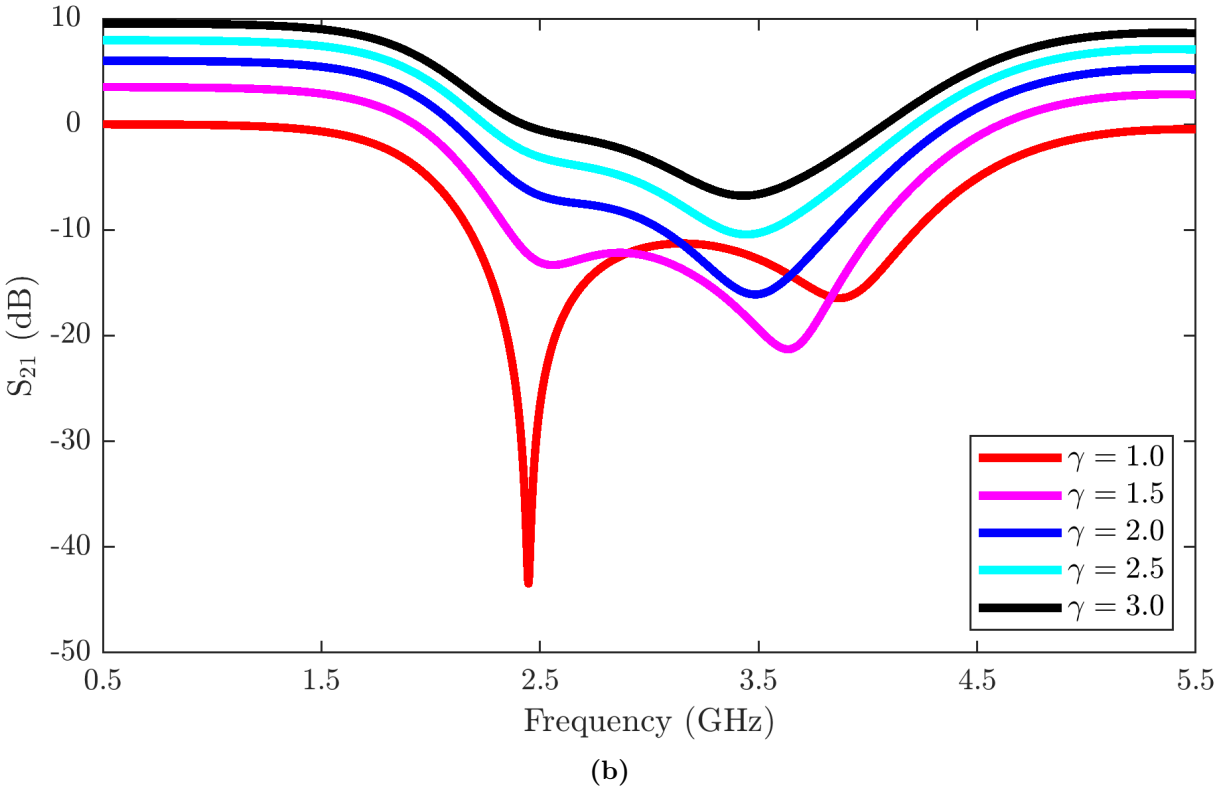


(b)

Figure 4.24. Transmission coefficient (a) S_{12} for $\gamma \leq 1$ (b) S_{21} for $\gamma \leq 1$ on the two-port injection matched antenna when $\varphi = 180°$.



(a)



(b)

Figure 4.25. Transmission coefficient (a) S_{12} for $\gamma \geq 1$ (b) S_{21} for $\gamma \geq 1$ on the two-port injection matched antenna when $\varphi = 180°$.

4.3.5 Injection matching operation

The Z-matrix and terminal impedances for the simultaneously excited two-port injection matched antenna at $\gamma = 1$ and $\varphi = 180°$ are investigated to establish the injection matched operation of the antenna whose TARC resonance is shown in Figure 4.16. After the two ports of the antenna are locked, the relative amplitude $\gamma = \gamma_1$ and phase shift $\varphi = \varphi_1$ are applied at port two. The antenna is simulated, and the terminal impedances Z_{1_1} and Z_{2_1} at the two ports are recorded. The injection matching is repeated with $\gamma = \gamma_2$ and $\varphi = \varphi_2$ at port two, and the impedances Z_{1_2} and Z_{2_2} are obtained. Using Equations (3.2) and (3.3), for γ_1 and φ_1 the following equations are written,

$$Z_{11} = Z_{1_1} - Z_{12}\gamma_1 e^{j\varphi_1} \tag{4.1}$$

and

$$Z_{22} = Z_{2_1} - \frac{Z_{21}}{\gamma_1 e^{j\varphi_1}} \tag{4.2}$$

For γ_2 and φ_2 the following equations are also written,

$$Z_{1_2} = Z_{11} + Z_{12}\gamma_2 e^{j\varphi_2} \tag{4.3}$$

and

$$Z_{2_2} = Z_{22} + \frac{Z_{21}}{\gamma_2 e^{j\varphi_2}} \tag{4.4}$$

Substituting Equation (4.1) into Equation (4.3), and Equation (4.2) into Equation (4.4) gives,

$$Z_{1_2} = Z_{1_1} - Z_{12}\gamma_1 e^{j\varphi_1} + Z_{12}\gamma_2 e^{j\varphi_2} \tag{4.5}$$

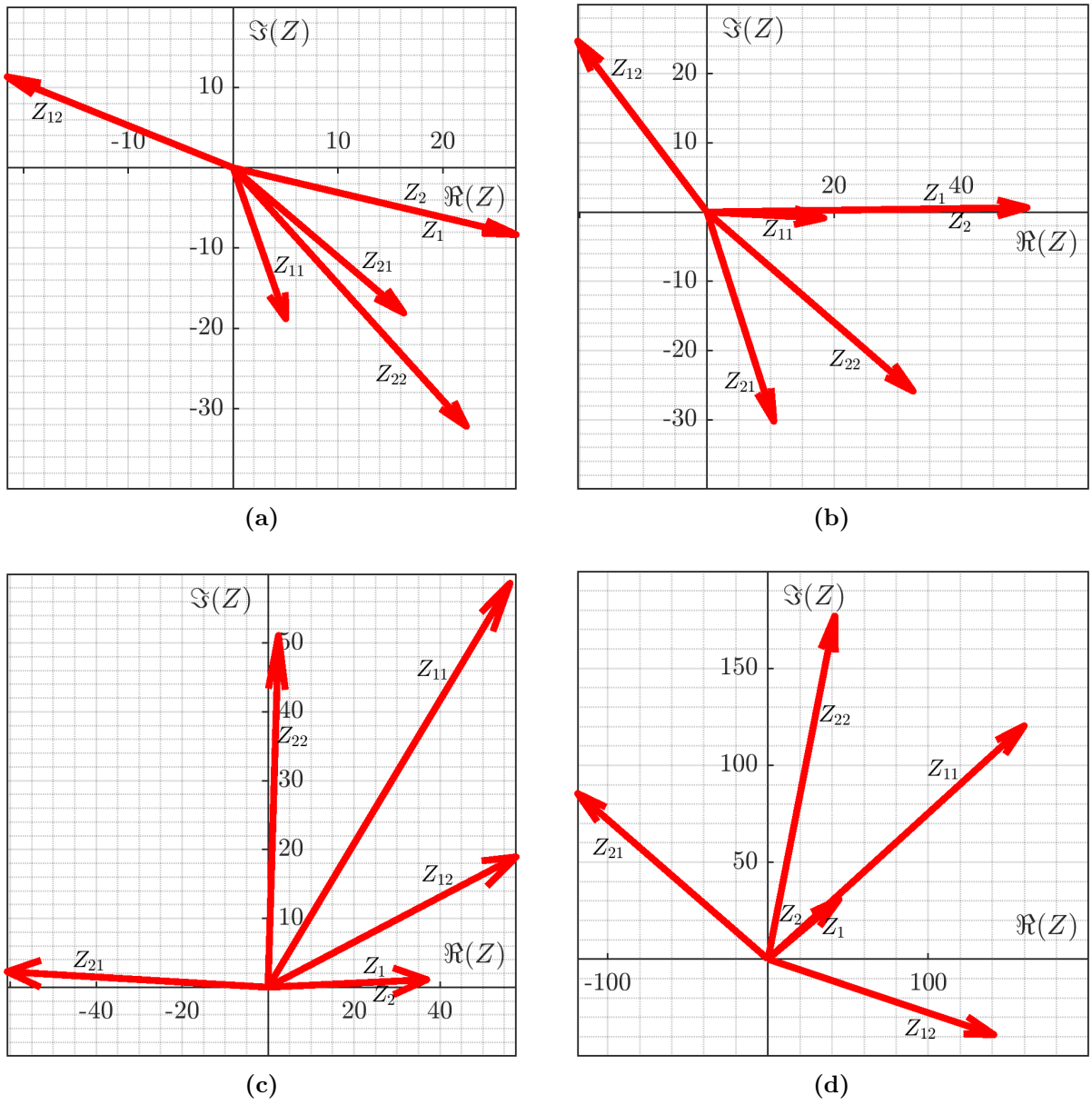


Figure 4.26. Simulated active impedances on the differentially excited two-port injection matched antenna whose TARC resonance is depicted in Figure 4.16 at (a) 2.175 GHz (b) 2.447 GHz (c) 3.881 GHz and (d) 4.221 GHz frequencies.

and

$$Z_{2_2} = Z_{2_1} - \frac{Z_{21}}{\gamma_1 e^{j\varphi_1}} + \frac{Z_{21}}{\gamma_2 e^{j\varphi_2}} \tag{4.6}$$

Solving for Z_{12} and Z_{21} in Equations (4.5) and (4.6) gives,

$$Z_{12} = \frac{Z_{1_2} - Z_{1_1}}{\gamma_2 e^{j\varphi_2} - \gamma_1 e^{j\varphi_1}} \tag{4.7}$$

and

$$Z_{21} = \frac{Z_{2_2} - Z_{2_1}}{\gamma_1 e^{j\varphi_1} - \gamma_2 e^{j\varphi_2}} \gamma_1 \gamma_2 e^{j(\varphi_1 + \varphi_2)} \tag{4.8}$$

Substituting Equations (4.7) and (4.8) into Equations (4.1) and (4.2), respectively, gives

$$Z_{11} = Z_{1_1} - \frac{Z_{1_2} - Z_{1_1}}{\gamma_2 e^{j\varphi_2} - \gamma_1 e^{j\varphi_1}} \gamma_1 e^{j\varphi_1} \tag{4.9}$$

and

$$Z_{22} = Z_{2_1} - \frac{Z_{2_2} - Z_{2_1}}{\gamma_1 e^{j\varphi_1} - \gamma_2 e^{j\varphi_2}} \gamma_1 e^{j(\varphi_1)} \tag{4.10}$$

Using Equations (4.7), (4.8), (4.9), and (4.10), for $\gamma_1 = \gamma_2 = 1$, $\varphi_1 = 180°$ and $\varphi_2 = 360°$, the $Z-$matrix for the injection matched antenna under investigation when $\gamma = 1$ and $\varphi = 180°$ is plotted in Figure 4.26.

Comparing the $Z-$matrix for the two-port antenna under investigation shown in Figure 4.26 with the passive $Z-$matrix for the same antenna when its two ports were not locked (Figure 4.27), at the monitored frequencies (2.175, 2.447, 3.881 and 4.221 GHz), it is shown that the passive $Z-$matrix for the two-port antenna is modified through the application of the injecting matching technique on the two-port antenna.

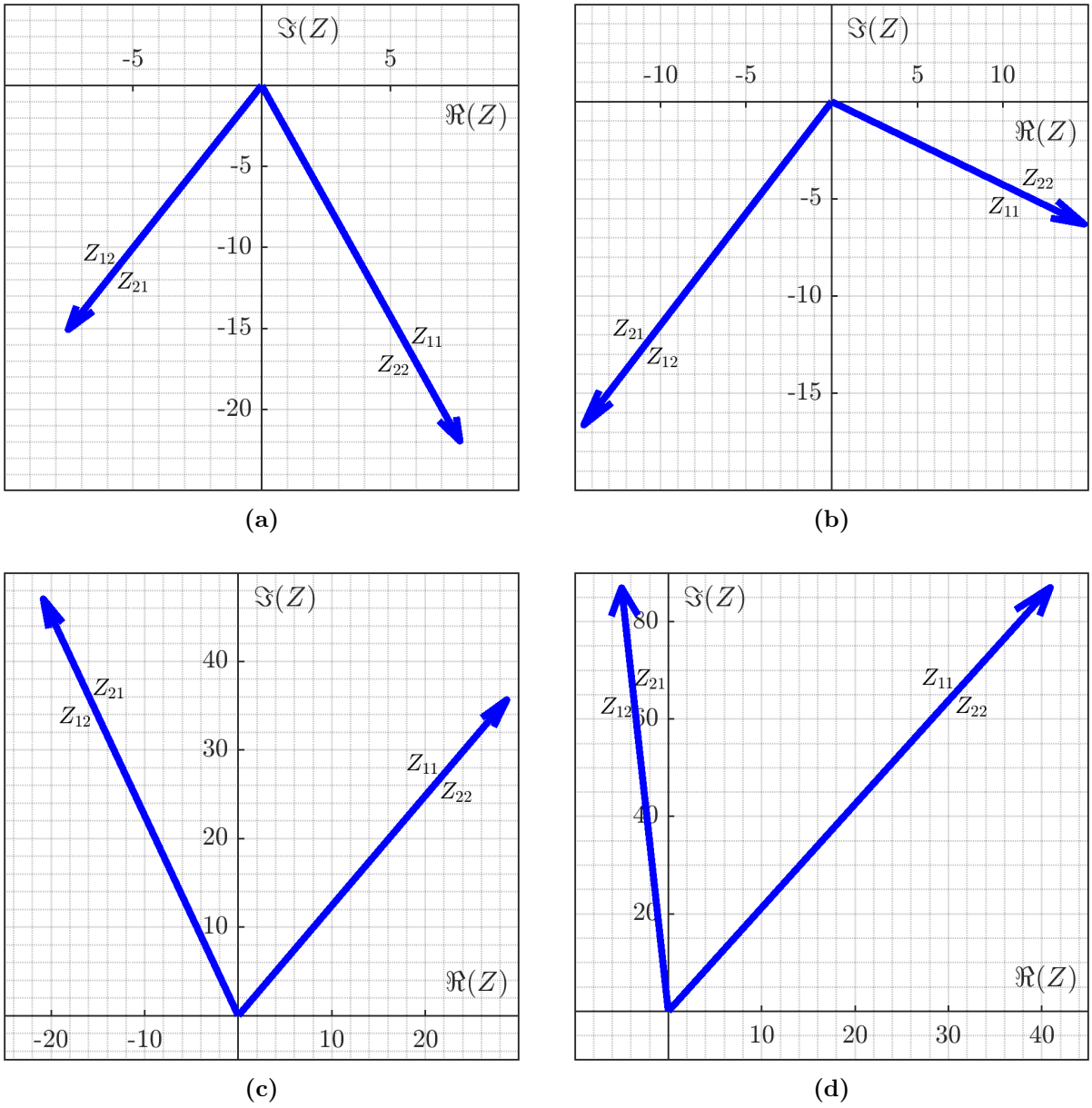


Figure 4.27. Simulated passive impedances on the two-port antenna at (a) 2.175 GHz (b) 2.447 GHz (c) 3.881 GHz and (d) 4.221 GHz frequencies, before injection matching operation is applied to the antenna whose TARC resonance is depicted in Figure 4.16.

The passive mutual impedances between the two ports of the antenna (Z_{12} and Z_{21}), which were in the same quadrant before the injection matching technique was applied to the antenna (when the antenna ports were unlocked), as shown in Figure 4.27, are shifted to opposite quadrants adjacent to their previous occupied quadrants through the application of the injection matching technique, as shown in Figure 4.26. The resulting terminal impedances Z_1 and Z_2 at the monitored frequencies are in the first quadrant, which demonstrates the presence of injection matching operation. The passive Z-matrix is also modified to achieve the injection matching.

4.3.6 Simulated surface current

The simulated surface current on the two-port injection matched antenna whose TARC resonance is depicted in Figure 4.16 is shown in Figure 4.28, while the surface current on the corresponding one-port antenna is depicted in Figure 4.29.

It is shown in Figure 4.28 that the surface currents on the patch for two-port injection matched antenna at 2.175 and 2.447 GHz frequencies are similar to mode J_{01} current shown in Figure 4.6a, indicating that mode J_{01} has been excited at a 2.447 GHz resonant frequency. Similarly, the fair alignment between the surface currents on the patch at 3.881 and 4.221 GHz frequencies and mode J_1 current shown in Figure 4.6b indicates the excitation of mode J_1 at a 3.881 GHz resonant frequency. However, the two modes J_{01} and J_1 are weakly excited by the corresponding one-port antenna as shown in Figure 4.29 at 2.647 and 3.150 GHz, and 3.843 GHz, respectively.

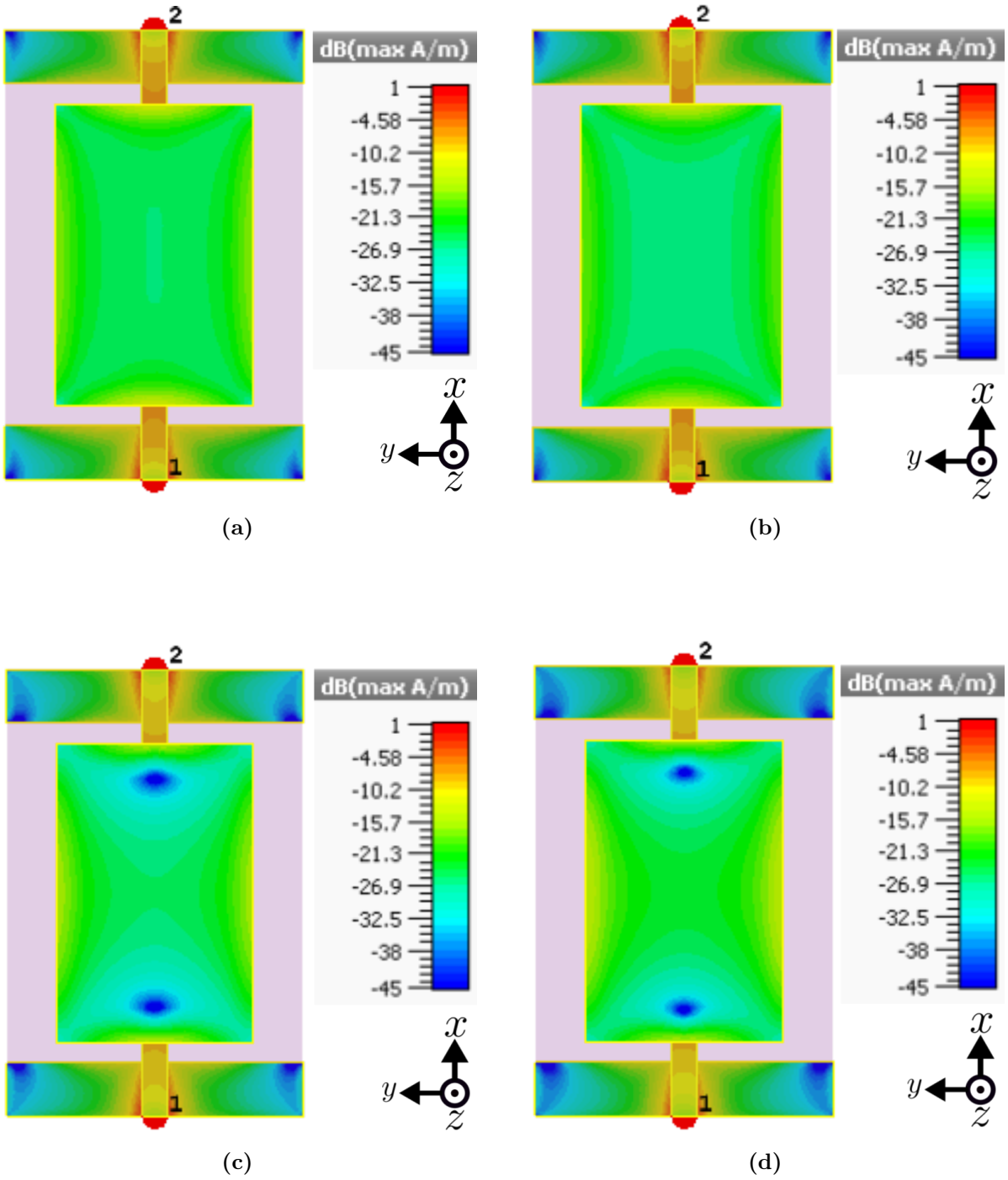
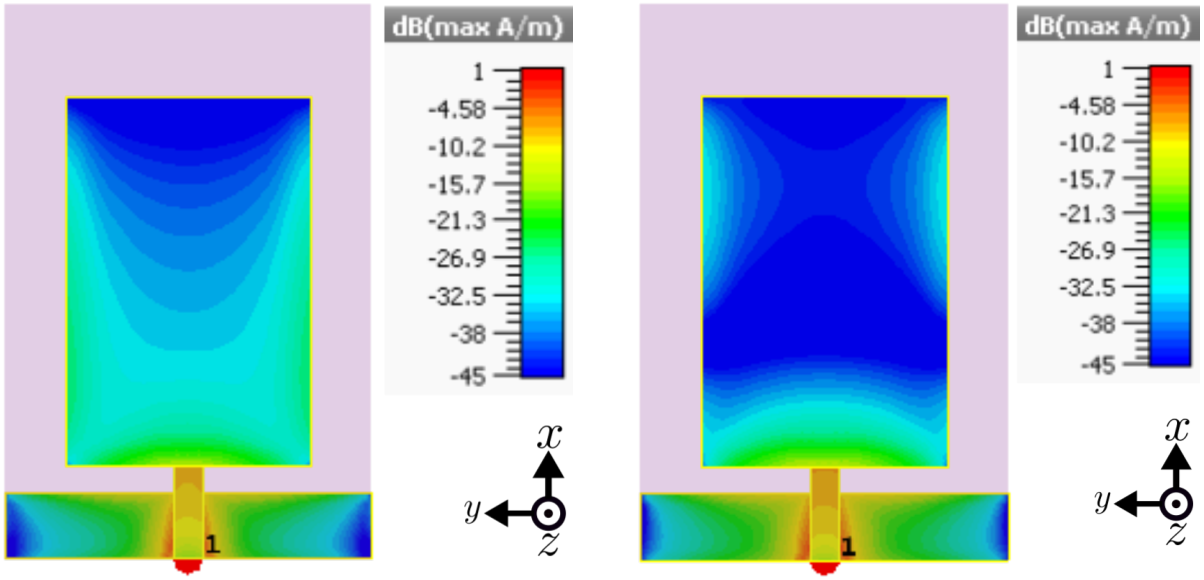


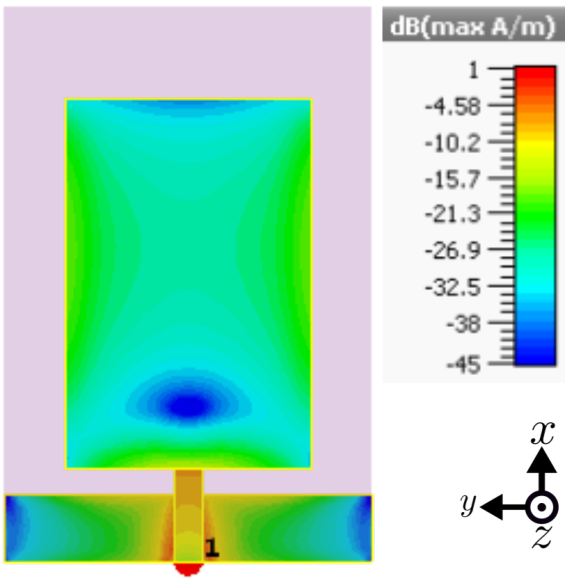
Figure 4.28. Surface current on the differentially excited two-port injection matched patch antenna (including partial grounding planes) at (a) 2.175 GHz (b) 2.447 GHz (c) 3.881 GHz and (d) 4.221 GHz frequencies. The simulated TARC for this antenna is shown in Figure 4.16.

It is also shown in Figure 4.28 that the surface current on the two-port injection matched antenna is more dominant on the PGPs than on the patch, at all the frequencies



(a)

(b)



(c)

Figure 4.29. Simulated surface current on the corresponding one-port patch antenna (including partial grounding plane) in the (a) 2.647 GHz (b) 3.150 GHz and (c) 3.843 GHz frequencies. The simulated S_{11} for this antenna is shown in Figure 4.16.

used in the investigation, which indicates that the two-port patch antenna has been converted to a dipole antenna. Similar behaviour is noted in Figure 4.29, where the surface current is also dominant at the PGP, indicating that the one-port patch antenna has been converted to a monopole antenna. These observations are also justified by the simulated H-plane ($\phi = 90°$) radiation patterns for the two antennas, which are approximately omnidirectional as shown in Figure 4.40 and 4.41, respectively.

4.3.7 Injection matched antenna reciprocity

Reciprocity analysis of the two-port injection matched antenna under investigation (shown in Figure 4.16) is simulated using the arrangement shown in Figure 4.30. In this setup, two identical antennas whose dimensions are depicted by TARC7 resonance in Table B.3 are modelled in CST MWS, and are placed along the line of sight of each other with their radiating elements facing one another. The two antennas are separated by an arbitrary distance d, which in this setup is chosen to be 5 m. All four ports for the two antennas are unlocked, and the antennas are passively simulated in the CST MWS using a Time Domain Solver.

After the passive S-parameters for the two antennas are obtained, a setup in Figure 4.30 is created in CST DS to investigate an injection matched reciprocity operation. In this setup, the two-phase shifters, named Phase shifter 1 and Phase shifter 2, are integrated with attenuators for modulating the amplitudes γ_2 and γ_4 for the excitation signals coming from the two signal splitters, named Signal splitter 1 and Signal splitter 2, into the two two-port antennas embedded in the S-parameter block. The phase shifts φ_2 and φ_4 were tuned in the two phase shifters 1 and 2, respectively. The four probes P1, P2,

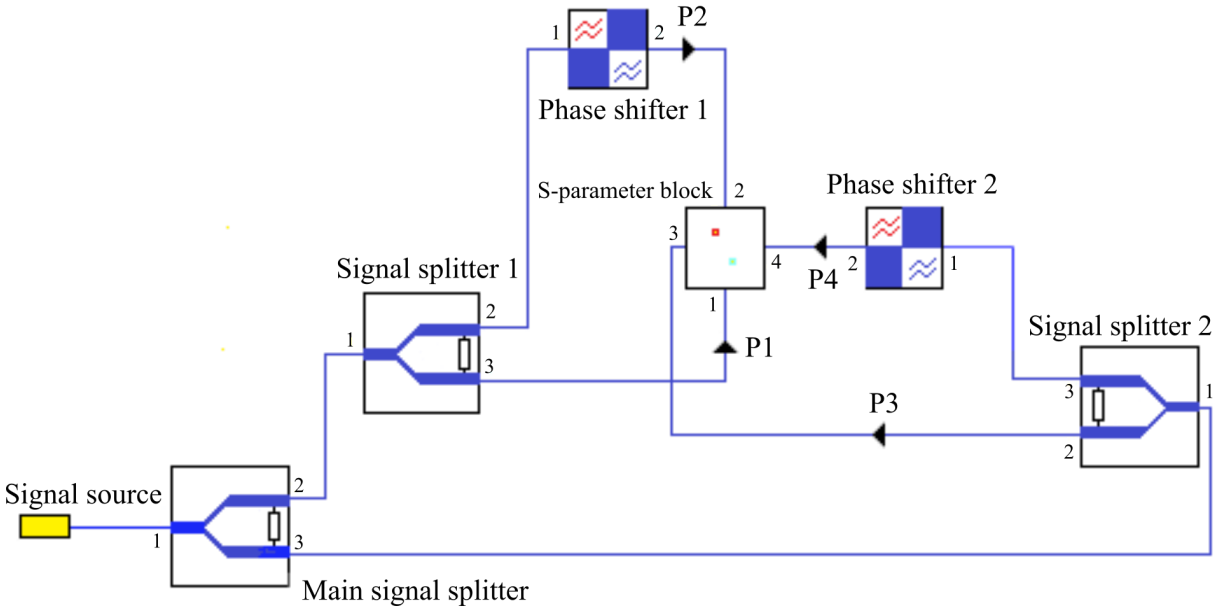


Figure 4.30. Circuit implementation of the two-port injection matched antenna reciprocity in CST DS.

P3 and P4 are used for monitoring the terminal voltages V_1, V_2, V_3 and V_4, and currents I_1, I_2, I_3 and I_4 at the four ports of the two antennas, which are used in evaluating the received voltages V_1^-, V_2^-, V_3^-, V_4^- and transmitted currents I_1^+, I_2^+, I_3^+, I_4^+ to validate the reciprocity Equation (3.66) as shown in Figure 4.31a.

However, simulations for the two-port injection matched antenna reciprocity could not be experimentally validated because of the limitation of the R&S ZVA67 VNA to achieve the coherence mode with all four ports. The four-port R&S ZVA67 VNA has four internal signal sources. When the coherence mode is activated, one of the sources is reserved for the main signal generation, leaving only three sources available for the coherence mode operation at the ports. So to have the coherence mode working in four ports, five signal sources are needed, a feature which the R&S ZVA67 VNA cannot provide.

It is shown in Figure 4.31 that the reciprocity Equation (3.66) is validated, which shows that the two antennas satisfy the reciprocity condition. Also, it is shown that the

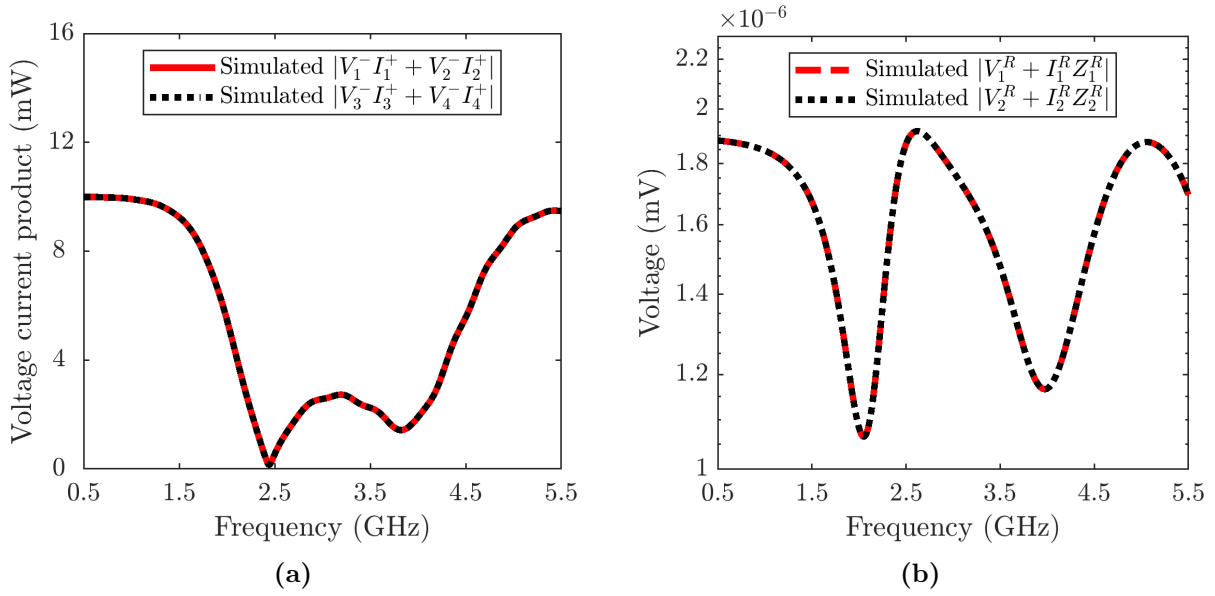


Figure 4.31. (a) Simulated reciprocity of the two two-port injection matched antennas (b) simulated receive mode of the two-port injection matched antenna.

radiation characteristics of the two-port injection matched antenna are preserved, where at the antenna passband, the two-port antenna reflects less power than at frequencies outside the passband of the antenna. This shows that power is conserved when the two-port injection matched antenna is operating reciprocally with a similar antenna.

Receive mode

The receive mode for the two-port injection matched antenna is validated through simulation using a setup in Figure 4.32 in AWR® Microwave Office because of the observed failure of the phase shifter block in CST DS to induce the injection matching operation on the two-port antenna while the antenna is configured in the receive mode. A one-port antenna is used to transmit EM energy received by the two-port antenna configured in the injection matched receive mode with $\gamma = 1$ and $\varphi = 180°$.

In this configuration, the S-parameter block S1 for the two antennas configured in the line of sight of each other, exported from CST MWS, is excited at ports 1, 2 and 3.

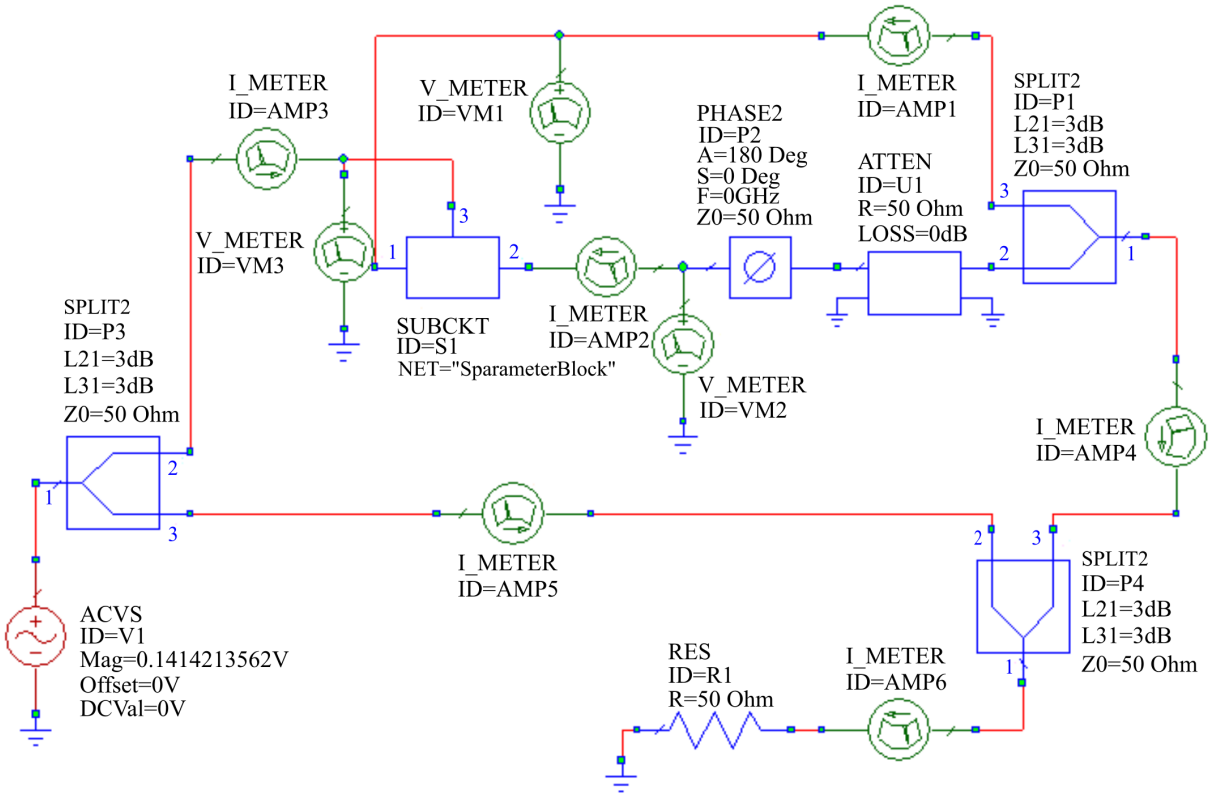


Figure 4.32. An experimental setup for simulating the receive mode of the two-port injection matched antenna in AWR® Microwave Office.

The line of sight distance of separation between the two antennas is arbitrarily chosen to be 3.5 m. The injection matched receive mode operation is configured in the two-port antenna via ports 1 and 2, while port 3 is for exciting the transmitting antenna. The relative amplitude γ and phase shift φ between signals at ports 1 and 2 are locked by the use of attenuator U1 and phase shifter P2 and are combined by the signal splitter P1 towards the 50 Ω load. To maintain the excitation coherence between the two antennas, signal splitters P3 and P4 are used.

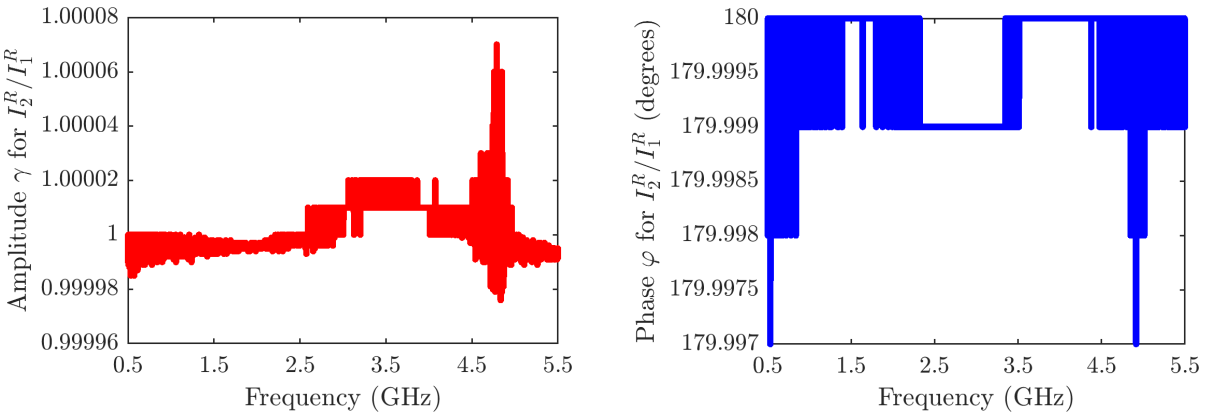


Figure 4.33. (a) Simulated relative amplitude γ (b) simulated phase shift φ between the currents I_1^R and I_2^R when the two-port injection matched antenna is configured to work in the receive mode.

The terminal currents I_1^R, I_2^R, voltages V_1^R, V_2^R and impedances Z_1^R, Z_2^R on the two-port receiving antenna, as well as the terminal current I_3 and voltage V_3 on one-port transmitting antenna are monitored through the ammeters AMP1, AMP2, AMP3 and voltmeters VM1, VM2, VM3, and are used to validate Equation (3.70) as shown in Figure 4.31b. The relative amplitude γ, and phase shift φ between the currents I_1^R and I_2^R when the two-port antenna is in the receive mode, are shown in Figure 4.33.

It is shown in Figure 4.31b that the receive mode Equation (3.70) is verified, which signifies that voltage is conserved at the two ports when the two-port injection matched

antenna is configured to work in the receive mode. Also, the relative amplitude γ and the phase shift φ for the currents at the two-port antenna remained approximately fixed at 1 and 180°, respectively, as shown in Figure 4.33. This observation is an indication that the same feeding network arrangement used by the injection matched antenna in transmit mode can be used by the same antenna in the receive mode. However, the simulated receive mode of an injection matched antenna could not be experimentally validated because of the limitation of the R&S ZVA67 VNA to work differentially in the receive mode.

4.4 Validation of injection matching technique

4.4.1 Measurement of TARC, terminal impedances and currents

The fabricated two-port antenna and the corresponding one-port antenna shown in Figure 4.34 were experimentally investigated.

TARC for the two-port injection matched antenna was experimentally measured using the R&S ZVA67 VNA. The VNA was thermally stabilised over a period of approximately 30 minutes, and ports one and two (of the VNA) were calibrated using the TOSM calibration technique with the Keysight 85052D calibration kit. The calibration plane was taken at the end of the 1.85 mm to 3.5 mm SMA adapters connected into the VNA. The two ports were then configured to be excited in coherence mode. Next, ports one and two of the VNA were connected to ports one and two of the antenna via two SMA adapters. Ferrite beads (shown in Figure 4.35) were used in this experiment to minimise the effect of

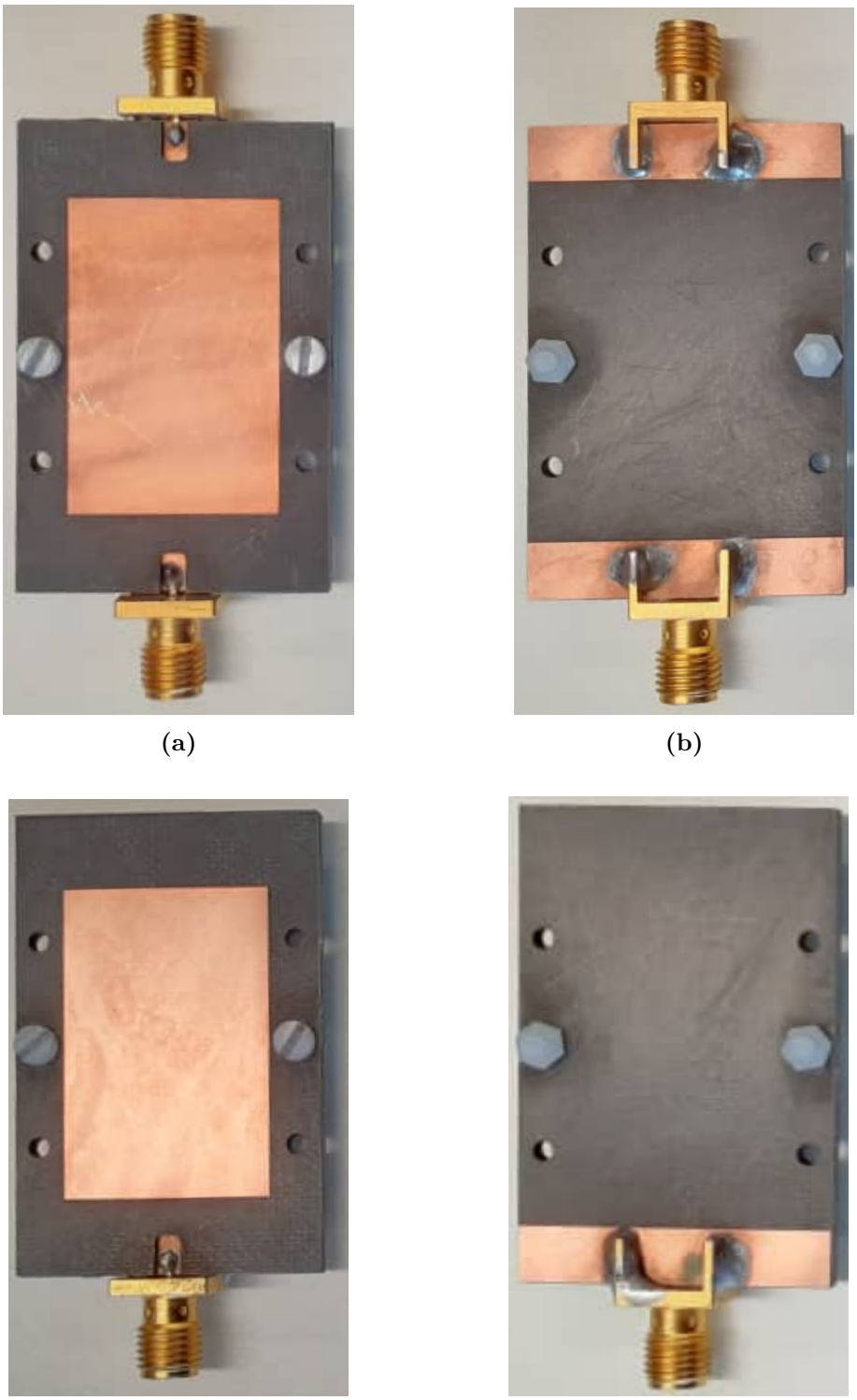


Figure 4.34. (a) Front view of the printed two-port antenna (b) back view of the printed two-port antenna (c) front view of the printed corresponding one-port antenna (d) back view of the printed corresponding one-port antenna. The two antennas have dimensions corresponding to the TARC7 resonance shown in Table B.3.

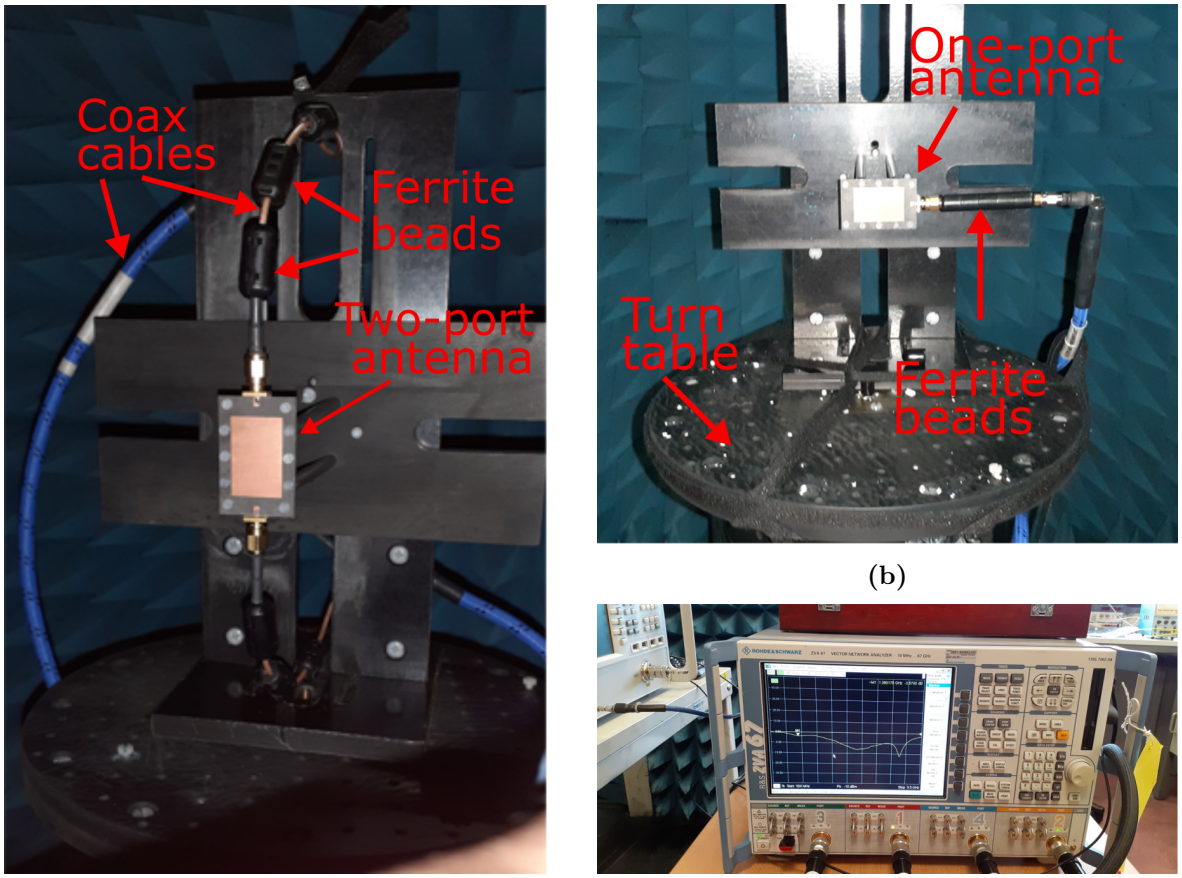


Figure 4.35. Picture showing (a) the use of ferrite beads in measuring the radiation patterns of a two-port antenna (b) the use of ferrite beads in measuring the radiation patterns of a one-port antenna (c) the RS ZVA67 VNA. The same ferrite beads were used in the experiment for characterising TARC for the two-port antenna and S_{11} for the corresponding one-port antenna using techniques outlined in [89].

residual currents rising from the outer shield of the feeding coaxial cables from interfering with the antenna resonance.

While port one of the VNA was configured with an amplitude of 0 dB and phase of 0°, port two was configured with a relative amplitude of 0 dB and phase shift of 180°. The TARC, terminal currents, incident and reflected waves a_i and b_i at each i^{th} port of the antenna as well as the terminal impedances were then monitored by following the procedure outlined in Appendix C, and are plotted in Figure 4.36, 4.37 and 4.38.

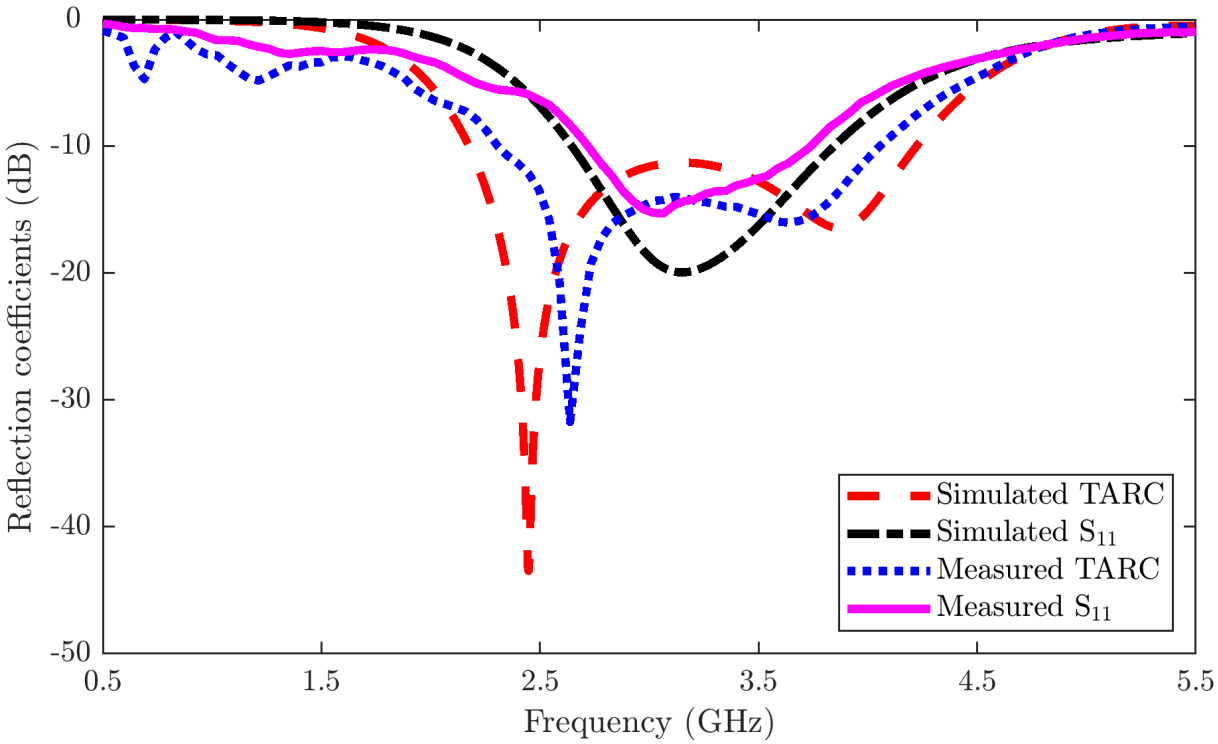


Figure 4.36. Measured and simulated TARC for the differentially excited two-port injection matched antenna compared to S_{11} for the corresponding one-port antenna. The simulated and printed antennas are shown in Figure 4.16 and 4.34, respectively.

It is shown in Figure 4.36 that there is a significant deviation of the measured TARC from the simulated one. This deviation is accounted for by observing the measured responses of the applied amplitude γ and phase shift φ to the two-port antenna during the injection matching operation shown in Figure 4.37. The simulated applied γ and

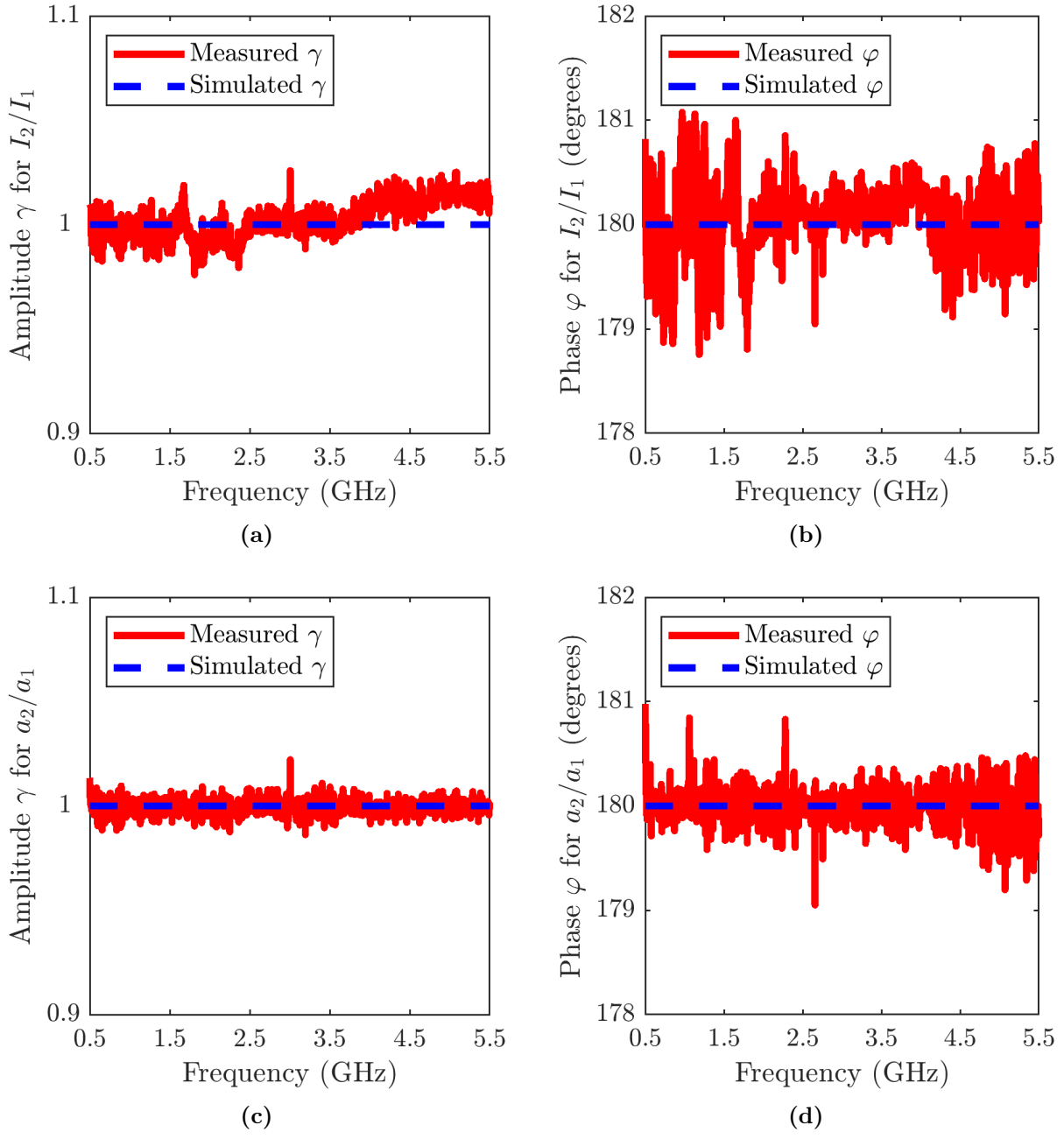


Figure 4.37. Measured and simulated response of the applied (a) relative amplitude γ between the currents I_1 and I_2 (b) phase shift φ between the currents I_1 and I_2 (c) relative amplitude γ between the waves a_1 and a_2 (d) phase shift φ between the waves a_1 and a_2 when the patch antenna was injection matched at $\gamma = 1$ and $\varphi = 180°$. The simulated and printed antennas are shown in Figure 4.16 and 4.34, respectively.

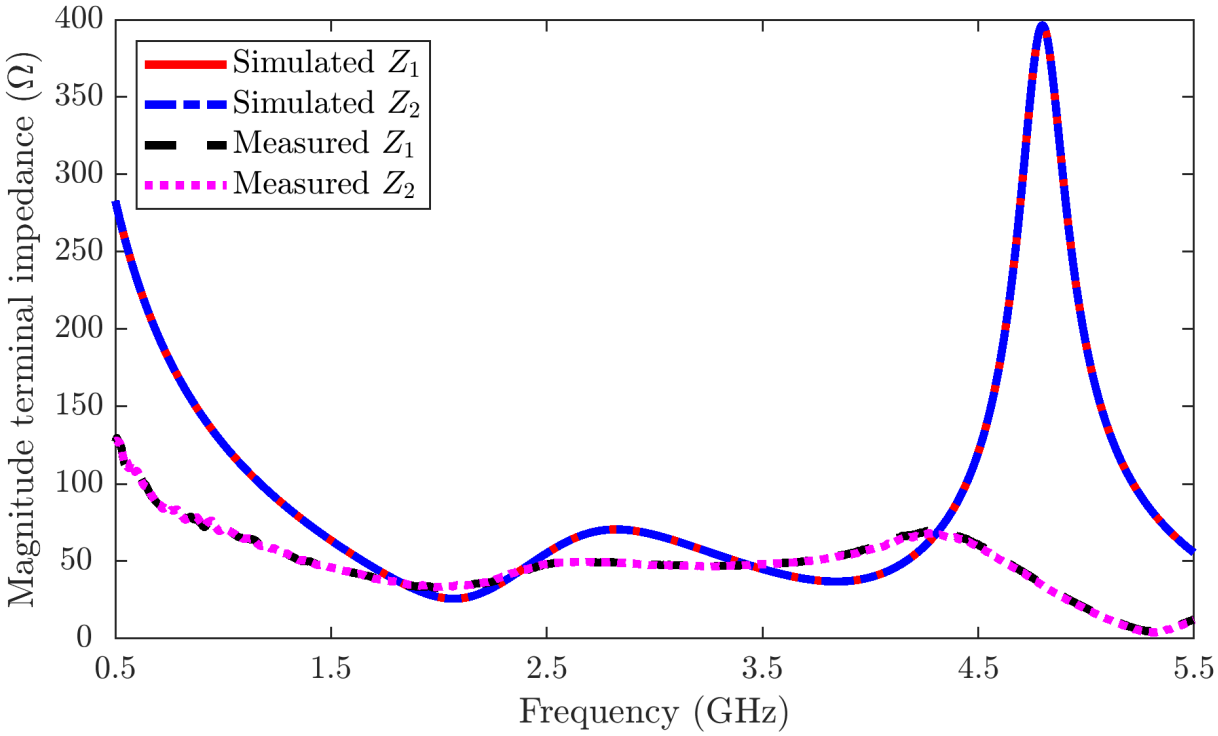


Figure 4.38. Simulated and measured terminal impedances for the differentially excited two-port antenna. The simulated and printed antennas are shown in Figure 4.16 and 4.34, respectively.

phase φ responses for the current ratio I_2/I_1 and wave ratio a_2/a_1 are approximately fixed at 1 and 180°, respectively, across the entire frequency range of investigation.

However, there is a significant variation of the measured applied γ and phase φ responses for the current ratio I_2/I_1. This variation indicates that residual currents are being coupled to the SMA connectors and PGPs from the outer shield of the two feeding coaxial cables to cause variability in the terminal impedances on the input terminals of the printed two-port antenna, as shown in Figure 4.38, which could not be eliminated by the use of ferrite beads (Figure 4.35). As a result, because of the small size of the grounding planes, the residual currents give rise to radiation from the two PGPs to cause undesired resonances at different frequencies across the entire frequency range of investigation, and mainly at frequencies below 2.7 GHz and above 3.5 GHz. These resonances interfere with

the main resonance to distort the measured TARC shown in Figure 4.36, as well as the measured radiation patterns shown in Figure 4.40.

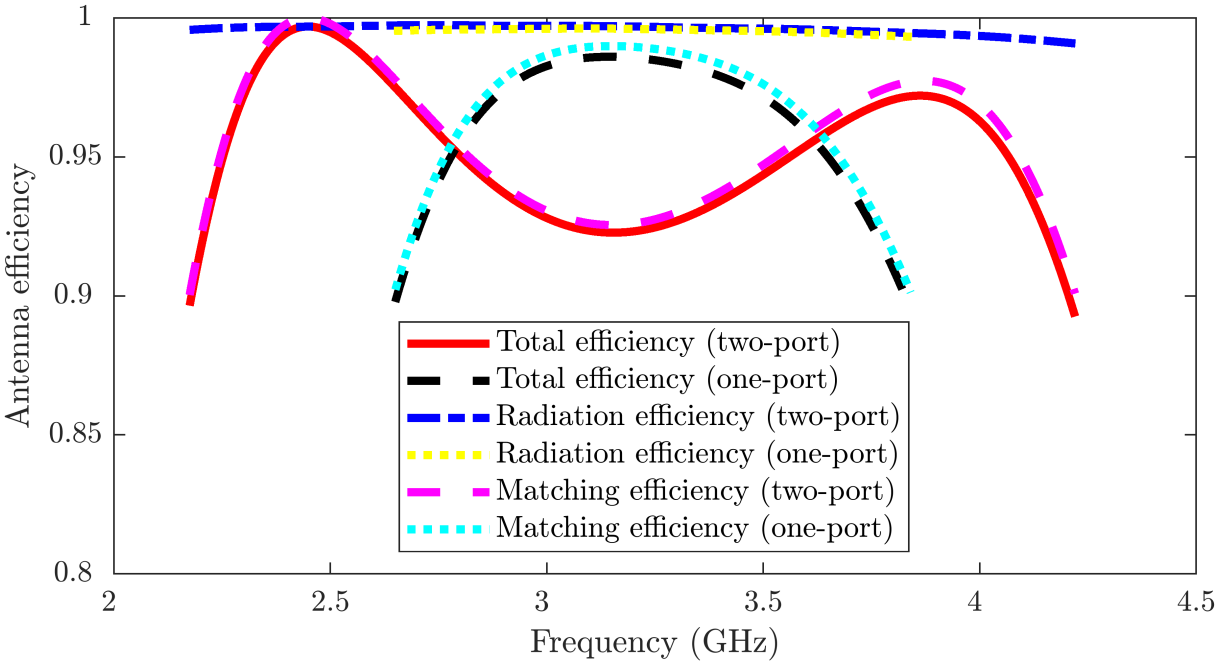


Figure 4.39. Simulated efficiency for the differentially excited two-port injection matched antenna in comparison with the simulated efficiency for the corresponding one-port antenna. The simulated and printed antennas are shown in Figure 4.16 and 4.34, respectively.

The simulated matching efficiency for the two-port antenna shown in Figure 4.39 is greater than 89% across the -10 dB operational bandwidth. This efficiency is generally higher than the efficiency for the corresponding one-port antenna, except at frequencies between 2.8 and 3.6 GHz, where the one-port antenna demonstrates a higher efficiency than the two-port antenna as shown in Figure 4.39. The higher matching efficiency attained by the two-port antenna is attributed to good impedance matching achieved through the injection matching technique. Also, the excitation of two similar characteristic modes of the patch antenna achieves a slightly higher radiation efficiency on the two-port antenna compared to the radiation efficiency of the corresponding one-port antenna. However, the two antennas have radiation efficiency higher than 99% attributed to the low

loss tangent ($\tan\delta = 0.0009$) and low dielectric constant ($\varepsilon_r = 2.2$) substrate material used in the design. Besides, because of the high matching efficiency and high radiation efficiency attained by the two antennas, the total efficiency for the two antennas is generally higher than 89% across the antennas' passbands.

The simulated -10 dB FBW for the two-port injection matched antenna (which was calculated using Equation (B.1) in Appendix B.4) is around 64%, whereas the FBW of the corresponding one-port antenna is about 36.9%. This observation shows that excitation of the two similar modes through injection matching technique allows bandwidth enhancement of the two-port patch antenna.

4.4.2 Measurement of radiation patterns

Experimental validation of the radiation patterns for the two-port injection matched antenna under investigation followed the procedure outlined in Section 3.4 using the setup in Figure 3.3. The R&S ZVA67 VNA was thermally stabilised over a period of approximately 30 minutes, and the three ports of the VNA were calibrated before measurements were conducted. The calibration plane was taken at the end of the three coaxial cables that connect the VNA and the two antennas (two-port AUT and reference antenna). After calibration, the three cables were connected to the two antennas, where ports 1 and 2 of the VNA were connected to ports 1 and 2 of the two-port AUT, and port 3 of the VNA was connected to the reference antenna. Ferrite beads (shown in Figure 4.35) were used in this experiment to minimise the effect of residual currents rising from the outer shield of the feeding coaxial cables from interfering with the antenna resonance.

The AUT was in transmit mode, while the reference antenna (open boundary quad-ridged horn antenna model 3164-08 in Appendix D) was in receive mode. Ports 1 and 2 of the VNA were configured to transmit in coherence mode. While port 1 was configured with an amplitude of 0 dB and phase of 0°, port 2 was configured with a relative amplitude of 0 dB and phase shift of 180°. Port 3 was configured as a receiving port. A 10 decibel milliwatt (dBm) transmit power was configured in the VNA and the waves a_i and b_i were monitored and recorded across the -10 dB bandwidth of the antenna in both E and H-planes. These waves were finally measured at 2.353, 2.638, 3.635 and 4.015 GHz frequencies, and the corresponding patterns were calculated using Equation (3.45). The measured co-polar patterns for the two-port injection matched antenna in comparison to the corresponding simulated patterns are given in Figure 4.40.

Characterisation of the measured radiation patterns for the corresponding one-port antenna followed a similar procedure, but in this case only two ports of the VNA were used, where port one was configured in transmit mode and port two in the receive mode. The co-polar radiation patterns for the one-port antenna under investigation are shown in Figure 4.41.

It is shown in Figure 4.40 that both the E and H-plane co-polar patterns for the two-port antenna are misaligned with the corresponding simulated patterns. The deviation between the measured and simulated patterns in each plane is caused by residual currents on the SMA connectors and PGPs that were coupled from the outer shield of the coaxial cables. Though ferrite beads (shown in Figure 4.35) were used during the measurement, the effect of residual currents could not be eliminated completely. Because of the small size of the ground planes, the residual currents give rise to radiation from the two PGPs to cause spurious radiation, which is spanned across the entire frequency range of obser-

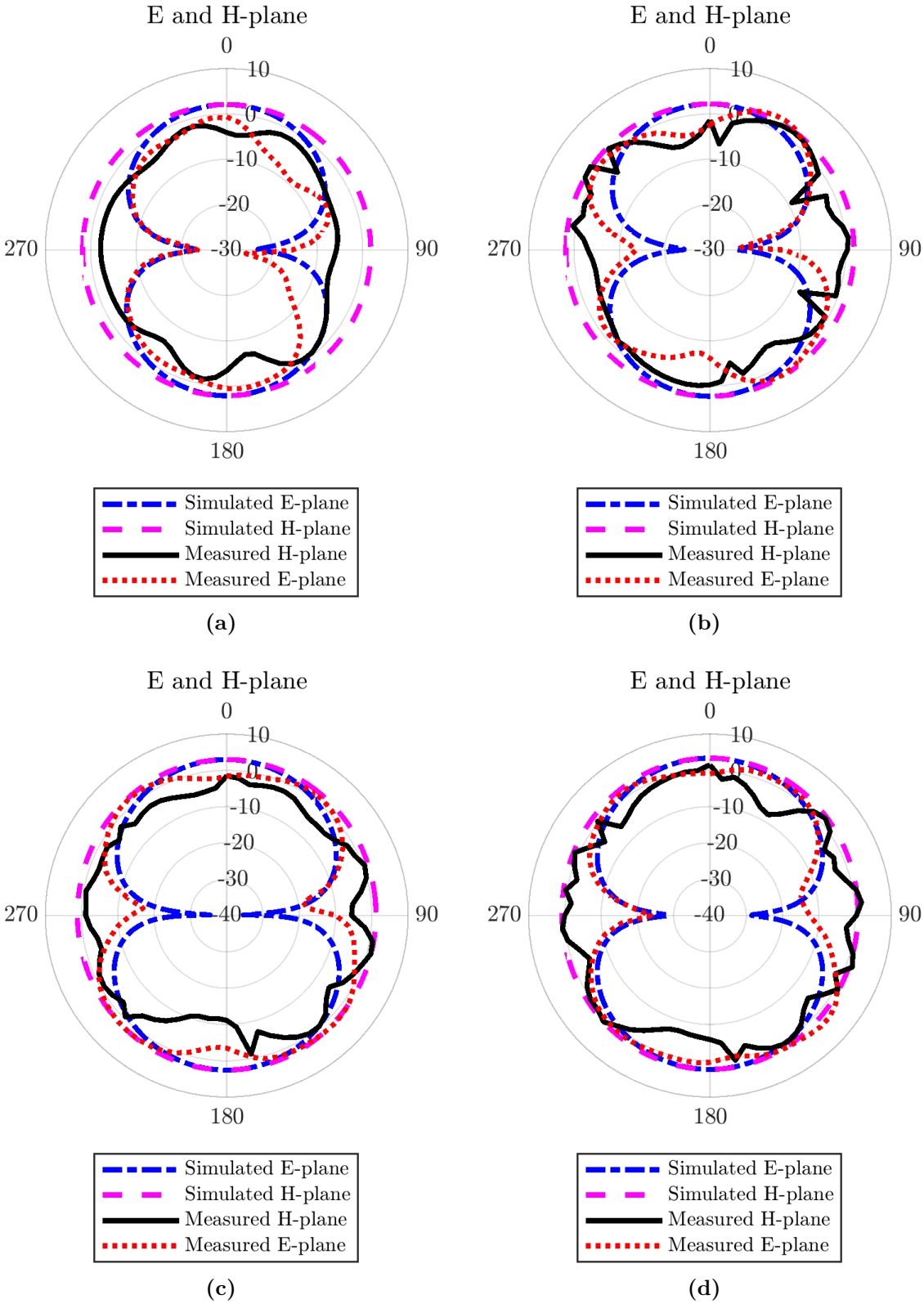


Figure 4.40. Simulated and measured co-polar patterns for the differentially excited two-port injection matched antenna in the (a) 2.175 and 2.353 GHz (b) 2.447 and 2.638 GHz (c) 3.881 and 3.635 GHz (d) 4.221 and 4.015 GHz frequencies, respectively. The simulated and printed antennas are shown in Figure 4.16 and 4.34, respectively.

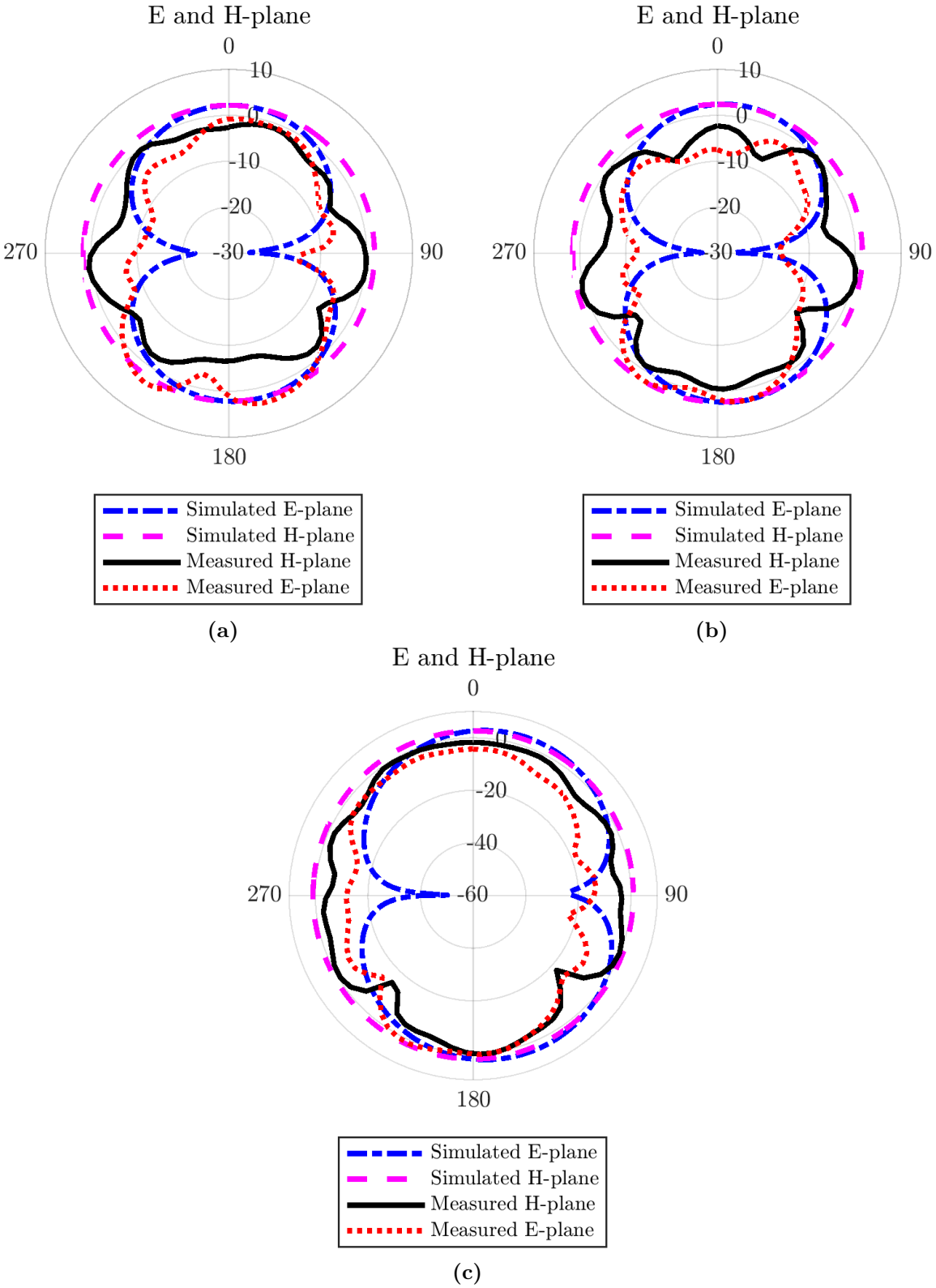


Figure 4.41. Simulated and measured co-polar radiation patterns for the corresponding one-port antenna in the (a) 2.647 and 2.733 GHz (b) 3.150 and 3.065 GHz and (c) 3.843 and 3.730 GHz frequencies. The simulated and printed antennas are shown in Figure 4.16 and 4.34, respectively.

vation. The measured one-port patterns shown in Figure 4.41 are also affected because of the same factors.

Considering the simulated patterns, the two-port antenna patterns are more stable than the patterns for the corresponding one-port antenna as a result of driving the two-port antenna from the two ends. However, the simulated patterns for both antennas are approximately omnidirectional in the H-plane as the two antennas have been converted to dipole and monopole antennas, respectively.

4.5 Results and discussion

It is shown in this chapter that the injection matching technique is based on the excitation of characteristic modes of the patch antenna, which is differentially or coherently (in common mode) achieved. In each case, the wideband operation is attained by exciting the multiple correlated modes. Frequency tuning is attained through the application of the differential and common mode excitations to the antenna by configuring $\gamma = 1$ and $\varphi = 180°$ or $\gamma = 1$ and $\varphi = 0°$ at port two of the antenna, though at the expense of losing the bandwidth from one of the two excitation modes because of the limited number of feed points (two feed points) supported by the injection matching technique. However, an outlined study of frequency tuning of modes is investigated in Chapter 6.

Typically, a -10 dB FBW of around 64% has been attained from the two-port proximity-fed patch antenna by exciting two correlated modes J_{01} and J_1 of the antenna. The achievement is also attributed to the adoption of PGPs, which essentially reduces the stored EM energy in the patch antenna to minimise the antenna Q to increase the bandwidth.

Comparing the measured TARC and radiation patterns for the two-port antenna with the corresponding simulations, as shown in Figure 4.36 and Figure 4.40, the observed slight deviations are attributed to the leakage currents from the outer shield of the coaxial cables, which were coupled into the SMA connectors and PGPs. Because of the small size of the partial grounds, the residual currents caused spurious radiation in the entire frequency range of observation. Though the use of ferrite beads (shown in Figure 4.35) minimised these currents, the effect spanned across the entire frequency range of observation, as shown in Figure 4.37, and affected the TARC resonance (Figure 4.36) and radiation patterns (Figure 4.40 and 4.41). Neglecting these deviations, the measured TARC and radiation patterns for the two-port injection matched antenna have generally verified the validity of the injection matching technique.

The two-port antenna has the maximum realised gain of around 2.9 dBi at 4.0 GHz frequency, as shown in Figure 4.42c, attributed to the excitation of mode J_1 of the antenna at this frequency, which is of a higher order than mode J_{01} excited at around 2.447 GHz frequency. There is an improvement of gain of around 0.5 dB from the two-port antenna compared to the maximum gain of 2.4 dBi attained by the corresponding one-port antenna at around 3.450 GHz frequency, as shown in Figure 4.42c, because of an effective excitation of mode J_1 of the antenna by the differential excitation at 4.0 GHz frequency than by the one-port excitation at 3.350 GHz frequency. However, at a 2.175 GHz boundary frequency, the two-port antenna has a gain of around 1.63 dBi, which is lower than the gain attained by the corresponding one-port antenna in all frequencies because of excitation of mode J_{01} at a 2.447 GHz resonant frequency which is of low-order compared to mode J_1 excited by the one-port antenna. Also, the gain realised by the two-port antenna is fairly stable at

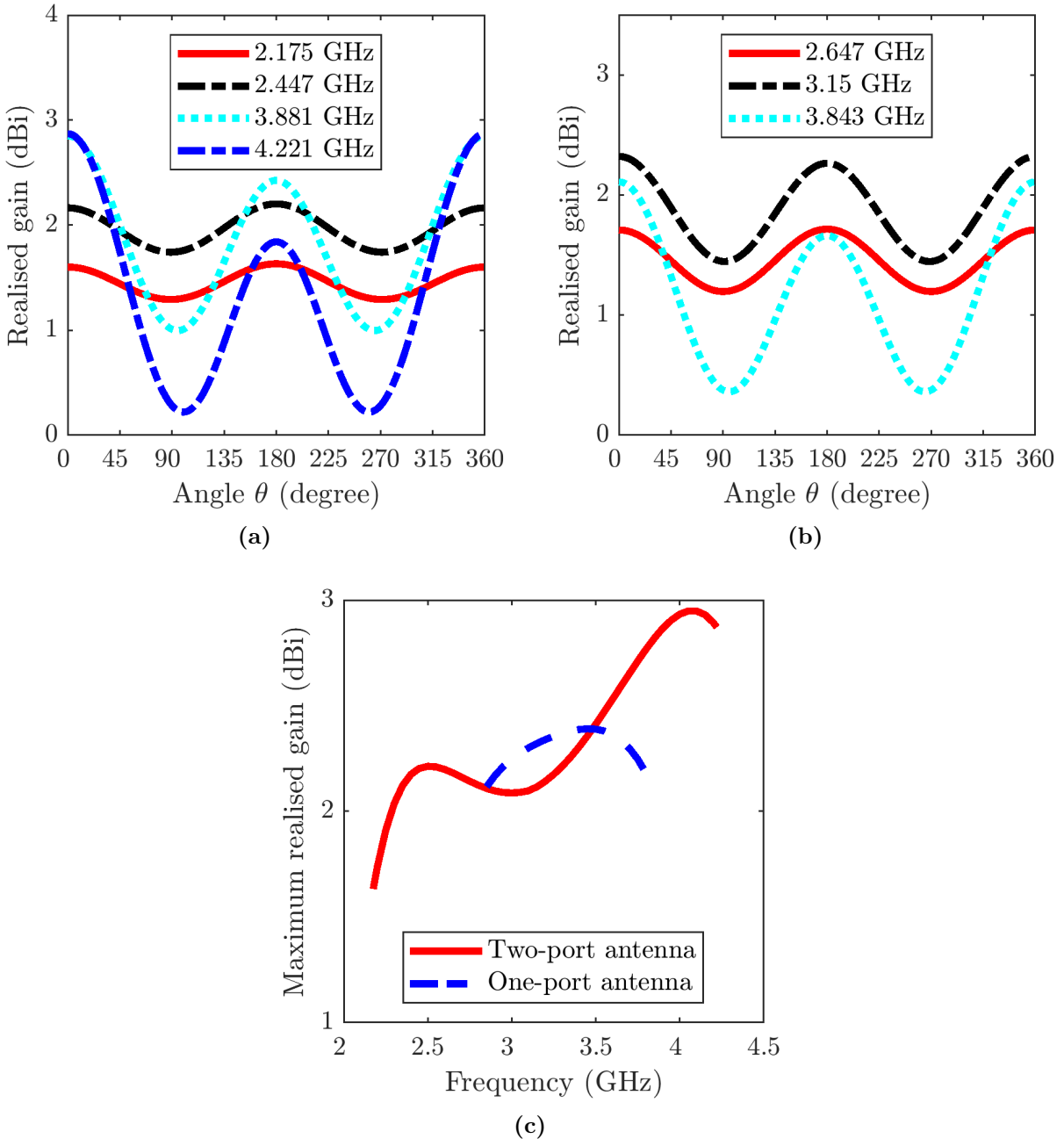


Figure 4.42. Simulated (a) H-plane ($\phi = 90°$) realised gain for the two-port injection matched patch antenna (b) H-plane ($\phi = 90°$) realised gain for the one-port patch antenna (c) H-plane ($\phi = 90°$) maximum realised gain for the two-port injection matched patch antenna and for the corresponding one-port antenna. The simulated TARC and S_{11} for the two antennas are shown in Figure 4.16.

2.175 and 2.447 GHz frequencies (with a gain reduction of around 0.5 dB between the two frequencies) than at 3.881 and 4.221 GHz frequencies, as shown in Figure 4.42a, because of excitation of mode J_{01} of the antenna at a 2.447 GHz resonant frequency, which has more stable patterns than mode J_1. On the other hand, there is a large variation of the gain achieved by the corresponding one-port antenna, as shown in Figure 4.42b, because of driving the antenna from one port. Generally, the two-port antenna's realised gain is improved compared to the gain of the corresponding one-port antenna due to driving the antenna from two ports.

Also, the two-port antenna in Figure 4.39 has good radiation, matching and total efficiencies because of the excitation of two similar characteristic modes of the antenna, use of low loss tangent ($\tan\delta = 0.0009$) and low dielectric constant ($\varepsilon = 2.2$) substrate material in the design, and excellent impedance matching attained through the injection matching technique. Besides, the theoretical validation of two-port injection matched antenna reciprocity and receive mode through simulation shows that the same feeding network arrangement used by the injection matched antenna in transmit mode can be fed by an injection matched two-port antenna in the receive mode. The two-port injection matched antenna can also work reciprocally with any antenna with similar radiation characteristics.

The use of theoretical γ and φ variations in the design process can be replaced by the theory of characteristic modes, which gives more flexibility in locating the feeding points to excite the desired modes efficiently. However, the theory of characteristic modes was not extensively applied in this investigation because it lies outside the scope of this study.

4.6 Summary

The design of two-port injection matched patch antennas is summarised into the following procedure:

(1) A one-port rectangular patch antenna with PGP is designed at the frequency of interest. The applied excitation is from one of the edges.

(2) The one-port antenna in (1) is converted to a two-port antenna by adding another excitation at the opposite edge with respect to the first excitation, and the second PGP for the second excitation. The antenna is simulated to obtain the passive S-parameters, which are used for calculating the TARC resonance when $\gamma = 1$ and $\varphi = 0°$, and $\gamma = 1$ and $\varphi = 180°$.

(3) Depending on the desired bandwidth and resonant frequency, the dimensions of the antenna are optimised while TARC is being monitored.

(4) Depending on the TARC convergence, the optimum TARC may be obtained by sweeping the dimensions of the antenna in a narrow range, near the dimensions of the best TARC in (3).

(5) After the desired TARC is obtained, the resulting two-port injection matched antenna dimensions are used to create the corresponding one-port antenna. Finally, the one-port antenna is simulated and the obtained results are used for comparison with the two-port antenna.

Chapter 5

Broadband injection matched antennas

5.1 Background

The previous chapter showed that the wideband operation could be attained by exciting multiple characteristic modes of a patch antenna. Also, the design procedure for injection matched antennas was discussed.

This chapter applies the design procedure established in Chapter 4 to realise wideband injection matched patch antennas. A four-port feeding mechanism is also discussed in Section 5.2 for the bandwidth and performance enhancements of the realised injection matched patch antenna.

5.2 Design, simulation and validation

Consider the bandwidth requirement for the wireless services in the 2.4 to 6.6 GHz frequency range. A wideband antenna operating in this frequency range can meet the need. This can be achieved by first, realising a one-port antenna at a 4.5 GHz centre frequency (of the specified band), and then widening the operational bandwidth through injection matching technique.

To begin with, a one-port proximity-fed patch antenna with FGP is designed in CST MWS to operate at around 4.5 GHz by following the procedure outlined in [85]. The antenna is realised on two layers of Rogers Duroid RT 5880 substrate with relative permittivity ε_r of 2.2, loss tangent of 0.0009, lower substrate height of 1.575 mm, upper substrate height of 0.787 mm, and copper cladding thickness of 0.035 mm. The antenna has a patch length $L_p = 20.83$ mm, patch width $W_p = 17.67$ mm, substrate length $L_s = 41.66$ mm, substrate width $W_s = 35.34$ mm, width of feed line $w = 1.86$ mm and the distance of the coupled line from the centre of the patch is $d = 0.0$ mm. Excitation of this antenna is achieved through a discrete face port created on the outer end-face of the feed line while the impedance of the excitation signal delivered at this port is maintained at 50 Ω. To enhance bandwidth, the one-port antenna is converted to a monopole patch antenna by truncating the grounding plane, as shown in Figure 5.1a. The length of partial ground $L_g = 10.42$ mm, which is the maximum length of the ground plane for which a patch antenna is converted to a monopole antenna, was calculated from $L_g = (L_s - L_p)/2$.

The S_{11} for the two antennas corresponding to these antenna dimensions are given in Figure 5.2, where it can be seen that the one-port antenna with a PGP has an improved −3 dB bandwidth attained through excitation of two modes at around 3.835 and

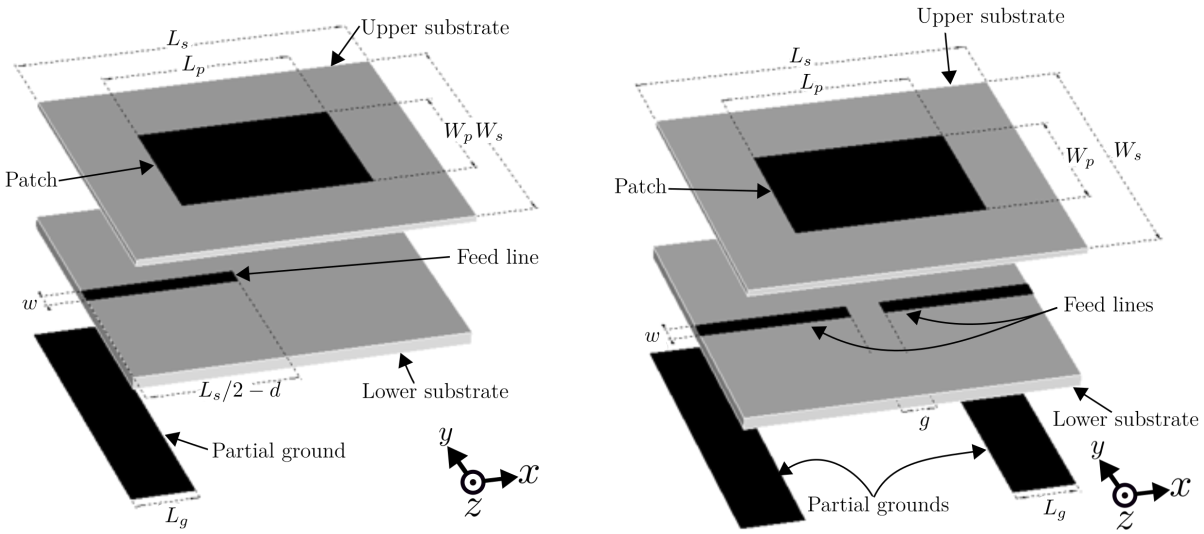


Figure 5.1. (a) Proximity-fed patch antenna with single feed line (b) proximity-fed patch antenna with two feed lines. The black colour indicates the layers of copper.

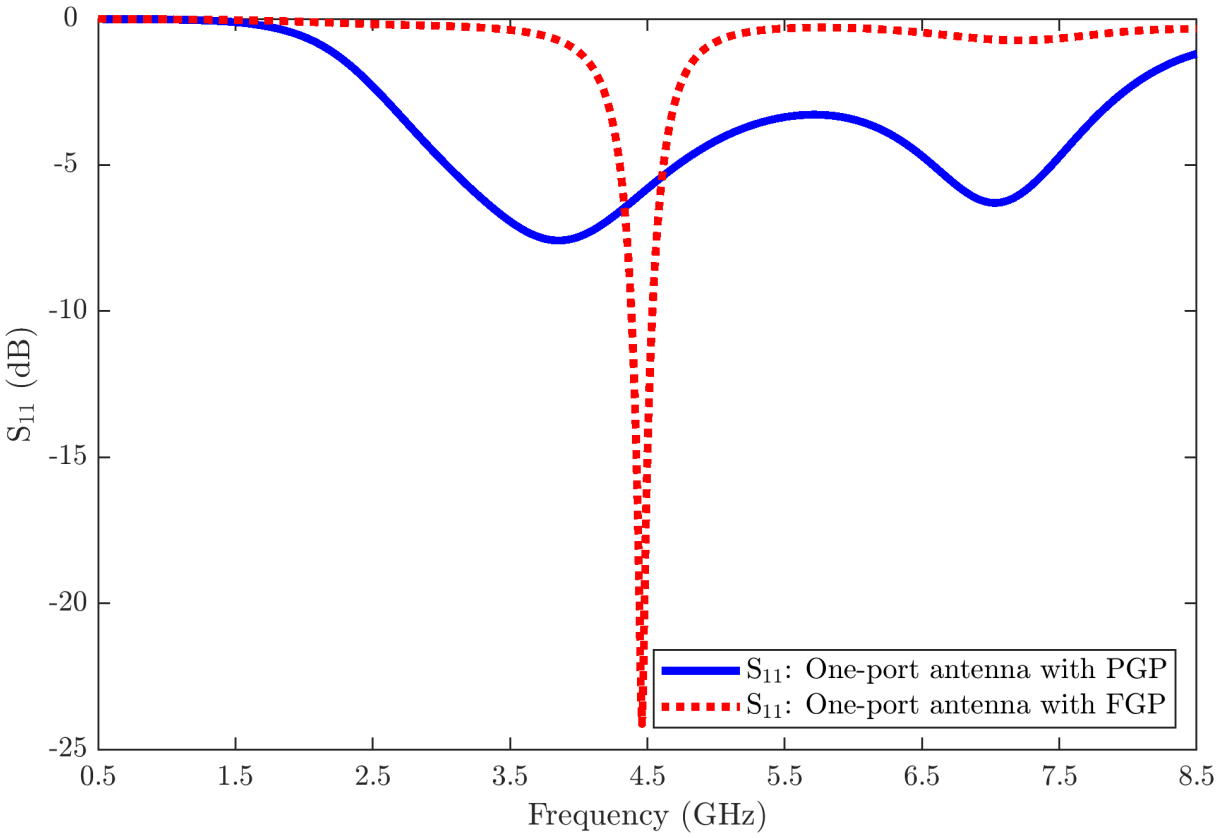


Figure 5.2. S-parameter for the one-port proximity-fed patch antenna under investigation.

7.013 GHz frequencies. However, the two modes of the resulting one-port antenna with PGP are poorly matched, as shown in Figure 5.2.

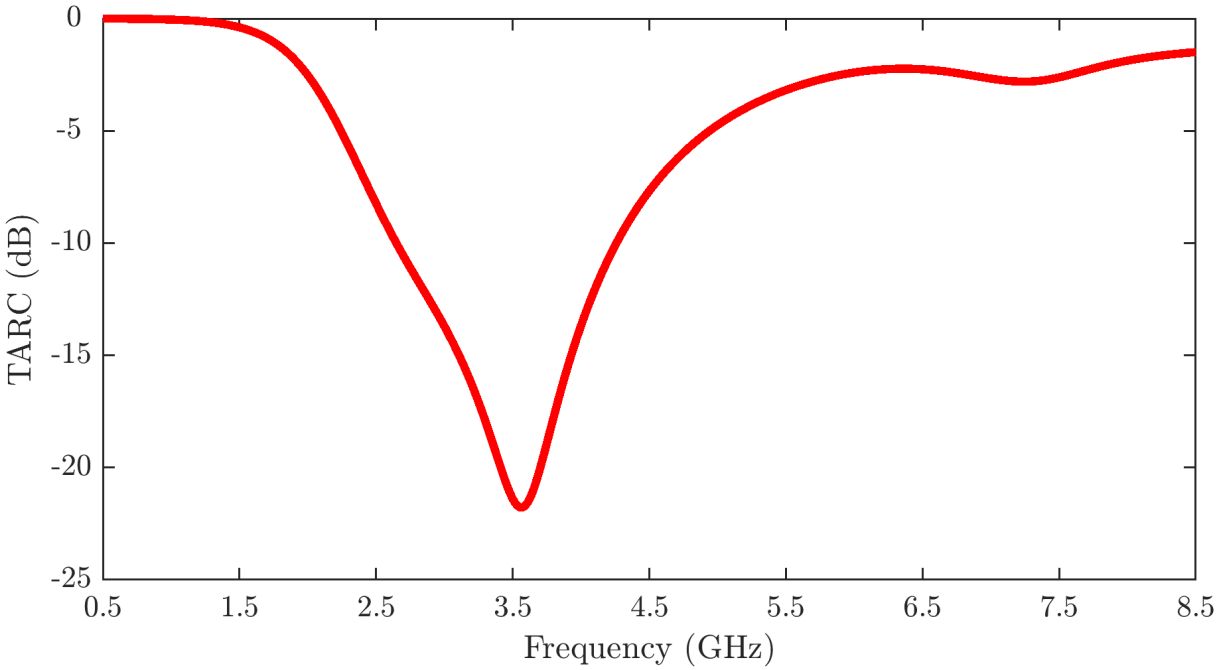


Figure 5.3. TARC for the differentially excited ($\gamma = 1$, $\varphi = 180°$) two-port proximity-fed patch antenna, which corresponds to the one-port antenna whose resonance is depicted in Figure 5.2.

Applying the injection matching technique to this antenna (in CST Studio Suite® (CST SS) by following the procedure outlined in Appendix B.1) improves the matching as well as the operational bandwidth. This is implemented in two steps: first, the one-port antenna is converted to a two-port antenna by adding the second coupled feed line, separated with a gap $g = 2d$ from the first feed line, where d is measured from the centre of the patch, and a PGP corresponding to the second feed line, as shown in Figure 5.1b. The gap between the feed lines is initially chosen to be $g = 1.6$ mm, but any value of g between 0.1 and 2.0 mm can be selected, which can later be adjusted by sweeping the parameter g in CST DS, between 0.1 and 2.0 mm. The second face port is created at the outer end-face of the second coupled feed line. The two excitation signals are then locked,

and the antenna is simulated with a relative amplitude $\gamma = 1$ and phase shift $\varphi = 180°$ at port two. The TARC for the resulting two-port injection matched antenna is shown in Figure 5.3.

The TARC resonance in Figure 5.3 resulting from excitation of the two modes (J_{01} and J_1) of the corresponding one-port antenna (discussed in Section 4.3.3) whose S_{11} is depicted in Figure 5.2 has a −10 dB FBW of around 46.2% (calculated using Equation (B.1) in Appendix B.4) at a 3.455 GHz centre frequency, which is still insufficiently wide to meet the design goal. The bandwidth is improved by optimising the antenna dimensions L_p, W_p, L_s, W_s, L_g, w and the gap g in CST DS between 20 and 25 mm, 16 and 21 mm, 38 and 44 mm, 30 and 36 mm, 7 and 10.42 mm, 1.7 and 4.3 mm, 0.1 and 1.9 mm, respectively. Typical converged results for this optimisation are shown in Figure 5.4 and Table 5.1.

Table 5.1. Antenna dimensions and −10 dB FBW for the optimised TARC resonances shown in Figure 5.4.

Simulation ID	Antenna dimensions (mm)							FBW
	L_p	W_p	L_s	W_s	L_g	w	g	
TARC1	20.4	17.0	43.1	32.2	8.2	2.3	0.6	-
TARC2	24.6	18	39.7	30.0	7.3	2.2	0.5	0.550
TARC3	21.2	16.0	41.4	32.9	7.9	2.4	0.2	-
TARC4	20.5	21.0	40.6	31.7	9.8	2.3	1.2	0.438
TARC5	22.8	21.0	41.8	31.2	7.6	2.3	1.6	0.666
TARC6	20.7	18.3	42.4	31.3	9.5	2.2	0.9	0.642

It is shown in Figure 5.4 and Table 5.1 that TARC5 resonance has the widest −10 dB bandwidth of around 66.6% at a 3.668 GHz centre frequency. This is further improved by fine-tuning the antenna dimensions W_p, W_s, and the gap g in the ranges between 20 and 22 mm, 30.2 and 32.2 mm, and 1.5 and 1.7 mm, respectively, through a parameter

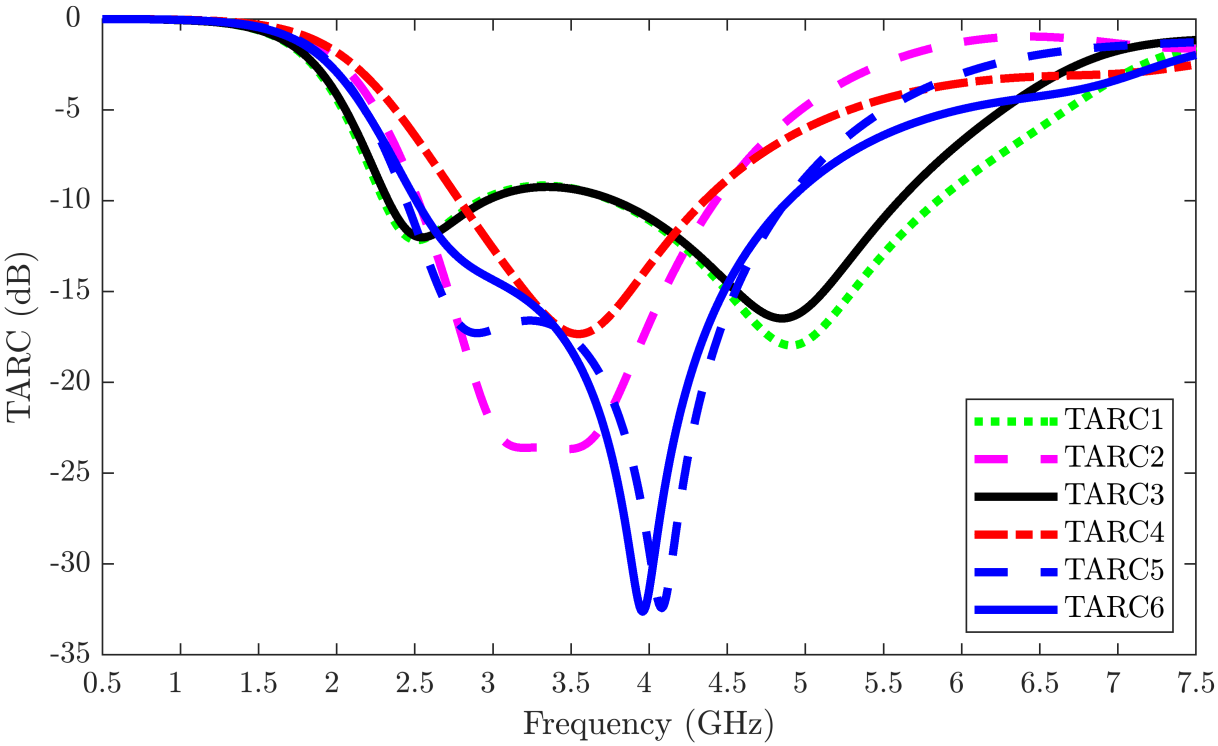


Figure 5.4. Typical results for the optimised TARC resonances for the differentially excited two-port proximity-fed patch antenna under investigation.

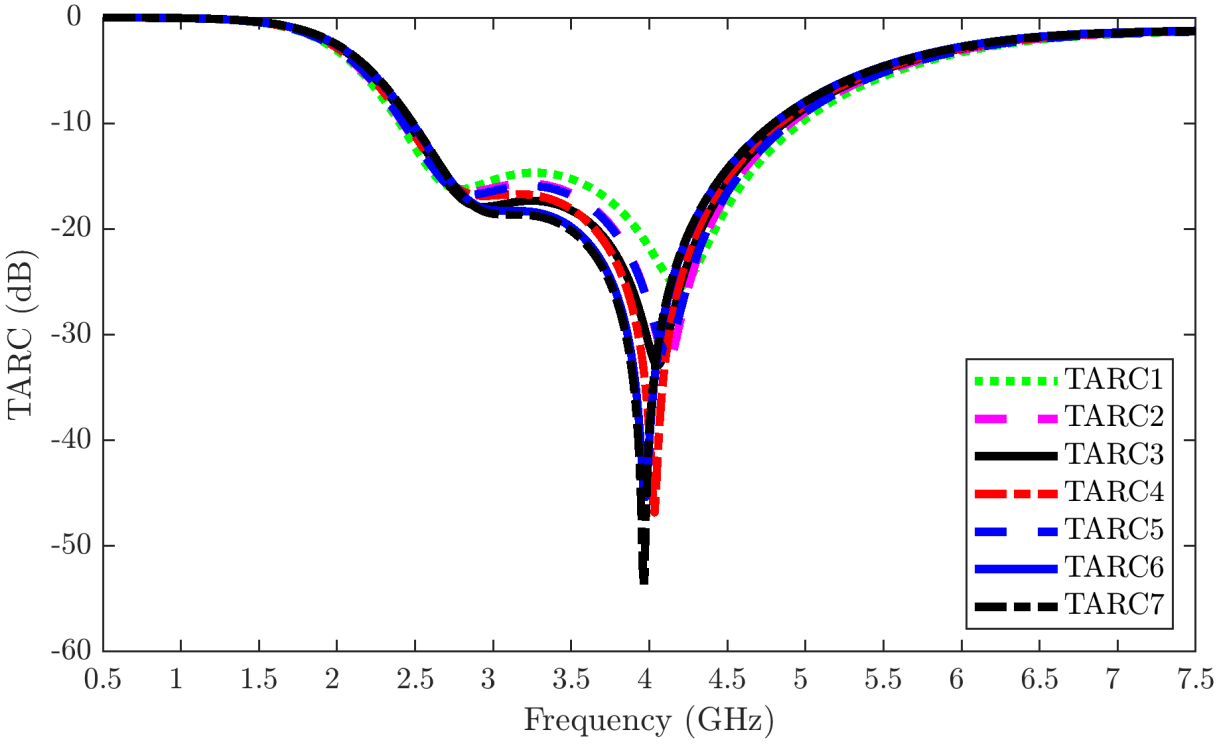


Figure 5.5. Typical results for the fine-tuned TARC resonances for the differentially excited two-port proximity-fed patch antenna under investigation.

Table 5.2. Antenna dimensions and −10 dB FBW for the fine-tuned TARC resonances shown in Figure 5.5.

Simulation ID	Antenna dimensions (mm)							FBW
	L_p	W_p	L_s	W_s	L_g	w	g	
TARC1	22.8	20.0	41.8	32.2	7.6	2.3	1.5	0.695
TARC2	22.8	21.0	41.8	32.2	7.6	2.3	1.5	0.675
TARC3	22.8	21.0	41.8	30.2	7.6	2.3	1.5	0.654
TARC4	22.8	22.0	41.8	32.2	7.6	2.3	1.6	0.655
TARC5	22.8	21.0	41.8	32.2	7.6	2.3	1.7	0.675
TARC6	22.8	22.0	41.8	30.2	7.6	2.3	1.5	0.634
TARC7	22.8	22.0	41.8	30.2	7.6	2.3	1.7	0.632

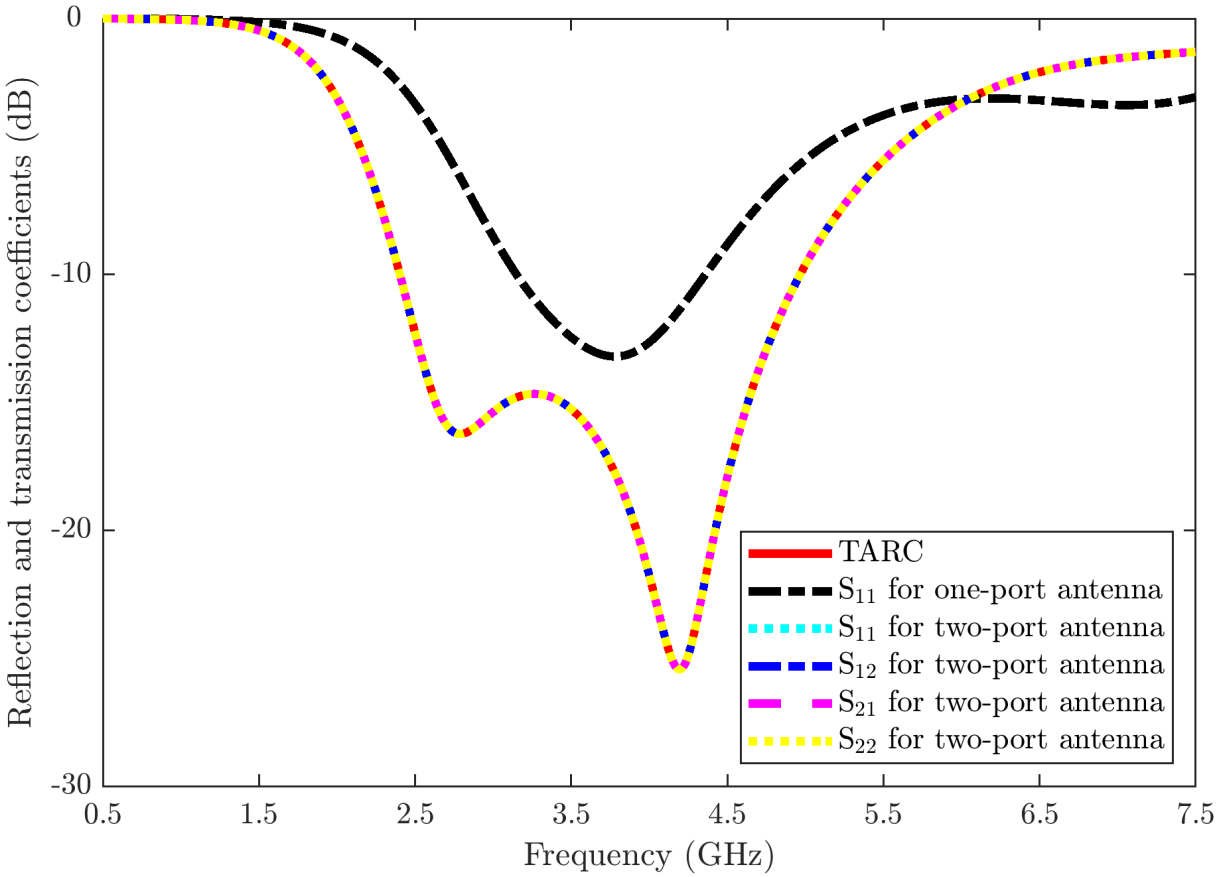


Figure 5.6. Optimum TARC (TARC1) resonance, individual port reflection coefficients, and transmission coefficients between the two ports for the differentially excited two-port proximity-fed patch antenna under investigation in comparison to the S-parameter for the corresponding one-port antenna. The dimensions for the two antennas are depicted by TARC1 resonance in Table 5.2.

sweep in the CST DS optimiser. Typical results for the fine-tuned TARC resonances are shown in Figure 5.5 with their corresponding antenna dimensions in Table 5.2.

Considering the −10 dB bandwidth, the TARC1 resonance, which is depicted in Figure 5.6 and Table 5.2, has the best impedance matched bandwidth compared to the remaining TARC resonances in Figure 5.5. The S_{11}, S_{21}, S_{12}, and S_{22} for the realised two-port antenna are also plotted in Figure 5.6 for comparison. It is shown in Figure 5.6 that the S_{11}, S_{21}, S_{12}, and S_{22} for the two-port antenna are equal to the TARC resonance because of the symmetry between the two feed points.

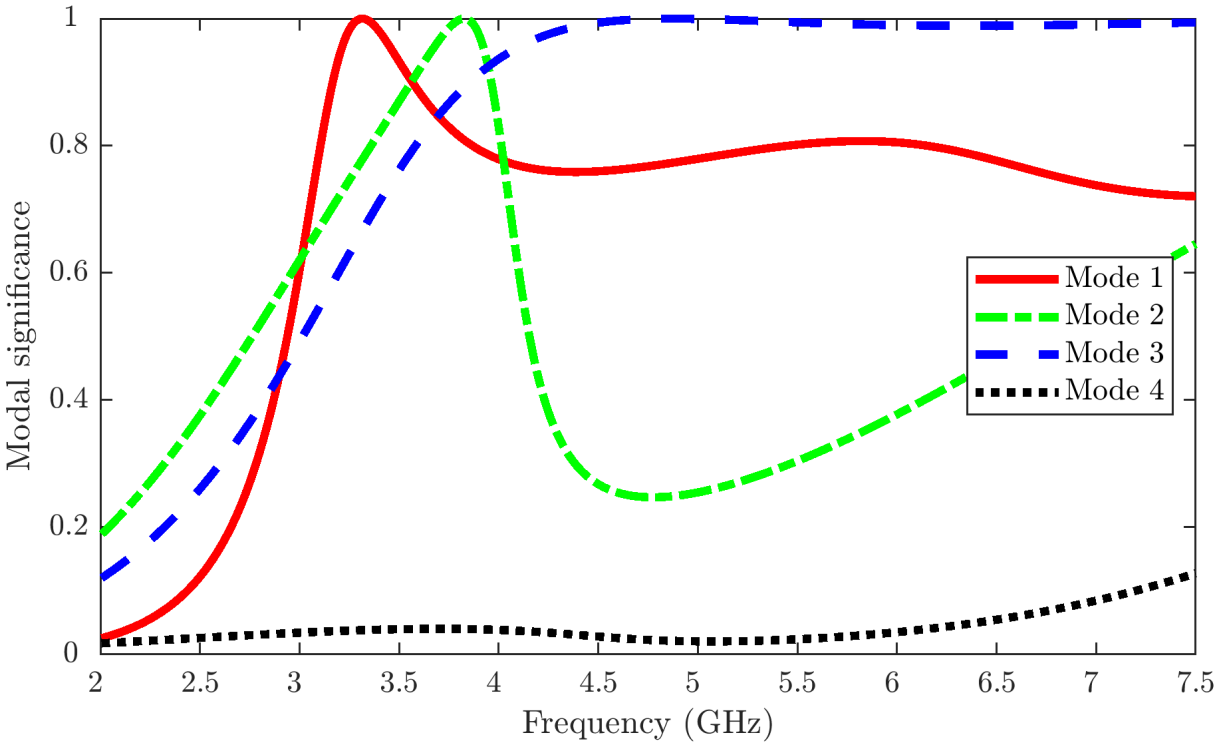


Figure 5.7. The modal significance for the first four characteristic modes of the proximity-fed patch antenna whose TARC is depicted in Figure 5.6.

The CMA of the antenna whose TARC resonance is depicted in Figure 5.6 is provided in Figure 5.7 and 5.8. The analysis was conducted in CST MWS using a Multilayer Solver with solver and mesh settings provided in Table B.1 and B.2 in Appendix B.2. It

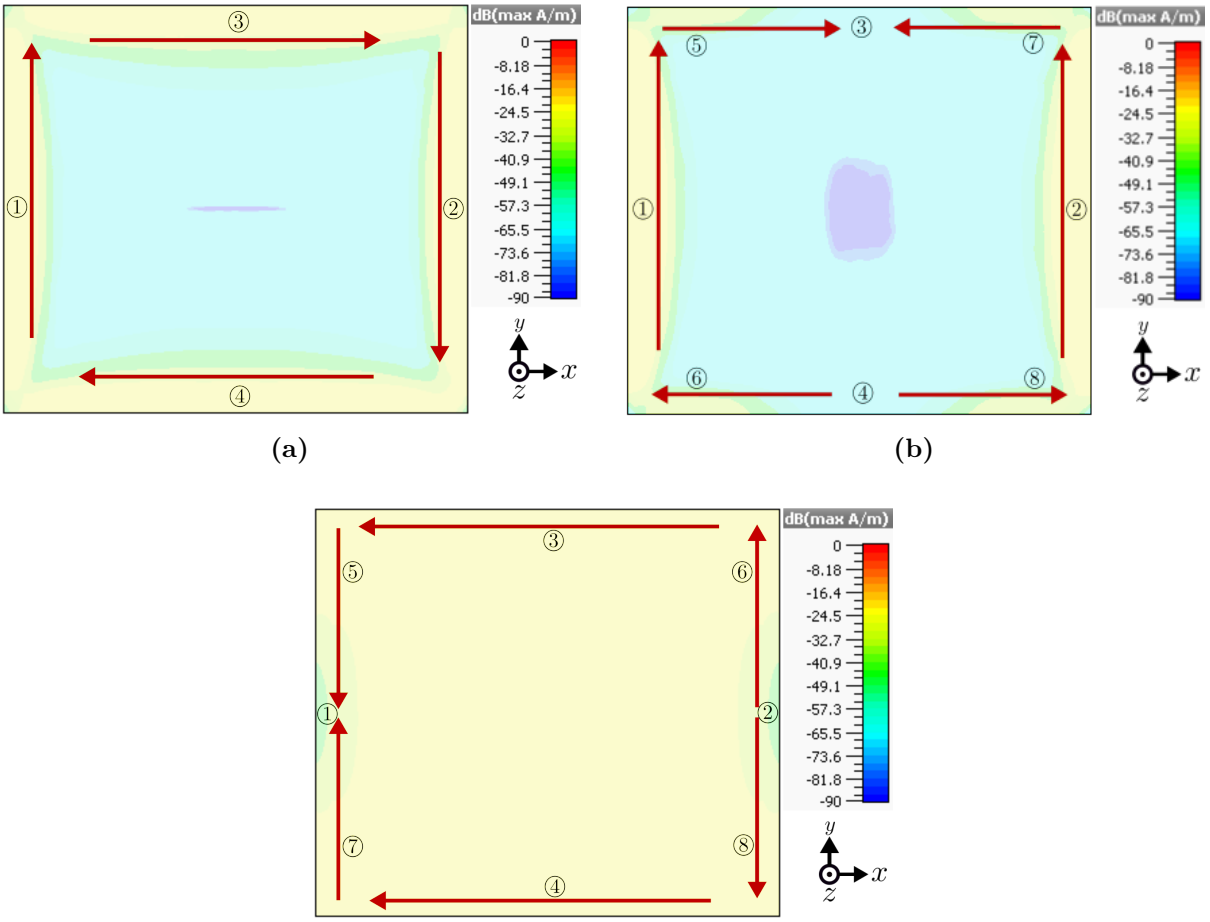


Figure 5.8. Characteristic surface current for (a) mode J_{01} at a 2.315 GHz frequency (b) mode J_2 at a 3.826 GHz frequency (c) mode J_1 at a 4.871 GHz frequency for the antenna depicted in Figure 5.6, whose modal significant is shown in Figure 5.7.

is shown in Figure 5.7 and 5.8a that mode one is an inductive fundamental mode J_{01}, having the principal characteristic current forming a horizontally directed closed loop on the patch. The principal current is also differentially oriented at the two short patch edges. Excitation of mode J_{01} is achieved by driving a differential pair of excitations delivered at the two short edges at the maxima positions 1 and 2. The H-plane ($\phi = 90°$) radiation patterns resulting from excitation of mode J_{01}, shown in Figure 5.23a and 5.24b at a 2.775 GHz resonant frequency, are approximately omnidirectional as predicted by mode J_{01} patterns in Figure 4.7a and 4.13a. However, at the same frequency, the E-plane ($\phi = 0°$) patterns have two deep nulls in the $\theta = 90°$ and $\theta = 270°$ directions (shown in Figure 5.24b) as a result of feeding the antenna at these locations.

Mode two shown in Figure 5.7 and 5.8b is a vertical mode J_2, having two branches of the principal characteristic current originating from position 4, attaining the maximum value at the maxima positions 1, 2 and 5 through 8 along the four patch edges and joining at position 3. Because of its polarisation and a differential orientation of the principal current at the two long patch edges [86], excitation of mode J_2 requires two differential pairs of excitations to be placed at the maxima positions 5 and 6, and 7 and 8. However, feeding at these locations is not feasible because of the absence of grounding planes below the two long patch edges of this antenna, as shown in Figure 5.1b. Excitation of this kind of mode is particularly discussed in Section 6.2.1.

On the other hand, mode three shown in Figure 5.7 and 5.8c is a horizontal mode J_1, having two branches of the principal characteristic current originating from the minima position 2 and joining at position 1. Because of its polarisation, mode J_1 is effectively excited through two pairs of differential excitations placed at the maxima positions 5 and 6, and 7 and 8, as depicted in Figure 5.8c. At these feeding positions, as illustrated

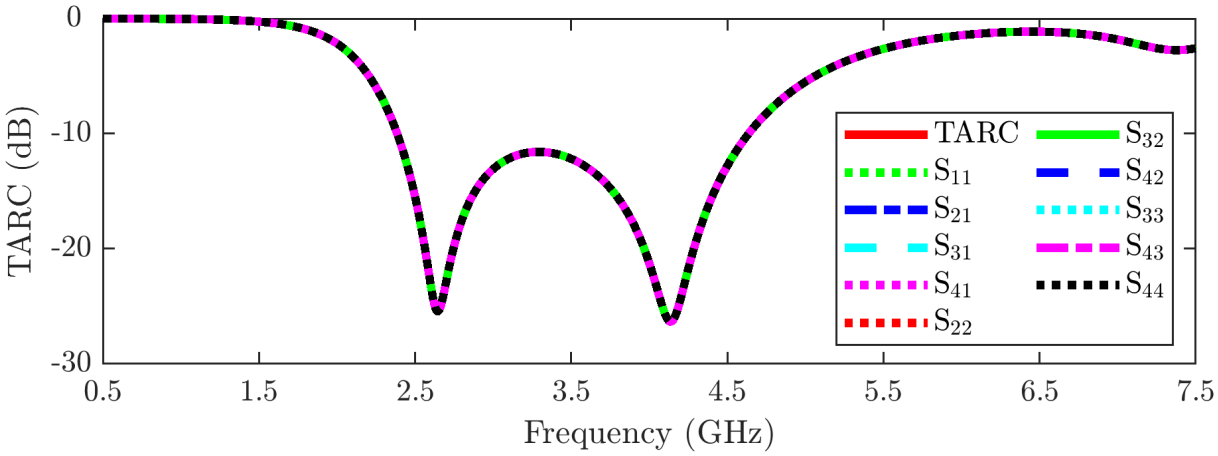


Figure 5.9. TARC resulting from excitation of modes J_{01} and J_1 of the patch antenna under investigation through two pairs of differential excitations delivered at the opposite short patch edges at the current maxima positions 5 and 6, and 7 and 8 of mode J_1, as shown in Figure 5.8, with $w = 0.7$ mm and $g = 1.5$ mm for each pair of the feed lines, while $L_p = 22.8$, $W_p = 20$, $L_s = 41.8$, $W_s = 32.2$, and $Lg = 7.6$ mm. The modified antenna layer two is shown in Figure 5.10.

in Figure 5.10, mode J_{01} is also jointly excited with mode J_1 to enable a wideband operation, as depicted by the TARC resonance in Figure 5.9. Also, because the strong mode J_1 characteristic current is widely distributed over the patch, feeding the antenna at positions 1 and 2 jointly excites modes J_{01} and J_1 to enable a wideband operation, as shown in Figure 5.8a, 5.8c, and 5.6. The H-plane ($\phi = 90°$) radiation patterns resulting from excitation of horizontal mode J_1, shown in Figure 5.23a and 5.24c at a 4.215 GHz resonant frequency, are approximately omnidirectional as predicted by mode J_1 patterns in Figure 4.7b and 4.13d. However, at the same frequency, the E-plane ($\phi = 0°$) patterns have two deep nulls in the $\theta = 90°$ and $\theta = 270°$ directions (shown in Figure 5.24c) as a result of feeding the antenna at these locations.

The realised four-port antenna has a radiation efficiency higher than 99% across its -10 dB bandwidth, as shown in Figure 5.11a, which is attributed to the low loss tangent ($\tan\delta = 0.0009$) and low dielectric constant ($\varepsilon = 2.2$) substrate material used in the

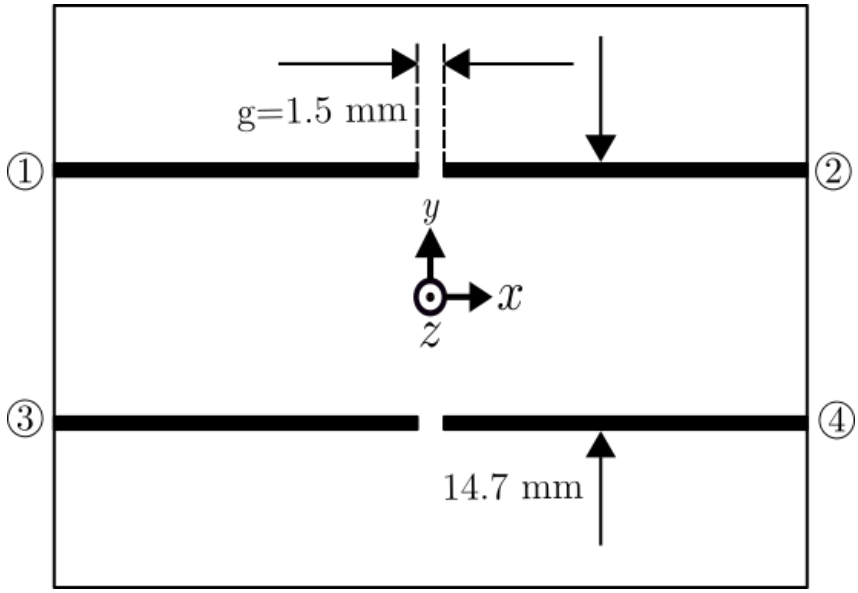
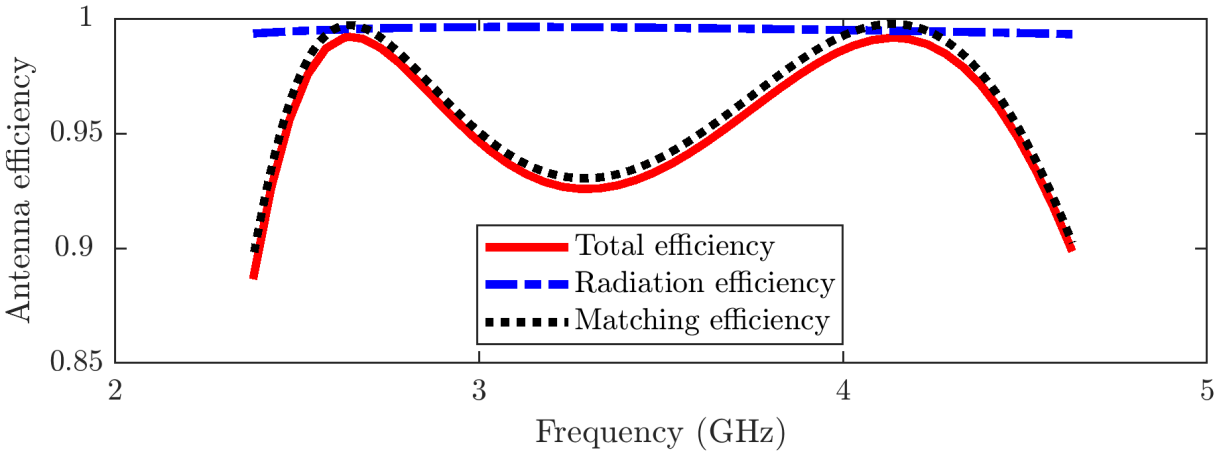
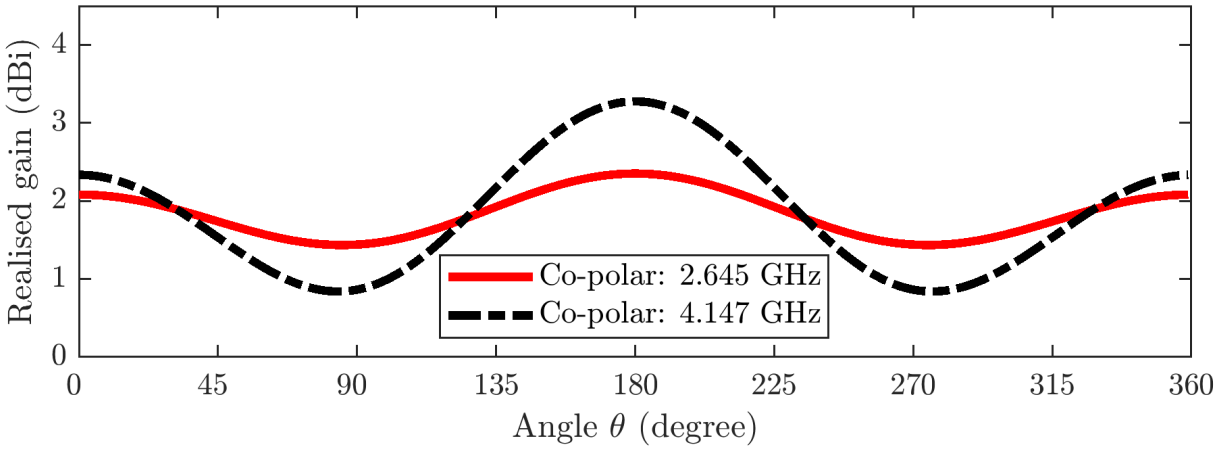


Figure 5.10. Layer two for the four-port proximity-fed patch antenna whose TARC resonance is depicted in Figure 5.9. The discrete face ports 1 through 4 are created on the outer end-faces of the feed lines at positions 1 through 4, respectively. Ports 1 and 2, as well as ports 3 and 4 excitations are differentially driven. The black colour indicates the copper layer, while the white colour indicates the substrate layer. Other antenna dimensions are $w = 0.7$ mm, $L_p = 22.8$, $W_p = 20$, $L_s = 41.8$, $W_s = 32.2$, and $Lg = 7.6$ mm.

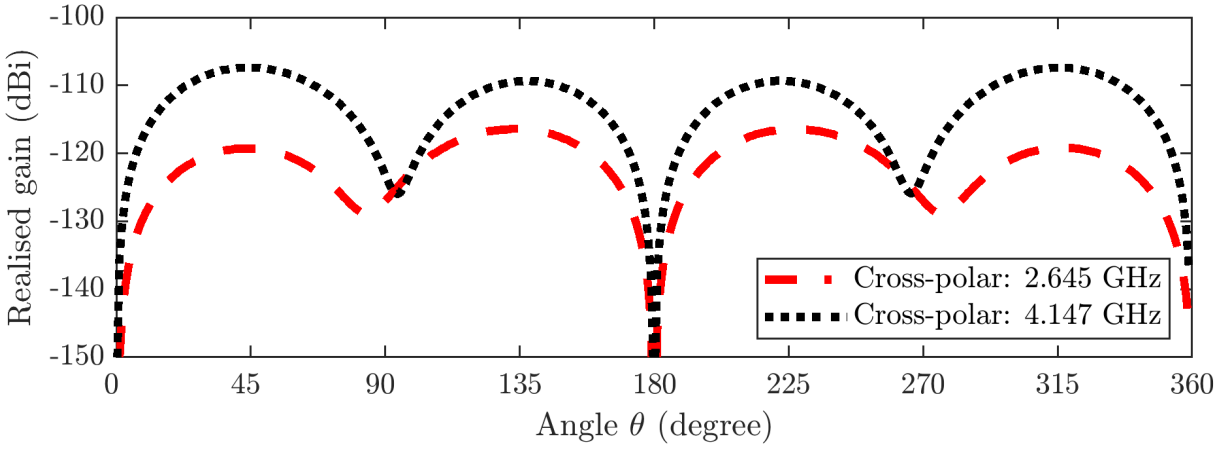
design, as well as to the excitation of two modes of the antenna. Also, because of good impedance matching attained by the four-port antenna through the application of the injection matching technique and the achieved high radiation efficiency, as shown in Figure 5.11a and 5.9, the total efficiency is higher than 88% across the antenna's passband. It is also shown in Figure 5.11b that the H-plane ($\phi = 90°$) co-polar gain attained by the four-port antenna at the two resonant frequencies (2.645 and 4.147 GHz) remained maximum at $\theta = 180°$ while its minimum values remained at $\theta = 90°$ and $\theta = 270°$, which demonstrates fair stability of the patterns. At these two resonant frequencies, the antenna has a H-plane ($\phi = 90°$) cross-polarised gain lower than -106 dBi, as shown in Figure 5.11c. These observations indicate the good performance of the realised four-port injection matched antenna. Also, the gain attained by the four-port antenna at a 2.645 GHz resonant frequency is relatively stable than the gain achieved at 4.147 GHz fre-



(a)



(b)



(c)

Figure 5.11. Simulated (a) efficiency (b) H-plane ($\phi = 90°$) co-polar patterns (c) H-plane ($\phi = 90°$) cross-polar patterns for the four-port proximity-fed injection matched patch antenna whose TARC resonance is depicted in Figure 5.9.

quency because of the excitation of an inductive mode J_{01} of the antenna at the 2.645 GHz frequency. Besides, it is shown in Figure 5.9 that all crosscutting and individual port S-parameters for the realised four-port antenna are equal to each other. All of them are also equal to TARC because of the symmetry between ports 1 and 2, ports 3 and 4, as well as equal displacement of the ports from the magnetic symmetry line of the patch.

On the other hand, the -10 dB FBW attained by the four-port injection matched antenna is around 63.9% at a 3.509 GHz centre frequency. This bandwidth is lower than the bandwidth of 69.5% achieved by the corresponding two-port antenna shown in Figure 5.6, and it does not meet the design goal laid out in this chapter. Because of the large number of ports, enhancing the bandwidth of the antenna in Figure 5.9 by changing the antenna dimensions and position of the feed lines requires a high computational cost that the available resources cannot meet. Also, because of the limitation of the R&S ZVA67 VNA to allow coherence mode operation with all four ports as discussed in Section 4.3.7, the four-port antenna in Figure 5.9 cannot be experimentally validated. Because of these factors, the two-port antenna whose TARC resonance is depicted in Figure 5.6 is studied for bandwidth improvement.

The bandwidth for the two-port antenna whose TARC resonance is depicted in Figure 5.6 can further be improved by adjusting the substrate thicknesses h_1 and h_2, feed lines width w and the gap g between the two feed lines between 0.3 and 1.6 mm, 0.3 and 0.8 mm, 1.8 and 2.3 mm, 1.5 and 1.7 mm, respectively. The optimum TARC resonances for this parameter sweep are provided in Figure 5.12 and Table 5.3.

Though the design goal is not met, the TARC4 resonance depicted in Figure 5.12 and Table 5.3 provides a -10 dB FBW of around 85.2% (calculated using Equation (B.1) in Appendix B.4) spanning between 2.326 and 5.775 GHz. More bandwidth can be attained

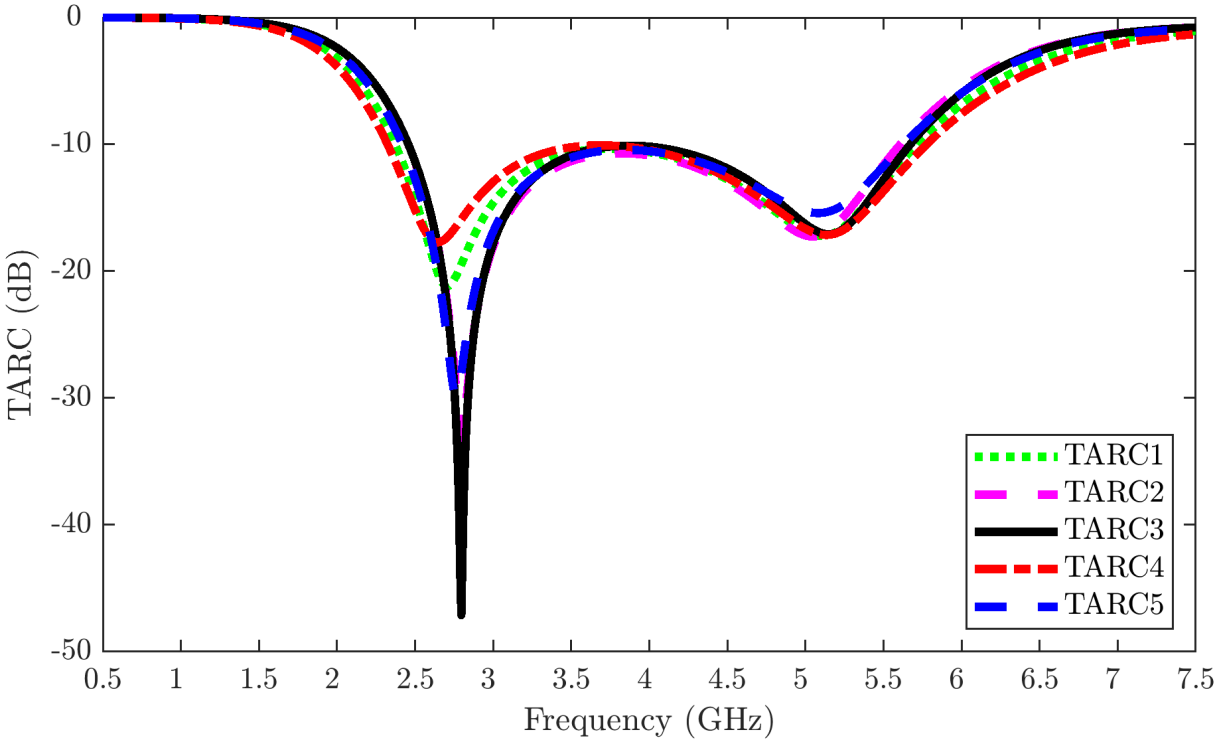


Figure 5.12. TARC resonances obtained by changing substrate heights h_1 and h_2, feed lines width w and the gap g between the two feed lines as shown in Table 5.3.

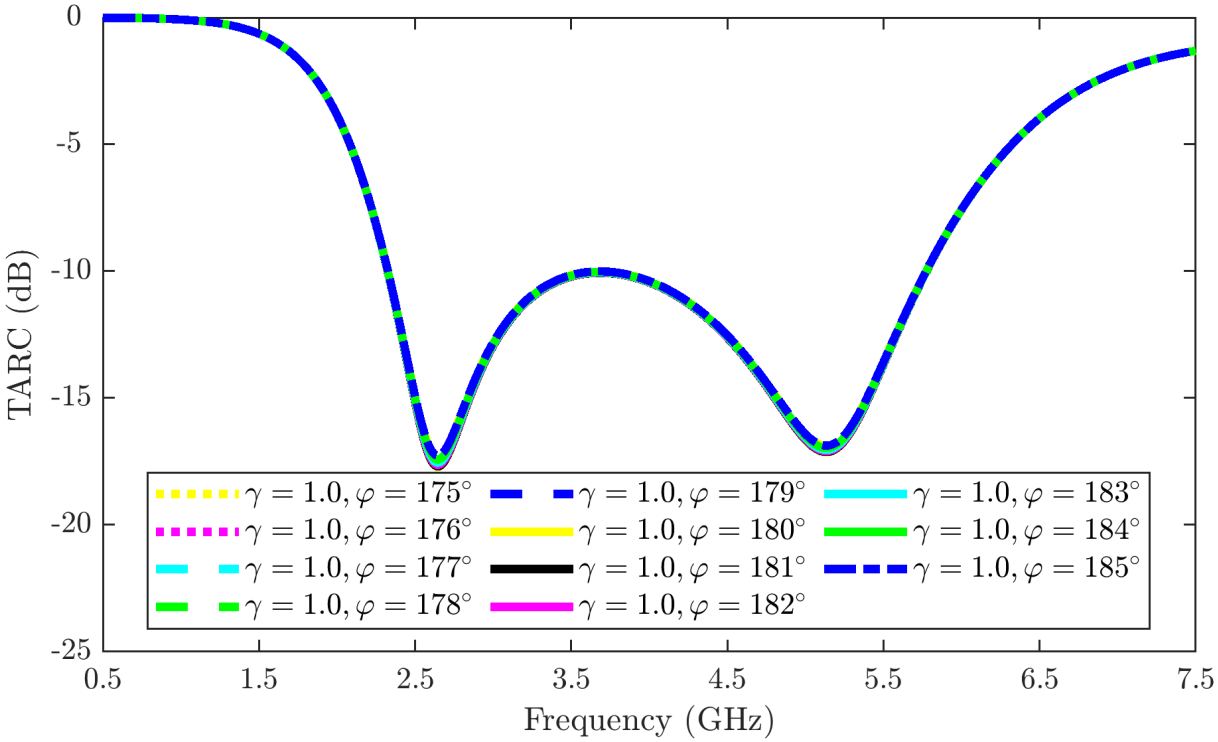


Figure 5.13. Typical differential mode TARC4 resonances when $\gamma = 1$ and φ are varied in the range of $175° \leq \varphi \leq 185°$.

Table 5.3. Antenna dimensions and −10 dB FBW corresponding to the TARC resonances shown in Figure 5.12.

Simulation ID	Antenna dimensions (mm)									FBW
	L_p	W_p	L_s	W_s	L_g	w	g	h_1	h_2	
TARC1	22.8	20.0	41.8	32.2	7.6	1.8	1.5	0.8	0.4	0.826
TARC2	22.8	20.0	41.8	32.2	7.6	1.8	1.5	0.8	0.6	0.782
TARC3	22.8	20.0	41.8	32.2	7.6	1.9	1.6	0.8	0.6	0.790
TARC4	22.8	20.0	41.8	32.2	7.6	1.8	1.5	0.8	0.3	0.852
TARC5	22.8	20.0	41.8	32.2	7.6	2.3	1.5	1.0	0.6	0.797

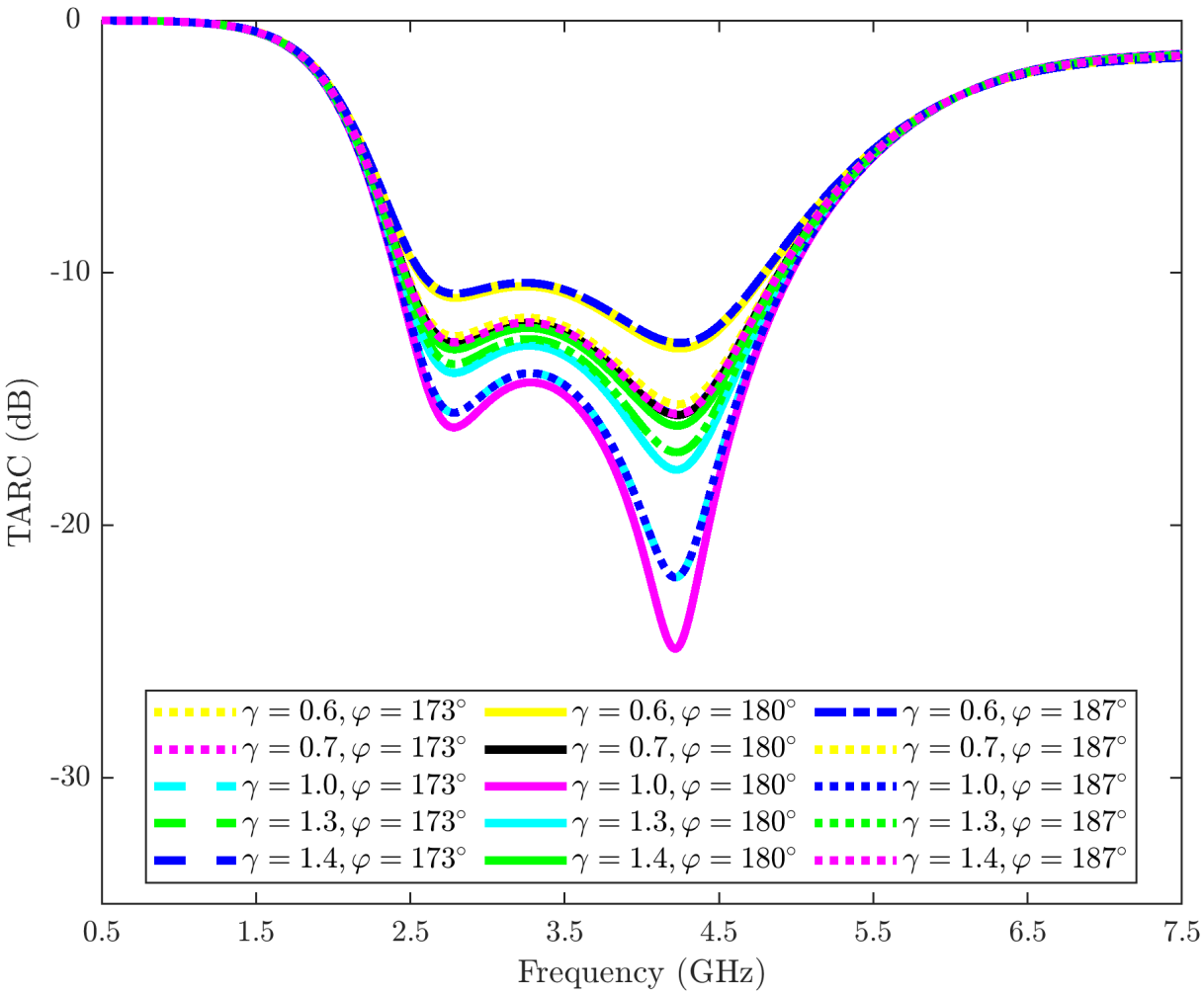


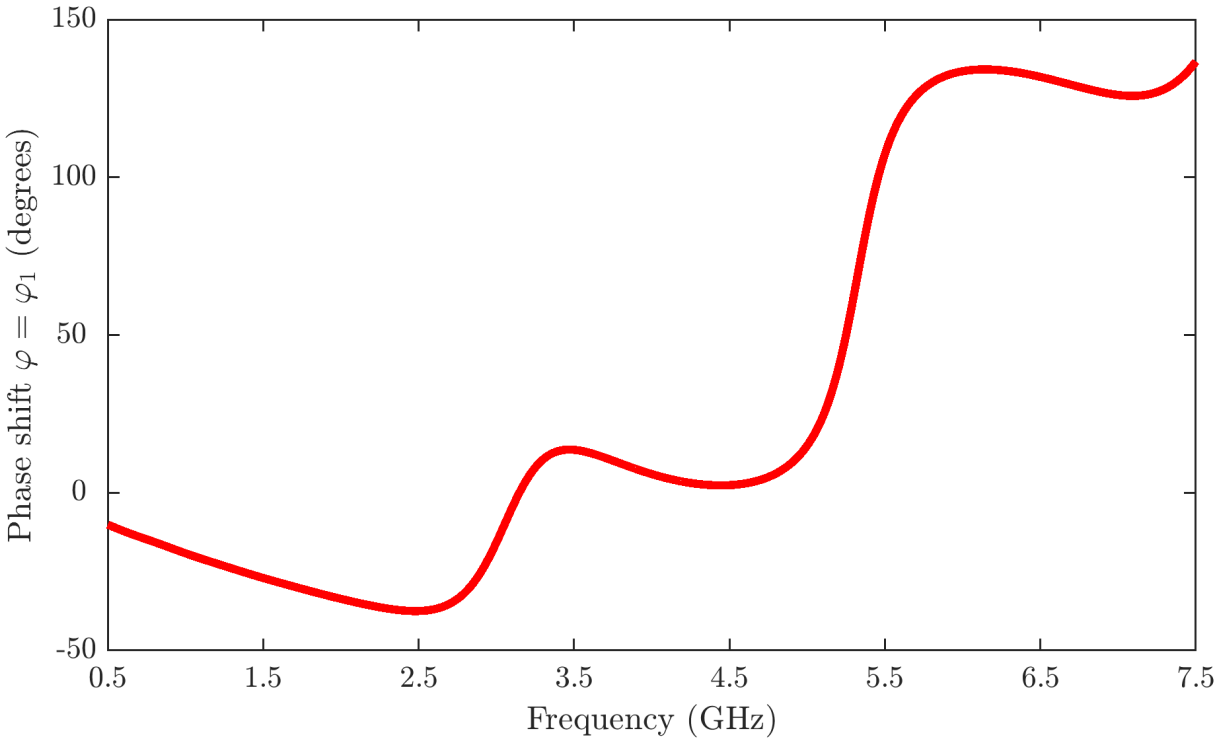
Figure 5.14. Typical differential mode TARC1 resonances when γ and φ are varied in the ranges of $0.6 \leq \gamma \leq 1.4$ and $173° \leq \varphi \leq 187°$.

by varying all the antenna dimensions, including the substrate thicknesses, but at the expense of the computational cost, which could not be implemented because of the limited resources. The -10 dB FBW for TARC4 resonance is maintained for $\gamma = 1$ and $\varphi = 180^\circ \pm 5^\circ$ as depicted in Figure 5.13.

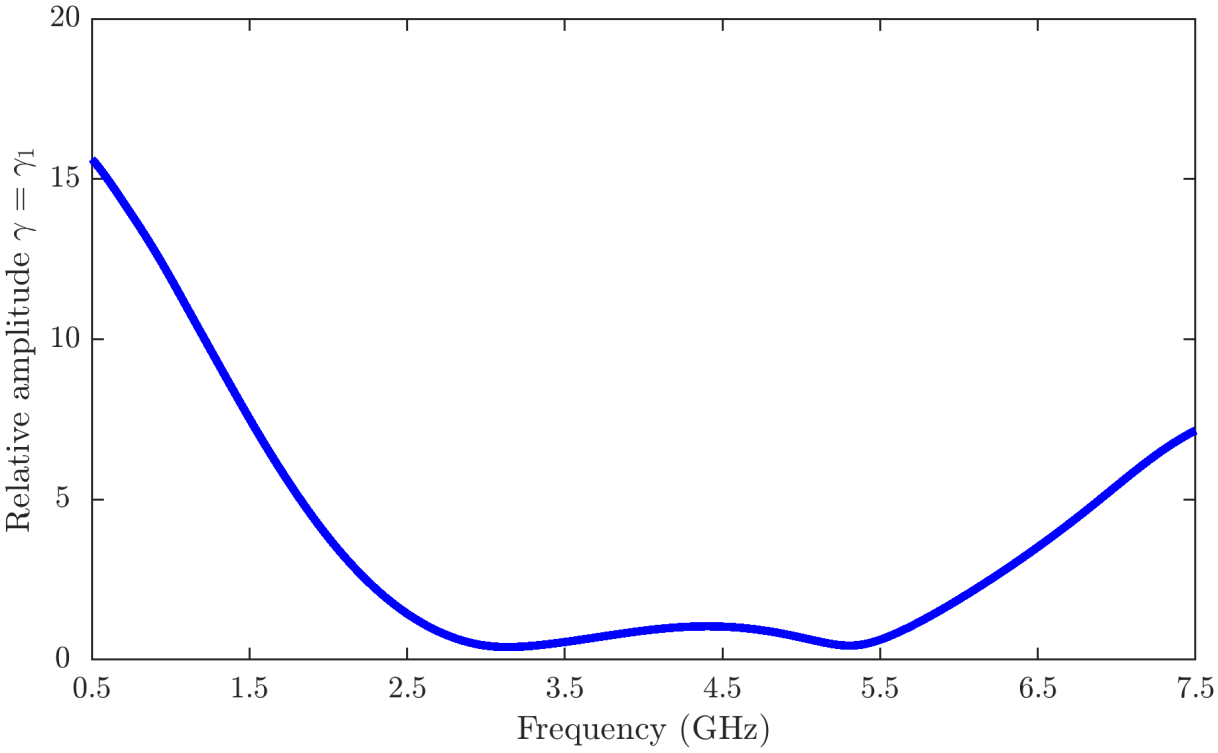
However, because of the unavailability of the substrates with nonstandard thickness used in attaining TARC4, the injection matching technique is experimentally validated by TARC1 resonance shown in Figure 5.6. The -10 dB FBW for TARC1 resonance of Figure 5.6 is fairly maintained for $\gamma = 1 \pm 0.4$ and $\varphi = 180^\circ \pm 7^\circ$ as shown in Figure 5.14 by the typical values of γ and φ derived in the optimisation domain of $0.6 \leq \gamma \leq 1.4$ and $173^\circ \leq \varphi \leq 187^\circ$. The theoretical γ and φ variations with frequency corresponding to the TARC1 resonance are plotted in Figure 5.15.

It is shown in Figure 5.15b that there are two minima for the theoretical γ variation at around 3.0 and 5.3 GHz frequencies, and a narrow flat region at frequencies near 4.5 GHz, whereas in Figure 5.15a there are two minima for the φ variations at around 2.5 and 4.5 GHz frequencies. Although the theoretical γ is neither constant nor having a minimum at around 2.5 GHz, because of the small change in γ at this frequency, injection matched operation is attained at around 2.5 GHz in combination with the φ minimum at the same frequency with a low TARC value.

Also, a combination of the minimum of φ at around 4.5 GHz and the flat region for γ at around 4.5 GHz frequency gives rise to another resonance. Because the two resonances represent two modes of the antenna that are correlated to each other [24], they merge to enable broadband injection matched operation. However, because of the high significant variation of the theoretical φ at around 5.3 GHz, it is not possible to achieve injection matched operation in combination with the minimum theoretical γ at this frequency.



(a)



(b)

Figure 5.15. Variation of the theoretical (a) phase shift φ (b) relative amplitude γ with frequency across the two-port antenna whose TARC resonance is depicted in Figure 5.6.

The resulting S-parameter for the corresponding one-port antenna is plotted for comparison with TARC in Figure 5.6. The two antennas in Figure 5.6 were experimentally validated to characterise TARC and radiation patterns by following the procedure outlined in Section 4.4, and the findings are discussed in Section 5.3. Also, the simulated realised gain, antenna radiation, matching and total efficiency, and surface currents for the two antennas in Figure 5.6 are discussed in Section 5.3.

5.3 Results and discussion

The printed versions of the two-port antenna and the corresponding one-port antenna whose TARC and S_{11} are depicted in Figure 5.6 are shown in Figure 5.16. The validated TARC and S_{11}, and radiation patterns for the two antennas are plotted in Figure 5.17, and 5.24 and 5.25, respectively.

It is shown in Figure 5.17 that the two-port antenna has a wide -10 dB FBW of around 69.5% (which was calculated using Equation (B.1) in Appendix B.4) compared to the FBW of around 37% attained by the corresponding one-port antenna. The higher bandwidth for the two-port antenna is attributed to the superposition of two characteristic modes (J_{01} and J_1) of the antenna at around 2.775 and 4.215 GHz resonant frequencies, which were differentially excited by applying two coherent excitation signals with relative amplitude $\gamma = 1$ and phase shift $\varphi = 180°$.

The slight deviation of the measured TARC from the simulated TARC, mainly at frequencies below 4.5 GHz, is believed to be caused by stray currents flowing on the outer shield of the two feeding coaxial cables via the SMA connectors connected to the PGPs, to cause variations in the terminal impedances at the input terminals of the fabricated

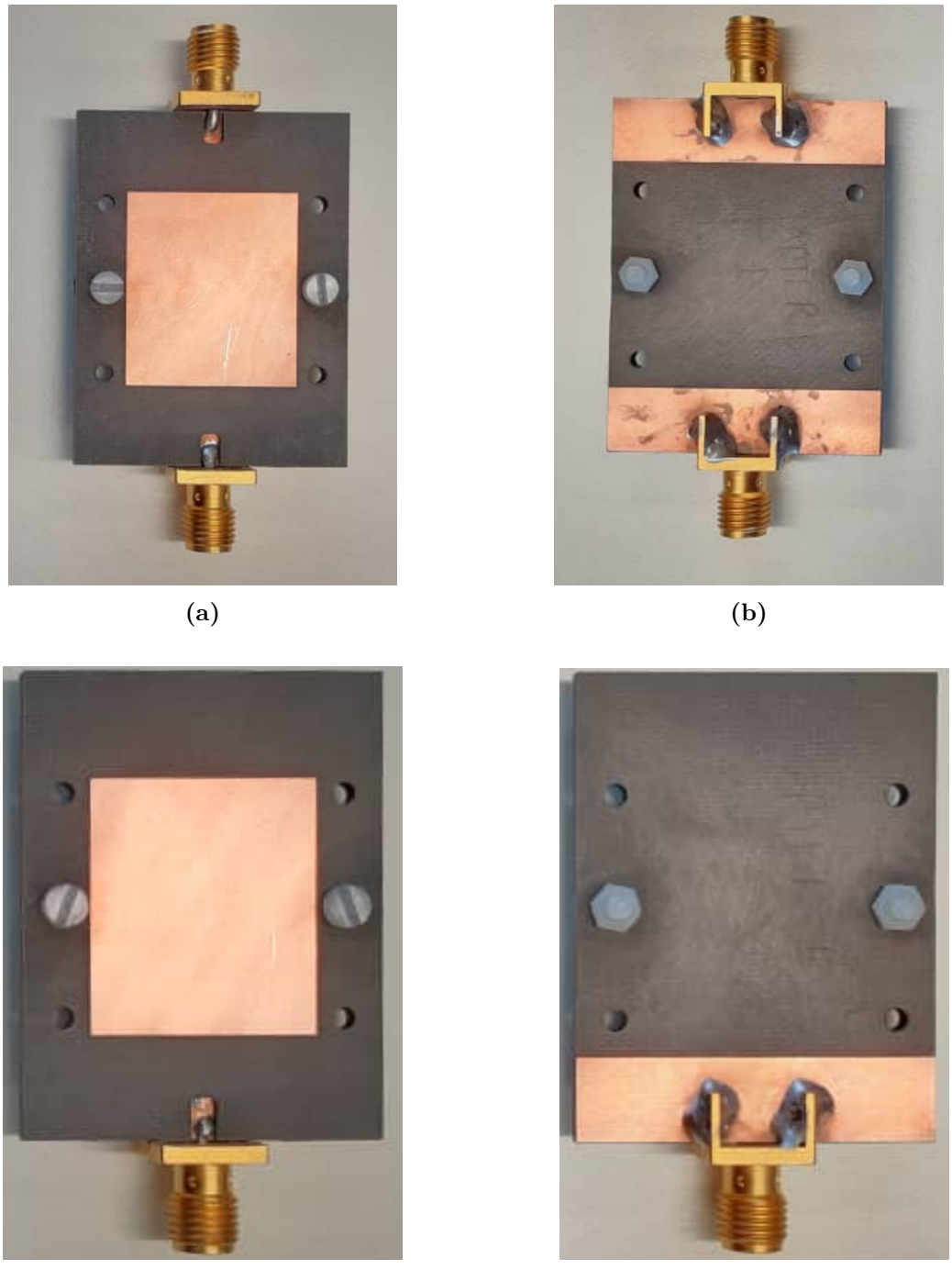


Figure 5.16. (a) Front view of the printed two-port patch antenna (b) back view of the printed two-port patch antenna (c) front view of the printed corresponding one-port patch antenna (d) back view of the printed corresponding one-port patch antenna. The two antennas have dimensions depicted by TARC1 resonance in Table 5.2.

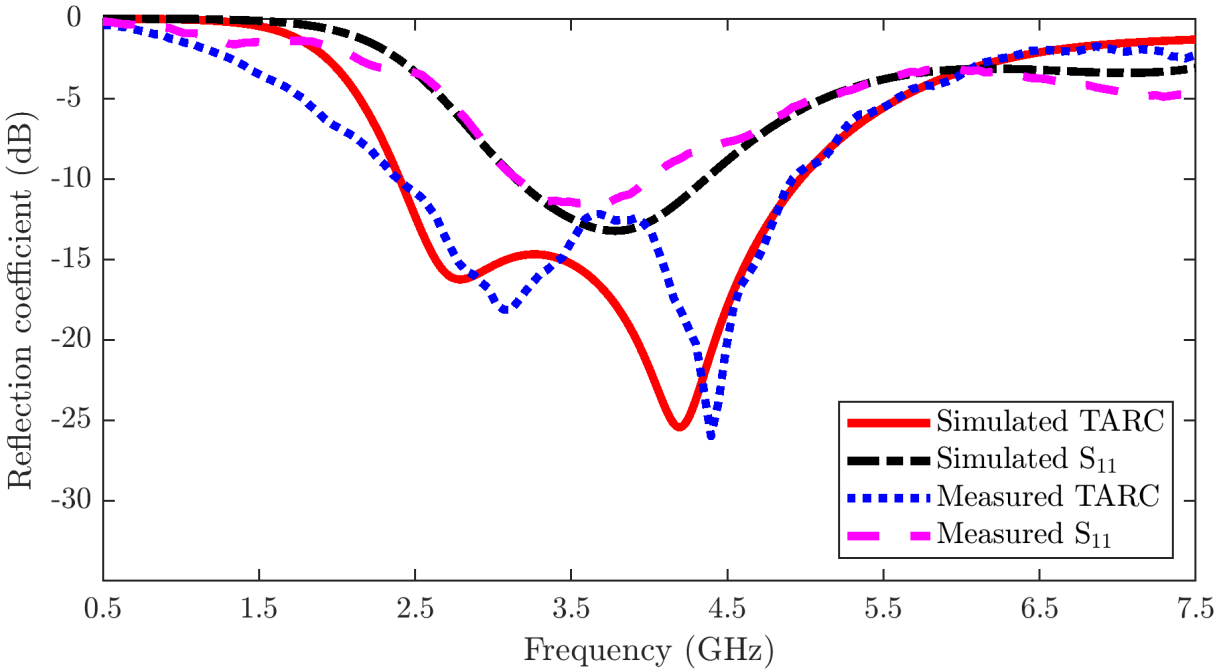
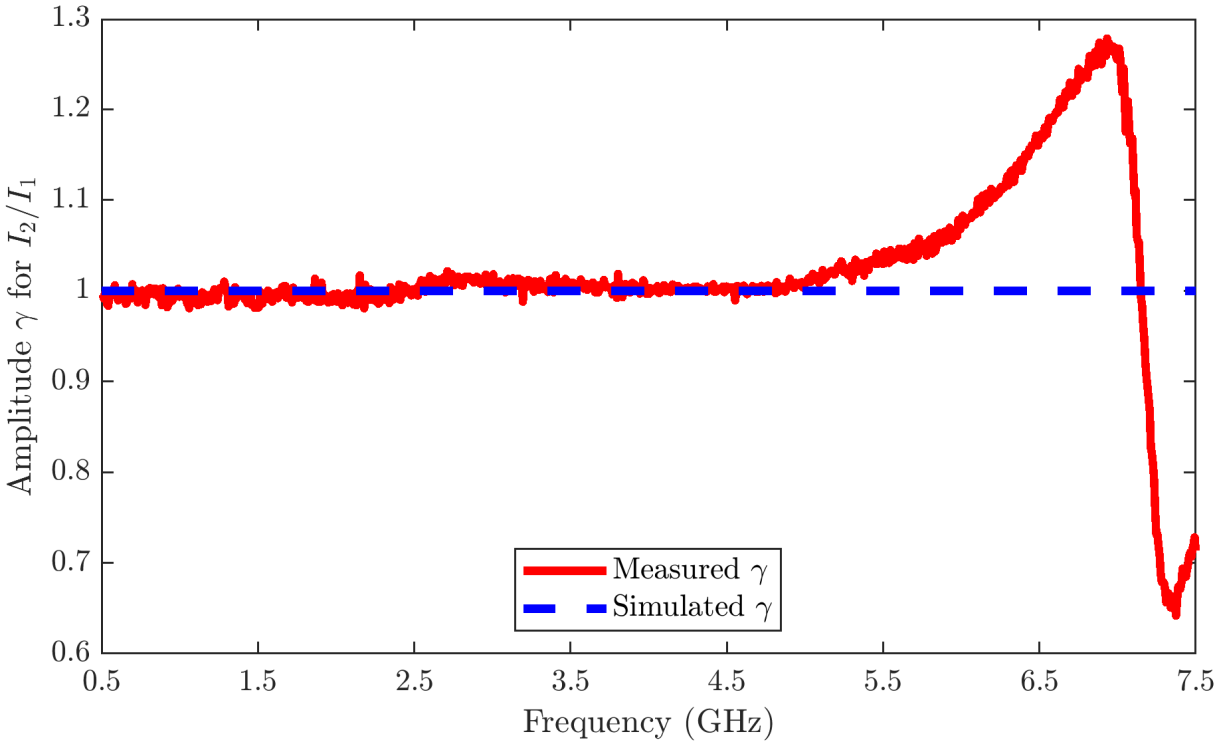


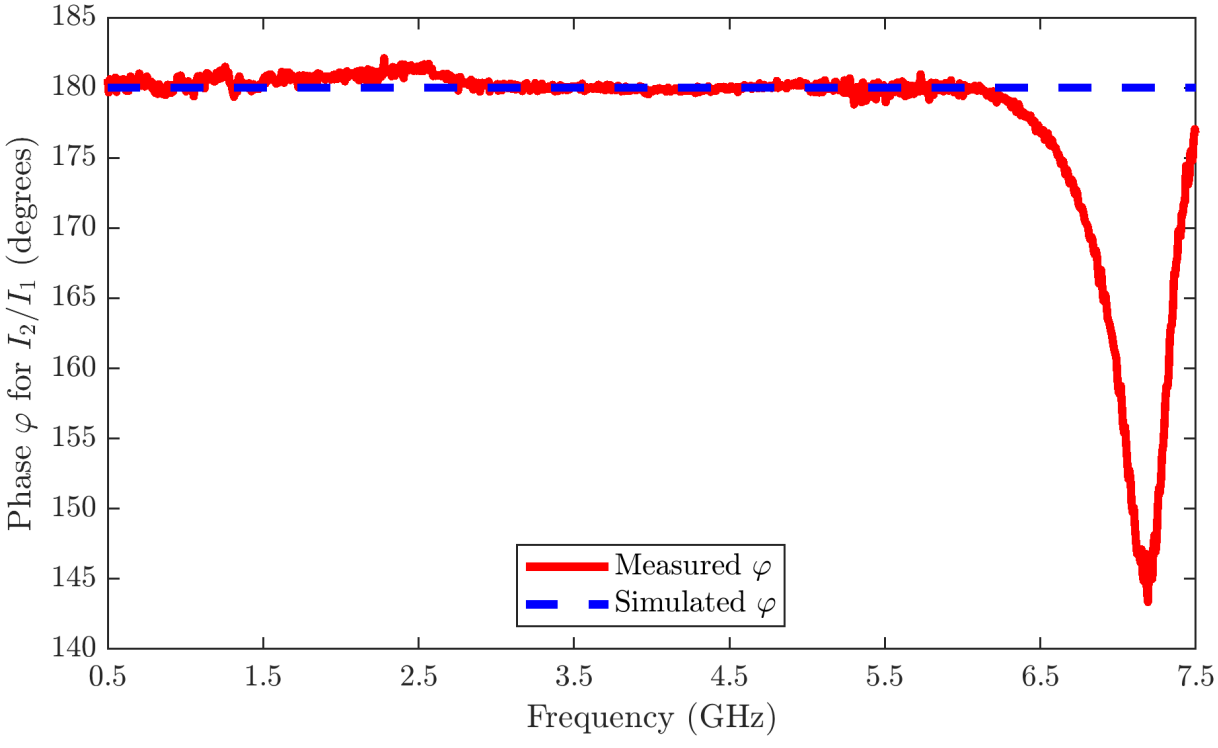
Figure 5.17. Measured and simulated reflection coefficients for the differentially excited two-port injection matched patch antenna in comparison to the S-parameters for the corresponding one-port antenna. The simulated and printed antennas are shown in Figure 5.6 and 5.16, respectively.

two-port antenna, as shown in Figure 5.18 and 5.19. Also, because of the small size of the PGPs, these residual currents caused undesired radiation at different frequencies across the entire frequency range of investigation. These resonances interfered with the main resonance to distort the TARC. Though ferrite beads (shown in Figure 4.35) were used during the measurement, the effect of residual currents could not be eliminated. Also, the high variations of the measured applied γ and φ at frequencies above 5.0 GHz, shown in Figure 5.18 caused significant variations in the terminal impedances (Figure 5.19) in the same frequencies, which caused the antenna to lose the injection matching at frequencies around 7.3 GHz.

The simulated matching efficiency for the two-port injection matched antenna shown in Figure 5.20 is generally higher than the matching efficiency for the corresponding one-port



(a)



(b)

Figure 5.18. Measured and simulated response of the applied (a) relative amplitude γ between the currents I_1 and I_2 (b) phase shift φ between the currents I_1 and I_2 when the patch antenna was injection matched at $\gamma = 1$ and $\varphi = 180°$. The simulated and printed antennas are shown in Figure 5.6 and 5.16, respectively.

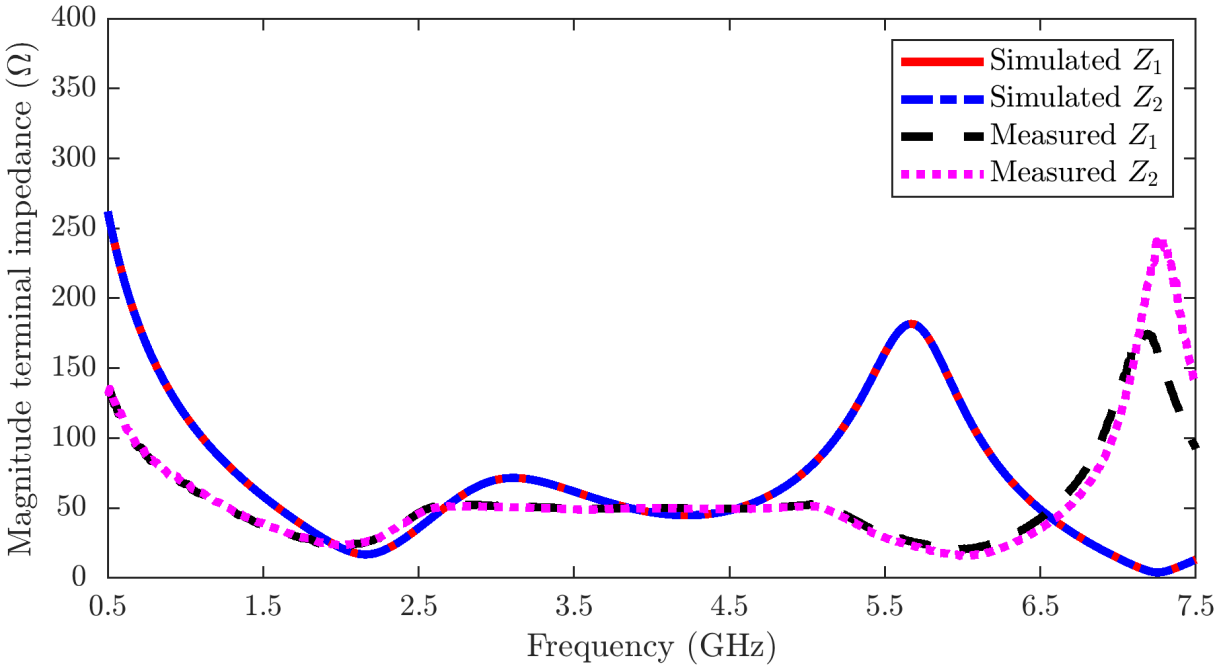


Figure 5.19. Simulated and measured terminal impedances for the differentially excited two-port patch antenna under investigation. The simulated and printed antennas are shown in Figure 5.6 and 5.16, respectively.

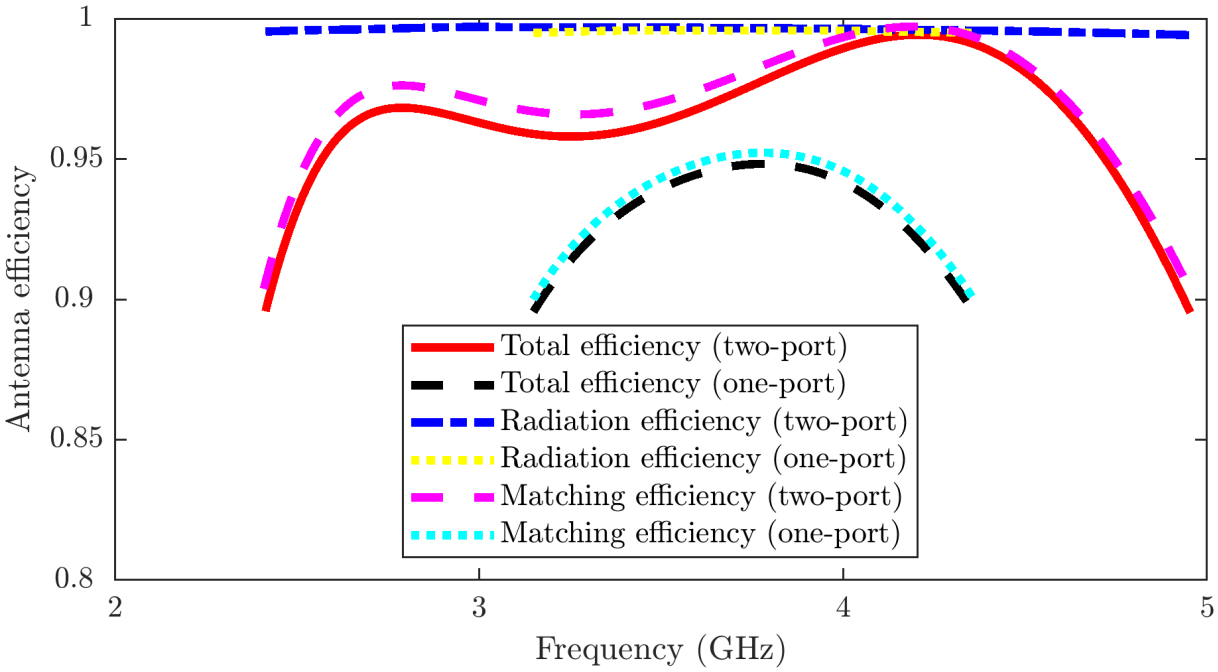


Figure 5.20. Simulated efficiency for the two-port injection matched patch antenna in comparison to the simulated efficiency for the corresponding one-port antenna. The simulated and printed antennas are shown in Figure 5.6 and 5.16, respectively.

antenna in all frequencies within the antenna's passband. The higher matching efficiency attained by the two-port antenna is attributed to good impedance matching achieved through the injection matching technique. Also, the excitation of two similar characteristic modes (J_{01} and J_1) of the patch antenna achieves a slightly higher radiation efficiency on the two-port antenna compared to the radiation efficiency of the corresponding one-port antenna. However, the two antennas have radiation efficiency higher than 99% attributed to the low loss tangent ($\tan\delta = 0.0009$) and low dielectric constant ($\varepsilon_r = 2.2$) substrate material used in the design. Besides, because of the high matching efficiency and high radiation efficiency attained by the two antennas, the total efficiency for the two antennas is generally higher than 89% across the antennas' passbands.

The simulated surface currents on the two-port injection matched antenna shown in Figure 5.21, as well as on the corresponding one-port antenna shown in Figure 5.22, are more substantial on the partial grounds than on the patches in all investigated frequencies. This observation is an indication that the two-port injection matched patch antenna effectively operates as a dipole patch antenna. In contrast, the one-port antenna operates as a monopole patch antenna.

Also, it is shown in Figure 5.21 that the surface currents on the patch for the two-port injection matched antenna at 2.414 and 2.775 GHz frequencies are similar to the mode J_{01} current shown in Figure 4.6a. This similarity indicates that mode J_{01} has been excited at a 2.775 GHz resonant frequency. Similarly, the fair alignment between the surface currents on the patch at 4.215 and 4.956 GHz frequencies and mode J_1 current shown in Figure 4.6b indicates the excitation of mode J_1 at a 4.215 GHz resonant frequency. On the other hand, the surface currents for the corresponding one-port antenna depicted in Figure 5.22 show that both modes J_{01} and J_1 are excited at 3.781 GHz frequency. Also,

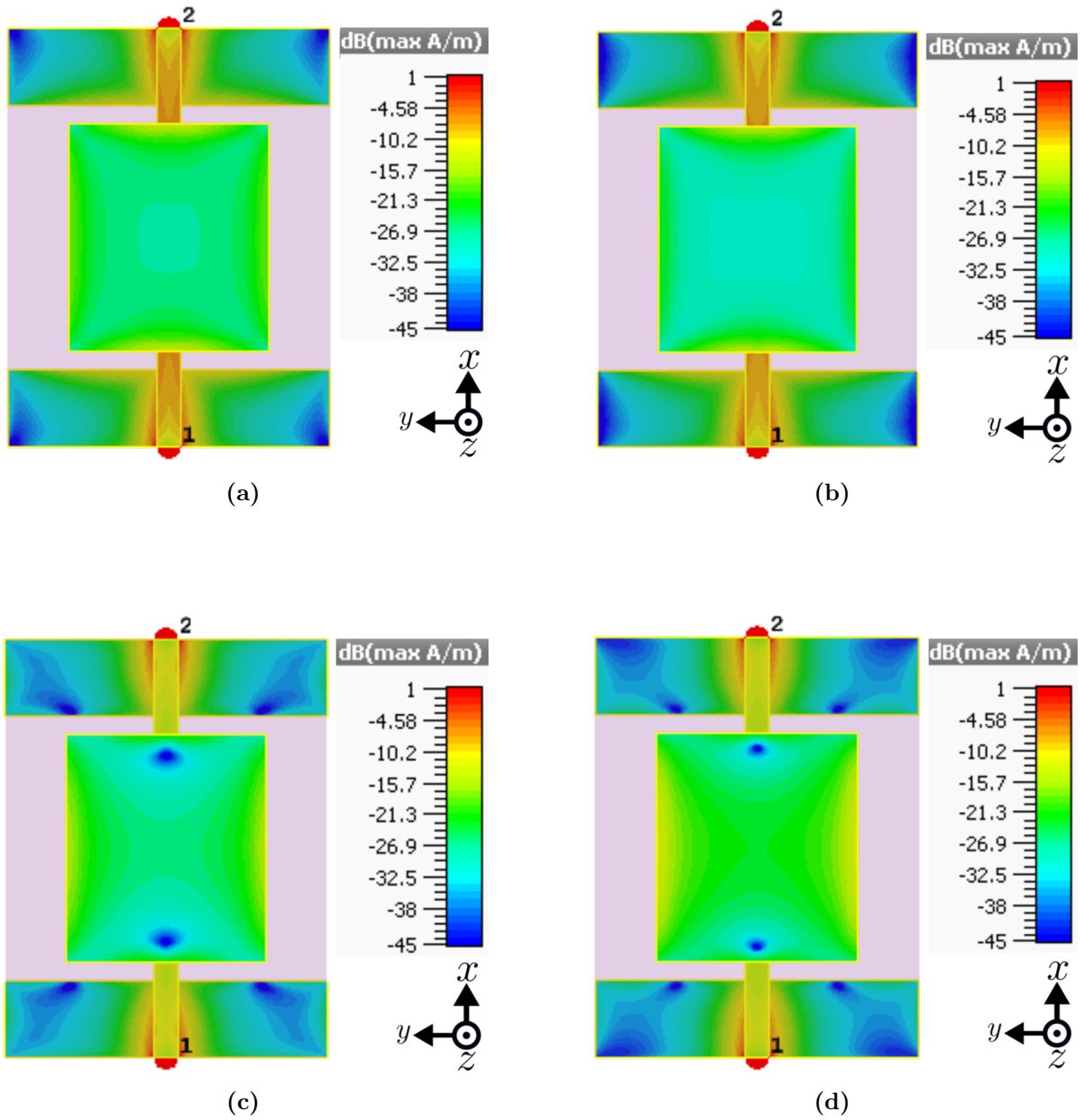


Figure 5.21. Simulated surface current on the two-port patch antenna at around (a) 2.414 GHz (b) 2.775 GHz (c) 4.215 GHz and (d) 4.956 GHz frequencies. The simulated TARC for this antenna is shown in Figure 5.6.

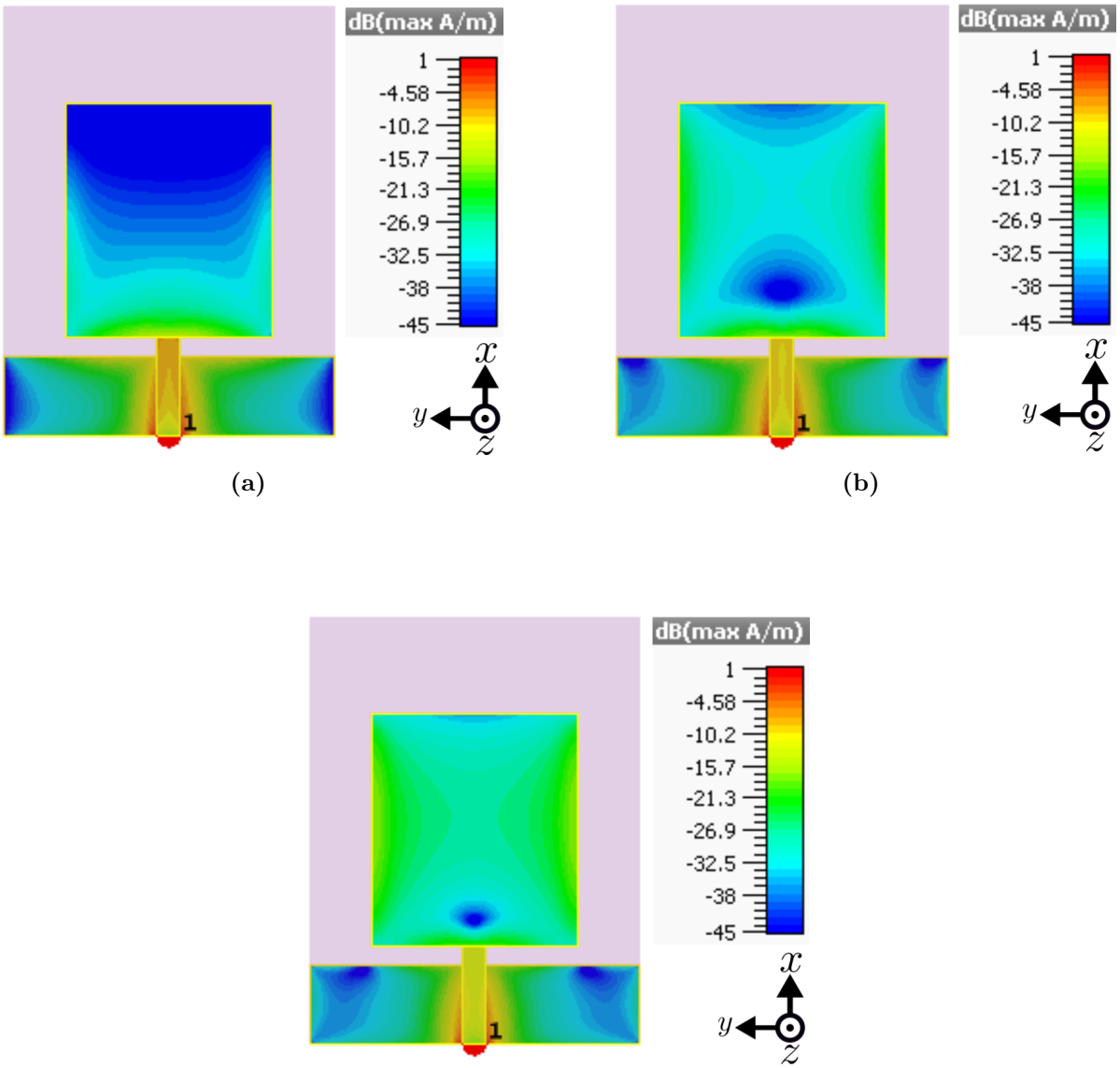


Figure 5.22. Simulated surface current on the single-port antenna in the (a) 3.150 GHz (b) 3.781 GHz and (c) 4.359 GHz frequencies. The simulated S_{11} for this antenna is shown in Figure 5.6.

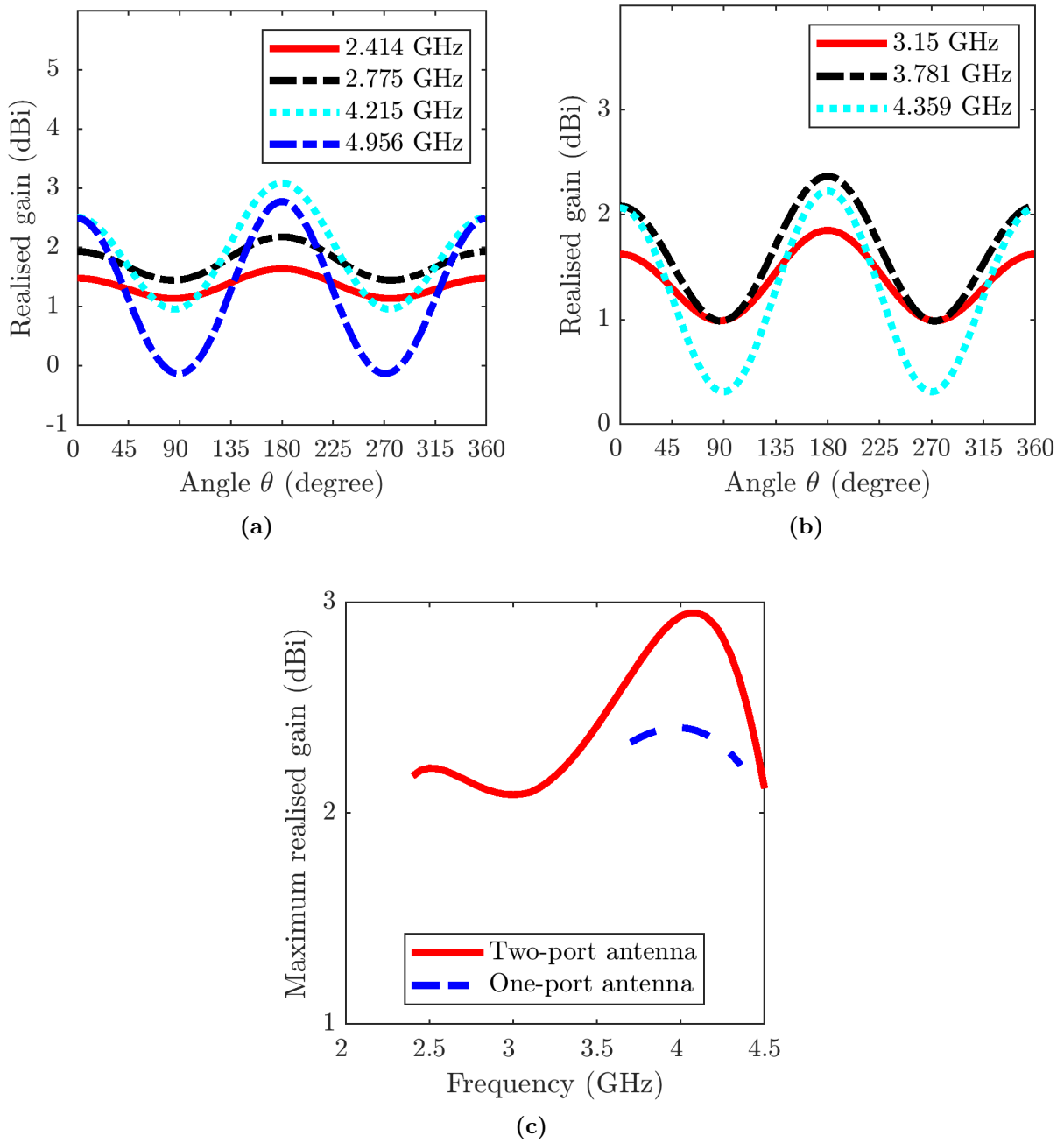


Figure 5.23. Simulated (a) H-plane ($\phi = 90°$) realised gain for the two-port injection matched patch antenna (b) H-plane ($\phi = 90°$) realised gain for the corresponding one-port patch antenna (c) H-plane ($\phi = 90°$) maximum realised gain for the two-port injection matched patch antenna and for the corresponding one-port patch antenna. The simulated TARC and S_{11} for the two antennas are shown in Figure 5.6.

at a 3.150 GHz lower boundary frequency, mode J_{01} is dominant while mode J_1 becomes dominant at a 4.359 GHz upper boundary frequency.

The two-port differentially excited antenna has the maximum realised gain of around 2.9 dBi at a 4.1 GHz frequency, as shown in Figure 5.23c. There is an improvement of gain of around 0.5 dB from the two-port antenna compared to the maximum gain of 2.4 dBi attained by the corresponding one-port antenna at around 4.0 GHz frequency, as shown in Figure 5.23c, because of driving the antenna from two ports. Also, the two-port antenna has a lower gain (of around 2.2 dBi) than the corresponding one-port antenna at the lower boundary frequencies of 2.4 and 3.7 GHz, respectively, as shown in Figure 5.23a and 5.23b, because of excitation of mode J_{01} by the two-port antenna, which is of a slightly lower order than mode J_1 that is excited by the corresponding one-port antenna at these frequencies. However, the lowest realised gain by the two-port antenna is observed at a 3.0 GHz frequency because of the intersection between the two modes around this frequency. Also, the realised gain for the two-port antenna is fairly stable at 2.414 and 2.775 GHz frequencies (with a gain reduction of around 0.5 dB between the two frequencies) than at 4.215 and 4.956 GHz frequencies, as shown in Figure 5.23a, because of excitation of mode J_{01} of the antenna at a 2.775 GHz resonant frequency, which is more stable than mode J_1 excited at 4.215 GHz resonant frequency. On the other hand, there is a significant variation in the gain attained by the corresponding one-port antenna, as shown in Figure 5.23b, because of driving the antenna from a single port. Generally, the two-port antenna's realised gain is improved compared to the gain of the corresponding one-port antenna due to driving the antenna from two ports.

The measured co-polar patterns for the two-port injection matched antenna largely deviate from the simulated ones, as shown in Figure 5.24, because of the residual currents

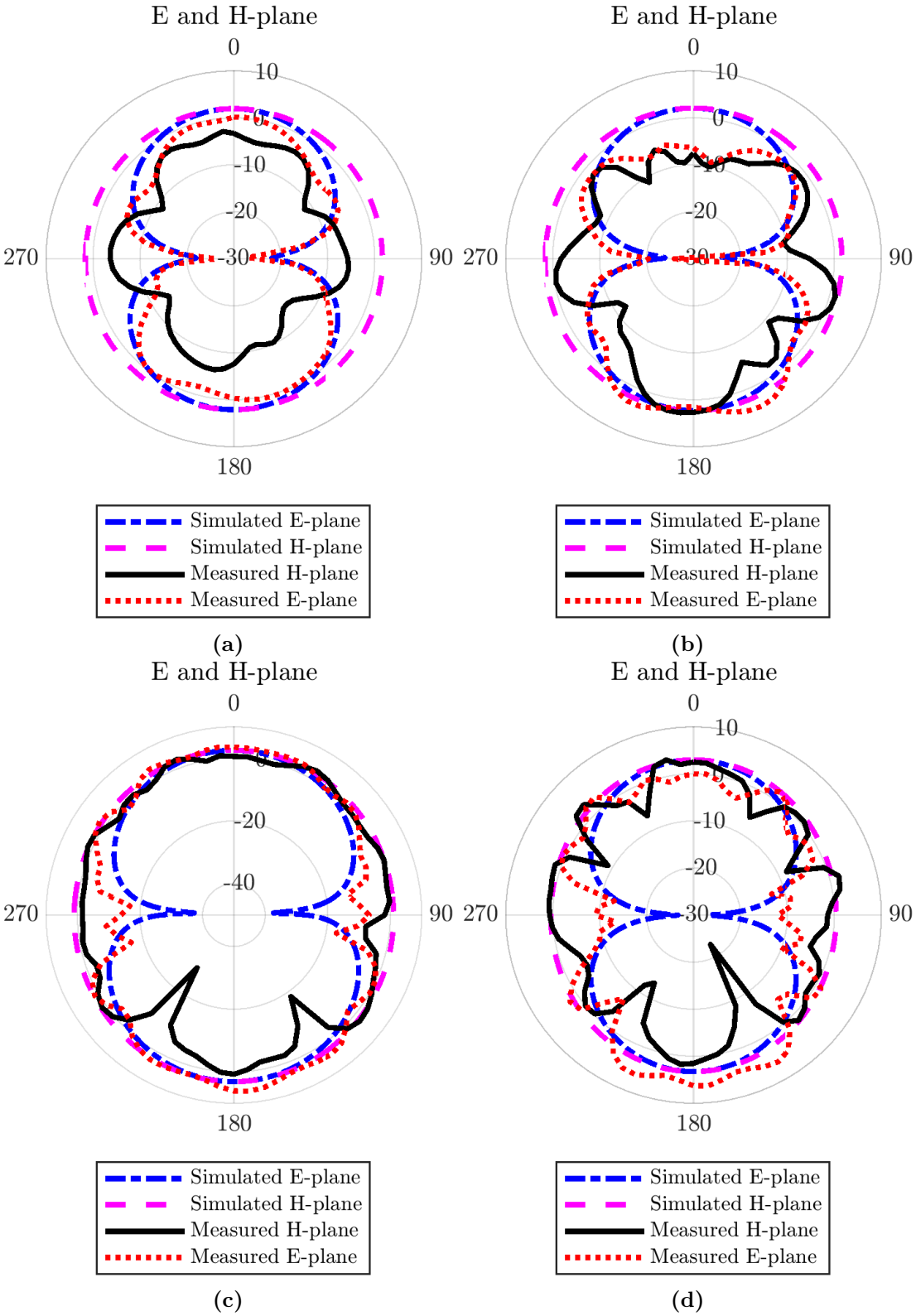


Figure 5.24. Simulated and measured co-polar patterns for the differentially excited two-port injection matched antenna in the (a) 2.414 and 2.353 GHz (b) 2.775 and 2.638 GHz (c) 4.215 and 3.635 GHz (d) 4.956 and 4.015 GHz frequencies, respectively. The simulated and printed antennas are shown in Figure 5.6 and 5.16, respectively.

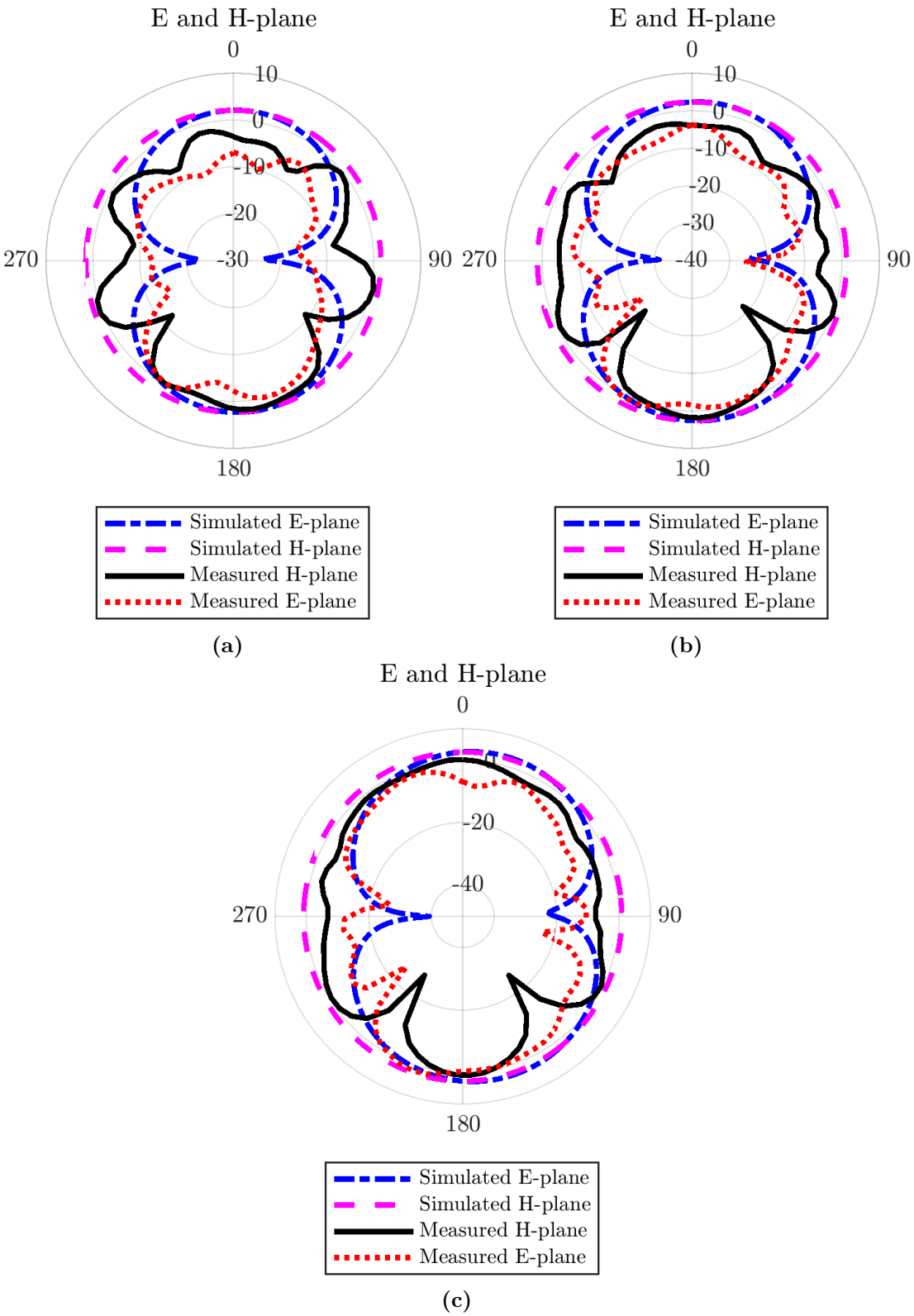


Figure 5.25. Simulated and measured co-polar patterns for the one-port antenna in the (a) 3.150 and 2.733 GHz (b) 3.781 and 3.065 GHz (c) 4.359 and 3.73 GHz frequencies, respectively. The simulated and printed antennas are shown in Figure 5.6 and 5.16, respectively.

on the SMA connectors and the outer shield of the feeding coaxial cables during measurement. Though ferrite beads (shown in Figure 4.35) were used during the experiment, the effect of residual currents could not be eliminated completely. Because of the small size of the PGPs, the leakage currents caused spurious radiation across the entire frequency range of investigation. Also, the measured co-polar patterns for the corresponding one-port antenna shown in Figure 5.25 were affected by the same factors. However, the nulls on the measured E-plane ($\phi = 0°$) patterns for the two-port injection matched antenna shown in Figure 5.24a and 5.24b exhibit good agreement with the simulations, indicating that the injection matching technique is verified. Generally, the simulated H-plane ($\phi = 90°$) co-polar radiation patterns for the two-port injection matched antenna and the corresponding one-port antenna (shown in Figure 5.24 and 5.25) are approximately omnidirectional, showing that the two antennas essentially operate as dipole and monopole patch antennas, respectively.

Despite the deviations between the measured and simulated TARC and between the measured and simulated radiation patterns, the injection matching technique has been validated experimentally to a reasonable degree.

5.4 Summary

It has been shown in this chapter that the excitation of multiple characteristic modes of the patch antenna leads to a wide bandwidth and high efficiency.

A -10 dB FBW higher than 69% has been attained from a two-port patch antenna through excitation of two characteristic modes (J_{01} and J_1) of the antenna by using the

injection matching technique. A radiation efficiency higher than 99% was also achieved from the two-port injection matched antenna.

The FBW of the validated two-port injection matched antenna in this chapter is around 69.5%, spanning between 2.403 and 4.964 GHz frequencies. In contrast, the FBW for the antenna that was not validated because of the unavailability of standard thickness substrates is around 85.2%, spanning from 2.326 to 5.775 GHz frequencies. Also, because of the excitation of modes J_{01} and J_1 of the antennas, both antennas have approximately omnidirectional H-plane ($\phi = 90°$) radiation patterns, allowing them to be used for the 5G and dynamically shared wireless services in the Sub-6 GHz high-band with the advantage of promoting the surrounding transmission and reception of signals.

Chapter 6

Tunable injection matched antennas

6.1 Background

It was shown in Chapter 4 that the frequency tuning of the two-port injection matched antenna is based on the switching of the excitation modes of the antenna between differential and common modes. Also, it was shown that the broadbanding of TARC resonance obtained through differential excitation reduces the bandwidth attained by the same antenna through the common mode excitation because of the limited number of feed points supported by the injection matching technique.

In this chapter, an outline investigation is made to bring the two TARC resonances close to each other so that the two-port injection matched antenna is progressively frequency tuned. The common mode excitation of the patch antenna is initially applied, and then the antenna is tuned to the differential mode excitation. Exciting the injection matched antenna through four ports is also discussed in Section 6.2. Besides, feeding the patch antenna from its corners to enhance the antenna bandwidth is discussed in Section 6.2.1.

6.2 Design, simulation and validation

Considering the bandwidth requirements for International Mobile Telecommunication services (IMT services) in 2.3 GHz, 3.5 GHz and 3.45 to 4.2 GHz, and Industrial, Scientific and Medical (ISM) services in 5 GHz frequency bands, a tunable antenna with -10 dB operational bandwidth spanning between 2.2 and 4.2 GHz, and 5.0 and 6.0 GHz will serve the purpose. Starting with a one-port antenna design at around 3.3 GHz, which is an approximately centre frequency for the 2.3 to 4.2 GHz frequency range, the desired bandwidth at this frequency range can be attained by broadening the one-port antenna resonance through the application of the injection matching technique. Also, the desired bandwidth in the 5.0 to 6.0 GHz frequency range can be obtained through the frequency tunability of the antenna.

Based on these requirements, a one-port proximity-fed patch antenna with the FGP is designed in CST MWS to operate at around 3.3 GHz frequency by following the procedure outlined in [85]. The antenna is realised on two layers of Rogers Duroid RT 5880 substrate with relative permittivity ε_r of 2.2, loss tangent of 0.0009, lower substrate height of 1.575 mm, upper substrate height of 0.787 mm, and copper cladding thickness of 0.035 mm. The antenna has patch length $L_p = 27.88$ mm, patch width $W_p = 23.57$ mm, substrate length $L_s = 55.76$ mm, substrate width $W_s = 47.14$ mm, width of feed line $w = 1.8$ mm and the distance of the coupled line from the centre of the patch is $d = 0.0$ mm. The antenna is excited through a discrete face port created on the outer end-face of the feed line while at the same time the impedance of the excitation signal is maintained at 50 Ω. To enhance the operational bandwidth, the patch antenna is converted to a monopole antenna by truncating the grounding plane, as shown in Fig-

ure 6.1a. The length of partial ground $L_g = 13.94$ mm, which is the maximum length of the ground plane for which a patch antenna is converted to a monopole antenna, was calculated from $L_g = (L_s - L_p)/2$.

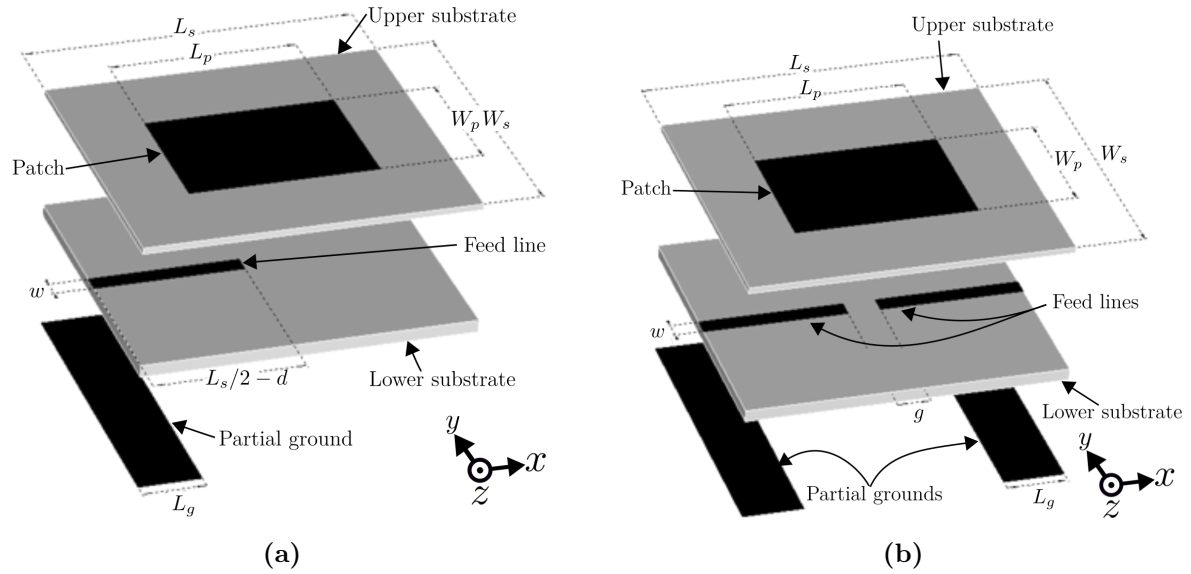


Figure 6.1. (a) Proximity-fed patch antenna with single feed line (b) proximity-fed patch antenna with two feed lines. The black colour indicates the layers of copper.

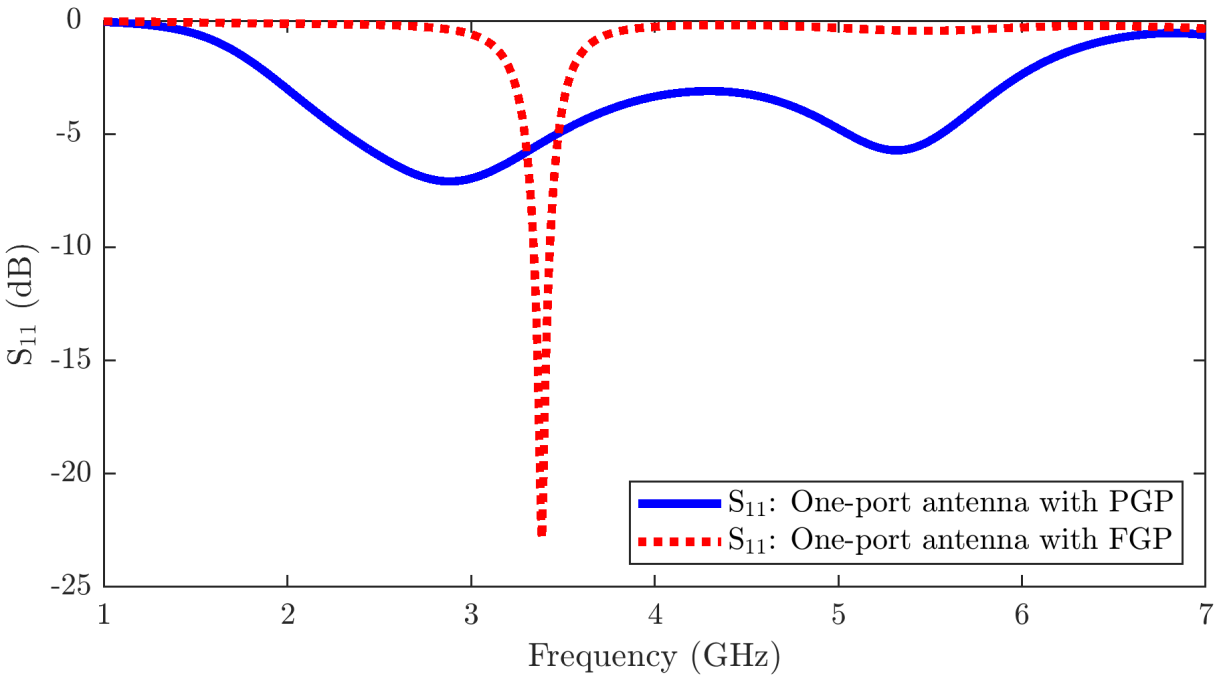


Figure 6.2. S-parameter for the one-port proximity-fed patch antenna under investigation.

The S-parameters for the one-port antennas resulting from these antenna dimensions are depicted in Figure 6.2. It can be seen in Figure 6.2 that the one-port antenna with PGP has an improved −3 dB bandwidth, and two modes at around 2.894 and 5.327 GHz frequencies, which are poorly matched. The lower mode resonance (2.894 GHz) for this antenna is fairly close to the design target (3.3 GHz) for the one-port antenna.

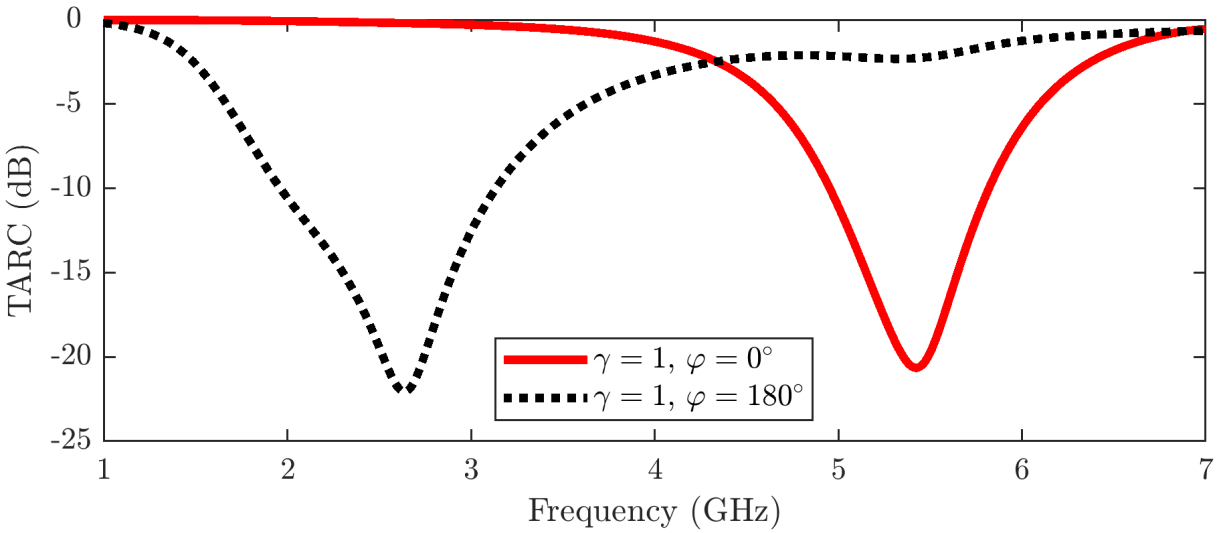
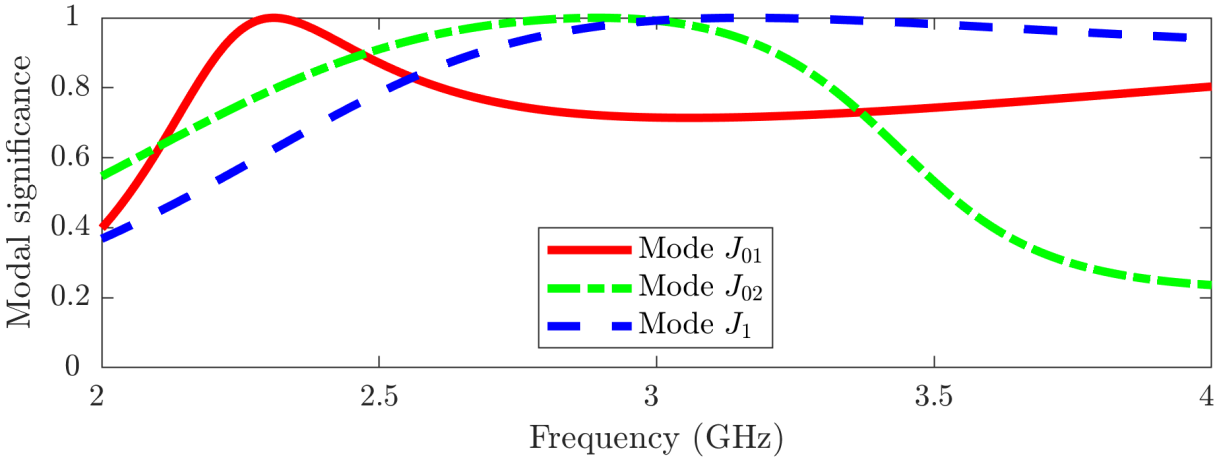


Figure 6.3. TARC resonances for the tunable two-port proximity-fed patch antenna derived from the one-port antenna with S-parameter resonance in Figure 6.2. The dimensions of this antenna are depicted by TARC0 in Table 6.1.

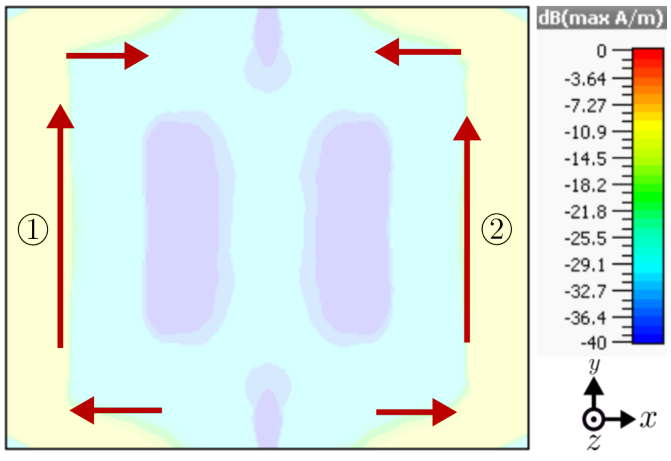
The two modes of the one-port antenna are tuned by applying the injection matching technique to the antenna in CST SS by following the procedure outlined in Appendix B.1. This is implemented in two stages: first, the one-port antenna with PGP is transformed into a two-port antenna by adding the second coupled feed line, separated with a gap $g = 2d$ from the first feed line, where d is measured from the centre of the patch, and a PGP corresponding to the second feed line, as shown in Figure 6.1b. The gap g is initially chosen to be $g = 1.2$ mm, but any value of g between 0.1 and 2.0 mm can be selected, which can later be adjusted by sweeping the parameter g in CST DS, between 0.1 and 2.0 mm. The second face port is created at the end-face of the second feed line. The

two-port antenna is then locked and simulated while the relative amplitude $\gamma = 1$ and phase shift $\varphi = 0°$ are configured at port two and tuned to $\gamma = 1$ and $\varphi = 180°$. The total active reflection coefficient (TARC) for the resulting tunable two-port injection matched antenna is shown in Figure 6.3.

It can be seen in Figure 6.3 that the impedance matching of the two characteristic modes of the one-port antenna is improved through the application of the injection matching technique to the antenna.



(a)



(b)

Figure 6.4. (a) Modal significance and (b) mode J_{02} surface current for the antenna whose TARC is shown in Figure 6.3. The surface currents for modes J_{01} and J_1 are similar to the ones shown in Figure 4.6. The CMA was conducted in CST MWS using a Multilayer Solver with solver and mesh settings provided in Appendix B.2.

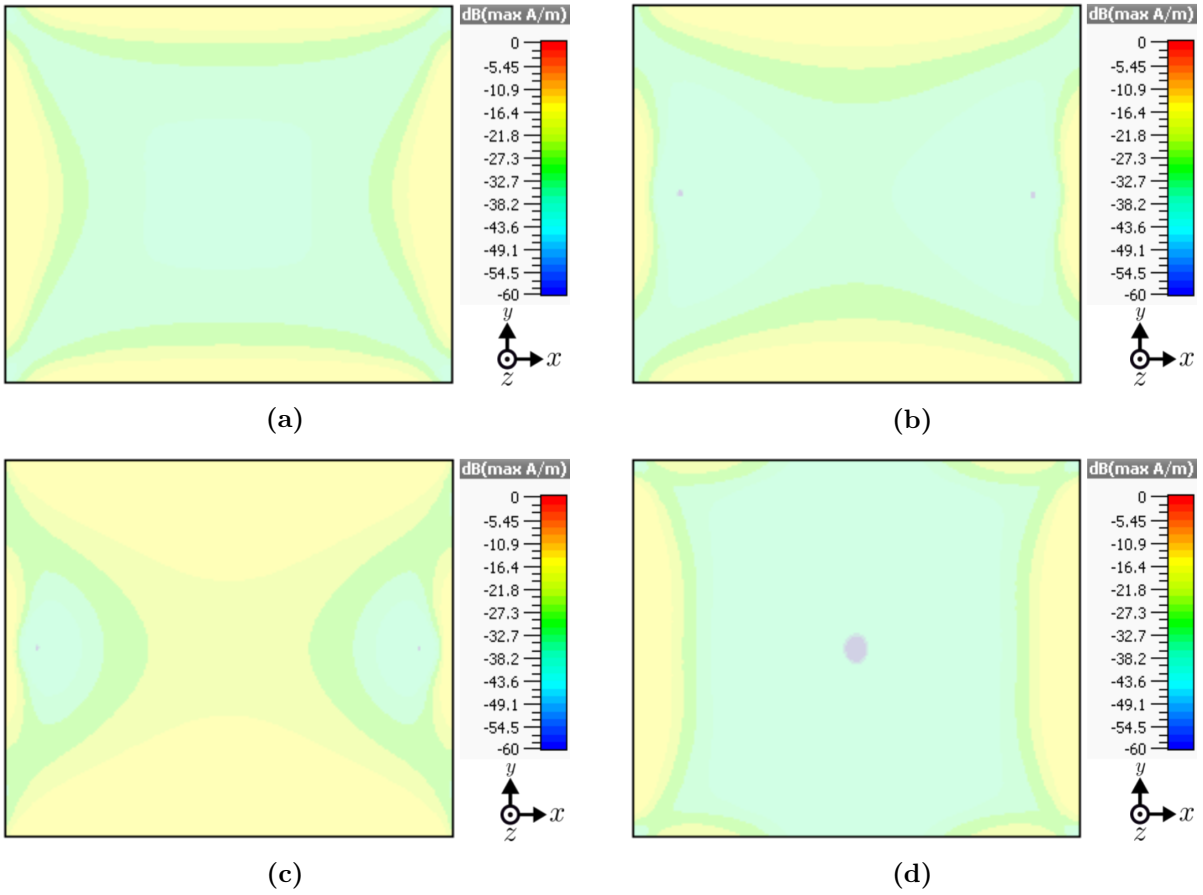


Figure 6.5. Simulated surface current at (a) 1.963 GHz (b) 2.639 GHz (c) 3.134 GHz and (d) 5.427 GHz frequencies resulting from the differential and common mode excitations of the antenna under investigation whose modal significance is shown in Figure 6.4a.

Also, the three characteristic modes shown in Figure 6.4a are excited by the two-port antenna excitations. Modes J_{01} and J_1 are excited through the differential excitation applied to the antenna. This is indicated by comparing the surface currents resulting from the differential excitation of the antenna at 1.963, 2.639 and 3.134 GHz frequencies shown in Figure 6.5 with modes J_{01} and J_1 currents shown in Figure 4.6. The surface current at 1.963 GHz frequency shown in Figure 6.5a fairly aligns with the mode J_{01} current shown in Figure 4.6a, indicating the excitation of mode J_{01} at this frequency. However, both features of modes J_{01} and J_1 currents (shown in Figure 4.6) are observed at 2.639 and 3.134 GHz frequencies, as shown in Figure 6.5b and 6.5c, indicating the joint

excitation of modes J_{01} and J_1 at the two frequencies. These observations indicate the high correlation between modes J_{01} and J_1 currents of the antenna under investigation.

On the other hand, the surface current for the two-port antenna resulting from the common mode excitation of the antenna at a 5.427 GHz resonant frequency shown in Figure 6.5d fairly aligns with the fundamental mode J_{02} current shown in Figure 6.4b. This observation indicates the excitation of mode J_{02} of the antenna at this frequency.

However, the bandwidths provided by the two TARC resonances shown in Figure 6.3 are displaced from the design specifications and are significantly insufficient to meet the specified design requirement. The higher mode resonance for the one-port antenna is shifted from 5.348 to 5.427 GHz frequency through the common mode excitation as a result of adding the second feed line. In contrast, the lower mode is shifted from 2.884 to 2.639 GHz frequency through the differential mode excitation applied to the antenna because of the same factor. This trend shows that taking the differential mode resonance from 2.639 to 3.3 GHz frequency will shift the common mode resonance to a frequency higher than 5.427 GHz. Because of this behaviour, it is not possible to bring the two modes close to each other to achieve the two design requirements or achieve a progressive frequency tuning. The remaining option is to achieve one of the design requirements and provide part of the bandwidth needed by the second design goal.

The common mode TARC resonance shown in Figure 6.3 has the -10 dB FBW of around 16.0% (calculated using Equation (B.1) in Appendix B.4) at a 5.387 GHz centre frequency, while the differential mode TARC has FBW of around 45.9% at a 2.548 GHz centre frequency, as depicted in Table 6.2. The high FBW attained by the differential TARC is attributed to the excitation of modes J_{01} and J_1 of the antenna. The ratio between the two TARC resonances is around $f_{\mathrm{dm}} : f_{\mathrm{cm}} = 1 : 2$, where $f_{\mathrm{dm}} = 2.639$ GHz

and $f_{\mathrm{cm}} = 5.427$ GHz are the differential mode and common mode TARC resonances for the two-port injection matched antenna, respectively. It is assumed that the ratio $f_{\mathrm{dm}} : f_{\mathrm{cm}}$ remains constant for the two-port antenna under investigation. Based on this assumption, to have a differential mode resonance at around 3.3 GHz, a common mode TARC resonance is needed at around 6.6 GHz. The (common mode TARC) resonance at around 6.6 GHz is attained by optimising the antenna dimensions L_p, W_p, L_s, W_s, L_g, w and g in CST DS between 20 and 28 mm, 16 and 24 mm, 38 and 56 mm, 38 and 48 mm, 7 and 13.94 mm, 1.6 and 4.1 mm, 0.1 and 5.0 mm, respectively, while the common mode TARC is monitored around the same frequency. Typical converged results for this optimisation are shown in Figure 6.6, and their corresponding dimensions are shown in Table 6.1.

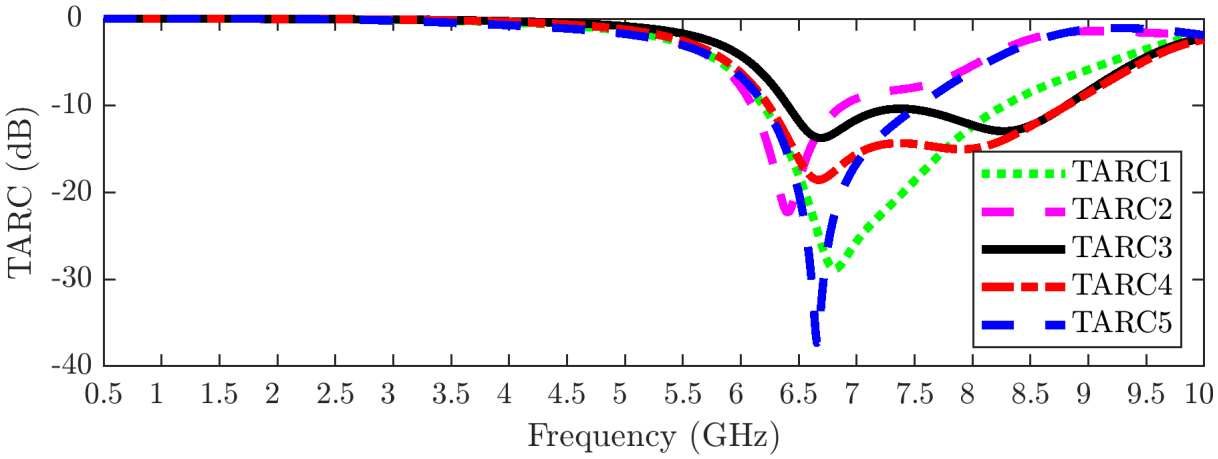


Figure 6.6. Optimised common mode TARC for the two-port proximity-fed injection matched patch antenna under investigation at different antenna dimensions depicted in Table 6.1.

All the common mode TARC resonances in Figure 6.6 have good impedance matching, though with different bandwidths. To decide which TARC meets the design requirements, the bandwidths provided by the TARC resonances resulting from the differential and common mode excitations, depicted in Figure 6.6, are investigated in Table 6.2. It is

Table 6.1. Dimensions for the optimised TARC resonances shown in Figure 6.6.

Simulation ID	Antenna dimensions (mm)						
	L_p	W_p	L_s	W_s	L_g	w	g
TARC0	27.88	23.57	55.76	47.14	13.94	1.8	1.2
TARC1	20.1	17.6	40.4	41.0	9.7	2.7	3.2
TARC2	24.7	16.2	41.0	39.5	8.9	2.43	4.1
TARC3	21.3	16.7	38.7	39.3	9.5	2.52	4.2
TARC4	20.8	16.5	39.2	40.5	9.7	3.1	3.7
TARC5	23.9	18.1	42.3	41.1	8.0	2.3	4.3

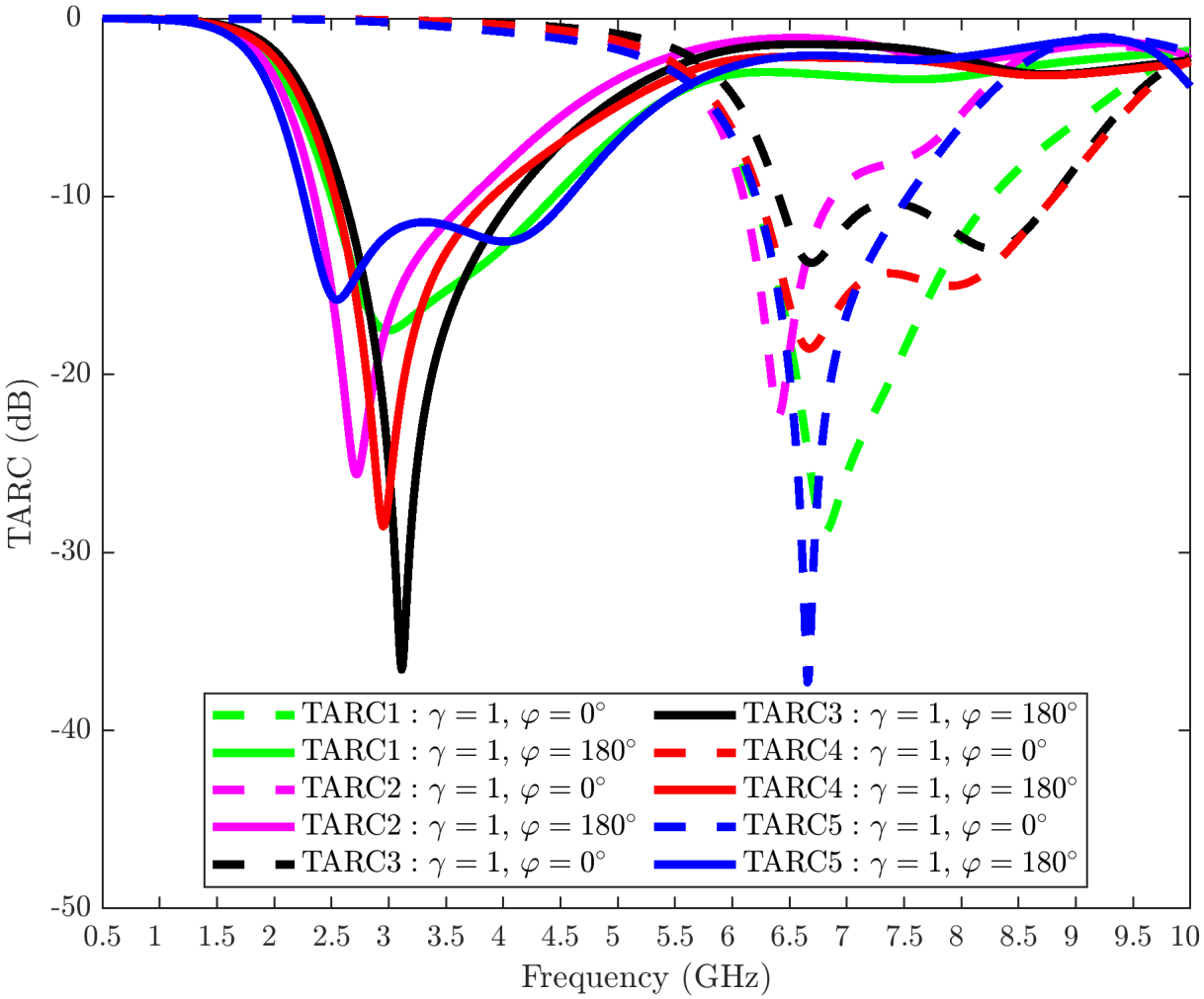


Figure 6.7. Differential and common mode TARC resonances for the tunable two-port proximity-fed patch antenna under investigation at different antenna dimensions depicted in Table 6.1.

Table 6.2. Calculated FBW for the tunable injection matched patch antennas with resonances depicted in Figure 6.7, where f_{LB}, f_{UB} and f_c are the −10 dB lower boundary, upper boundary, and centre frequencies, respectively.

Simulation ID	$\gamma = 1$ and $\varphi = 0°$				$\gamma = 1$ and $\varphi = 180°$			
	f_{LB} (GHz)	f_{UB} (GHz)	f_c (GHz)	FBW	f_{LB} (GHz)	f_{UB} (GHz)	f_c (GHz)	FBW
TARC0	4.956	5.818	5.387	0.160	1.963	3.134	2.548	0.459
TARC1	6.1925	8.2707	7.2316	0.287	2.4995	4.4428	3.4712	0.660
TARC2	6.0973	6.8825	6.4899	0.121	2.3507	3.73	3.0404	0.454
TARC3	6.4059	8.8073	7.6066	0.316	2.6092	4.0963	3.3528	0.444
TARC4	6.2395	8.8119	7.5257	0.342	2.5343	3.9034	3.2189	0.425
TARC5	6.2058	7.5362	6.871	0.194	2.2572	4.572	3.4146	0.678

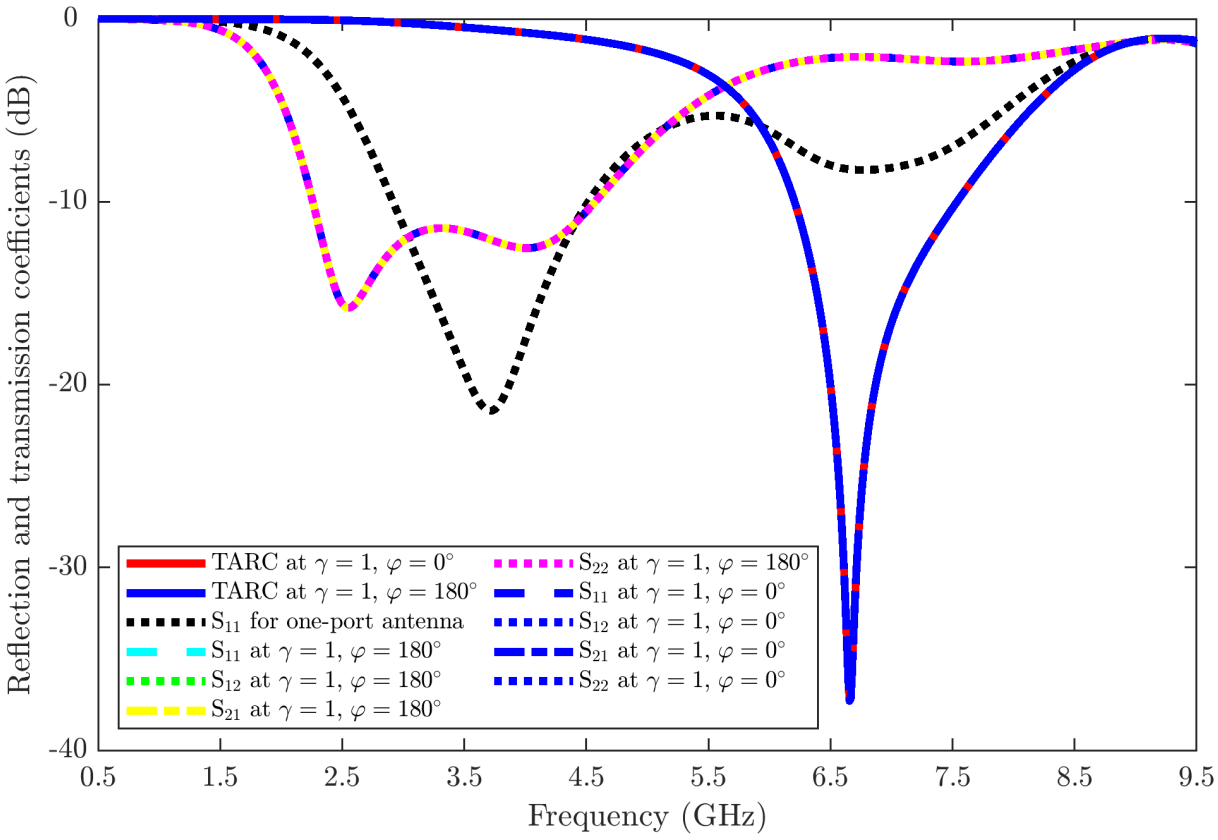


Figure 6.8. The TARC (TARC5) resonances, individual port reflection coefficients, and transmission coefficients between the two ports for the tunable two-port injection matched antenna in comparison to the S-parameter for the corresponding one-port antenna. The dimensions for the two antennas are depicted by TARC5 resonance in Table 6.1.

shown in Table 6.2 that TARC5 resonance has the highest −10 dB differential mode FBW of around 67.8% spanning from 2.257 to 4.572 GHz, which provides the bandwidth needed by IMT services in the 2.3 to 4.2 GHz frequency range. However, the bandwidth needed by the ISM services in the 5.0 to 6.0 GHz frequency range cannot be provided by the common mode TARC5 resonance which has a −10 dB FBW of around 19.4% spanning from 6.206 to 7.536 GHz. The optimisation goal for TARC cannot contain the two excitation modes (differential and common mode) simultaneously, making it impossible to control the two TARC resonances in CST DS. The TARC5 resonance is also depicted in Figure 6.8, where it is compared with S_{11}, S_{21}, S_{12}, and S_{22} for the realised two-port antenna, and S_{11} for the corresponding one-port antenna. It is shown in Figure 6.8 that the S_{11}, S_{21}, S_{12}, and S_{22} for the two-port antenna are equal to the TARC resonance because of the symmetry between the two feed points.

The CMA of the antenna whose TARC resonance is depicted in Figure 6.8 is provided in Figures 6.9 through 6.11. The analysis was conducted in CST MWS using a Multilayer Solver with solver and mesh settings provided in Table B.1 and B.2 in Appendix B.2. The modal significance for the first six resonant modes is plotted in a 2 to 8 GHz frequency range in Figure 6.9. It is shown in Figure 6.9 and 6.10a that mode one is an inductive fundamental mode J_{01}, having the principal current forming a single horizontally directed closed loop on the patch. An effective excitation of mode one (which is mode J_{01}) is achieved through a pair of differential excitations delivered at the maxima positions 1 and 2 from the two short patch edges, shown in Figure 6.10a, to enable a resonance at around 2.546 GHz with good impedance matching, as shown in Figure 6.8. The H-plane ($\phi = 90°$) radiation patterns resulting from excitation of mode J_{01} are approximately omnidirectional, as shown in Figure 6.34b and 6.37a at a 2.546 GHz resonant frequency,

as predicted by mode J_{01} patterns in Figure 4.7a and 4.13a. However, at the same frequency, the E-plane ($\phi = 0°$) patterns have two nulls in the directions $\theta = 90°$ and $\theta = 270°$ (shown in Figure 6.34b) as a result of feeding the antenna at these locations.

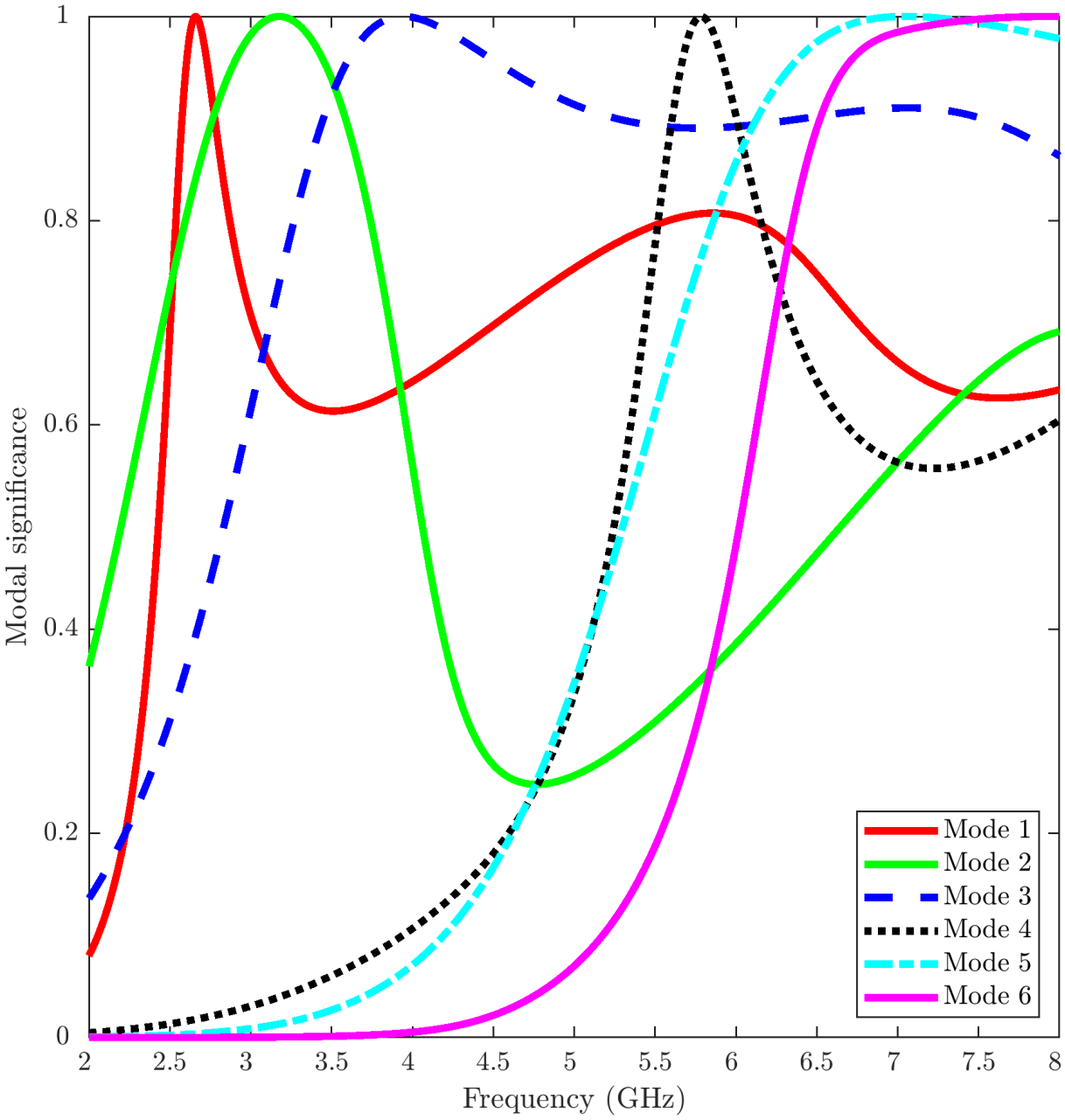


Figure 6.9. The modal significance for the first six resonant characteristic modes of the proximity-fed patch antenna whose TARC resonances are depicted in Figure 6.8 and 6.12.

Also, a horizontal mode three (which is mode J_1) shown in Figure 6.9 and 6.10c, is excited by applying two differential excitations on the antenna at the two short patch

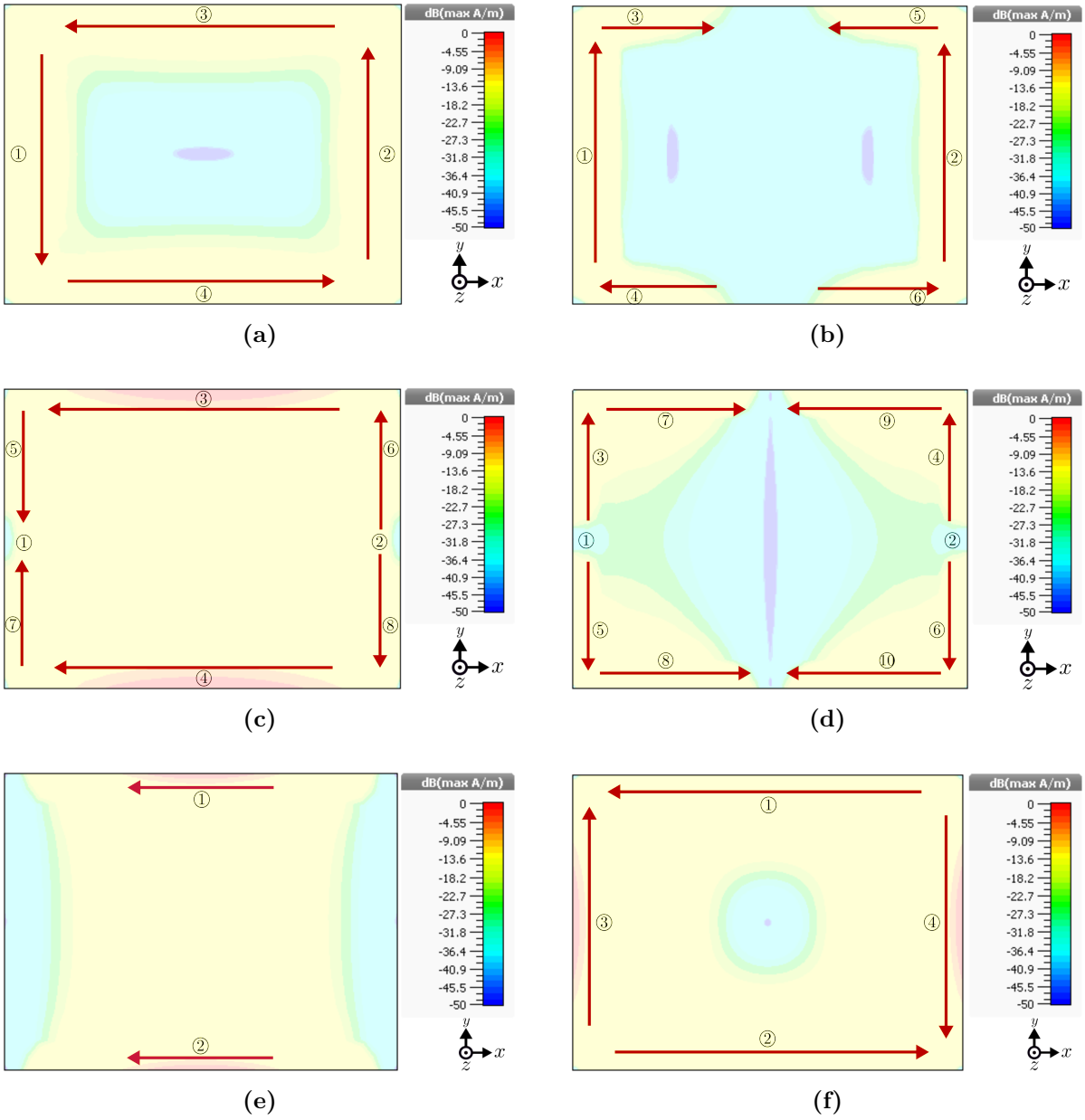


Figure 6.10. Characteristic surface current for (a) mode one at 2.660 GHz frequency (b) mode two at 3.176 GHz frequency (c) mode three at 3.938 GHz frequency (d) mode four at 5.786 GHz frequency (e) mode five at 7.052 GHz frequency (f) mode six at 7.934 GHz frequency for the patch antenna whose TARC resonances are depicted in Figure 6.8 and 6.12, and modal significance shown in Figure 6.9.

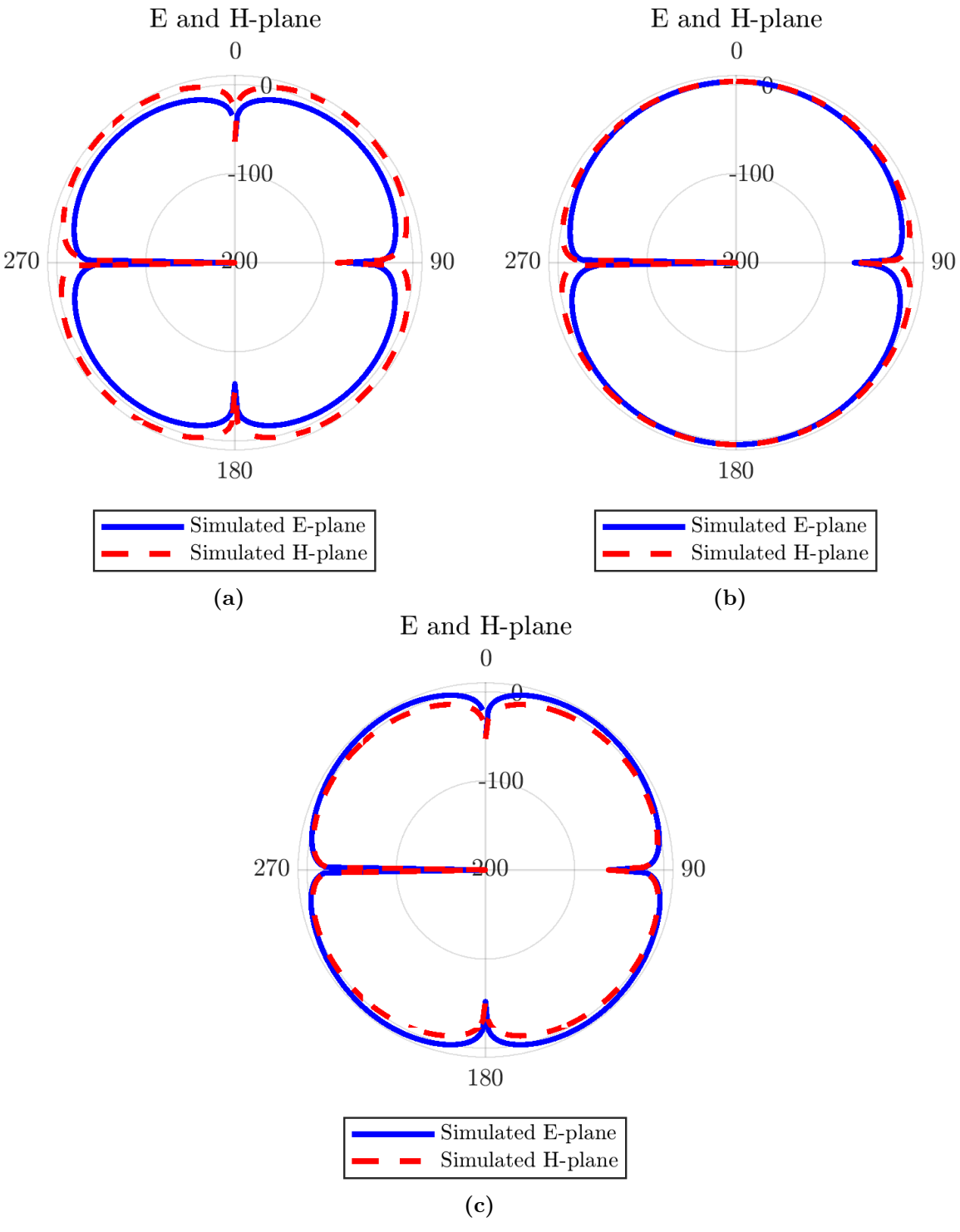


Figure 6.11. Characteristic directive radiation patterns for (a) mode four at 5.786 GHz (b) mode five at 7.052 GHz and (c) mode six at 7.934 GHz frequency for the patch antenna whose TARC resonance is depicted in Figure 6.8, and modal significance shown in Figure 6.9. The eigenpatterns for modes J_{01}, J_1, and J_2 of this antenna are similar to the patterns shown in Figure 4.7.

edges at the maxima positions 5 and 6, and 7 and 8, as shown in Figure 6.10c and 6.12, to enable a resonance at around 3.812 GHz frequency. With this feeding arrangement, shown in Figure 6.13, mode J_{01} is also jointly excited with mode J_1 at around 2.570 GHz frequency to enable a wideband operation, as shown in Figure 6.12.

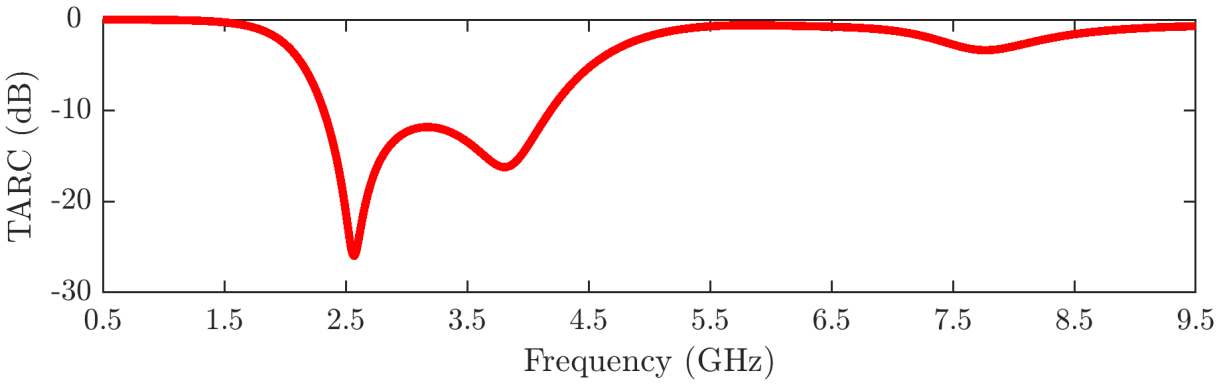


Figure 6.12. TARC resulting from excitation of mode J_{01} and J_1 of the patch antenna under investigation through two pairs of differential excitations delivered at the opposite short patch edges at the current maxima positions 5 and 6, and 7 and 8 of mode J_1, as shown in Figure 6.10c with $w = 0.7$ mm and $g = 4.29$ mm for each pair of the feed lines, while $L_p = 23.9$, $W_p = 18.1$, $L_s = 42.3$, $W_s = 41.1$, and $Lg = 8.0$ mm. The modified antenna layer two is shown in Figure 6.13.

Alternatively, differentially feeding the antenna at the maxima positions 1 and 2 for mode J_{01} also excites mode J_1 at around 4.060 GHz frequency with good -10 dB impedance matching, as shown in Figure 6.8 and 6.9. The H-plane ($\phi = 90°$) radiation patterns resulting from excitation of mode three (mode J_1), shown in Figure 6.34c and 6.37a at a 4.060 GHz resonant frequency are approximately omnidirectional, as predicted by mode J_1 patterns in Figure 4.7b and 4.13d. However, at the same frequency, the E-plane ($\phi = 0°$) patterns have two nulls in the directions $\theta = 90°$ and $\theta = 270°$ (shown in Figure 6.34c) as a result of feeding the antenna at these locations.

Also, mode four shown in Figure 6.9 and 6.10d is excited by two in phase driven excitations placed at the centre of the short patch edges 1 and 2 to enable a resonance at around 6.644 GHz frequency, as shown in Figure 6.8. The E and H-plane radiation

patterns resulting from excitation of mode four, shown in Figure 6.35b and 6.37c at a 6.644 GHz resonant frequency, have four lobes with two deep nulls in the directions $\theta = 0°$ and $\theta = 180°$ and two small nulls in the directions $\theta = 90°$ and $\theta = 270°$, as predicted by mode four patterns in Figure 6.11a.

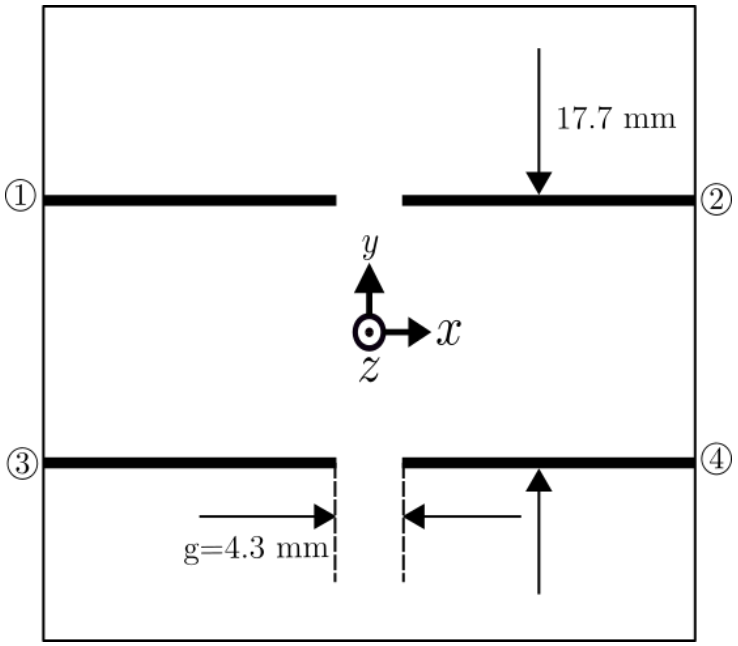
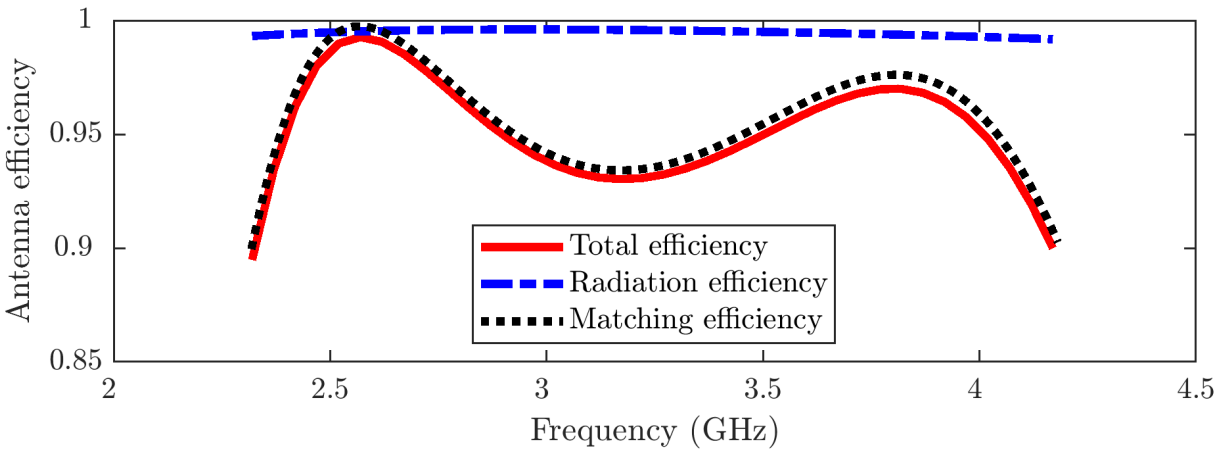


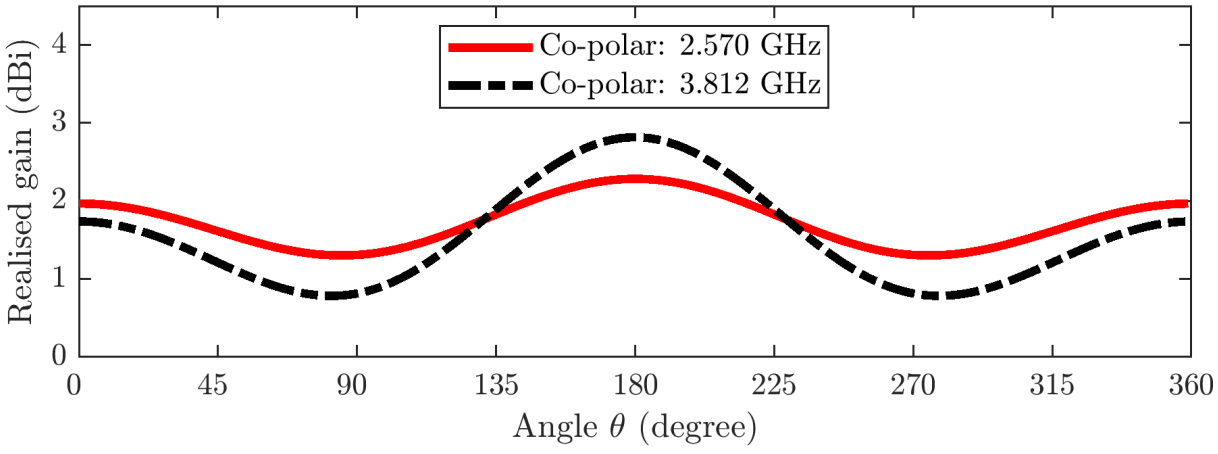
Figure 6.13. Layer two of the four-port proximity-fed patch antenna whose TARC resonance is depicted in Figure 6.12. The discrete face ports 1 through 4 are created at the outer ends of the feed lines at positions 1 through 4, respectively. Ports 1 and 2, as well as ports 3 and 4 excitations, are differentially driven. The black colour indicates the copper layer, while the white colour indicates the substrate layer. Other antenna dimensions are $w = 0.7$ mm, $L_p = 23.9$, $W_p = 18.1$, $L_s = 42.3$, $W_s = 41.1$, and $Lg = 8.0$ mm.

However, other characteristic modes of the antenna shown in Figure 6.10b, 6.10e, and 6.10f are not excited from this antenna because they require feeding on either long patch edges or a combination of long and short patch edges, which are not achieved on this antenna because of no partial grounds below the long edges. This issue is in particular discussed in Section 6.2.1.

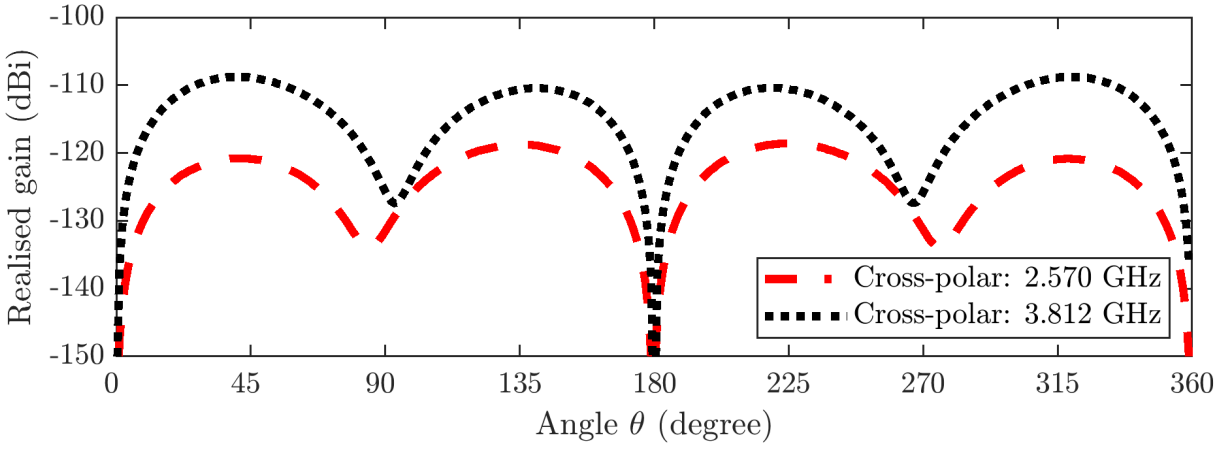
Hence, for the multiport antenna under investigation, there are two practical ways of exciting the modes—by feeding at the edges containing the maxima positions 1 and 2



(a)



(b)



(c)

Figure 6.14. Simulated (a) efficiency (b) H-plane ($\phi = 90°$) co-polar patterns (c) H-plane ($\phi = 90°$) cross-polar patterns for the four-port proximity-fed injection matched patch antenna whose TARC resonance is depicted in Figure 6.12.

shown in Figure 6.10a which excites modes one, three and four of the antenna, resulting in a tunable operation as shown by the TARC resonance in Figure 6.8, or by feeding at the edges containing the maxima positions 5 and 6, and 7 and 8 as shown in Figure 6.10c which excites modes one and three of the antenna, resulting in a wideband operation shown in Figure 6.12.

The -10 dB FBW attained by the four-port injection matched antenna whose TARC resonance is depicted in Figure 6.12 is around 57.4% at a 3.252 GHz centre frequency. This bandwidth is lower than the bandwidth of 67.8% attained by the corresponding two-port antenna through differential excitation, shown in Figure 6.8, and it cannot be tuned to meet the design goal. Also, the realised four-port antenna of Figure 6.12 has the radiation, matching and total efficiency higher than 99%, 90% and 89% (shown in Figure 6.14a), respectively, attributed to the excitation of two correlated modes J_{01} and J_1 of the antenna, use of low loss tangent ($\tan\delta = 0.0009$) and low dielectric constant ($\varepsilon = 2.2$) substrate material in the design and good impedance matching attained through the injection matching technique. At the two differential TARC resonances, the antenna attains a maximum gain of around 2.8 dBi in the direction $\theta = 180°$ at a 3.812 GHz resonant frequency, followed by the gain of around 2.3 dBi at a 2.570 GHz resonant frequency in the same direction, as shown in Figure 6.14b. The difference in realised gain at the two frequencies is attributed to the excitation of mode J_1 at 3.812 GHz, which is of a slightly higher order than mode J_{01}. The minimum gain for the two resonances remained fixed along $\theta = 90°$ and $\theta = 270°$ directions, indicating fair stability of the patterns. At these two resonant frequencies, the antenna has a H-plane ($\phi = 90°$) cross-polarised gain lower than -108 dBi, as shown in Figure 6.14c. These observations indicate the good performance of the realised four-port antenna. However, because of its potential

bandwidth, the two-port excitation is further investigated for the frequency tunability of the antenna.

Theoretical γ and φ plots

To investigate the possibility of achieving a progressive frequency tuning of the two-port antenna, the theoretical γ and φ variations with frequency for the antenna shown by TARC5 resonance in Figure 6.8 are plotted in Figure 6.15. It is shown in Figure 6.15b that the flat region in the theoretical γ variation at frequencies near 6.5 GHz coincides with the minimum of the theoretical φ variation at the same frequency, as depicted in Figure 6.15a. The correspondence between the two minima enables an injection matched operation at around 6.656 GHz, as depicted by the common mode TARC in Figure 6.8.

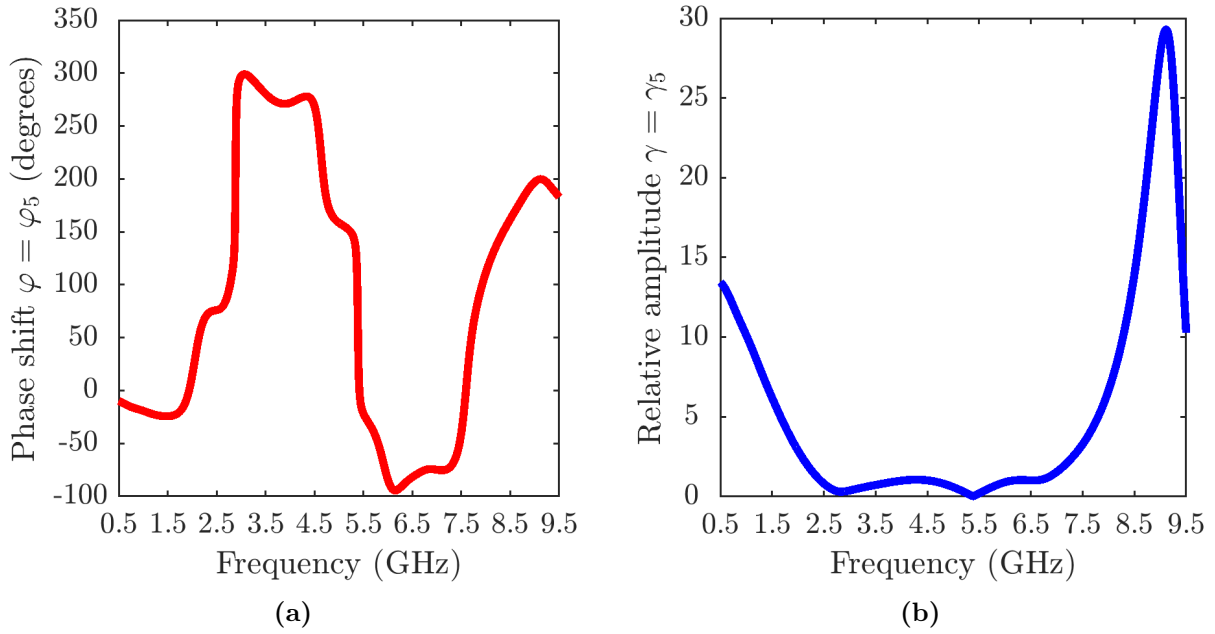


Figure 6.15. Variation of the theoretical (a) phase shift φ (b) relative amplitude γ with frequency across the two-port antenna with TARC5 resonances depicted in Figure 6.8.

Similarly, another injection matched operation at around 2.5 GHz is attributed to the correspondence between the minima of Figure 6.15b and 6.15a near the same frequency. Also, the minimum for the theoretical φ variation at around 4.0 GHz corresponds with

the fairly flat region in the γ variation near the same frequency. This correspondence forms another resonance at around 4.0 GHz, which merges with the 2.5 GHz resonance to enable wideband operation as depicted by the differential mode TARC in Figure 6.8.

Although the theoretical γ variation with frequency in Figure 6.15b is fairly constant at frequencies between 4.5 and 6.2 GHz, it is not possible to have injection matched operation between these frequencies because of the non-constant behaviour and nonexistence of the minima in the theoretical φ variation shown in Figure 6.15a at these frequencies. Because of these factors, it is impossible to have a progressive frequency tuning of the antenna under investigation from 2.3 to 7.5 GHz. This observation indicates that the injection matching technique can tune the two-port antenna at two different frequencies through differential and common mode excitations.

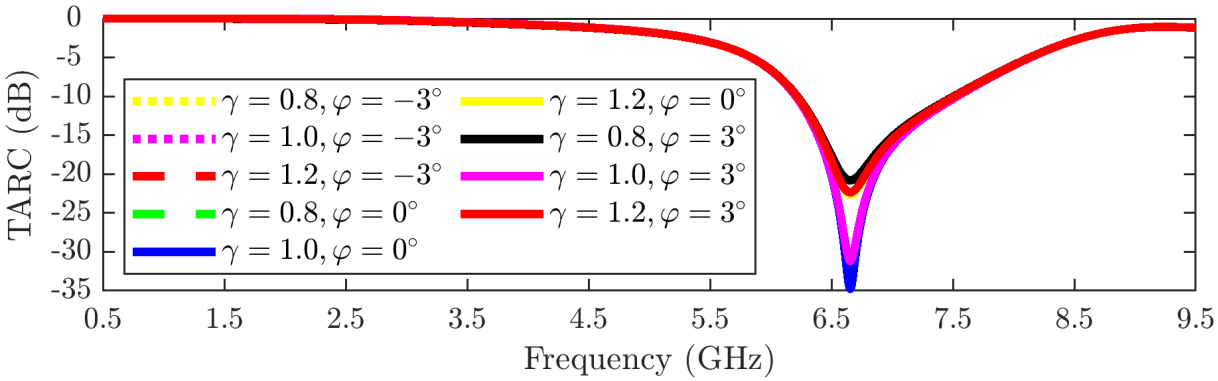


Figure 6.16. Typical common mode TARC resonances when γ and φ are varied in ranges of $0.8 \leq \gamma \leq 1.2$ and $-3° \leq \varphi \leq 3°$.

The common mode TARC fairly maintains its -10 dB FBW when $\gamma = 1 \pm 0.2$ and $\varphi = 0° \pm 3°$ are applied to the antenna, as shown in Figure 6.16 by the typical values of γ and φ derived from $0.8 \leq \gamma \leq 1.2$ and $-3° \leq \varphi \leq 3°$ optimisation domain. For the differential mode TARC, the -10 dB FBW is fairly maintained when $\gamma = 1 \pm 0.3$ and $\varphi = 180° \pm 5°$ are applied to the antenna as depicted in Figure 6.17 by γ and φ derived from $0.7 \leq \gamma \leq 1.3$ and $175° \leq \varphi \leq 185°$ optimisation domain.

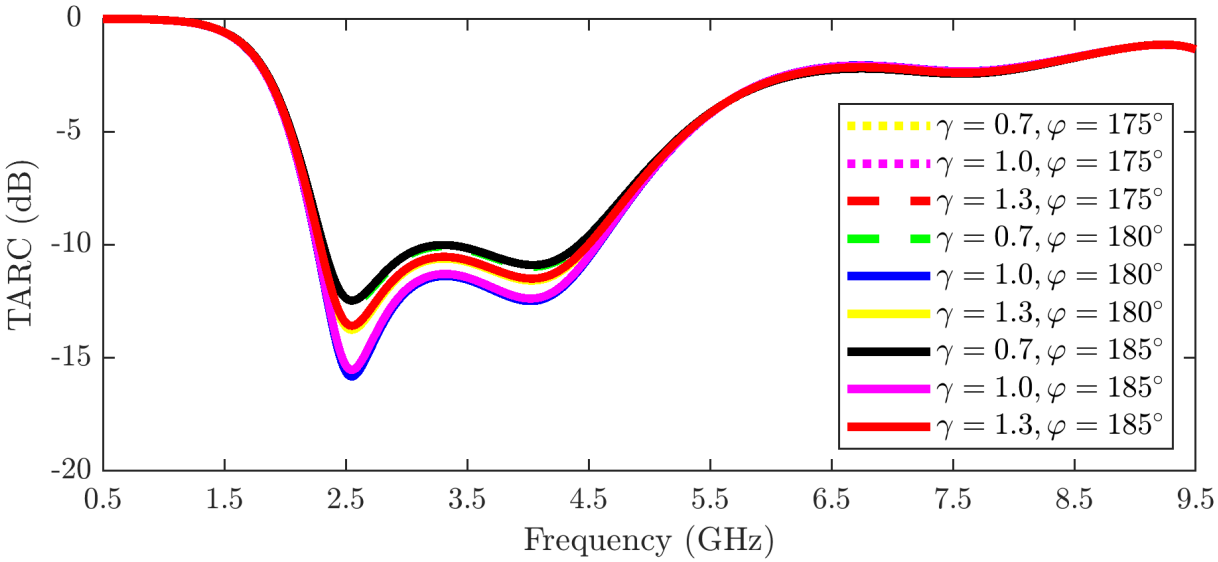


Figure 6.17. Typical differential mode TARC resonances when γ and φ are varied in ranges of $0.7 \leq \gamma \leq 1.3$ and $175° \leq \varphi \leq 185°$.

Because of the limitations posed by the theoretical γ and φ variations on the two-port patch antenna, a progressive frequency tuning by feeding the antenna along or parallel to the magnetic symmetry line of the antenna is not feasible. As such, another feeding mechanism of exciting a patch antenna from its two opposite corners is investigated in Section 6.2.1.

6.2.1 Feeding on two opposite corners of the patch

To allow the symmetrical feeding of the patch antenna from its opposite corners, the dimensions of the antenna are modified to form a square patch, as shown in Figure 6.18. Also, to preserve the electrical symmetry of the planar monopole antenna as discussed in Section 2.6.1, which is utilised in this thesis for bandwidth and performance enhancements of patch antennas, the two PGPs are maintained as shown in Figure 6.18a. The modal significance plot, modal surface currents and eigenpatterns for the resulting antenna are

provided in Figure 6.19, 6.20 and 6.21, respectively. Also, the Multilayer Solver and mesh settings used in generating these modes in CST MWS are provided in Table B.1 and B.2 in Appendix B.2.

At the corners 1 and 2 of the patch antenna shown in Figure 6.18b, modes one and five have differential principal currents, as shown in Figure 6.20a and 6.20e. On the other hand, modes two, three and four have in phase principal currents as shown in Figure 6.20b, 6.20c and 6.20d. Though the modal currents are not stronger at these corners, differentially driving the two excitations delivered at the two corners of the square patch as shown in Figure 6.18b enables multiband resonances at around 2.989 and 5.732 GHz frequencies, where the 2.989 GHz resonance has low impedance matching, as shown in Figure 6.23. These multiband resonances result from the excitation of modes one and five of the antenna, shown in Figure 6.20a and 6.20e. On the other hand, multiband resonances at around 2.946, 3.856, and 6.822 GHz frequencies, though the 6.822 GHz resonance is poorly matched, are attained by driving two in phase excitations at the corners of the patch using the same feeding mechanism shown in Figure 6.18b. These resonances result from the excitations of modes two, three and four of the patch antenna shown in Figure 6.20b, 6.20c and 6.20d. This observation shows that modes one through five of the antenna in Figure 6.18 can be excited through tuning of the phase shift φ at 0° and 180° while $\gamma = 1$ with fairly impedance matching of the few modes by driving the square patch antenna from its two opposite corners. However, only the 2.946, 3.856 and 5.732 GHz resonances attain the -10 dB FBWs, which are around 13.1%, 11.2% and 2.5% at 2.977, 3.824, and 5.734 GHz centre frequencies, respectively.

The three-dimensional (3D) patterns for the 2.946, 3.856 and 5.732 GHz resonances (resulting from excitation of modes two, three and five of the antenna shown in Fig-

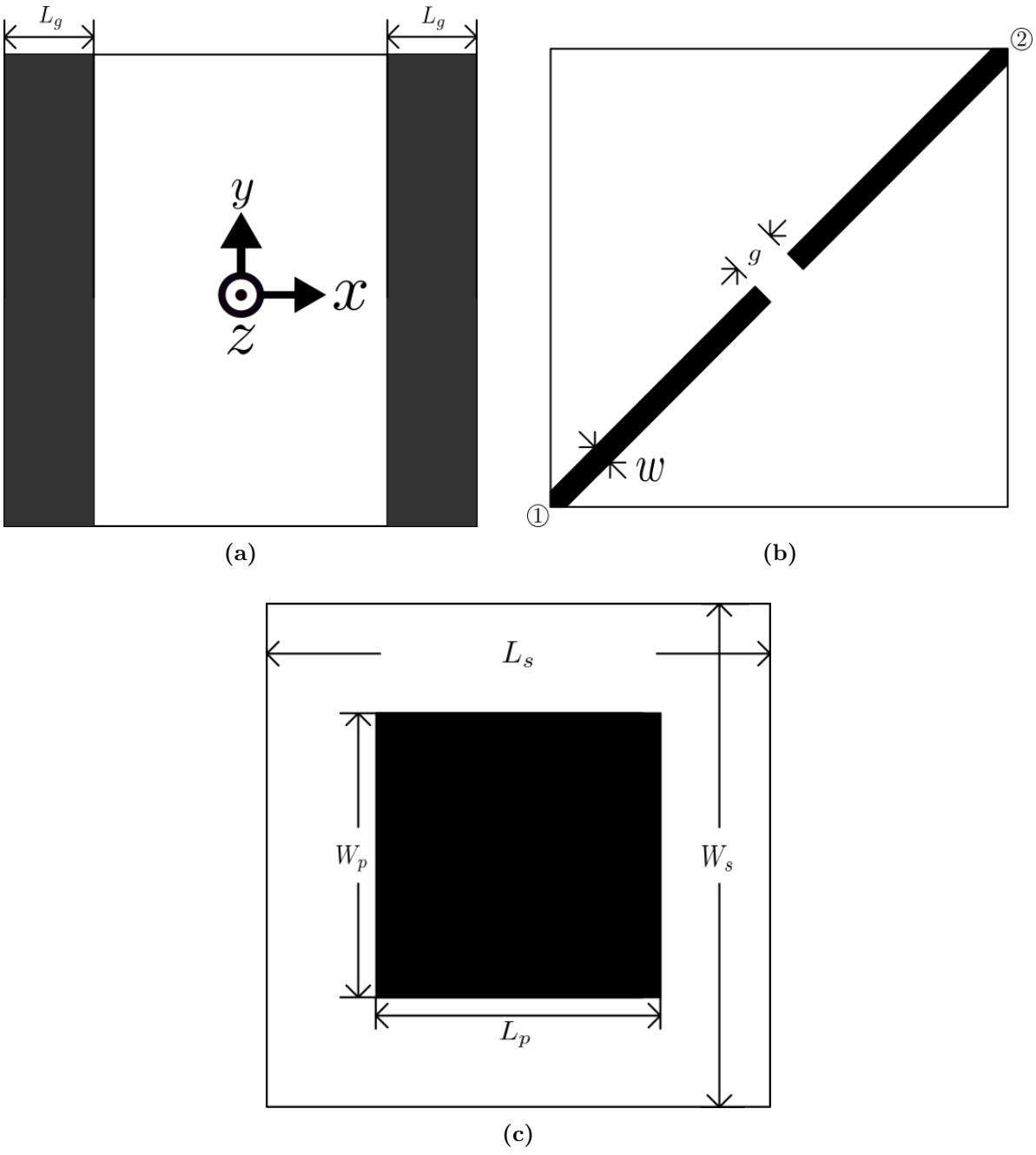


Figure 6.18. (a) Grounding planes (b) feed lines (c) patch for the square microstrip-fed patch antenna. The black colour indicates the layers of copper, while the white colour indicates the substrate layers. The antenna dimensions are $w = 3.6$, $L_p = W_p = 23.9$, $L_s = W_s = 42.3$, $g = 7.4$ and $L_g = 8$ mm, giving rise to the TARC resonances in Figure 6.23. The width, w and the gap, g at the attained TARC resonances were obtained through optimisation of w and g through parameter sweep in CST DS between 0.7 and 10 mm, and 0.1 and 33 mm, respectively.

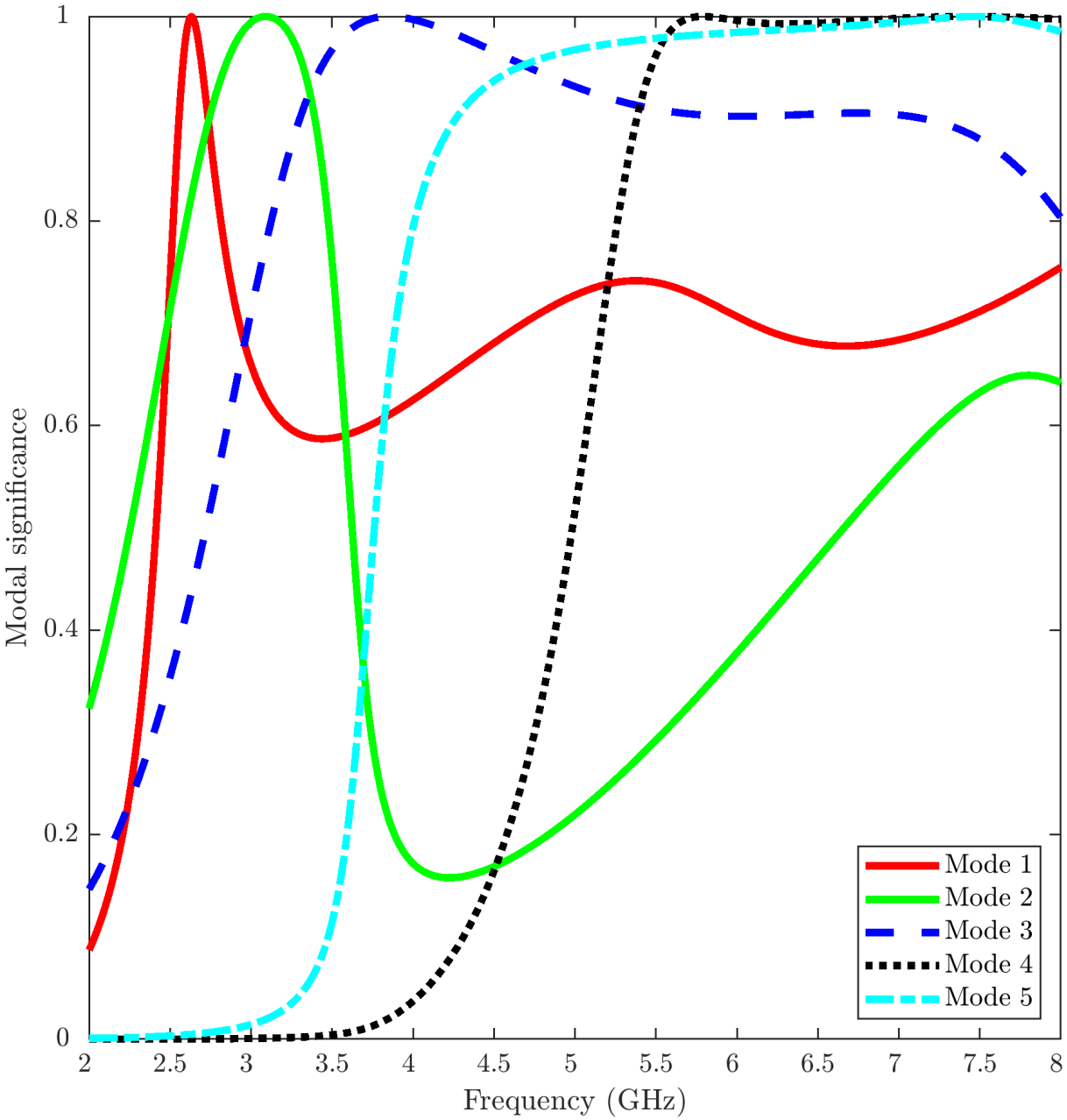


Figure 6.19. The modal significance for the first five resonant modes of the proximity-fed patch antenna whose dimensions are depicted in Figure 6.18.

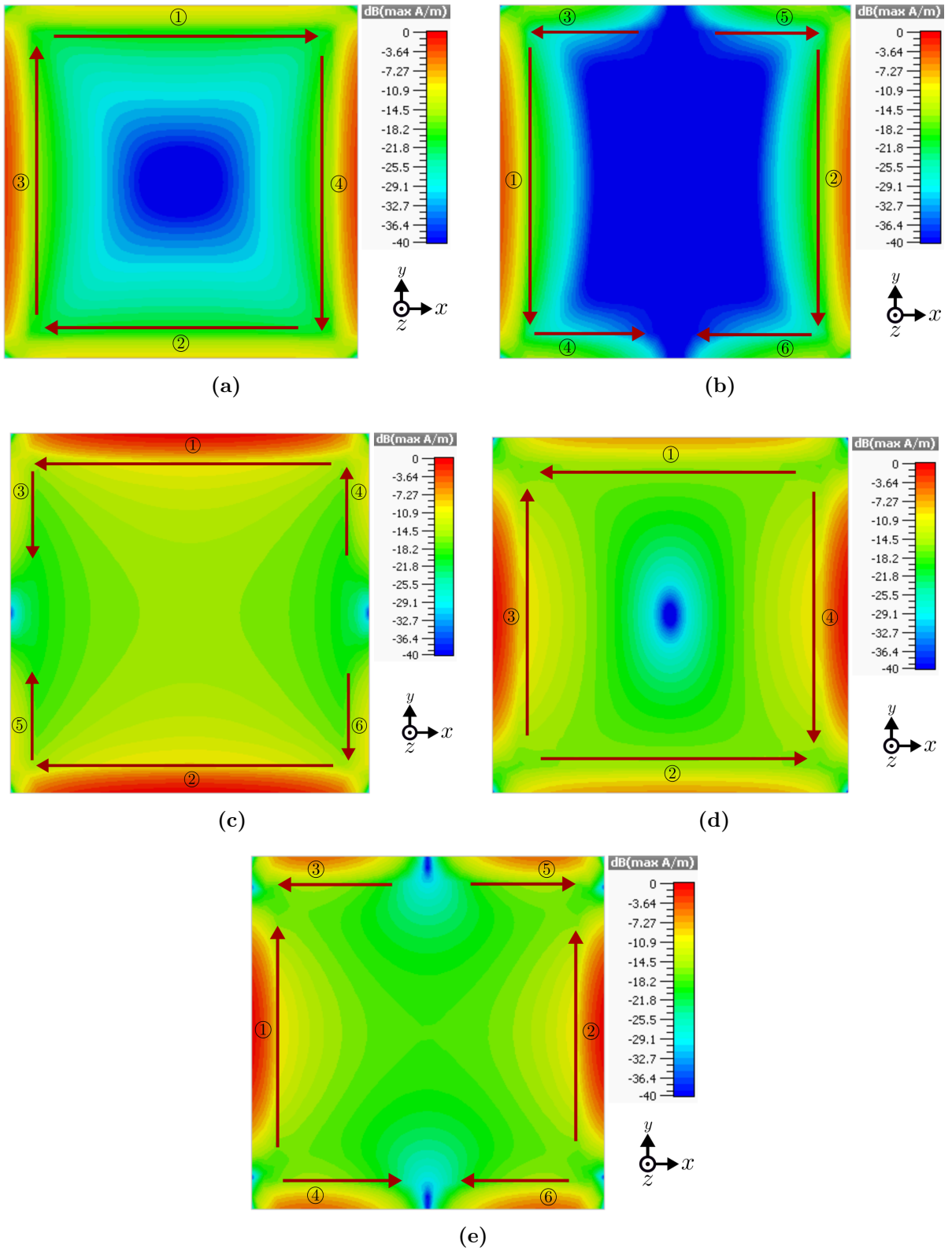


Figure 6.20. Characteristic surface current for (a) mode one at 2.630 GHz (b) mode two at 3.092 GHz (c) mode three at 3.854 GHz (d) mode four at 7.424 GHz (e) mode five at 7.460 GHz frequency for the antenna depicted in Figure 6.18, whose modal significant is shown in Figure 6.19.

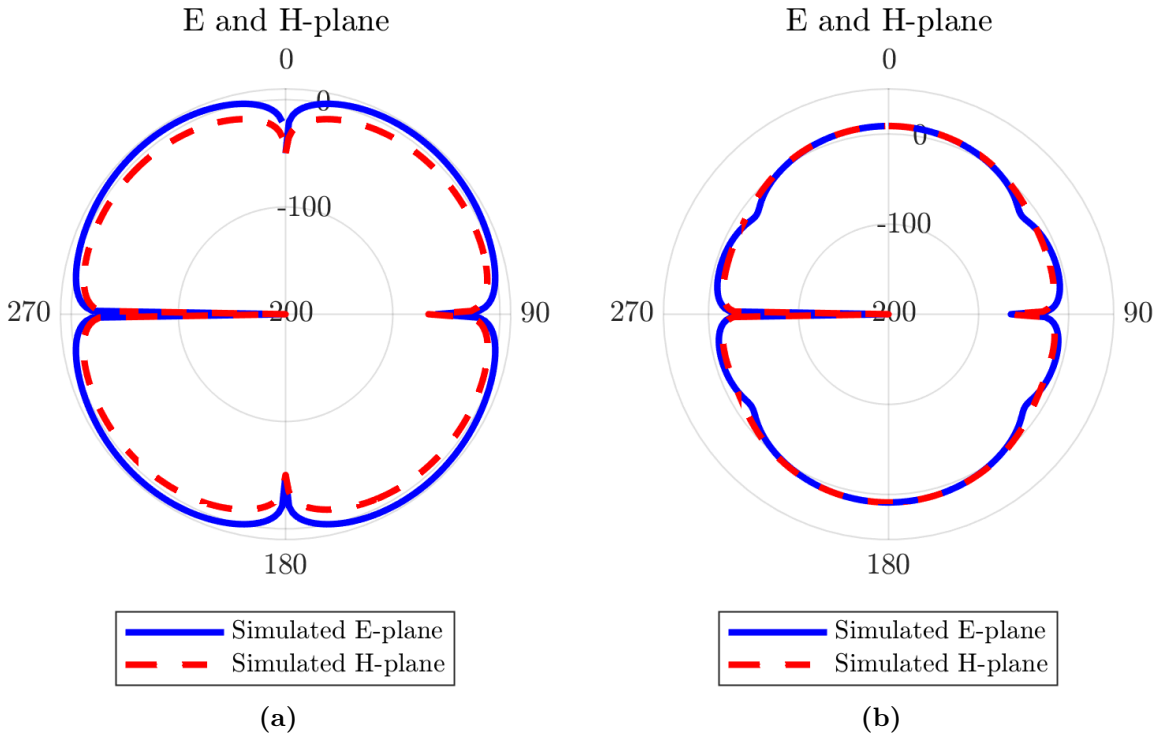
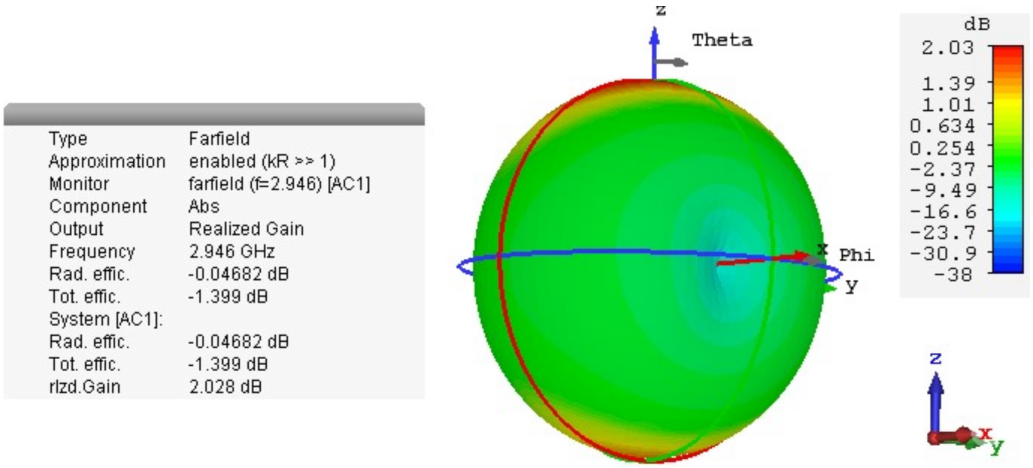
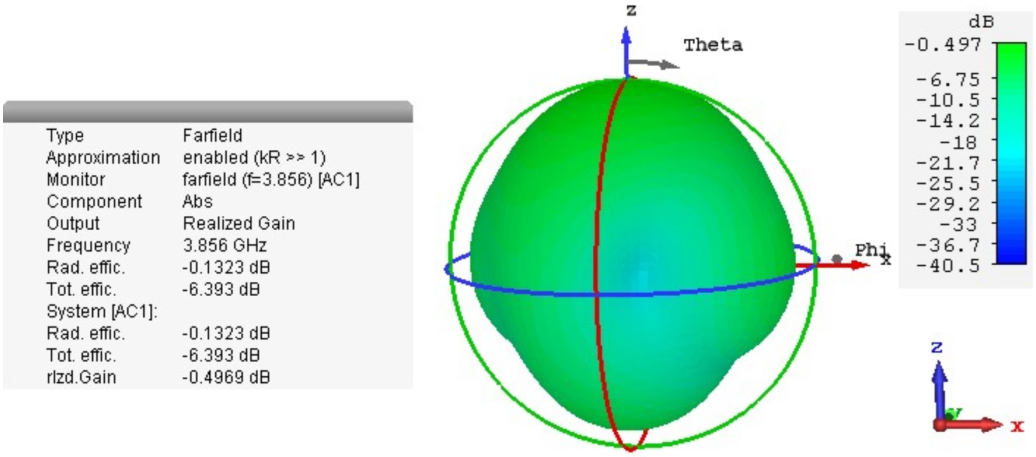


Figure 6.21. Characteristic directive radiation patterns for (a) mode four at 7.424 GHz and (b) mode five at 7.460 GHz frequency for the patch antenna whose TARC resonance is depicted in Figure 6.23, and modal significance shown in Figure 6.19. The patterns for mode J_{01}, J_1, and J_2 for this antenna are similar to the patterns shown in Figure 4.7.

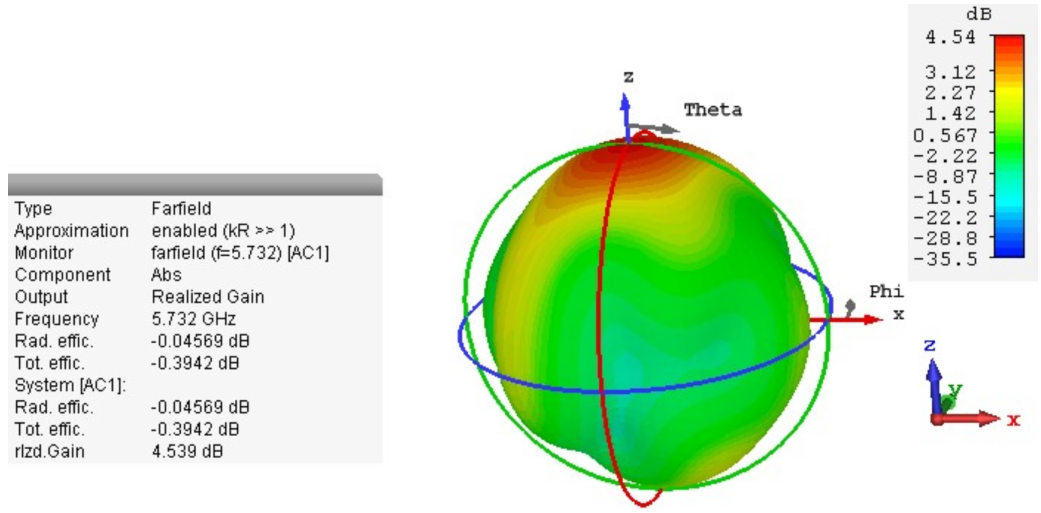
ure 6.18) are shown in Figure 6.22. At a 2.946 GHz resonant frequency, the antenna radiates along $\theta = 0°$ and $\theta = 180°$ directions, which slightly aligns with the predictions of mode J_2 patterns in Figure 4.7c. Also, at 3.856 GHz resonant frequency the antenna has the major lobe along $\theta = 0°$ with low gain and the minor lobe along $\theta = 180°$, which does not align with the predicted mode J_1 patterns in Figure 4.7b, showing that mode three (which is mode J_1) is weakly excited. On the other hand, at 5.732 GHz frequency, the antenna has the main lobe on the broadside ($\theta = 0°$) and weak side lobes, as predicted by mode five patterns in Figure 6.21b. Considering the E-plane ($\phi = 0°$) directive pattern for mode five shown in Figure 6.21b, feeding at $\theta = 45°$ and $\theta = 225°$ (near the minor nulls at around $\theta = 53°$ and $\theta = 236°$) suppresses the mode to reduce its directive gain from around 8.8 dBi to 4.5 dBi (Figure 6.21b and 6.22c).



(a)



(b)



(c)

Figure 6.22. Simulated 3D radiation patterns at (a) 2.946 GHz (b) 3.856 GHz and (c) 5.732 GHz frequencies, for the square microstrip-fed patch antenna whose TARC resonances are shown in Figure 6.23.

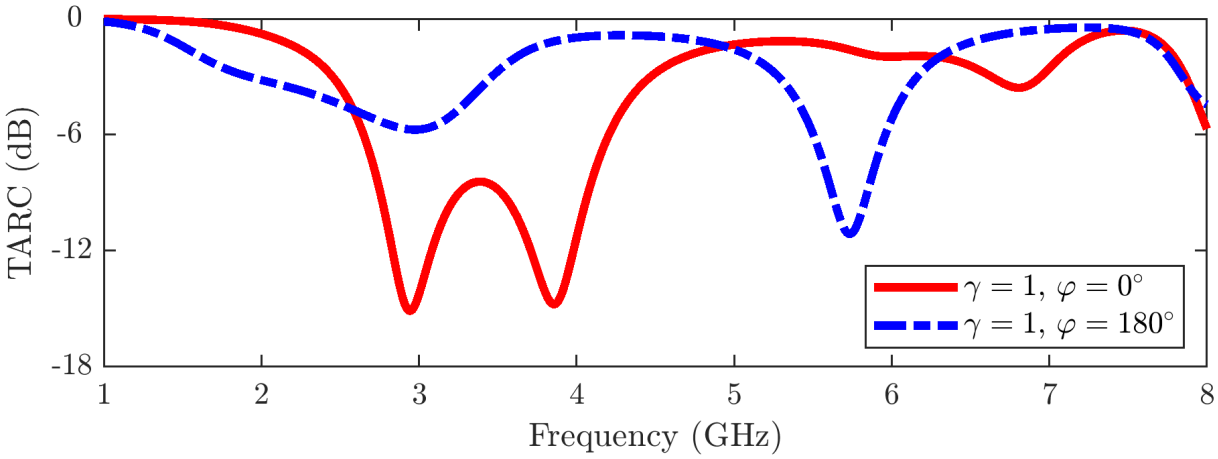


Figure 6.23. Simulated TARC for the tunable multiband antenna resulting from feeding on the opposite corners of the square proximity-fed patch antenna whose dimensions are depicted in Figure 6.18.

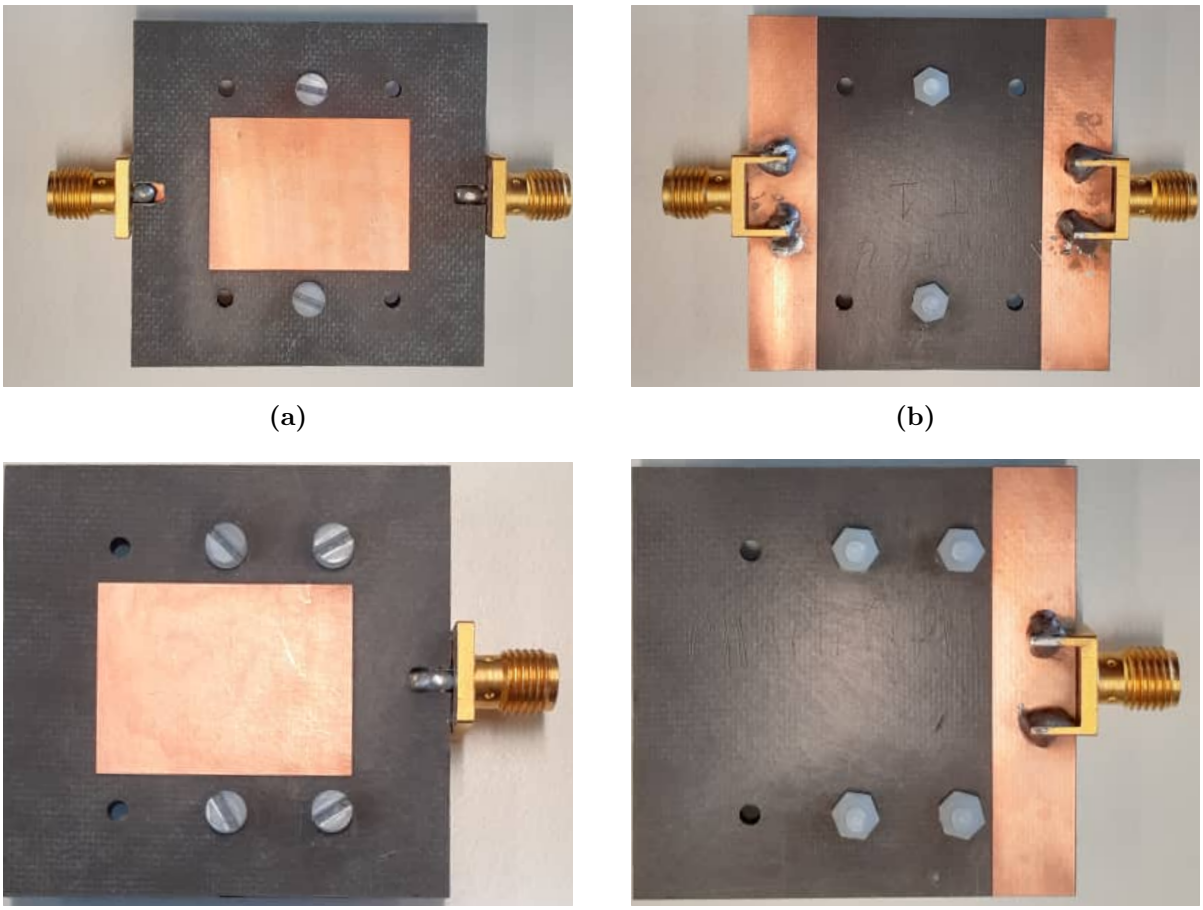
Also, it is shown in Figure 6.22 that the highest gain of around 4.5 dBi and radiation efficiency of 98.95% are attained at the 5.732 GHz resonant frequency, followed by a gain of 2.0 dBi and radiation efficiency of 98.93% at 2.946 GHz frequency. The 3.856 GHz resonance has the lowest gain of around -0.5 dBi and radiation efficiency of 97% because of the improper feeding mechanism used to excite mode three of the antenna as shown by its lowest total efficiency in Figure 6.22b. These observations indicate that exciting a planar monopole antenna outside its magnetic symmetry line or at other angles apart from 0° from the magnetic symmetry line cannot achieve wide bandwidths.

6.2.2 Antenna validation

The two-port antenna whose TARC resonance is depicted in Figure 6.8 attained the most significant FBWs of all other investigated antennas in this chapter. As such, this antenna was validated by following the procedure outlined in Section 4.4. Experimental results in comparison to the theory are provided and discussed in Section 6.3.

6.3 Results and discussion

The fabricated antennas depicted in Figure 6.24 were experimentally validated to characterise TARC and radiation patterns, which are shown in Figure 6.25, and 6.34 through 6.36, respectively.



(a) **(b)**

(c) **(d)**

Figure 6.24. (a) Front view of the printed two-port patch antenna (b) back view of the printed two-port patch antenna (c) front view of the printed corresponding one-port patch antenna (d) back view of the printed corresponding one-port patch antenna. The two antennas have dimensions depicted by TARC5 resonance in Table 6.1.

It is shown in Figure 6.25 that there is a significant deviation of the measured TARC attained through differential excitation from the simulated one, which is caused by the leakage currents on the SMA connectors and the outer shield of the feeding coaxial cables.

This effect is shown in Figure 6.26a and 6.26b, where there exists a significant variation of the applied γ and φ between 1.0 and 5.0 GHz frequencies, which causes large variations in the terminal impedances calculated from measurements in the same frequencies, as depicted in Figure 6.27. Though ferrite beads (shown in Figure 4.35) were used to suppress these currents during measurement, the effect persisted in the lower mode of the differential TARC.

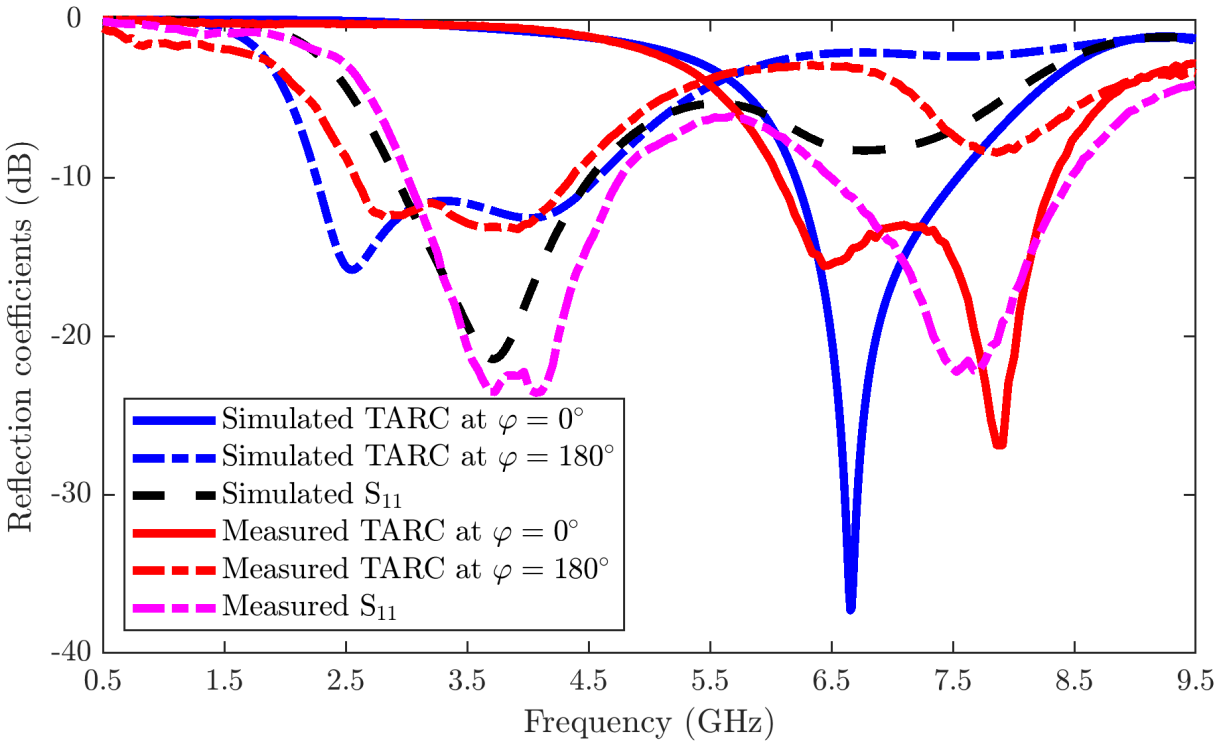
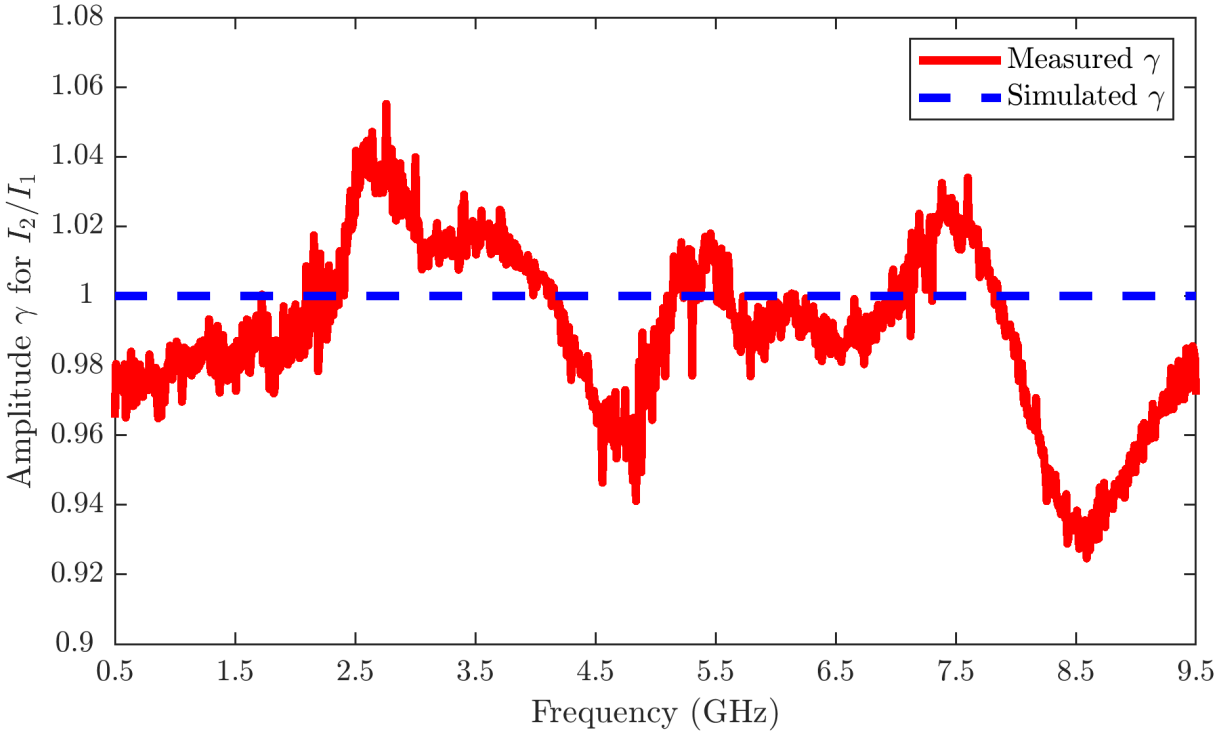
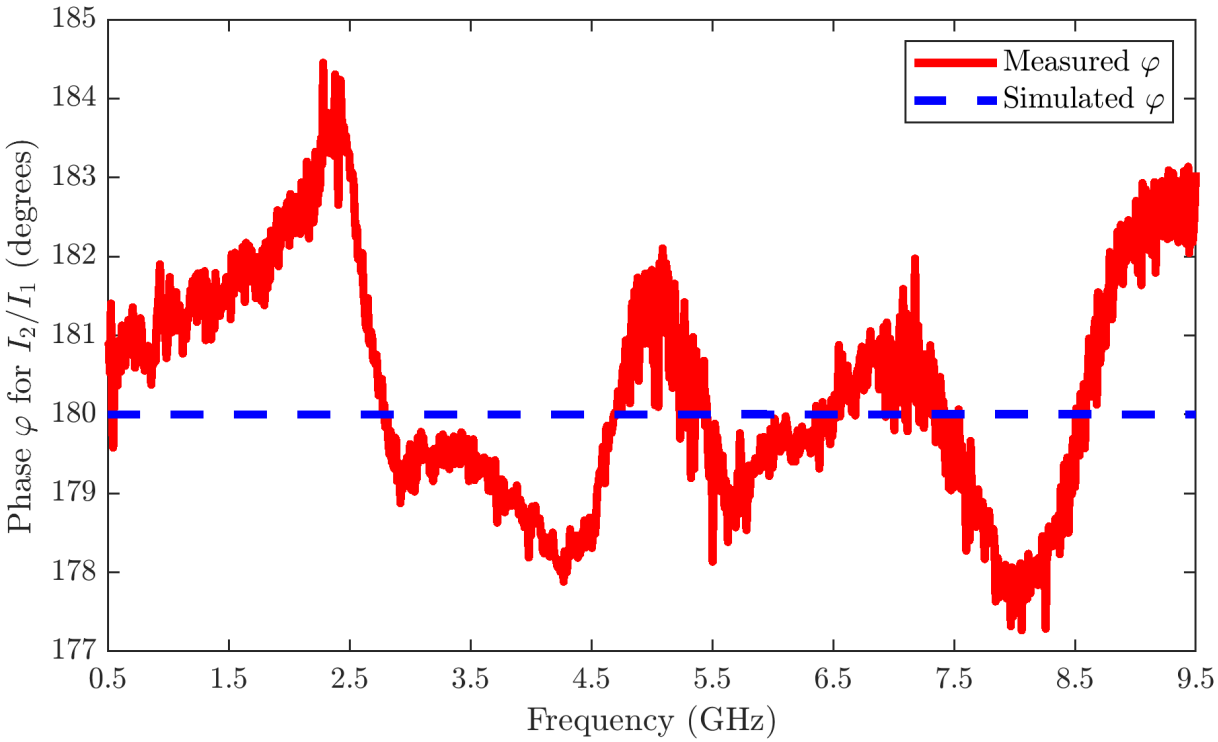


Figure 6.25. Simulated and measured TARC for the two-port injection matched patch antenna in comparison to the simulated and measured S-parameter for the corresponding one-port antenna. The simulated and printed antennas are shown in Figure 6.8 and 6.24, respectively.

Also, the measured TARC resonance attained through common mode excitation was largely distorted by the same factors and was shifted from 6.656 GHz to around 7.862 GHz. This effect is shown by the variations of the applied γ and φ at all investigated frequencies, as shown in Figure 6.28a and 6.28b, which caused a large deviation of the measured terminal impedances from the simulated values, as depicted in Figure 6.29. Besides, the



(a)



(b)

Figure 6.26. Measured and simulated response of the applied (a) relative amplitude γ between the currents I_1 and I_2 (b) phase shift φ between the currents I_1 and I_2 when the two-port patch antenna was injection matched at $\gamma = 1$ and $\varphi = 180°$. The simulated and printed antennas are shown in Figure 6.8 and 6.24, respectively.

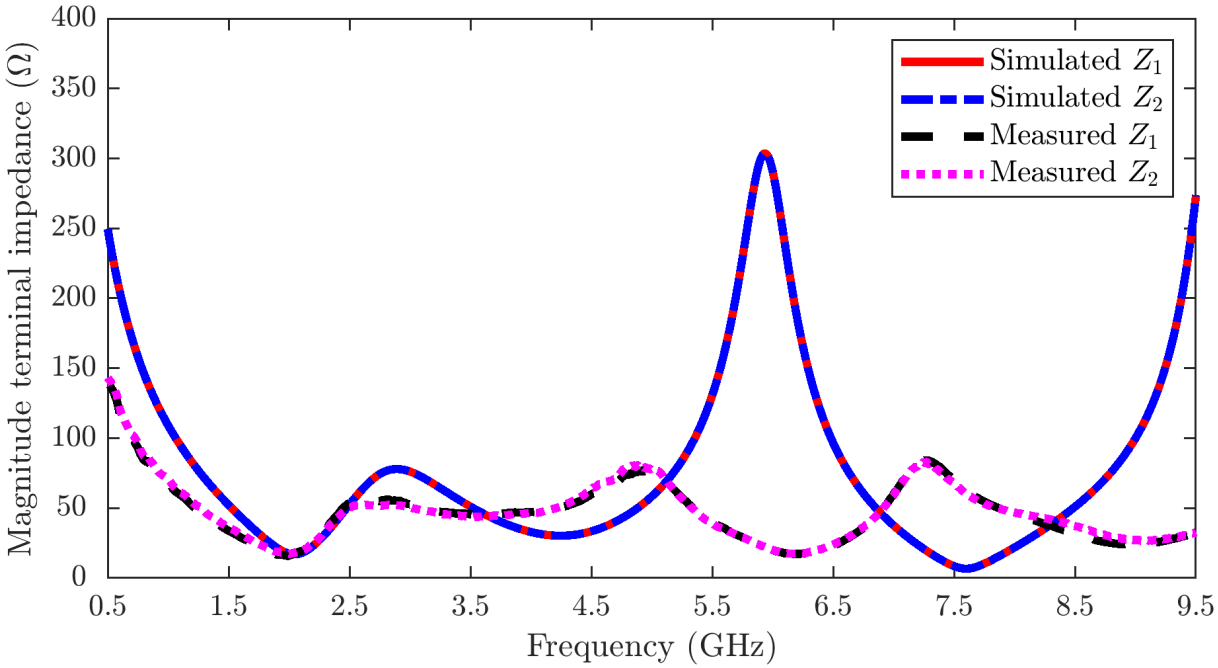
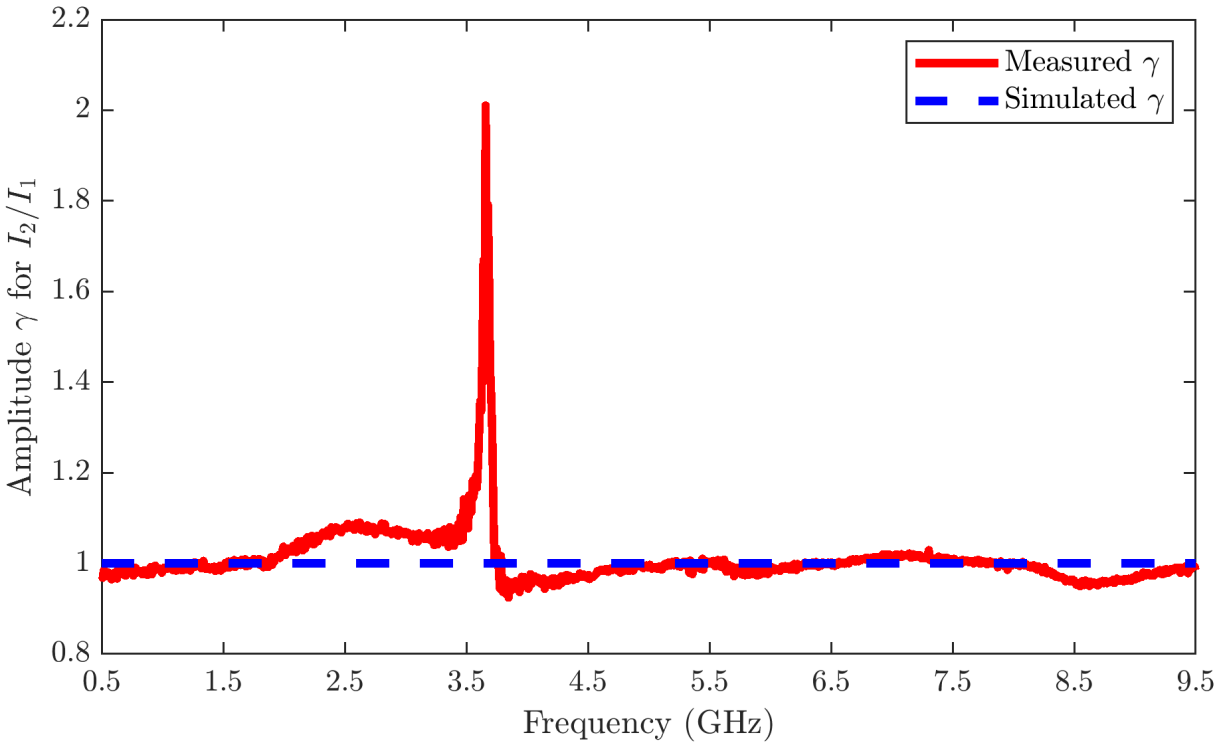


Figure 6.27. Simulated and measured terminal impedances for the differentially excited two-port injection matched patch antenna under investigation. The simulated and printed antennas are shown in Figure 6.8 and 6.24, respectively.

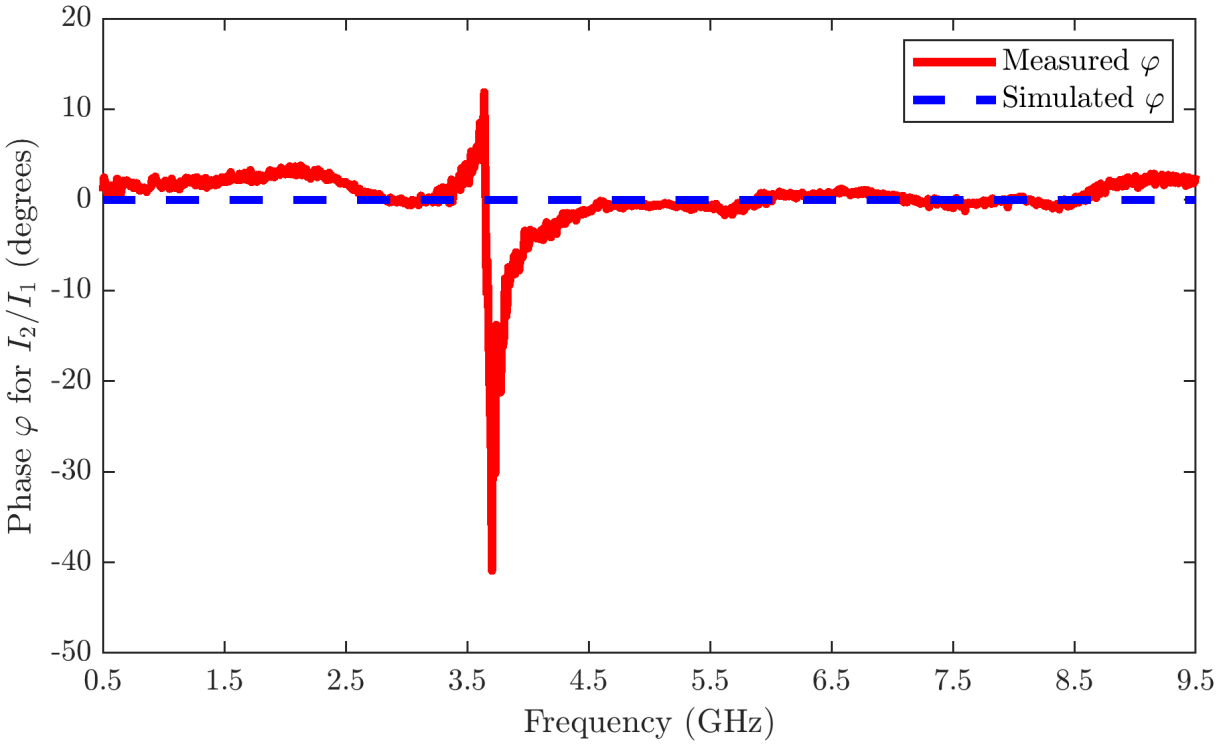
lower mode for the measured S-parameter for the corresponding one-port antenna depicted in Figure 6.25 was distorted by the same factors.

The realised two-port injection matched antenna has a simulated −10 dB FBW of around 67.8% and 19.4% (calculated using Equation (B.1) in Appendix B.4) attained through the differential and common mode excitations, respectively, applied to the antenna. The achieved high bandwidth in the differential excitation mode is attributed to the excitation of two characteristic modes (J_{01} and J_1) of the antenna through the application of the injection matching technique.

The matching efficiency for the differential mode TARC is higher than 89% across its −10 dB impedance matched bandwidth, while that of the common mode TARC is higher than 84%, as shown in Figure 6.30. However, at resonance, the common mode TARC has higher matching efficiency than the differential TARC because of the high impedance



(a)



(b)

Figure 6.28. Measured and simulated response of the applied (a) relative amplitude γ between the currents I_1 and I_2 (b) phase shift φ between the currents I_1 and I_2 when the two-port patch antenna was injection matched at $\gamma = 1$ and $\varphi = 0°$. The simulated and printed antennas are shown in Figure 6.8 and 6.24, respectively.

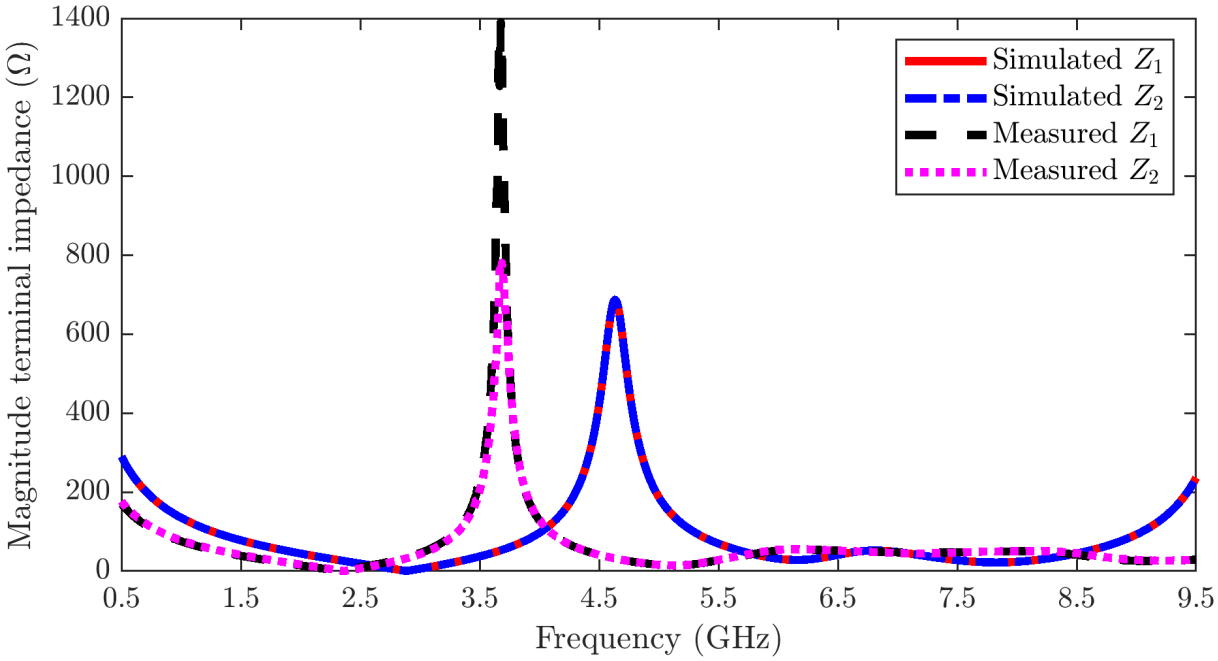


Figure 6.29. Simulated and measured terminal impedances for the common mode excited two-port injection matched patch antenna under investigation. The simulated and printed antennas are shown in Figure 6.8 and 6.24, respectively.

matching attained by the common mode TARC. On the other hand, the corresponding one-port antenna has higher matching efficiency than the differentially excited two-port antenna because of good impedance matching attained by the one-port antenna. Also, the differentially excited two-port antenna achieves the highest radiation efficiency than the common mode excited antenna and the corresponding one-port antenna because of the excitation of two similar modes J_{01} and J_1 in the differential TARC [90]. Generally, all antenna excitations have attained radiation efficiencies higher than 98% because of the low loss tangent ($\tan\delta = 0.0009$) and low dielectric constant ($\varepsilon_r = 2.2$) substrate material used in the design. However, the radiation efficiency for the common mode excited two-port antenna is slightly lower than the efficiencies for the other excitations because of the increased number of nulls in its radiation patterns caused by excitation of a higher-order mode of the antenna, as shown in Figure 6.35. Generally, the total

efficiency for the common mode excited two-port antenna, at resonance, is higher than the total efficiency for the differentially excited two-port antenna and corresponding one-port antenna because of the high matching efficiency attained through the common mode excitation applied to the antenna.

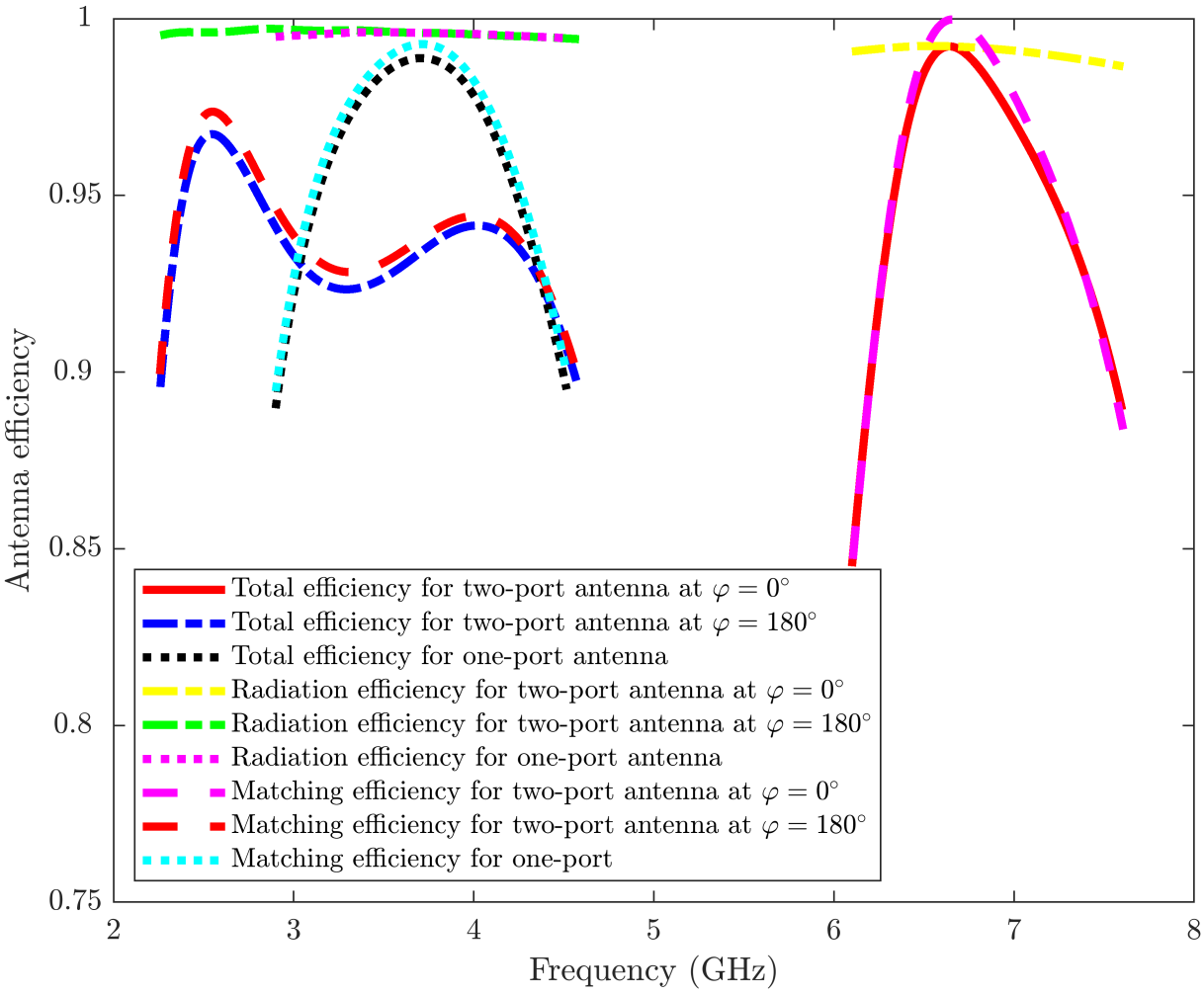


Figure 6.30. Simulated efficiency for the injection matched patch antenna in comparison to the simulated efficiency for the corresponding one-port antenna whose TARC and S_{11} resonances are shown in Figure 6.8.

The simulated surface currents for the common mode and differentially excited two-port injection matched antenna shown in Figure 6.31 and 6.32, respectively, are more dominant on the PGPs than on the patch. This observation indicates that the two-port patch antenna has been transformed into a miniaturised dipole patch antenna. Similar

behaviour is noted in Figure 6.33, where the corresponding one-port patch antenna has been transformed into a monopole antenna.

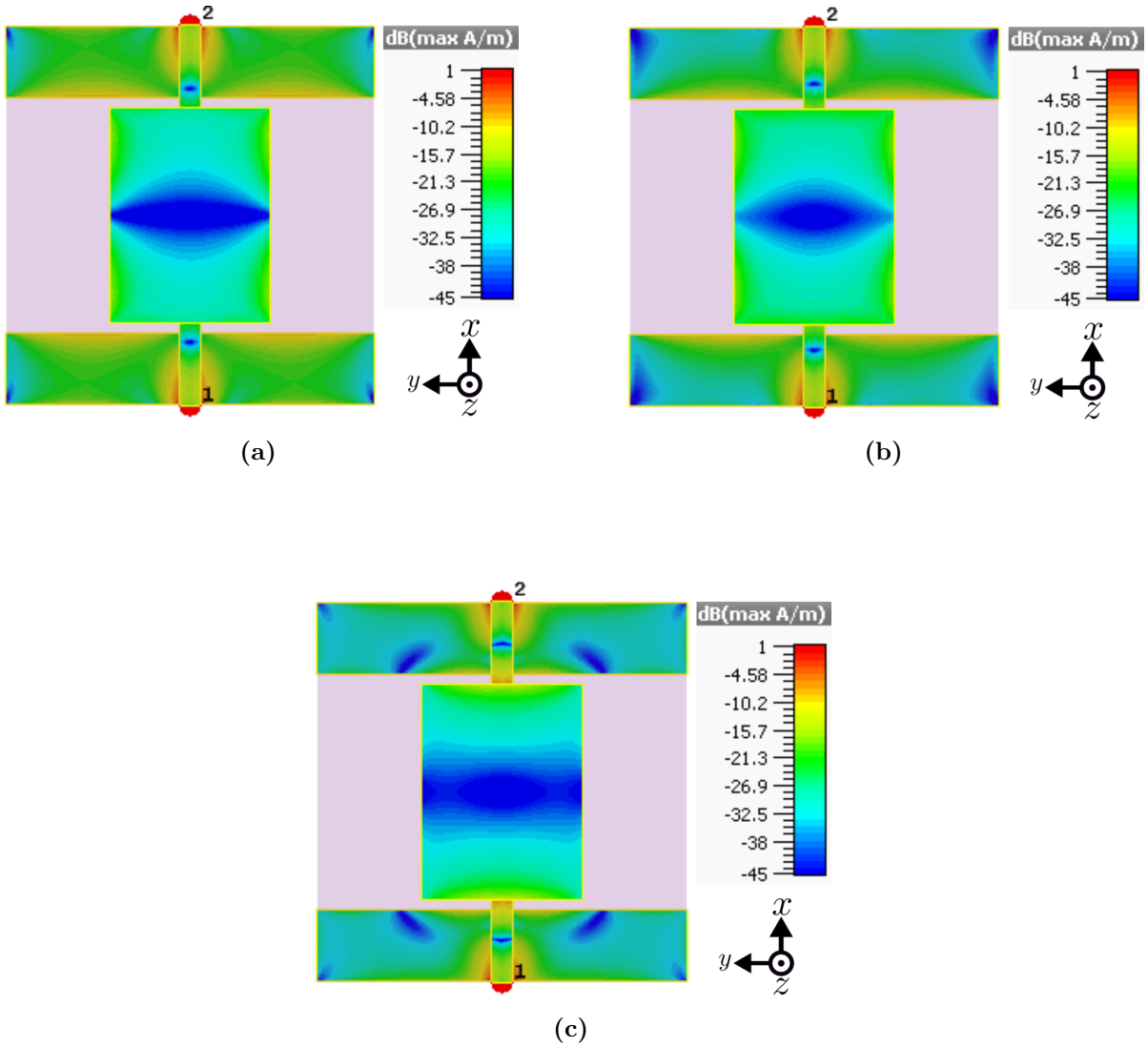
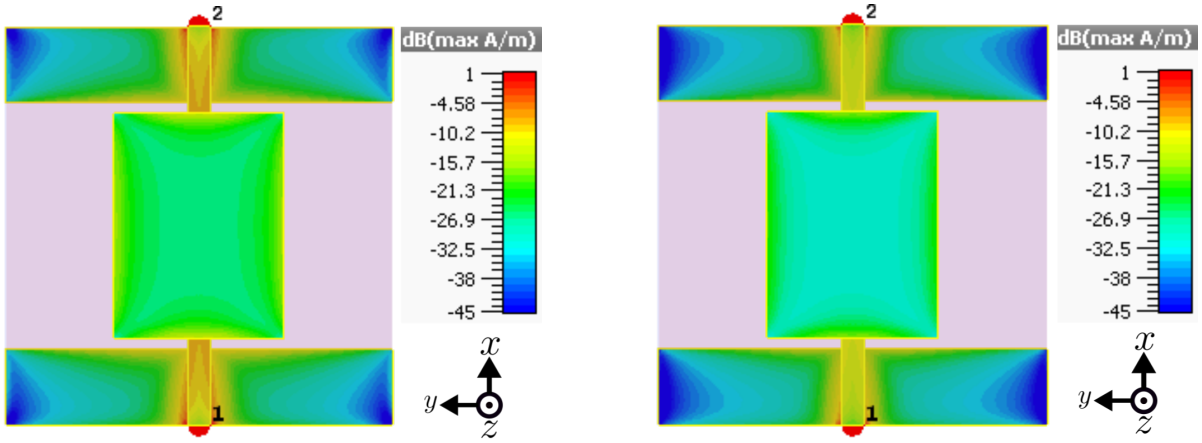


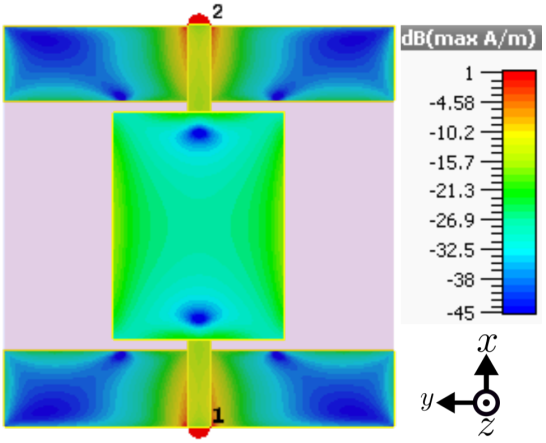
Figure 6.31. Simulated surface current on the two-port patch antenna at (a) 6.190 GHz (b) 6.644 GHz and (c) 7.607 GHz frequencies, when the antenna was injection matched at $\gamma = 1$ and $\varphi = 0°$ as shown in Figure 6.8.

Also, the surface currents resulting from the common mode excitation of the antenna shown in Figure 5.21 are similar to the mode four current shown in Figure 6.10d. This observation indicates that mode four of the antenna has been excited at a 6.644 GHz resonant frequency. On the other hand, the surface currents on the differentially excited

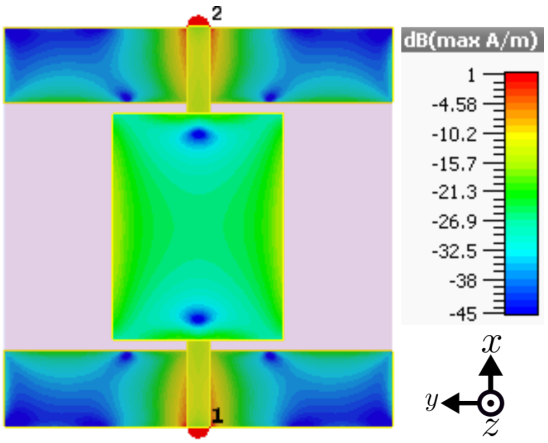


(a)

(b)



(c)



(d)

Figure 6.32. Simulated surface current on the two-port patch antenna at (a) 2.260 GHz (b) 2.546 GHz (c) 4.060 GHz and (d) 4.585 GHz frequencies, when the antenna was injection matched at $\gamma = 1$ and $\varphi = 180°$ as shown in Figure 6.8.

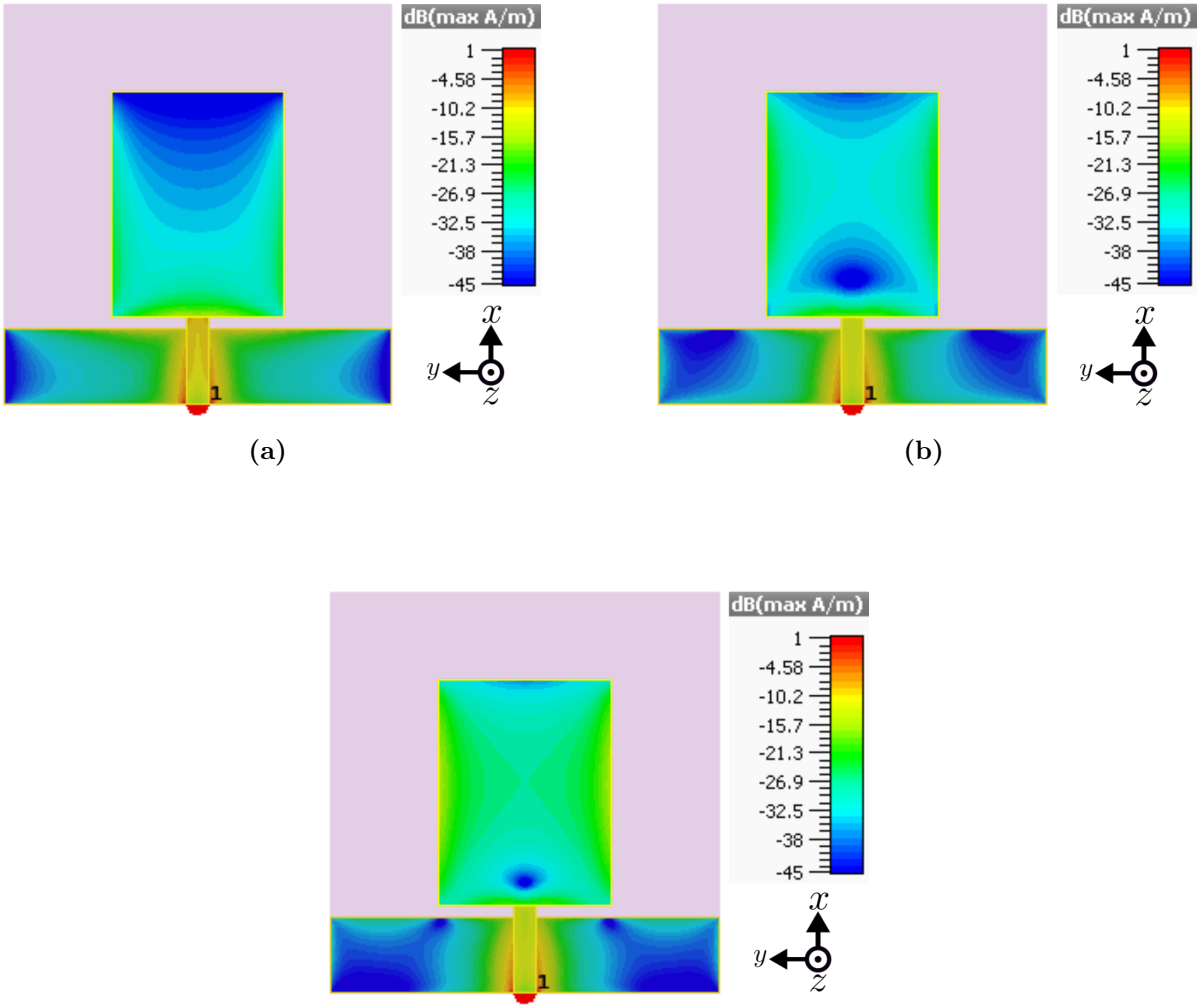


Figure 6.33. Simulated surface current on the one-port patch antenna at (a) 2.916 GHz (b) 3.713 GHz and (c) 4.515 GHz frequencies. The simulated S_{11} for this antenna is shown in Figure 6.8.

two-port patch antenna at 2.260 and 2.546 GHz frequencies, as shown in Figure 6.32, indicate the excitation of mode J_{01} shown in Figure 4.6a. In contrast, the currents at 4.060 and 4.585 GHz frequencies shown in Figure 6.32 indicate the excitation of the horizontal mode J_1 at a 4.060 GHz resonant frequency, as shown in Figure 4.6b. On the other hand, the surface current for the corresponding one-port antenna depicted in Figure 6.33 shows that both modes J_{01} and J_1 are excited at 3.713 GHz. However, mode J_{01} is dominant at 2.916 GHz lower boundary frequency, while mode J_1 is dominant at 4.515 GHz upper boundary frequency.

The measured co-polar patterns for both the two-port antenna and the corresponding one-port antenna, shown in Figure 6.34 through 6.36, have been distorted by the leakage currents on the SMA connectors and PGPs. For the two-port antenna working in the differential mode, the distortion was more severe in the frequency range of 2.590 to 2.780 GHz than in the remaining monitored frequencies, as shown in Figure 6.34, because of the significant distortion of TARC at these frequencies, as shown in Figure 6.25. For the common mode excitation of the antenna, the H-plane ($\phi = 90°$) co-polar patterns shown in Figure 6.35 were largely distorted than the E-plane ($\phi = 0°$) patterns because of the same factors. Also, both the measured E and H-plane patterns for the corresponding one-port antenna shown in Figure 6.36 were largely distorted by the leakage currents on the SMA connectors and PGP. Though ferrite beads (shown in Figure 4.35) were used during measurement, the effect of residual currents could not be eliminated. The simulated H-plane ($\phi = 90°$) co-polar patterns for the differentially excited two-port antenna and the corresponding one-port antenna are approximately omnidirectional, indicating that the two antennas have been transformed into dipole and monopole patch antennas,

respectively. However, the common mode excitation of the higher-order mode of the two-port antenna does not achieve conversion to a monopole antenna.

The common mode excited two-port antenna attains the maximum gain of around 5.6 dBi at a 6.400 GHz frequency, as shown in Figure 6.37d, which shows that the antenna is not converted to a monopole antenna by this excitation. The high gain achieved by the antenna at this frequency is attributed to the excitation of a higher-order characteristic mode of the antenna [91], which is illustrated by the horizontal and vertical nulls exhibited by the antenna at the monitored 6.190, 6.644 and 7.607 GHz frequencies, as shown in Figure 6.37c. On the other hand, the differentially excited two-port antenna attains the maximum gain of 2.5 dBi at a 4.200 GHz frequency as shown in Figure 6.37d, which is slightly higher than the maximum gain attained by the corresponding one-port antenna because of an effective excitation of mode J_1 of the antenna by the applied differential excitation than the one-port excitation of the same characteristic mode. It is shown in Figure 6.37d that the differential and single-port excitations fairly convert the antenna to monopole antenna operations.

Also, the differential excitation of the antenna achieves the lowest gain (of around 1.5 dBi at a 2.260 GHz frequency) compared to the gain attained by other excitations, as shown in Figure 6.37a, because of excitation of mode J_{01} at this frequency, which is of a lower order than the other excited modes of the antenna. Besides, the gain achieved by the differential excitation mode of the two-port antenna, shown in Figure 6.37a, is fairly stable at 2.260 and 2.546 GHz frequencies (with a gain reduction of around 0.5 dB between the two frequencies) than at 4.060 and 4.585 GHz frequencies. This stability is attributed to the excitation of mode J_{01} of the antenna at a 2.546 GHz resonant frequency, which is of a lower order than mode J_1 of the same antenna excited at a 4.060 GHz

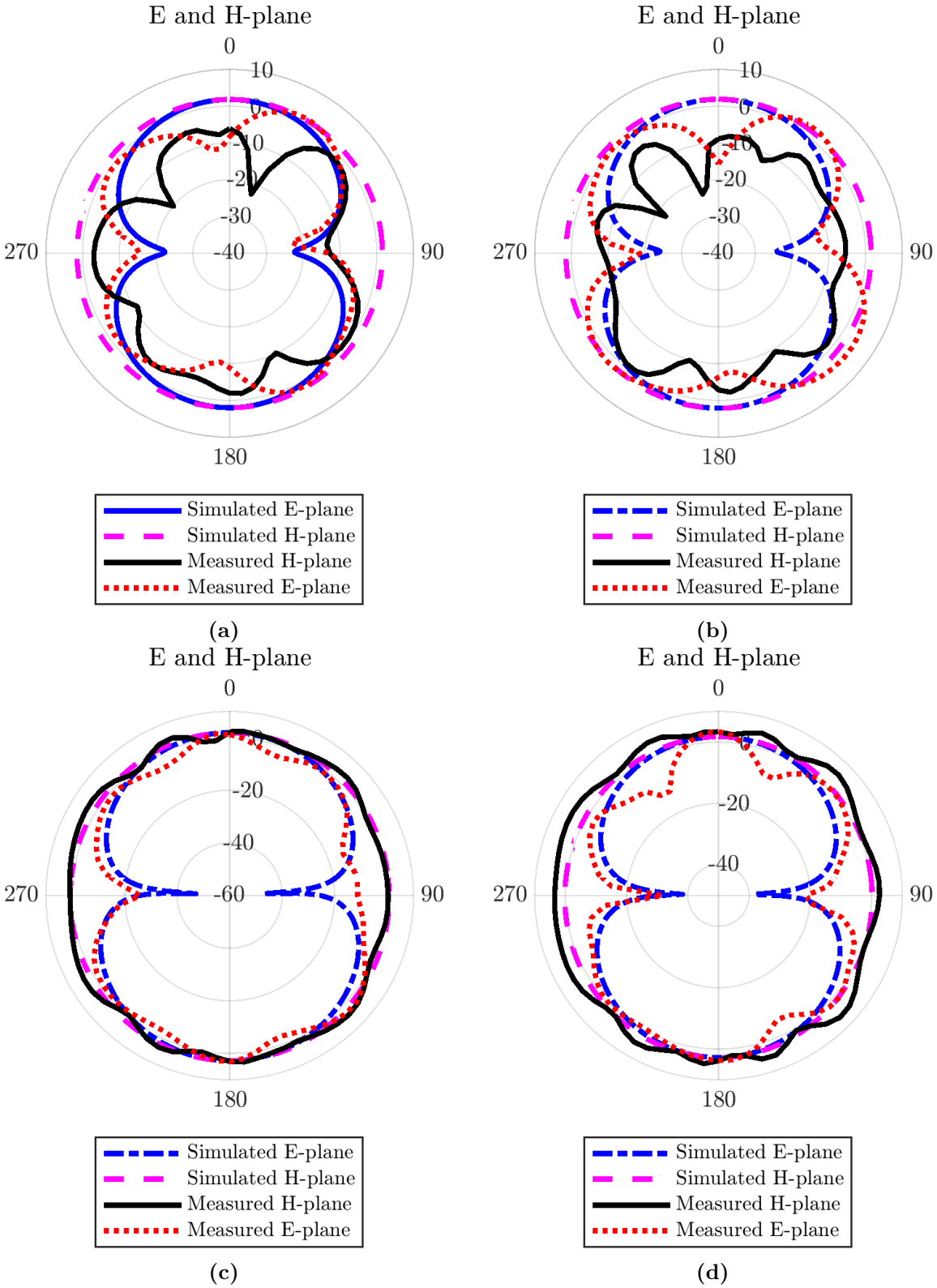


Figure 6.34. Simulated and measured co-polar patterns for the differentially excited two-port injection matched patch antenna in the (a) 2.260 and 2.590 GHz (b) 2.546 and 2.780 GHz (c) 4.060 and 4.063 GHz (d) 4.585 and 4.348 GHz frequencies, respectively. The simulated and printed antennas are shown in Figure 6.8 and 6.24, respectively.

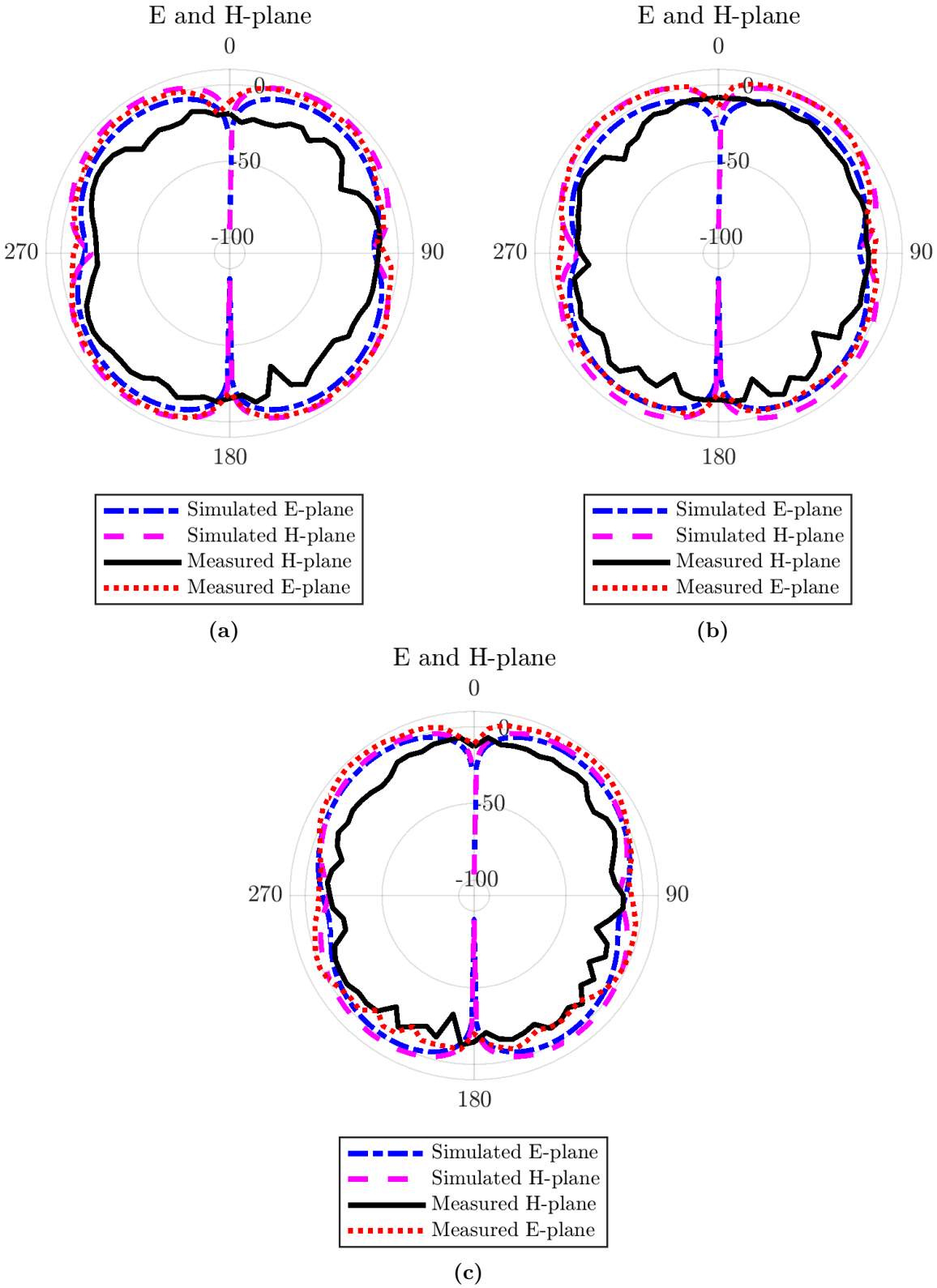


Figure 6.35. Simulated and measured co-polar patterns for the common mode excited two-port injection matched patch antenna in the (a) 6.190 and 6.105 GHz (b) 6.644 and 7.863 GHz (c) 7.607 and 8.290 GHz frequencies, respectively. The simulated and printed antennas are shown in Figure 6.8 and 6.24, respectively.

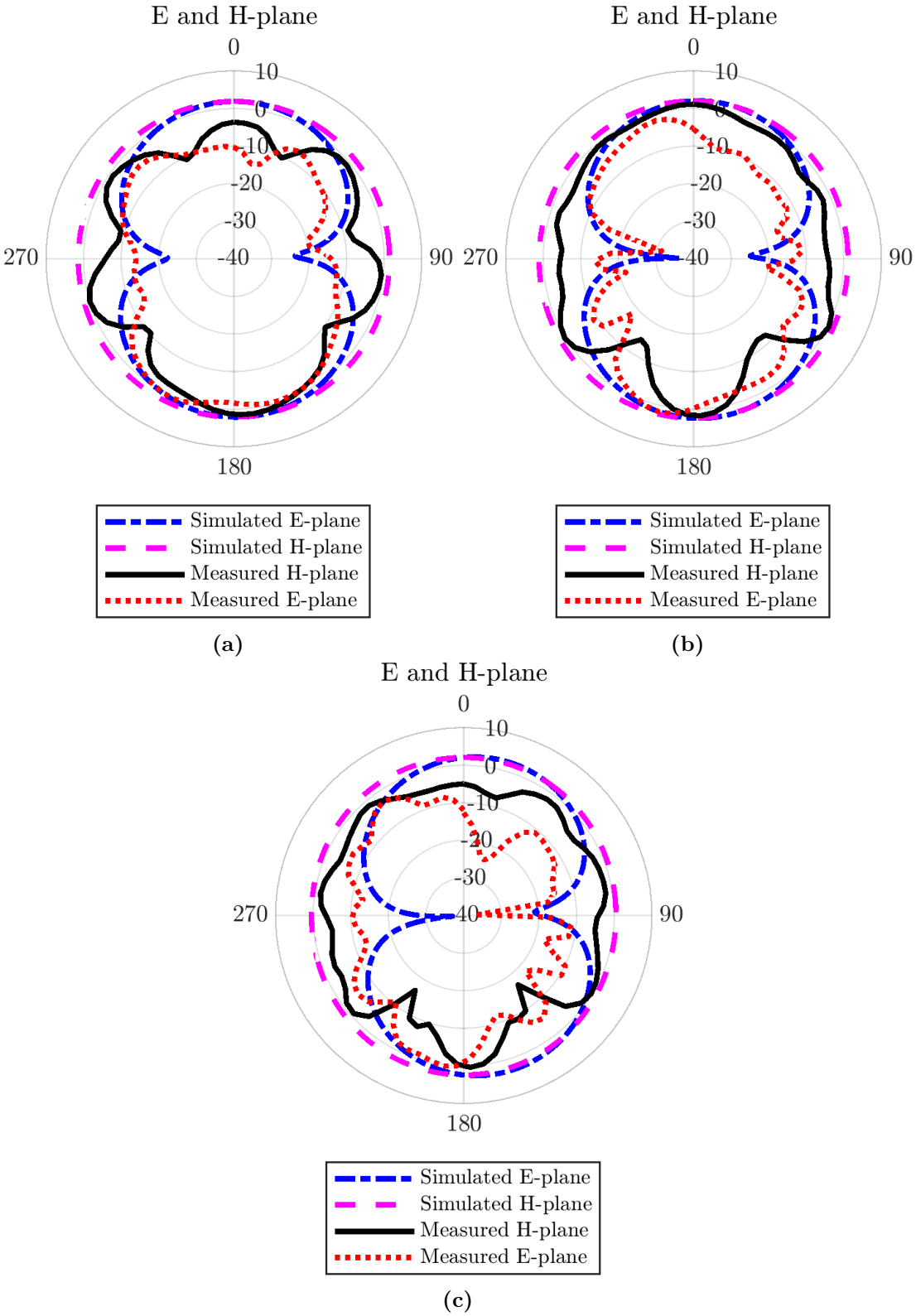


Figure 6.36. Simulated and measured co-polar patterns for the one-port patch antenna in the (a) 2.916 and 3.018 GHz (b) 3.713 and 3.92 GHz (c) 4.515 and 4.728 GHz frequencies, respectively. The simulated and printed antennas are shown in Figure 6.8 and 6.24, respectively.

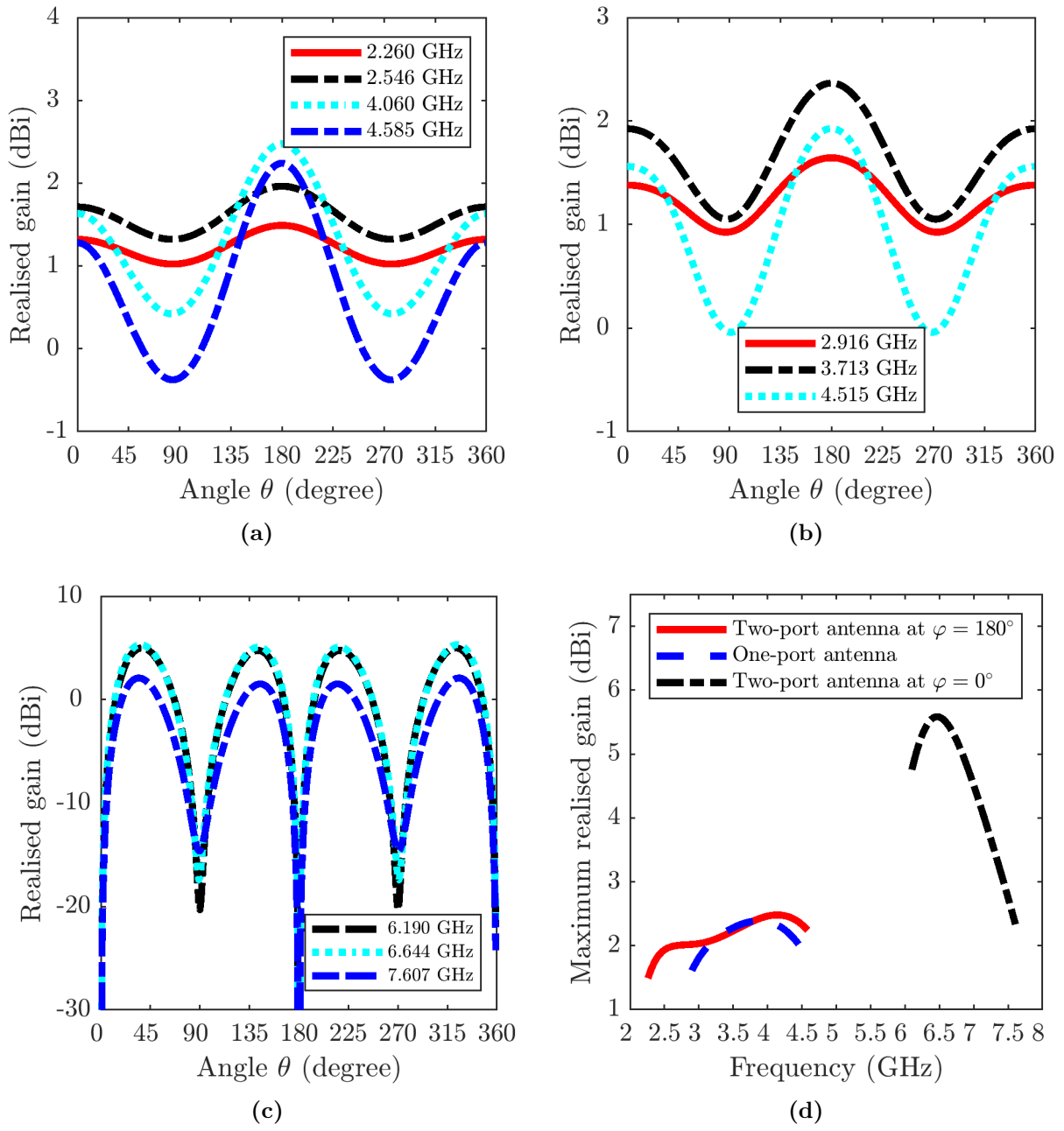


Figure 6.37. Simulated (a) H-plane ($\phi = 90°$) realised gain for the differentially excited two-port injection matched patch antenna (b) H-plane ($\phi = 90°$) realised gain for the one-port patch antenna (c) H-plane ($\phi = 90°$) realised gain for the common mode excited two-port injection matched patch antenna (d) H-plane ($\phi = 90°$) maximum realised gain for the two-port injection matched antenna and for the corresponding one-port antenna. The simulated TARC and S_{11} for the two antennas are shown in Figure 6.8.

resonant frequency. Also, the common mode excited antenna has stable patterns at 6.190 and 6.644 GHz frequencies but experiences a large reduction in gain of up to 3.4 dB at 7.607 GHz boundary frequency, as shown in Figure 6.37c, because of excitation of mode four of the antenna which has multiple lobes as indicated by its eigenpatterns in Figure 6.11a. On the other hand, there is a large variation of the gain attained by the corresponding one-port antenna, as shown in Figure 6.37b, because of driving the antenna from a single port. Generally, the two-port antenna's realised gain is improved compared to the gain of the corresponding one-port antenna due to driving the antenna from two ports.

Despite the observed deviations of the measured TARC and radiation patterns for the two-port injection matched antenna from the simulated TARC and patterns, the injection matching technique has been verified to an acceptable degree in that the expected characteristic of an antenna operating under the injection matched condition have been observed experimentally.

6.4 Summary

It has been shown in this chapter that the tuning of the operational frequency for the two-port patch antenna through the application of the injection matching technique is feasible at two distinct γ and φ combinations of $\gamma = 1$, $\varphi = 0°$ and $\gamma = 1$, $\varphi = 180°$. The modes whose principal currents at the two opposite patch edges are symmetrically in phase and differentially oriented are excited at these two combinations. Specifically, the frequency tuning of the two-port antenna by feeding the antenna along its magnetic symmetry line enables wide bandwidth in the differential mode excitation and a narrow bandwidth

resonance in the common mode excitation. On the other hand, the excitation of the modes by feeding a patch antenna from its opposite corners achieves tunable multiband resonances, which, however, have low bandwidth and low impedance matching because of the weak modal currents available at the patch corners.

However, it is impossible to progressively tune the operational frequencies in the frequency range of interest because of the limitations posed by the theoretical variations of the relative amplitude γ and phase shift φ with frequency across the antenna. It is also generally shown that the frequency tuning of a two-port injection matched patch antenna by tuning the two excitation modes is achieved at the expense of reduced bandwidth in one of the operational modes.

Typically, FBWs of around 67.8% and 19.4% with radiation efficiency higher than 98%, and total efficiency higher than 84% were attained from the differential and common mode excitations of the patch antenna (fed along its magnetic symmetry line), respectively, using the injection matching technique. The attained FBW of 67.8% spanning between 2.257 and 4.572 GHz frequencies provides part of the bandwidth (BW) needed by the 5G and dynamically shared wireless services in the Sub-6 GHz high-band.

Chapter 7

Electrically small injection matched antennas

7.1 Background

In the previous chapters, two applications of the injection matching technique in broadening the bandwidth and frequency tuning of patch antennas were investigated. This chapter presents another application of injection matching technique in actively modulating (or at least lengthening) the effective electrical length of patch antennas to allow the antennas to operate in electrically small mode. This was initially investigated in [14, 15], and it is revised in this chapter to explore three major issues which were not adequately characterised. One of the issues is the reflection coefficient which did not consider the reflections from the two ports. Another issue is the coupling between the two ports, which was not reported. Also, the use of an LC matching network in the realisation of an electrically small injection matched antenna, which contradicts the findings of the ability of the injection matching technique in achieving the electrically small operation [54] is explored.

Besides, the efficiencies (radiation, matching and total efficiency), current distributions, and radiation patterns for the realised two-port ESA and the corresponding one-port ESA are discussed.

7.2 Design and simulation

It was shown in Chapter 4 that it is not possible to have an electrically small operation on a patch antenna through the application of the injection matching technique only. So, in this section, the injection matching technique is applied to a two-port patch antenna to increase the electrical length to the maximum possible value. After that, other tuning techniques are used to shift the resonance into a lower frequency of operation for the antenna. The design starts with a physically small antenna that can fit in a mobile phone [61]. For example, a patch antenna operating at around 5.6 GHz meets this requirement.

A one-port proximity-fed patch antenna with the FGP is designed in CST MWS to operate at around 5.583 GHz by following the procedure outlined in [85]. The antenna is designed on two layers of Rogers Duroid RT 5880 substrate with relative permittivity ε_r of 2.2, loss tangent of 0.0009, lower substrate height of 1.575 mm, upper substrate height of 0.787 mm, and copper cladding thickness of 0.035 mm. The antenna has patch length $L_p = 16.04$ mm, patch width $W_p = 19.09$ mm, substrate length $L_s = 32.08$ mm, substrate width $W_s = 38.18$ mm, the width of the feed line $w = 2.5$ mm and the distance of the coupled feed line from the centre of the patch $d = 0.0$ mm. The antenna is excited through a discrete face port created on the outer end-face of the feed line while the impedance of the excitation signal delivered at this port is maintained at 50 Ω. Truncation of the grounding plane for the one-port antenna to form a PGP, as shown in Figure 7.1a,

converts the antenna to a monopole patch antenna, and the −3 dB bandwidth of the antenna is increased at the expense of degradation of the impedance matching of the one-port antenna with FGP, as shown in Figure 7.2. The length of the partial ground $L_g = 8.02$ mm, which is the maximum length of the ground plane for which a patch antenna is converted to a monopole antenna, was calculated from $L_g = (L_s - L_p)/2$.

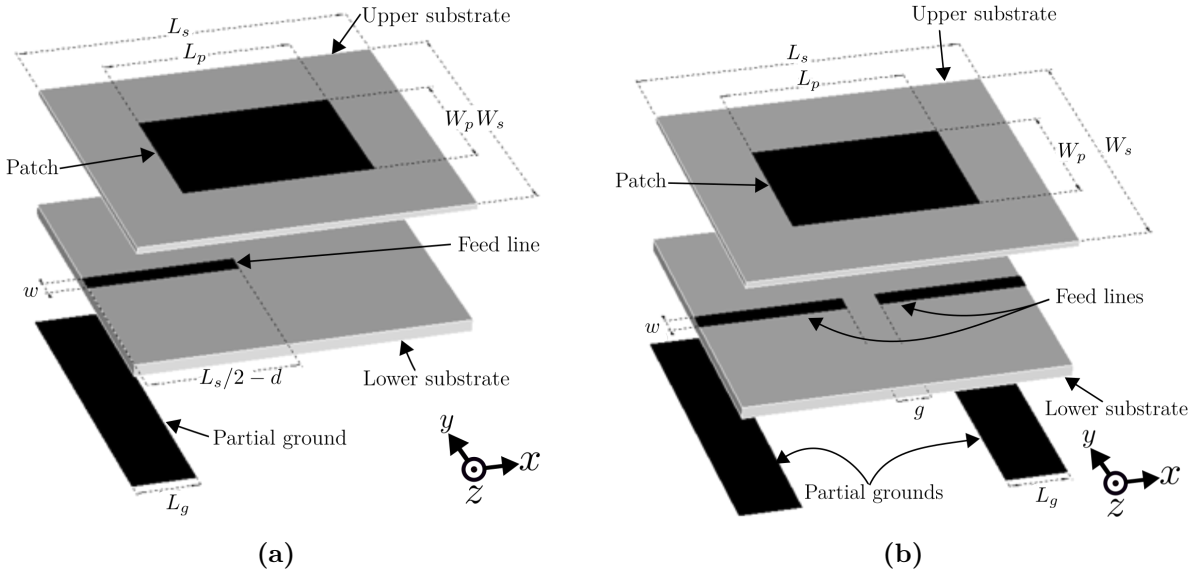


Figure 7.1. (a) Proximity-fed patch antenna with single feed line (b) proximity-fed patch antenna with two feed lines. The black colour indicates the layers of copper.

The bandwidth and impedance matching of the lower mode S_{11} resonance (5.031 GHz) for the one-port antenna with PGP depicted in Figure 7.2 is improved by applying the injection matching technique to the antenna in CST SS by following the procedure outlined in Appendix B.1. This is achieved through two major steps: first, the one port antenna is converted to a two-port antenna by adding the second feed line, separated with a gap $g = 2d$ from the first feed line, where d is measured from the centre of the patch, and a PGP corresponding to the second feed line, as shown in Figure 7.1b. The gap g is initially chosen to be $g = 1.6$ mm, but any value of g between 0.1 and 2.0 mm can be selected, which can later be adjusted by sweeping the parameter g in CST DS, between 0.1 and

2.0 mm. The second discrete face port is created on the outer end-face of the second feed line. The two-port antenna is then locked and simulated while the relative amplitude $\gamma = 1$ and phase shift $\varphi = 180°$ are configured at port two. The TARC for the resulting two-port antenna is depicted in Figure 7.3.

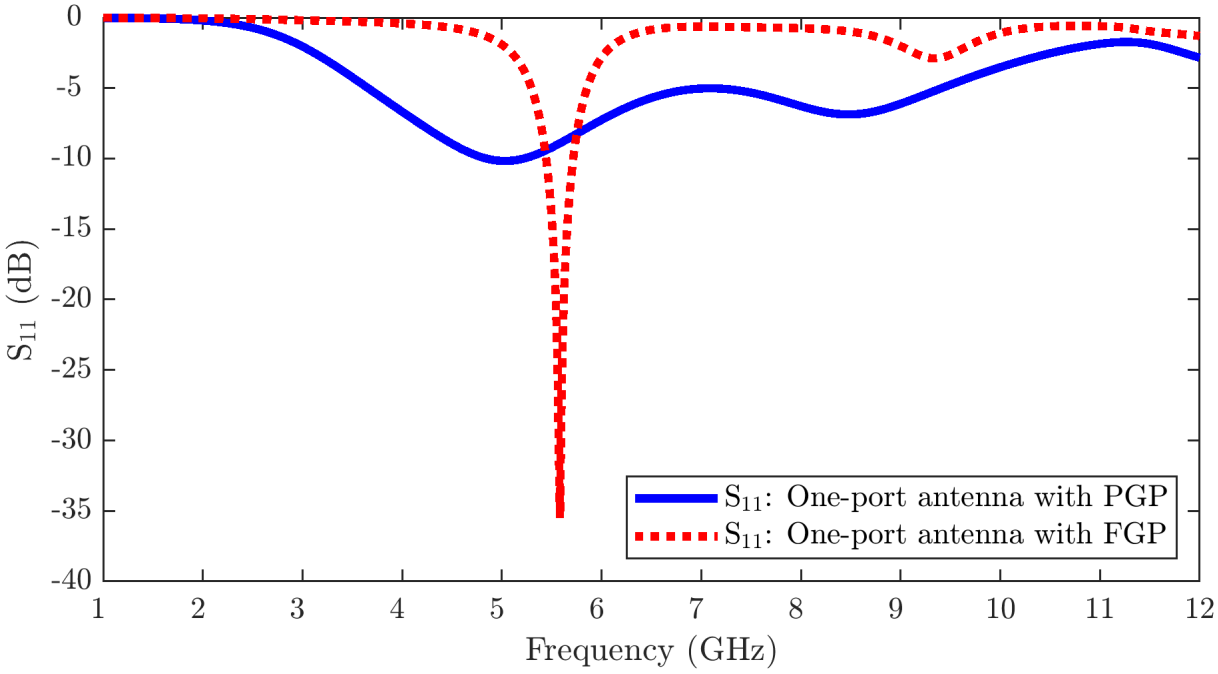


Figure 7.2. S-parameter for the one-port proximity-fed patch antenna under investigation.

The TARC resonance shown in Figure 7.3 has a −10 dB FBW of about 47.5% (calculated using Equation (B.1) in Appendix B.4) at a 4.391 GHz centre frequency. The electrical length at 4.456 GHz resonant frequency is around $ka = 2.1$. To decrease the ka value at resonance, the antenna is optimised in CST DS by changing the antenna dimensions L_p, W_p, L_s, W_s, L_g, w and the gap g in CST DS between 16 and 24 mm, 16 and 24 mm, 32 and 48 mm, 32 and 48 mm, 7 and 12 mm, 1.5 and 4.0 mm, 0.1 and 2.5 mm, respectively, while TARC is being monitored. The theoretical γ and φ variations with frequency of Equations (3.8) and (3.9), which correspond to the TARC resonances are also generated for analysis purposes. Typical optimised results for TARC, theoretical

γ and φ, as well as variation of the electrical length with frequency at different antenna dimensions, are depicted in Figure 7.4 and 7.5. The dimensions for the optimised TARC resonances are depicted in Table 7.1.

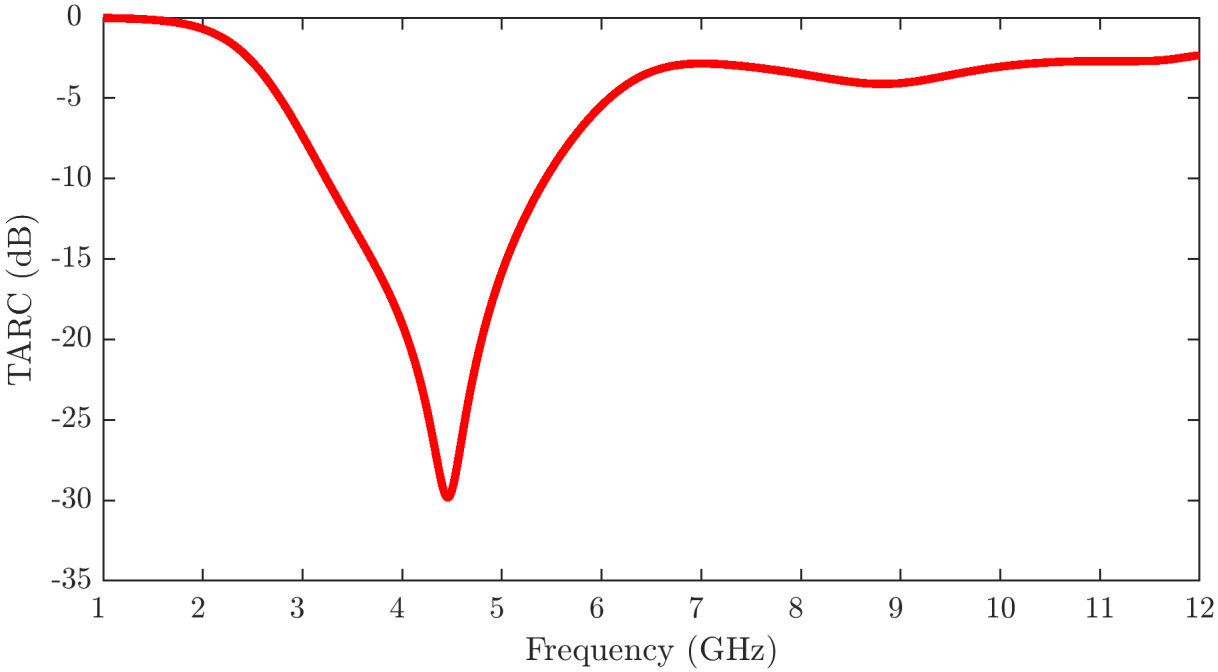
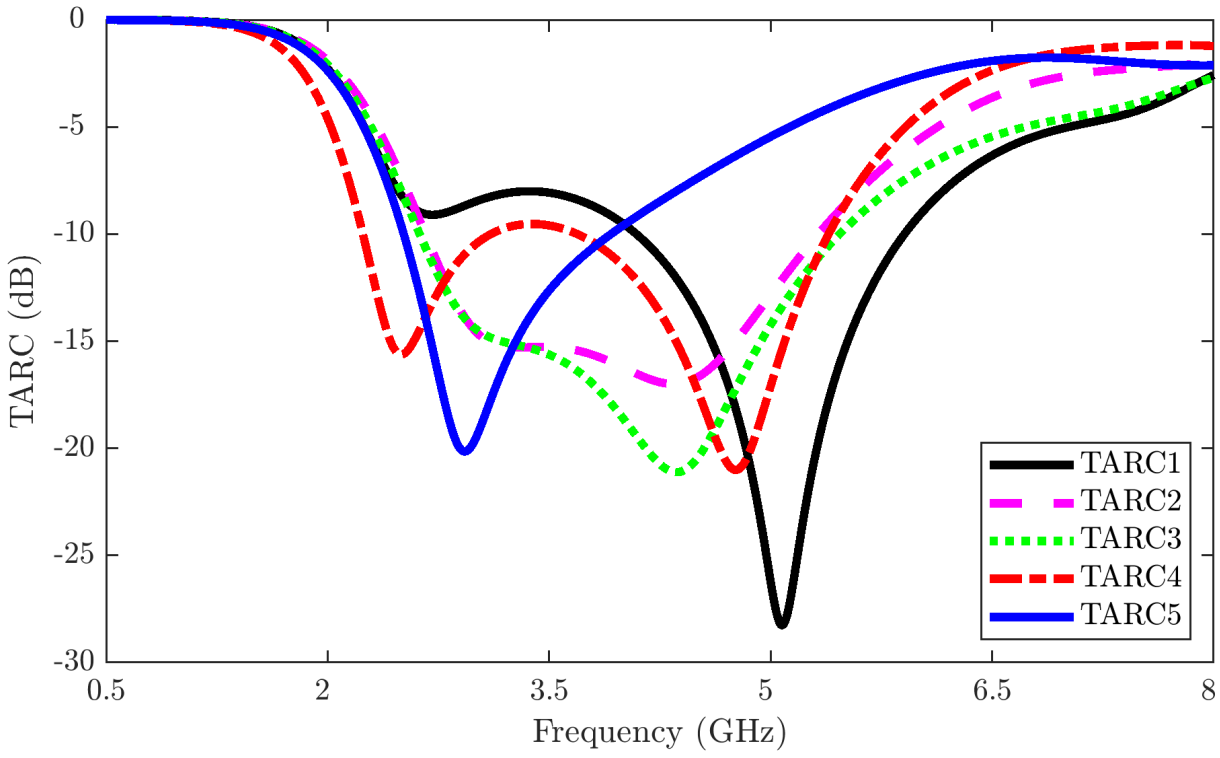


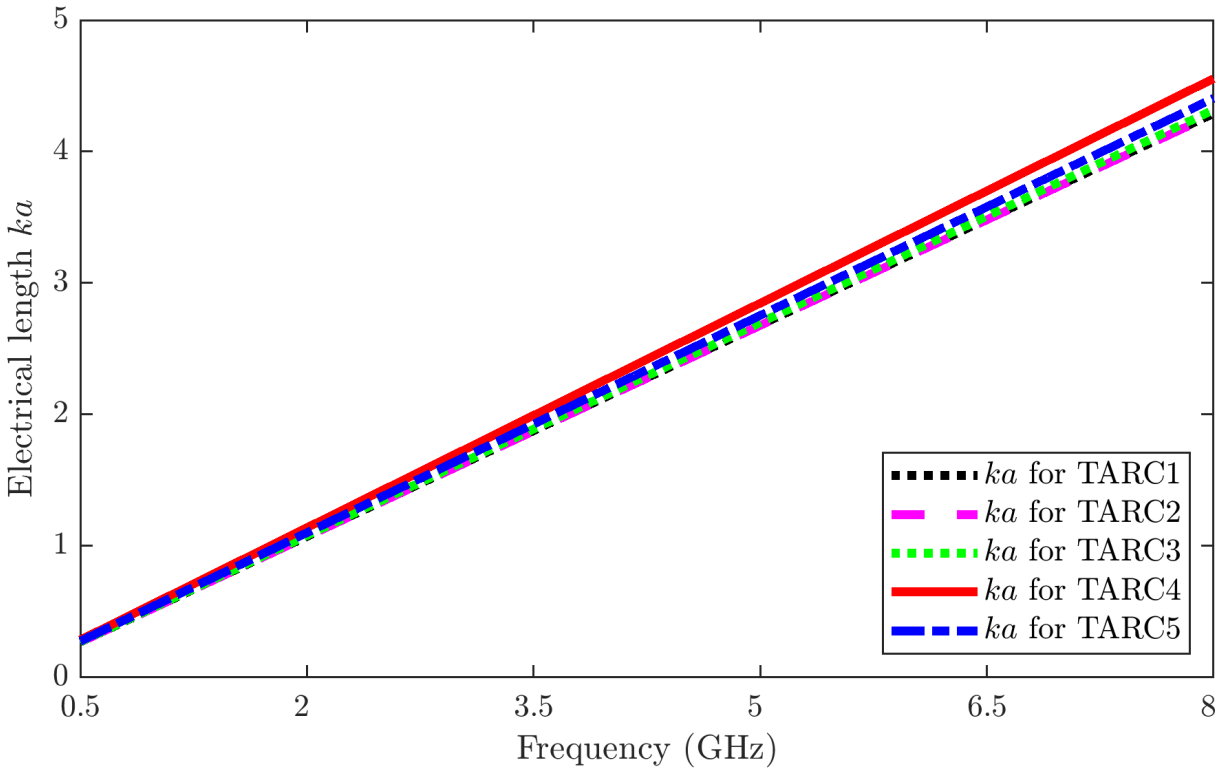
Figure 7.3. TARC resonance for the differentially excited ($\gamma = 1$, $\varphi = 180°$) two-port proximity-fed patch antenna derived from the one-port antenna with S-parameter resonance in Figure 7.2. The dimensions of this antenna are depicted by TARC0 in Table 7.1.

It can be seen in Figure 7.4 and Table 7.1 that TARC4 resonance has the smallest electrical length of around 1.41 at its lower mode frequency (2.480 GHz) than the remaining TARC resonances at their lower mode frequencies. For example, TARC1 resonance has an electrical length of around 1.45 at its lower mode frequency (2.705 GHz), while the remaining TARC responses have ka values larger than 1.6 at their lower modes.

Also, TARC4 resonance depicted in Figure 7.4 and Table 7.1 has better theoretical φ variation at frequencies slightly below 2.480 GHz as shown in Figure 7.5, which gives room for fine-tuning the resonance to improve the matching as well as the corresponding electrical length. Because of this factor, the TARC4 resonance is re-investigated in

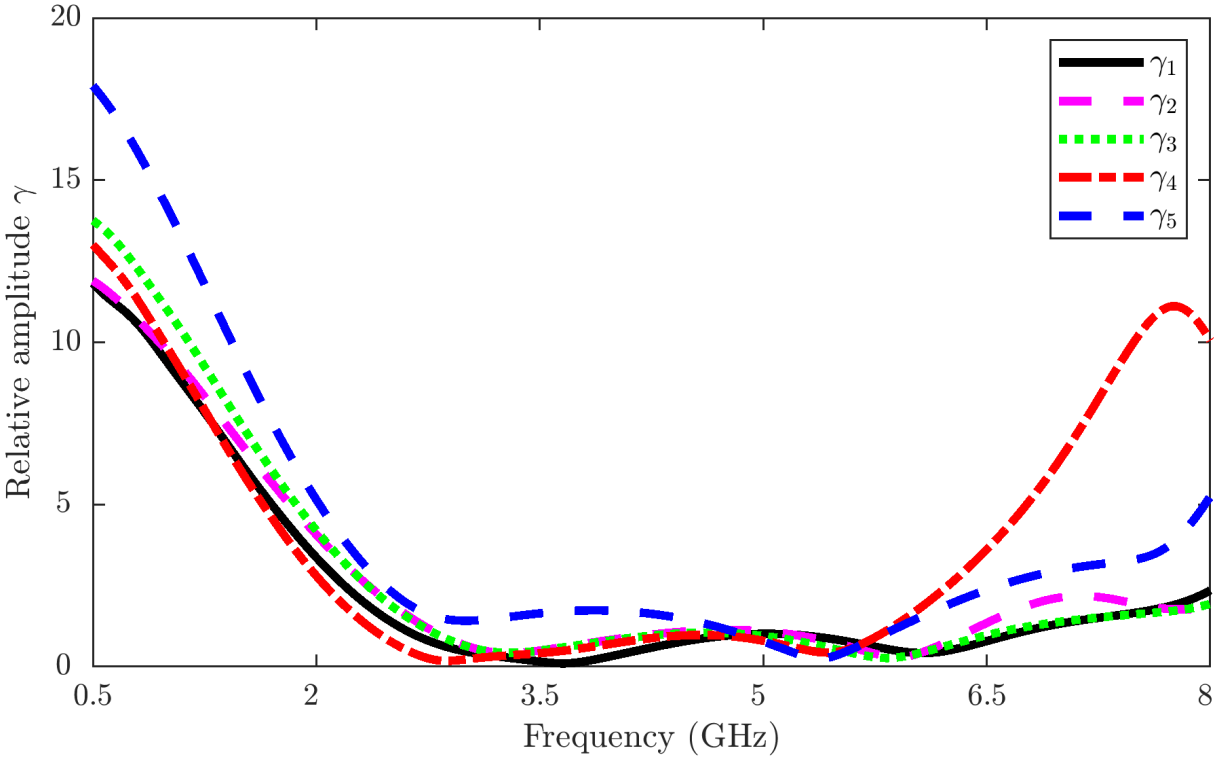


(a)

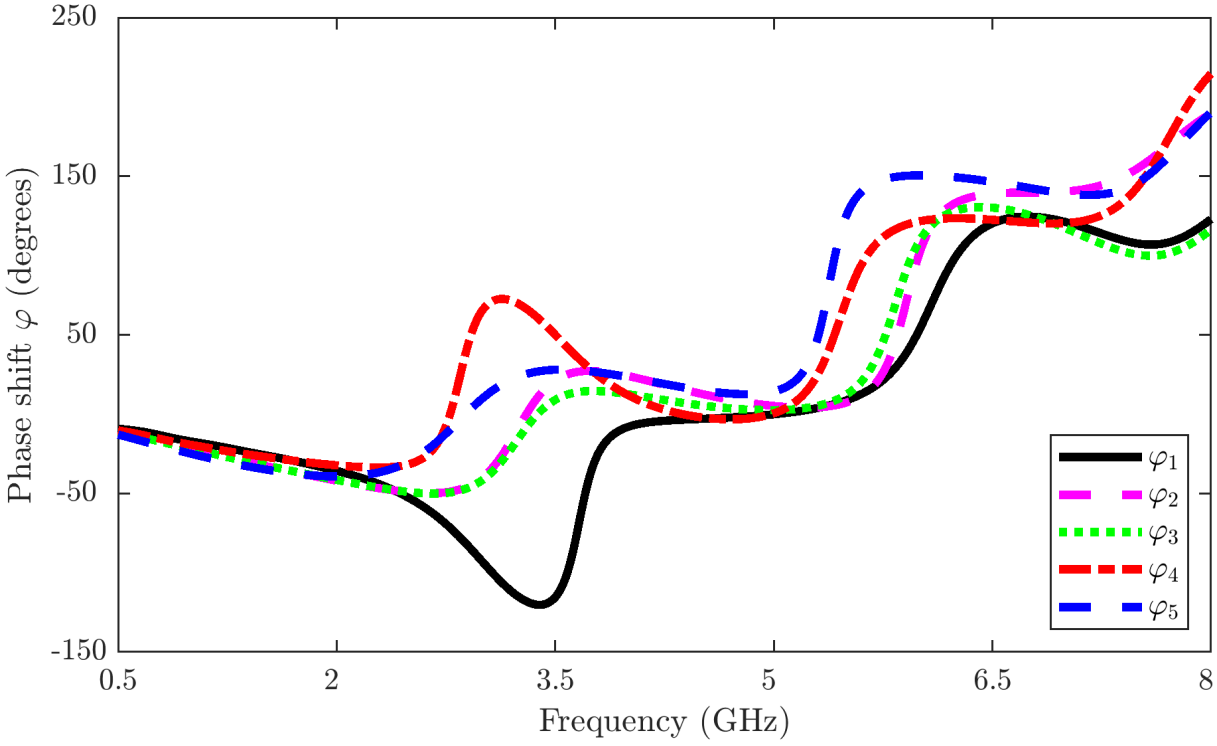


(b)

Figure 7.4. Optimised (a) TARC responses that correspond to the γ and φ variations in Figure 7.5a and 7.5b (b) electrical length corresponding to the TARC resonances in (a).



(a)



(b)

Figure 7.5. Optimised (a) theoretical γ variations with frequency of Equation (3.9) (b) theoretical φ variations with frequency of Equation (3.8) on the two-port antenna. These variations correspond to the TARC resonances depicted in Figure 7.4a.

Table 7.1. Dimensions for the optimised TARC resonances shown in Figure 7.4a and for TARC0 in Figure 7.3, and their corresponding ka values calculated at resonant frequencies, f_r.

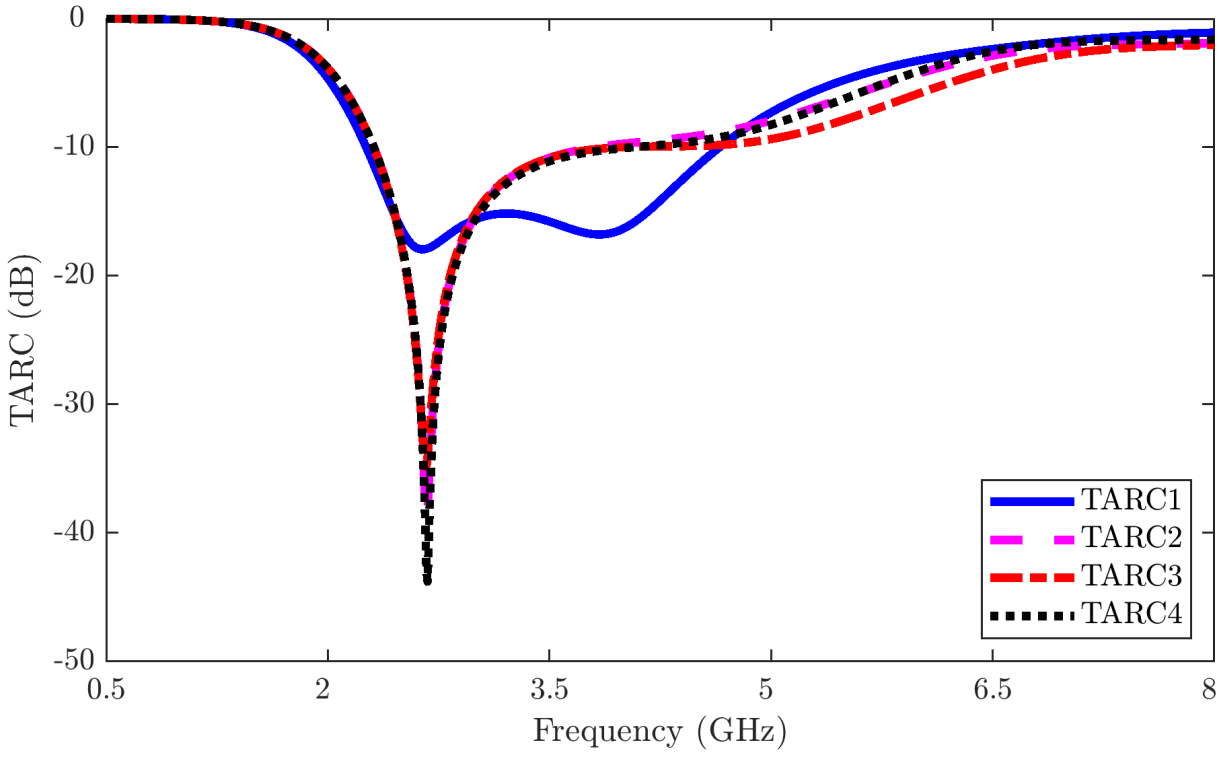
Simulation ID	Antenna dimensions (mm)							ka	f_r (GHz)
	L_p	W_p	L_s	W_s	L_g	w	g		
TARC0	16.04	19.09	32.08	38.18	8.02	2.5	1.6	2.1055	4.583
TARC1	18.0	16.68	38.32	33.69	7.61	1.69	0.5	1.4505	2.705
TARC2	19.6	17.3	36.74	35.31	8.18	2.73	0.3	1.6816	3.140
TARC3	18.97	17.83	39.26	33.11	8.91	2.56	0.9	1.6381	3.035
TARC4	22.72	18.33	43.0	32.98	7.13	2.48	1.3	1.4122	2.480
TARC5	23.9	18.49	41.83	31.57	9.17	3.27	2.5	1.6015	2.908

CST DS through parameter sweep by fine-tuning the antenna dimensions L_p, W_p, L_s, W_s, L_g, w and the gap g between the coupled lines in ranges 21.72 to 23.72 mm, 17.33 to 19.33 mm, 43 to 45 mm, 31.98 to 34.98 mm, 7.13 to 9.13 mm, 1.48 to 3.48 mm, 1.2 and 2.5 mm, respectively.

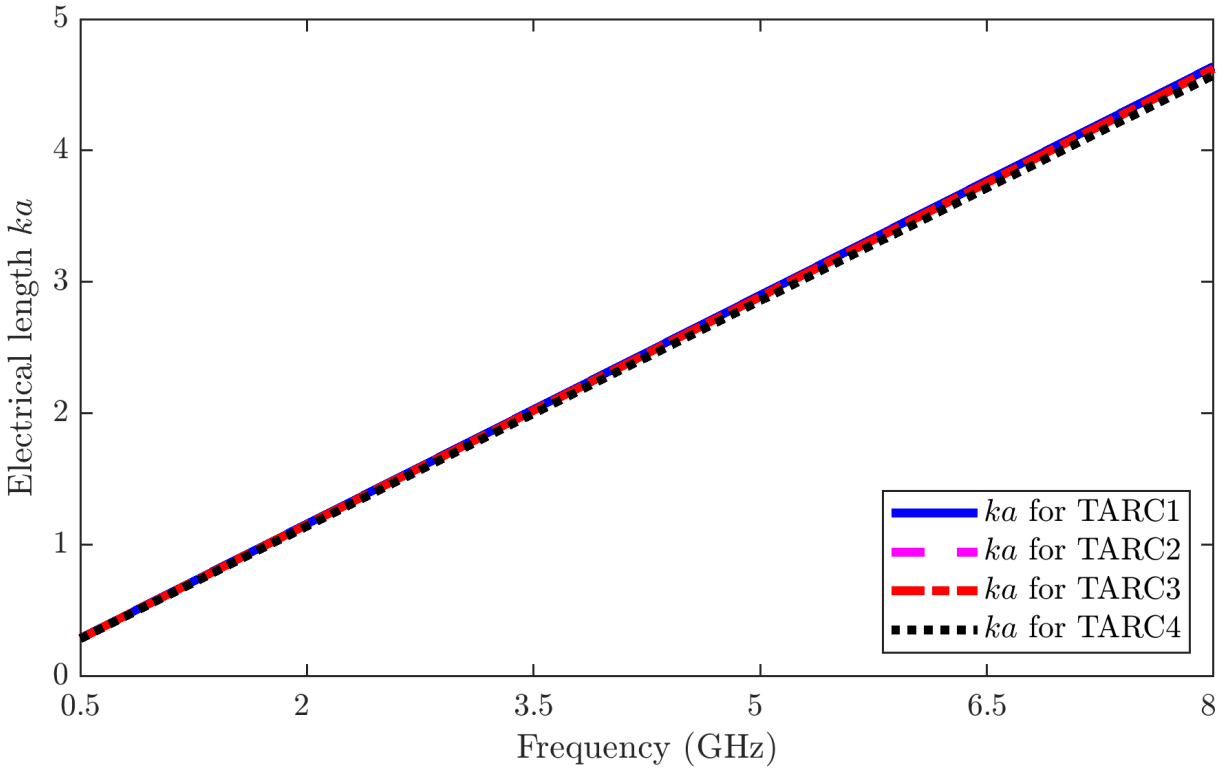
Table 7.2. Dimensions for the fine-tuned TARC resonances shown in Figure 7.6a, and the corresponding ka values calculated at resonant frequencies, f_r.

Simulation ID	Antenna dimensions (mm)							ka	f_r (GHz)
	L_p	W_p	L_s	W_s	L_g	w	g		
TARC1	23.72	18.33	45.0	31.98	9.13	2.48	1.5	1.5300	2.6375
TARC2	23.72	18.33	44.0	32.98	9.13	3.48	2.5	1.5413	2.6675
TARC3	22.72	18.33	44.0	32.98	9.13	3.48	2.5	1.5370	2.660
TARC4	23.72	18.33	44.0	31.98	9.13	3.48	1.5	1.5290	2.675

Typical results for the fine-tuned TARC resonances, as well as for the corresponding theoretical γ and φ variations, are provided in Figure 7.6 and 7.7. The antenna dimensions, which correspond to the fine-tuned TARC resonances, and their corresponding electrical lengths are depicted in Table 7.2. The optimum TARC resonances, as well as the corresponding theoretical φ and γ variations in Figure 7.6 and 7.7 are inspected to identify

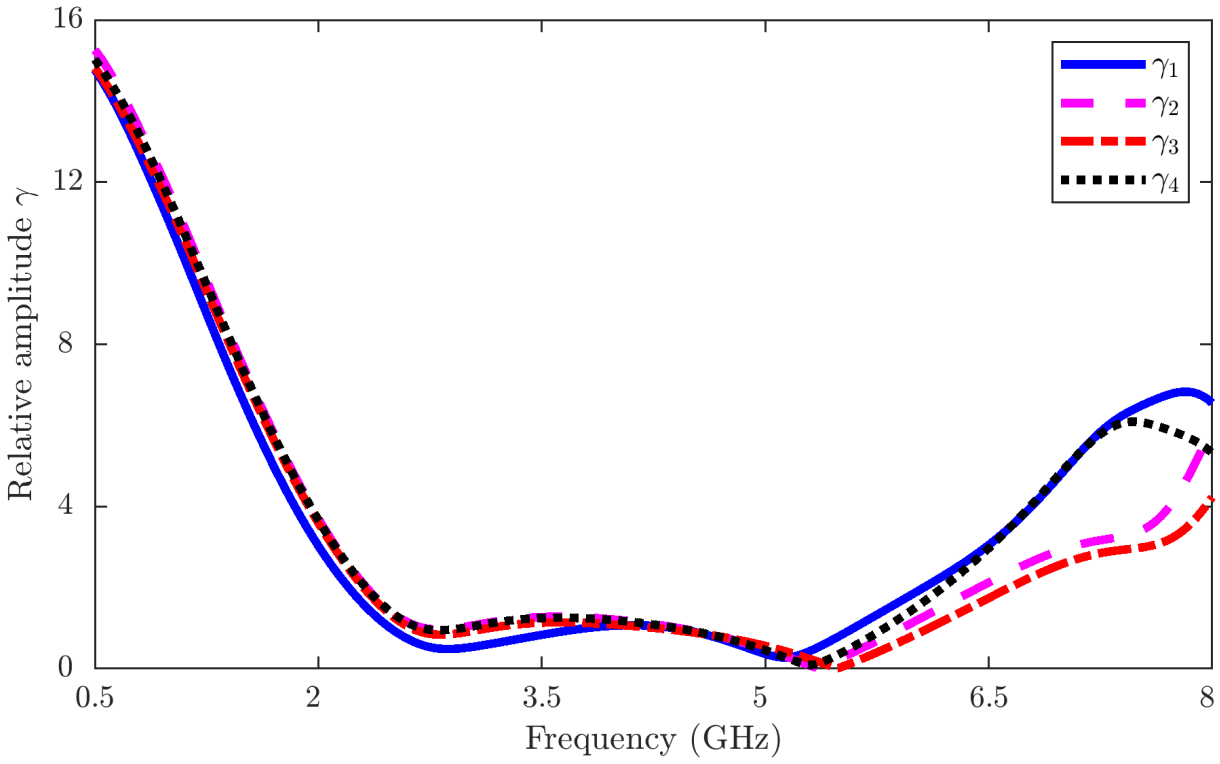


(a)

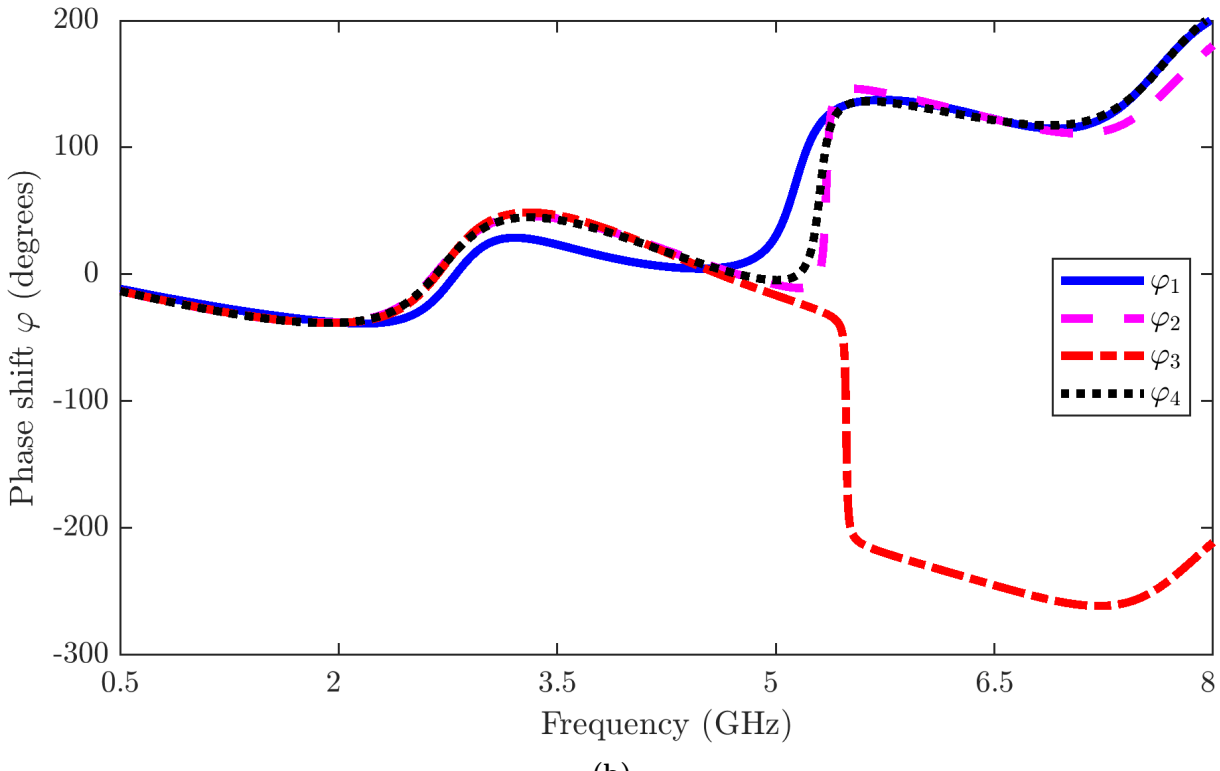


(b)

Figure 7.6. Refined (a) TARC resonances corresponding to the γ and φ variations in Figure 7.5a and 7.5b (b) electrical length corresponding to the TARC resonances in (a).



(a)



(b)

Figure 7.7. Refined results for (a) theoretical γ variations with frequency (b) theoretical φ variations with frequency on the two-port antenna. These variations correspond to the TARC resonances depicted in Figure 7.6a.

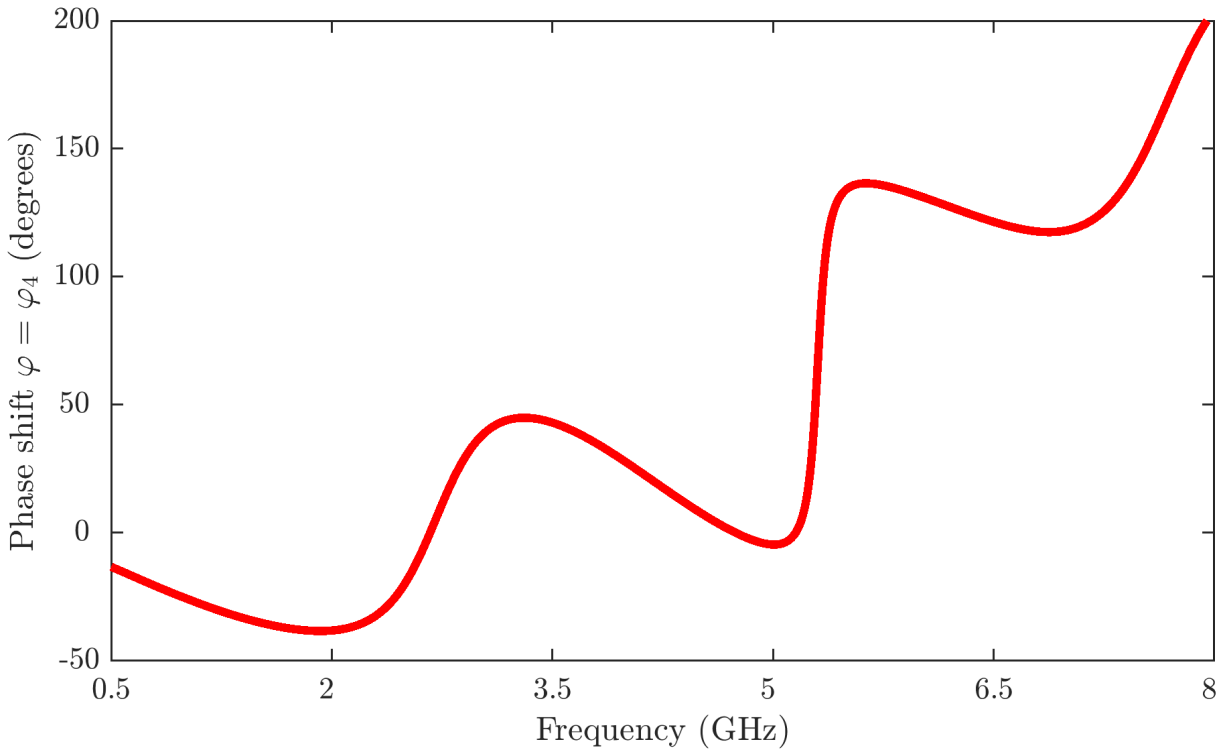
the best TARC with the lowest electrical length. This inspection is done by identifying flat or minima regions, or a combination of the two regions that appear simultaneously in the theoretical φ and γ curves, which present resonant modes for the antenna, as well as the corresponding electrical length for each resonance.

Though all TARC responses in Figure 7.6a have electrical lengths greater than 1.5 at their lower resonances, TARC4 has better theoretical γ and φ variations, shown in Figure 7.7a and 7.7b, at frequencies slightly below 2.675 GHz with $ka = 1.529$ at resonance. These variations ($\varphi = \varphi_4$ and $\gamma = \gamma_4$) are well depicted in Figure 7.8, where it is shown that γ is fairly constant in the frequency range between 3.4 and 3.7 GHz, 7.3 and 8.0 GHz, and has two minima at around 2.6 and 5.3 GHz.

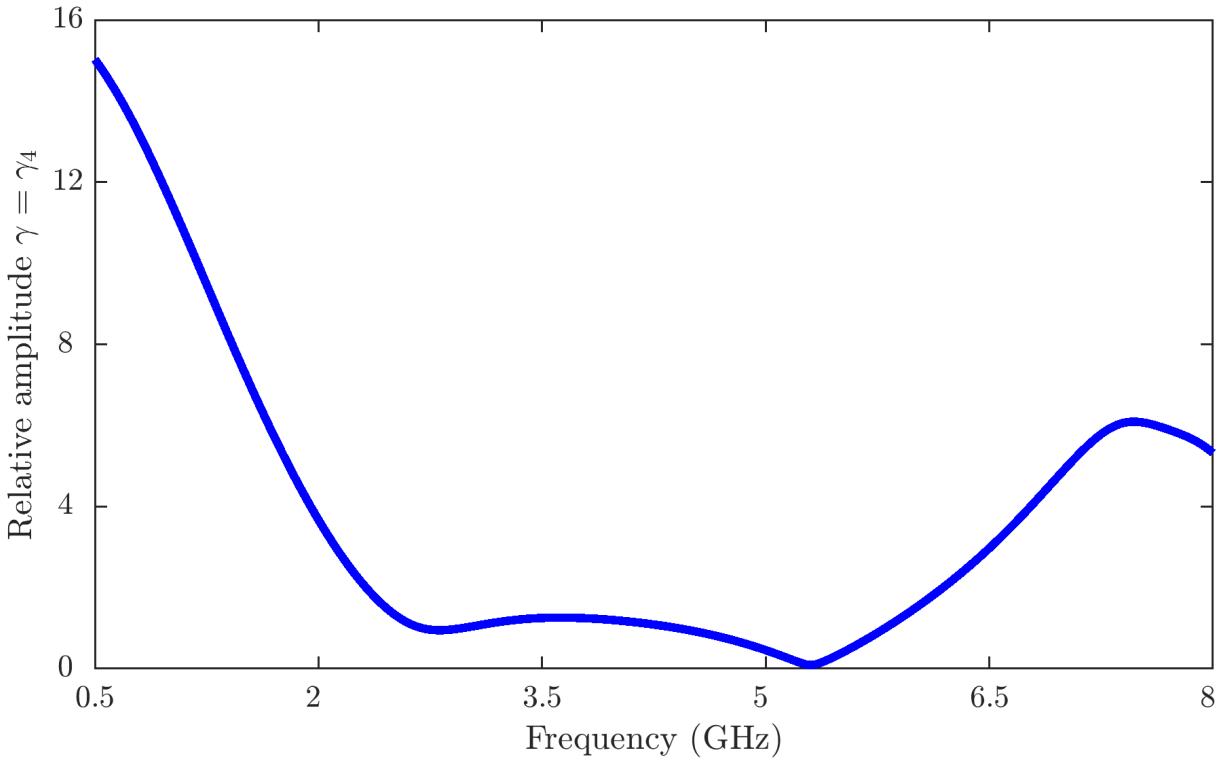
However, because there is neither a flat region nor a minimum in the corresponding φ variations in Figure 7.8a at frequencies between 3.4 and 3.7 GHz, it is not possible to have an injection matched operation at these frequencies. Also, despite the occurrence of the minimum at 5.3 GHz in the γ variation in Figure 7.8b, because of an abrupt change in φ variation at the same frequency in Figure 7.8a, it is impossible to have an injection matched operation at around this frequency.

Besides, the φ minimum at around 7.0 GHz corresponding to a reasonably flat region for the γ variation between 7.3 and 8.0 GHz forms another resonance, which is a higher-order mode requiring a common mode excitation arrangement, as depicted by the TARC resonance with $\gamma = 1$ and $\varphi = 0°$ in Figure 7.9.

The dimensions for the two-port antenna, which correspond to the theoretical γ and φ variations in Figure 7.8, as well as the TARC resonance in Figure 7.9 are provided in Table 7.2. The S-parameter for the corresponding one-port antenna is also compared with



(a)



(b)

Figure 7.8. Variation of the theoretical (a) phase shift φ (b) relative amplitude γ with frequency across the two-port antenna with TARC4 resonance depicted in Figure 7.6a.

TARC in Figure 7.9. The applied γ and φ remained approximately constant across the entire range of investigated frequencies as shown in Figure 7.10.

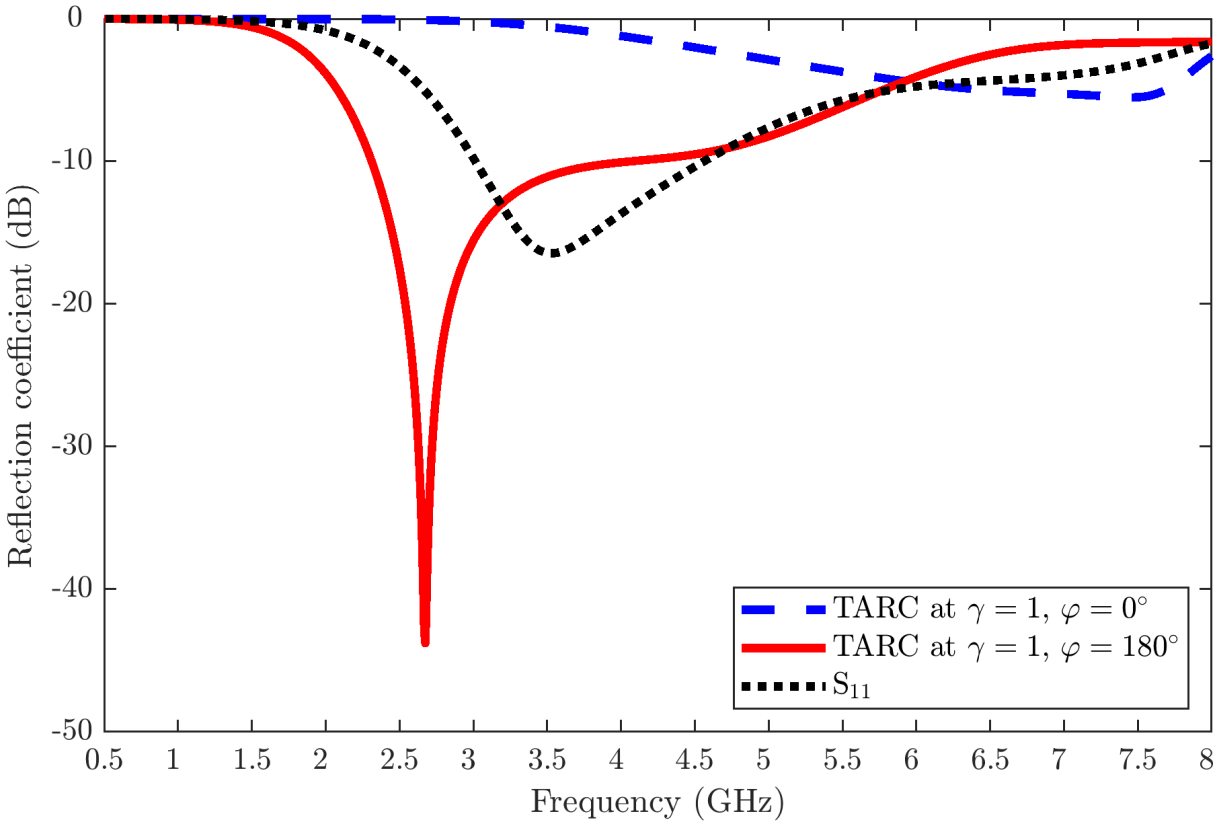
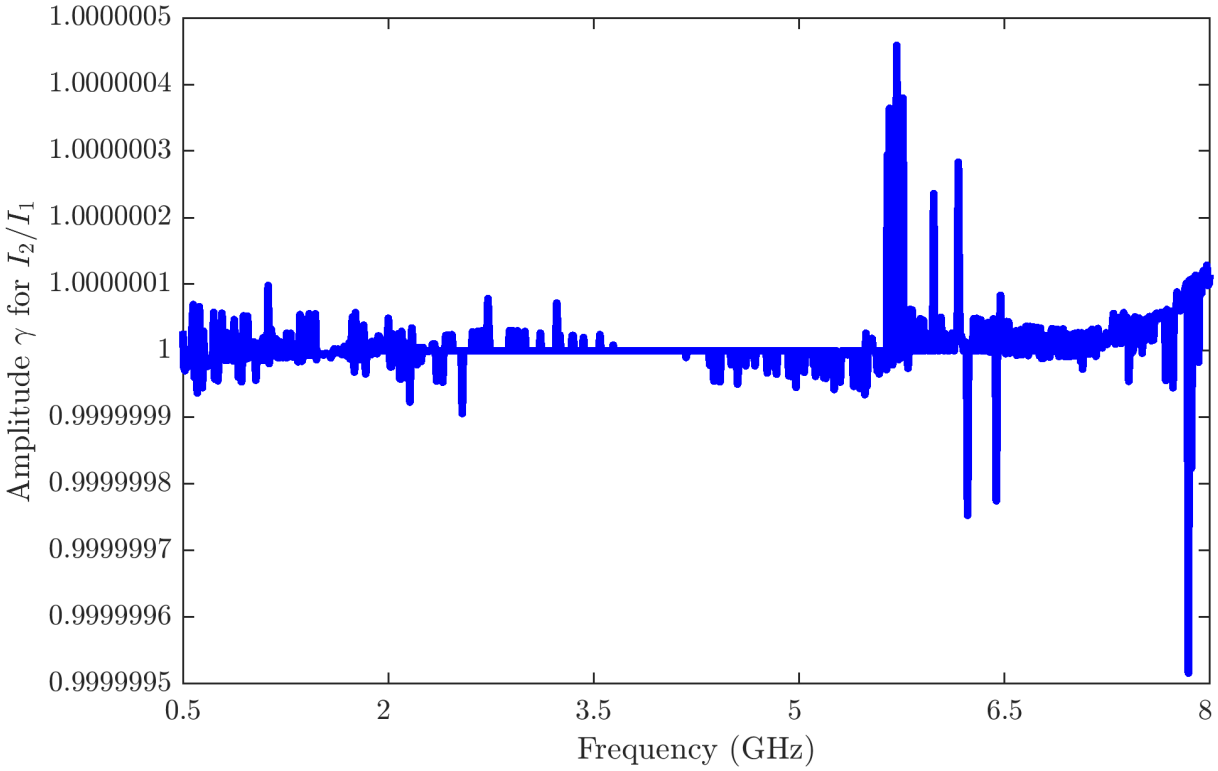
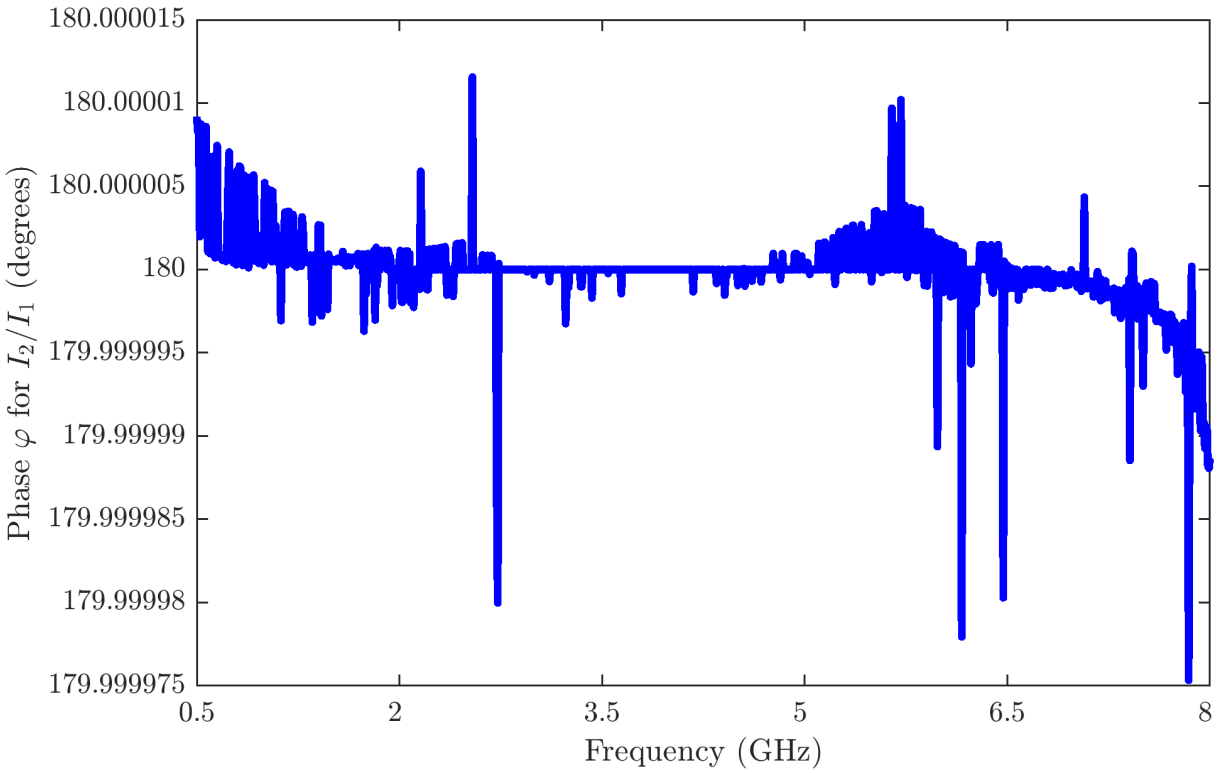


Figure 7.9. Optimum TARC for the differentially excited two-port electrically large antenna in comparison to the common mode TARC, and S-parameter for the corresponding one-port antenna.

The optimum TARC resonance in Figure 7.9 was attained at around 2.675 GHz through differential excitation with $\gamma = 1$ and $\varphi = 180°$ and has an electrical length $ka = 1.5$, which is still an electrically large antenna (ELA) operation. Because of the limitation posed by the non-constant behaviour of the theoretical γ and φ variations with frequency across the antenna at frequencies below 2.675 GHz, caused by the absence of resonant modes at the frequencies, it is not possible to get an electrically small operation without incorporating other techniques. Therefore, tuning with lumped elements is investigated in Section 7.2.1.



(a)



(b)

Figure 7.10. Response of the applied (a) relative amplitude γ (b) phase shift φ to the two-port electrically large antenna whose TARC resonance is depicted in Figure 7.9.

7.2.1 Tuning with LC network

The injection matched antenna depicted in Figure 7.1 with TARC resonance shown in Figure 7.9 is now matched with an L-section of lumped elements at each of its ports using a configuration given in Figure 7.11. The main objective here is to tune the antenna into some electrically small resonances with $ka < 1$ just below the 2.675 GHz resonance. The inductance and capacitance at ports one and two are simultaneously varied in the ranges $C_1 \in (1, 20)$ picofarad (pF) and $L_1 \in (1, 20)$ nanohenry (nH), and $C_2 \in (1, 20)$ pF and $L_2 \in (1, 20)$ nH, respectively, through parameter sweep in CST DS. The corresponding TARC for this parameter sweep is given in Figure 7.12.

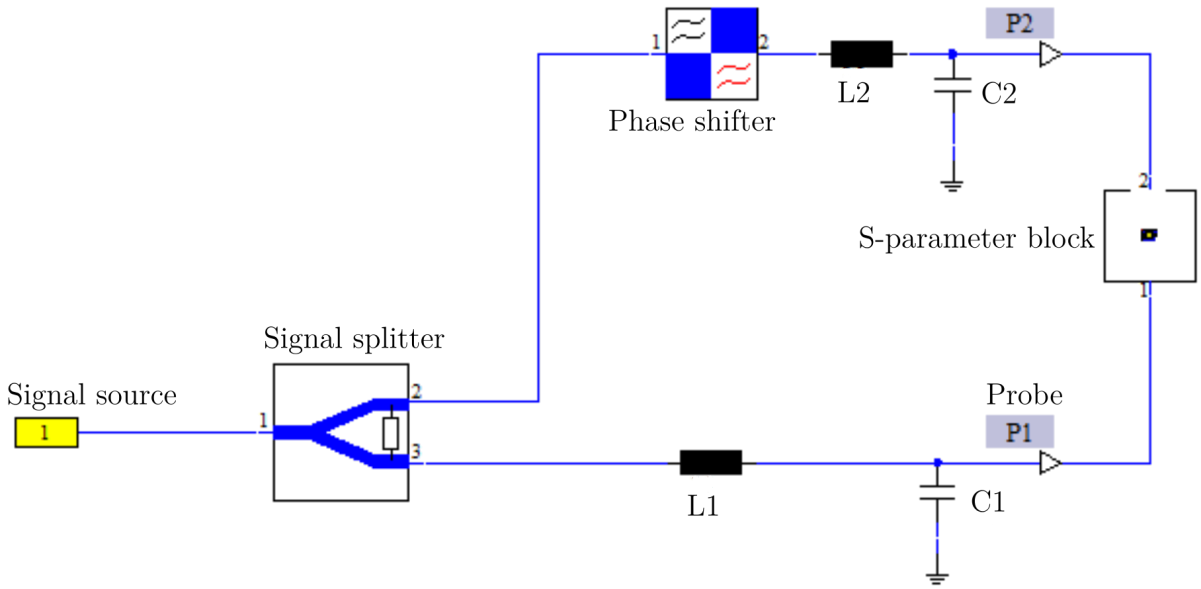


Figure 7.11. Architecture for an L-section of lumped elements matching of an injection matched antenna in CST DS.

A careful investigation of how the applied capacitances and inductances at the two ports affect the matching of the two-port injection matched antenna shows that when $C_1 = C_2$ and $L_1 = L_2$, such as $C_1 = C_2 = 18$ pF and $L_1 = L_2 = 10$ nH, the TARC resonance of Figure 7.9 is slightly improved by increasing the matching depth by up to around 4 dB,

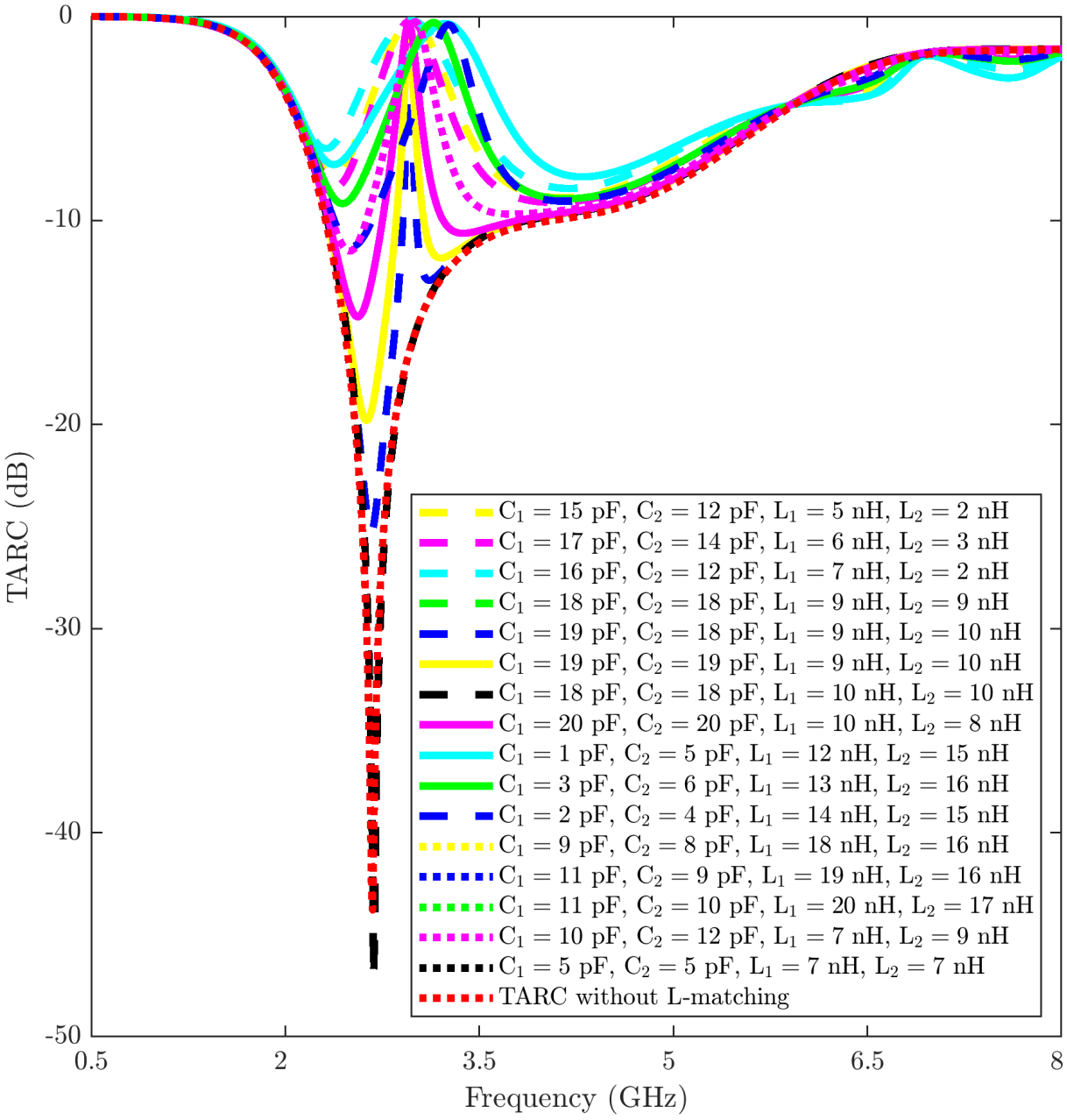
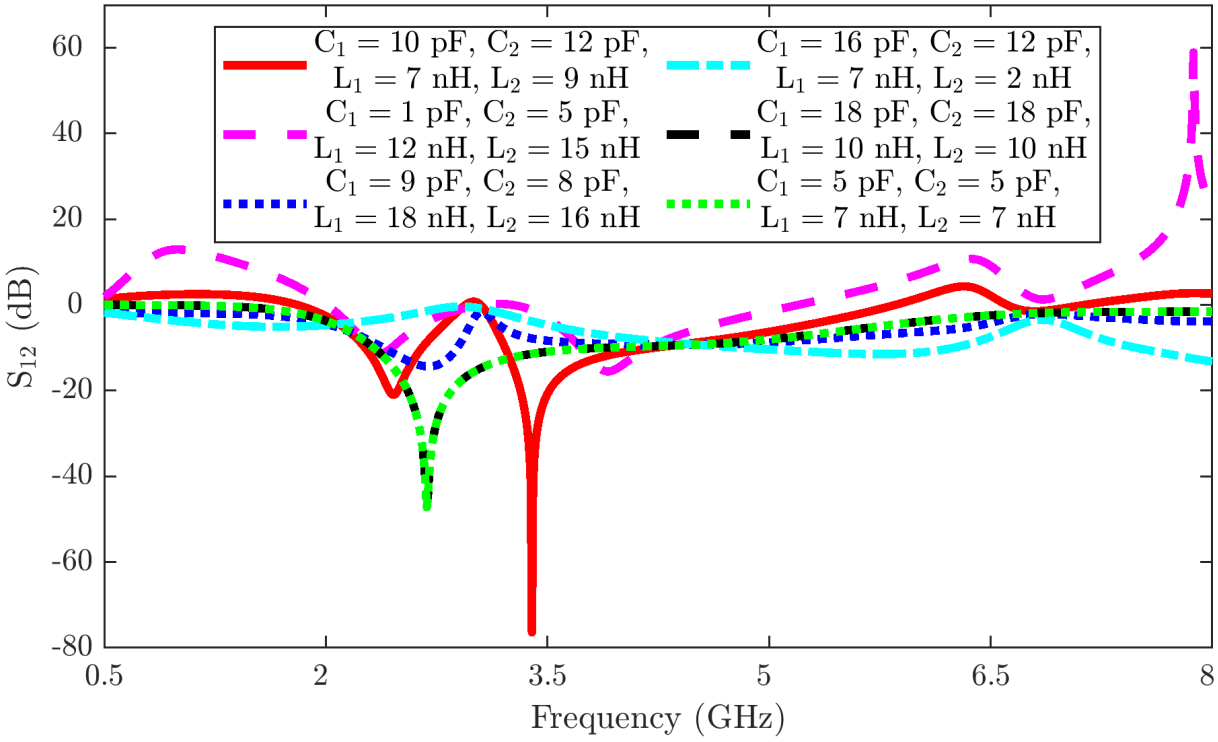


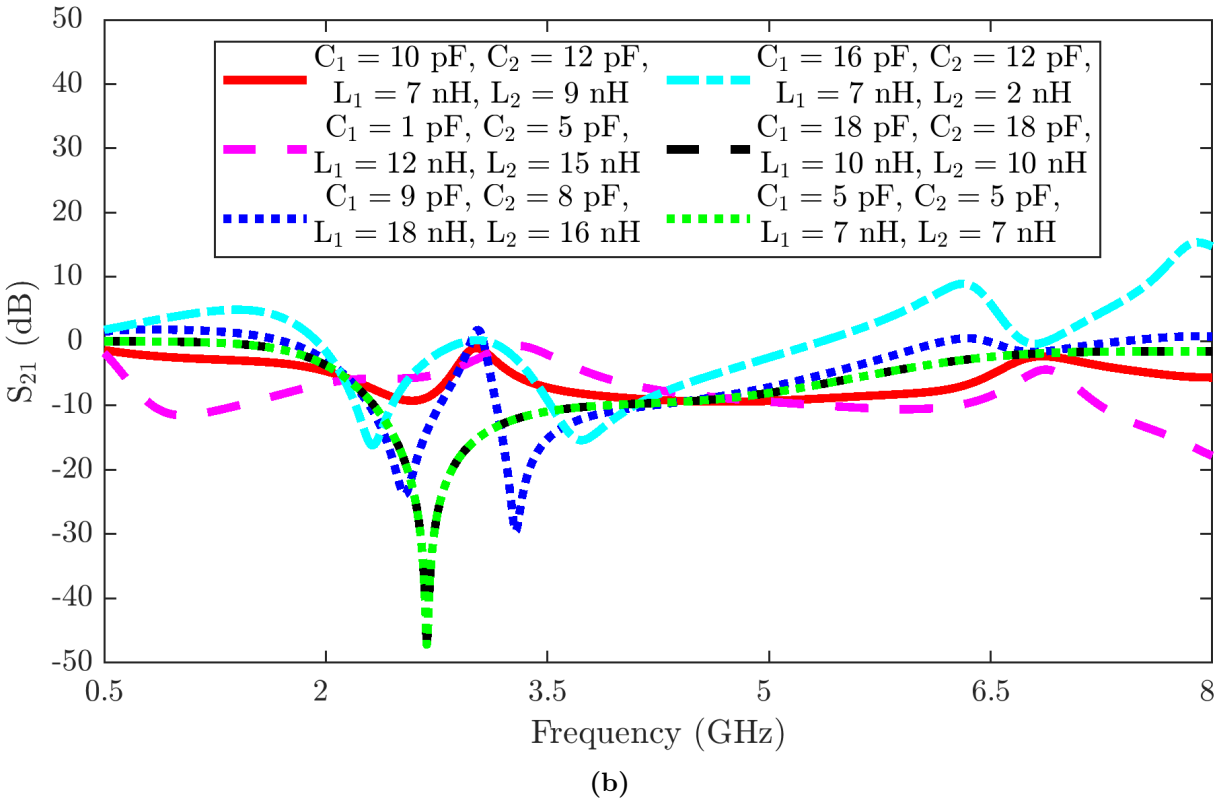
Figure 7.12. Typical optimisation results for TARC when the two-port patch antenna whose TARC resonance is depicted in Figure 7.9 was matched with LC networks at its two ports.

but the resonance remains unchanged. Other combinations of C_1, L_1, C_2, and L_2 such as $C_1 = 10$ pF and $L_1 = 7$ nH, $C_2 = 12$ pF and $L_2 = 9$ nH, distort the matching by causing large variations in the applied γ and φ as shown in Figure 7.14a and 7.14b, which cause the antenna to lose the injection matching. Because of this phenomenon, the TARC resonances attained through $C_1 \neq C_2$ and $L_1 \neq L_2$ combinations of lumped elements are largely enveloped by the injection matched TARC response without LC matching as shown in Figure 7.12. This observation can also be accounted for by investigating the coupling losses between the two ports when the injection matched antenna is matched with lumped elements shown in Figure 7.13a and 7.13b.

It is shown in Figure 7.13a and 7.13b that there is a significant direct flow of energy between the two ports when $C_1 \neq C_2$ and $L_1 \neq L_2$, which shows that the applied relative amplitude γ is modified to values greater or less than $\gamma = 1$. Typically, when $C_1 = 1$ pF, $C_2 = 5$ pF, $L_1 = 12$ nH, and $L_2 = 15$ nH there is a flow of energy from port two to port one, which is caused by $\gamma < 1$ at port two in some frequencies, such as between 0.5 and 2 GHz, and 6 and 8 GHz as shown in Figure 7.14a. On the other hand, when $C_1 = 16$ pF, $C_2 = 12$ pF, $L_1 = 7$ nH, and $L_2 = 2$ nH there is a flow of energy from port one to port two caused by $\gamma > 1$ at port two in frequencies between 0.5 and 2 GHz, and 5.8 and 8 GHz. Also, the applied γ and φ variations when combinations $C_1 \neq C_2$ and $L_1 \neq L_2$ of the lumped elements (such as $C_1 = 1$ pF, $C_2 = 5$ pF, $L_1 = 12$ nH, and $L_2 = 15$ nH) are used for matching, as shown in Figure 7.14a and 7.14b, are not maintained across the entire frequency range of investigation, which is contrary to the injection matching theory. However, for the combinations $C_1 = C_2$ and $L_1 = L_2$ (such as $C_1 = C_2 = 5$ pF and $L_1 = L_2 = 7$ nH), the applied γ and φ variations with frequency (shown in Figure 7.14)

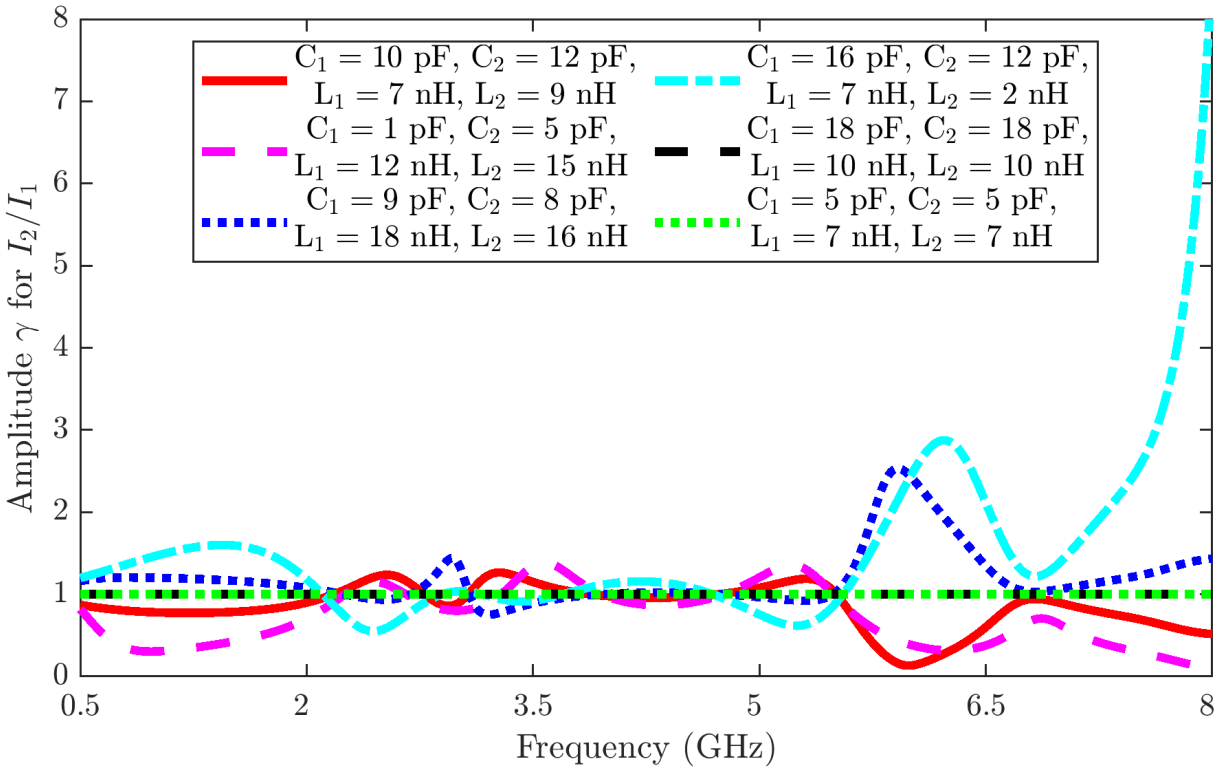


(a)

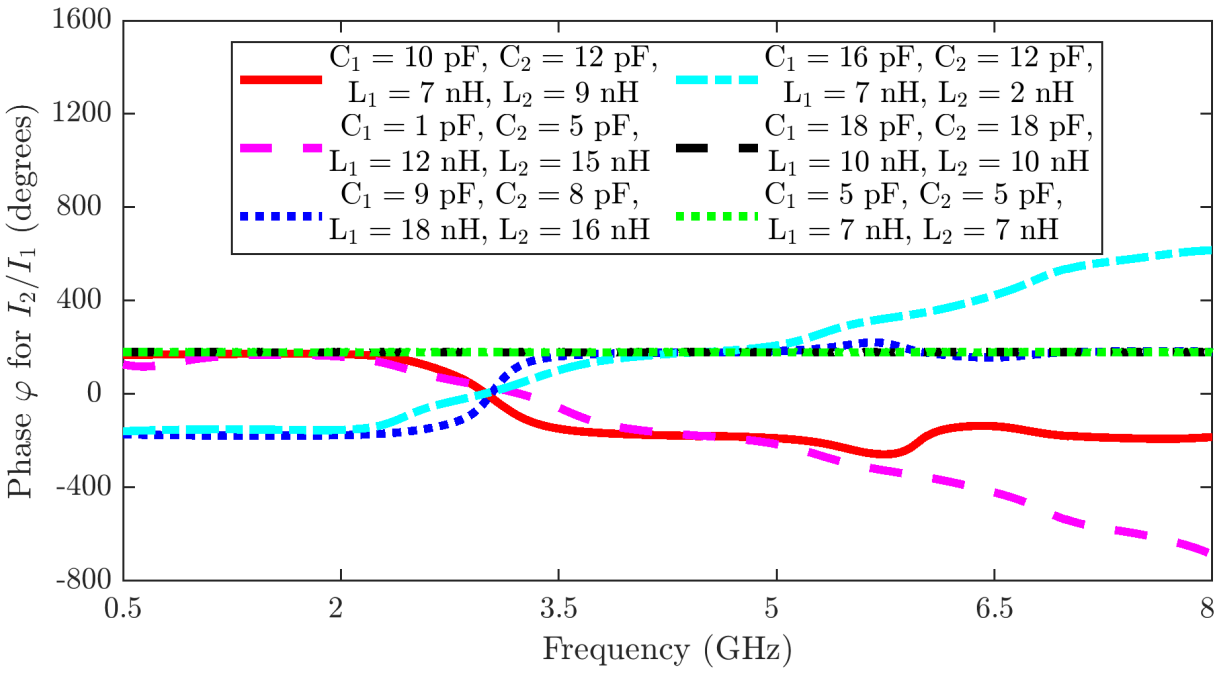


(b)

Figure 7.13. Typical optimised (a) S_{12} for an LC matched two-port injection matched patch antenna (b) S_{21} for the LC matched injection matched patch antenna.



(a)



(b)

Figure 7.14. Simulated response of the applied (a) relative amplitude γ between the currents I_1 and I_2 when the LC matched two-port patch antenna was injection matched at $\gamma = 1$ and $\varphi = 180°$ (b) phase shift φ between the currents I_1 and I_2 when the LC matched two-port patch antenna was injection matched at $\gamma = 1$ and $\varphi = 180°$.

are constantly maintained at $\gamma = 1$ and $\varphi = 180°$, respectively, across the entire frequency range of investigation, which shows that the injection matching theory is satisfied.

It is desired that after the injection matched operation, the applied γ and φ responses should maintain approximately constant values across the entire frequency range of investigation. However, this condition has largely not been satisfied after adding lumped elements to the injection matched antenna, making it impossible to tune an injection matched antenna with lumped elements outside the TARC response attained by the applied γ and φ values before lumped elements are employed. This is because the injection matching technique is based on the excitation of characteristic modes that require excitation signals with equal amplitudes and with 180° phase shift between them to allow a differential excitation of the modes or the in phase excitation signals for the common mode excitation of the modes. Therefore, the concept of tuning an injection matched antenna with lumped elements to an ESA mode is not feasible. Instead, another concept of modifying the radiating element of an injection matched antenna to lengthen the current path is investigated in the next section.

7.2.2 Slow-wave structure

The radiating element for the two-port antenna is modified by creating slots and slits around it. These (slots and slits) can extend the current flow path to increase the antenna's electrical length while the overall dimensions of the antenna remain unchanged. In this way, the surface current wave propagating on the antenna takes a longer path to propagate between the two antenna ports than it could take before the radiating element is modified. Because the wave takes a longer path to propagate between the two ends of the modified

antenna, the EM wave is referred to as a slow-wave, and the structure is called a slow-wave structure.

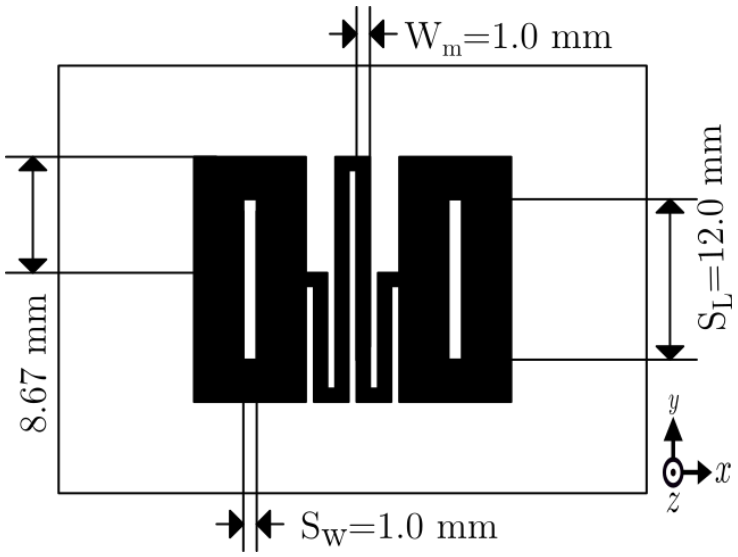


Figure 7.15. Modified layer 3 of the two-port patch antenna under investigation. Other dimensions of the antenna remained unchanged.

While the antenna is injection matched at $\gamma = 1$ and $\varphi = 180°$, the width of the slot S_w, length of the slot S_L, and width of the meandered section W_m on the modified antenna in Figure 7.15 are varied between 0.5 and 1 mm, 8 and 12 mm, and 0.5 and 1 mm, respectively, in CST DS. The TARC resulting from this parameter sweep is given in Figure 7.16. Though all TARC responses in Figure 7.16 satisfy the criterion $ka < 1$, the antenna is still poorly matched. So there is a need to investigate the modal significance of the modified antenna (in Figure 7.15) to determine whether the antenna was properly excited. It is shown in Figure 7.17 that mode one is resonant at around 1.553 GHz and has the best modal significance in that frequency.

Also, the characteristic current in Figure 7.18 shows that the principal current for mode one is differential with respect to the opposite short edges of the patch, which has been excited by applying two differentially driven excitation signals from the opposite edges

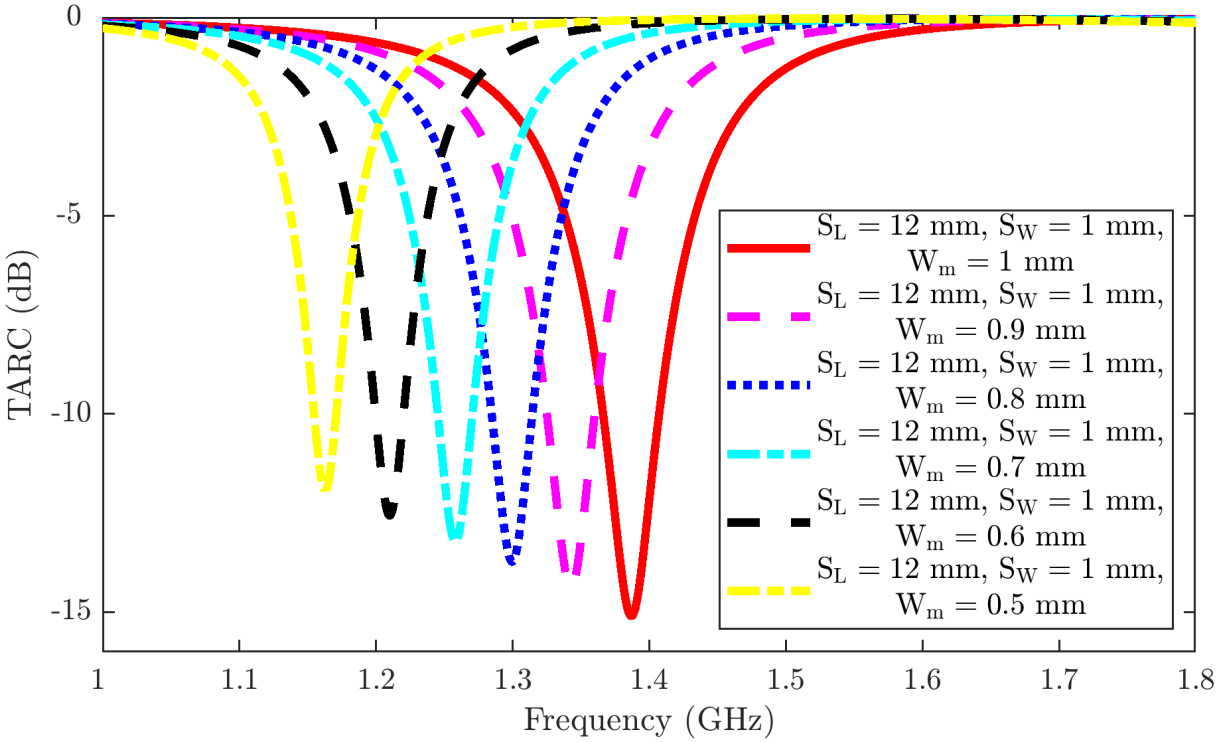


Figure 7.16. Optimised TARC values for the two-port ESA.

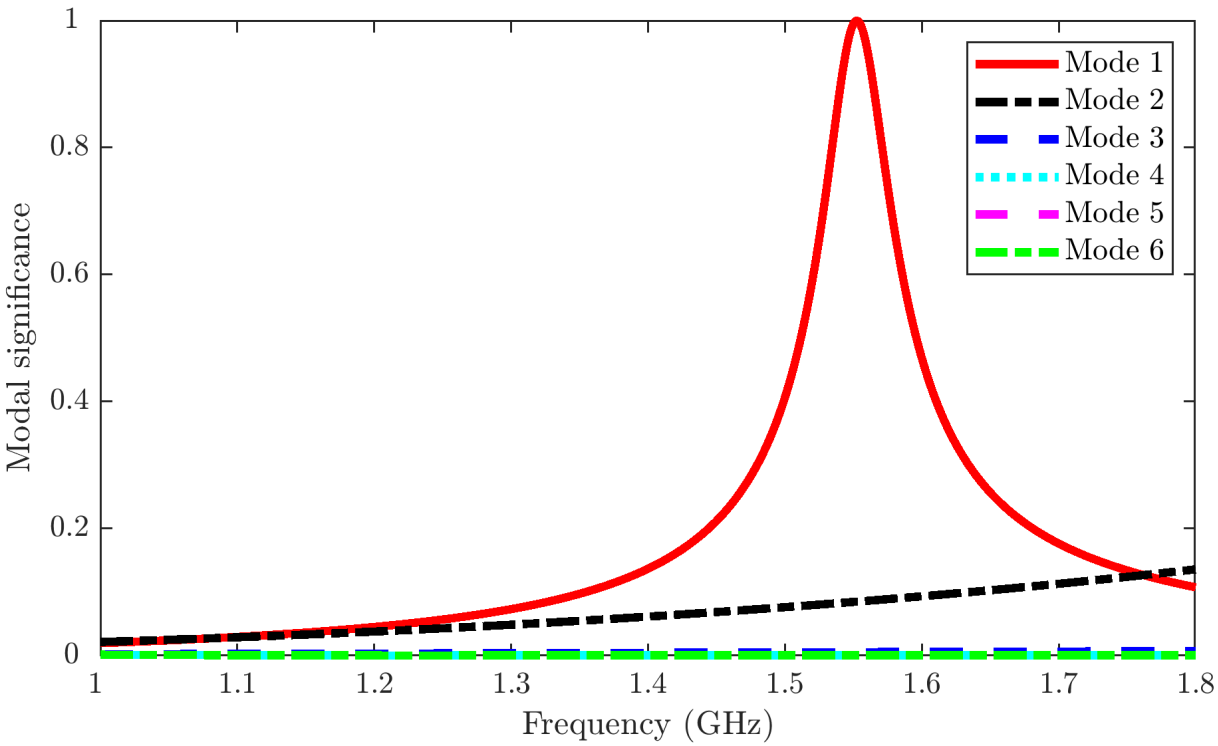


Figure 7.17. Modal significance for the first six characteristic modes of the ESA under investigation sorted at around 1.386 GHz. The CMA was conducted in CST MWS using a Multilayer Solver with solver and mesh settings provided in Appendix B.2.

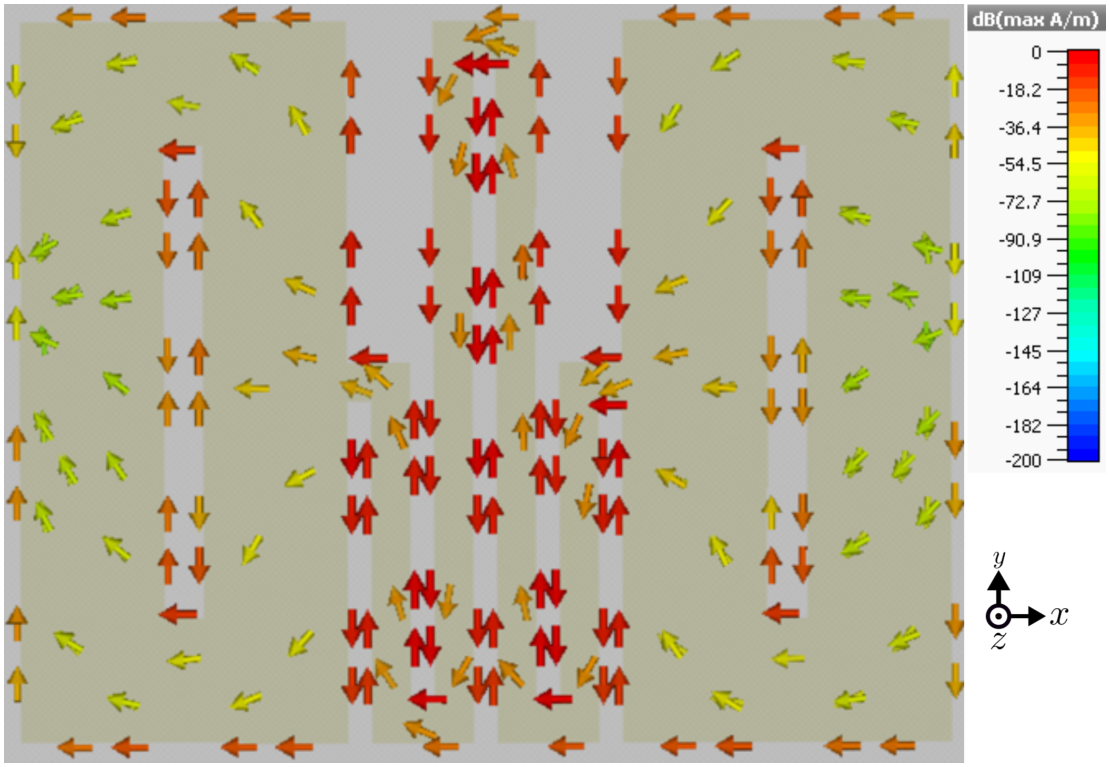


Figure 7.18. Characteristic mode one current on the ESA whose modal significance is shown in Figure 7.17.

of the patch through the two coupled lines. Besides, the characteristic modal current is strongest at the meandered section of the modified patch. These observations reveal that the TARC resonance can be improved by changing the width of the coupled lines and the gap between the two lines so that the coupled lines are aligned with the central part of the meandered section where the modal current is strongest. Typically, the width w and gap g between the coupled lines are varied between 1.5 and 3.5 mm, and 1.5 and 23 mm, respectively, through parameter sweep in CST DS and the results for this parameter sweep are provided in Figure 7.19.

Considering the -10 dB bandwidth and better matching criterion, the TARC resonance with $g = 10.5$ mm and $w = 1.7$ mm in Figure 7.19 is selected, re-simulated with an increased number of field monitors, plotted (in Figure 7.20) and discussed in Section 7.3.

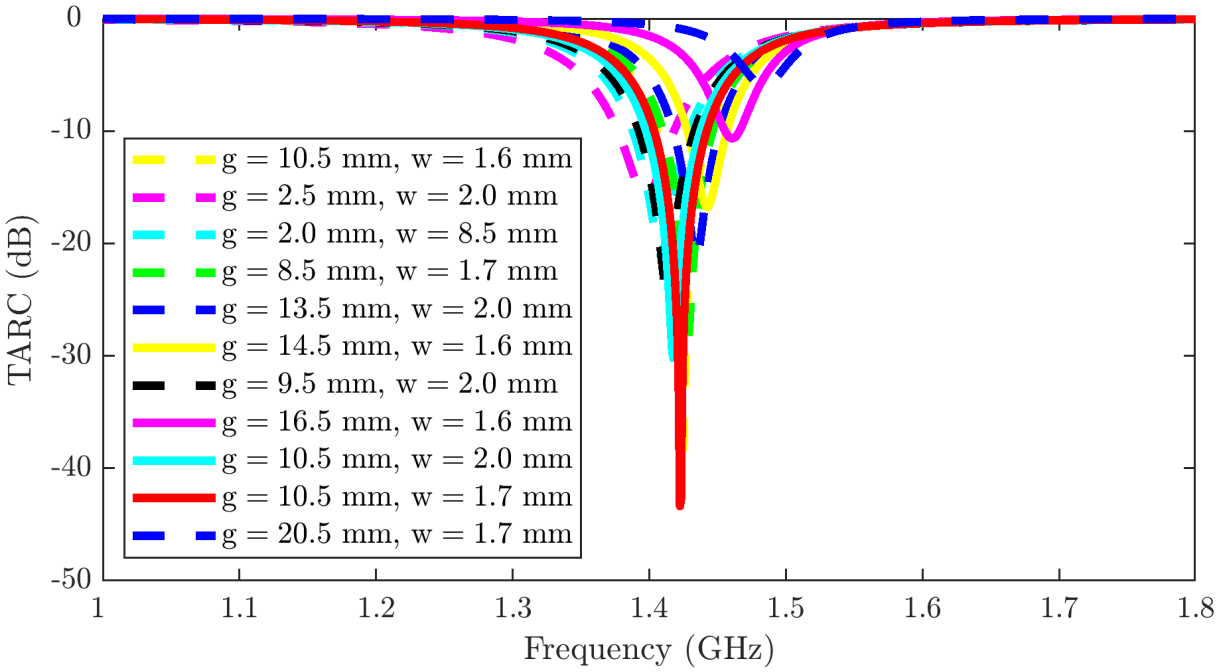


Figure 7.19. Typical optimisation results for the TARC when the two-port ESA was matched by varying the gap between two coupled lines and the width of the coupled lines.

7.3 Results and discussion

The TARC for the two-port antenna and the S-parameter for the corresponding one-port antenna given in Figure 7.20 show that the two antennas are electrically small with electrical lengths of $ka = 0.81$ and $ka = 0.87$, at the centre frequencies of 1.423 and 1.514 GHz, respectively. The S_{11}, S_{21}, S_{12}, and S_{22} for the two-port ESA, shown in Figure 7.20, are equal to the TARC resonance because of the symmetry between the two feed points. The Q factor for the two-port antenna (calculated using Equation (B.5) in Appendix B.5) at the centre frequency is about 37.1, which is approximately to $12Q_{Chu}$ (Q_{Chu} was calculated using Equation (B.4) in Appendix B.5), while that of the corresponding one-port antenna is about 99.6, which is approximately to $37Q_{Chu}$. Because of the difference in Q-factors, the two-port antenna has a slightly wider -10 dB FBW of about 2.7% (calculated

using Equation (B.1) in Appendix B.4) compared to the bandwidth of 1.0% attained by the corresponding one-port antenna.

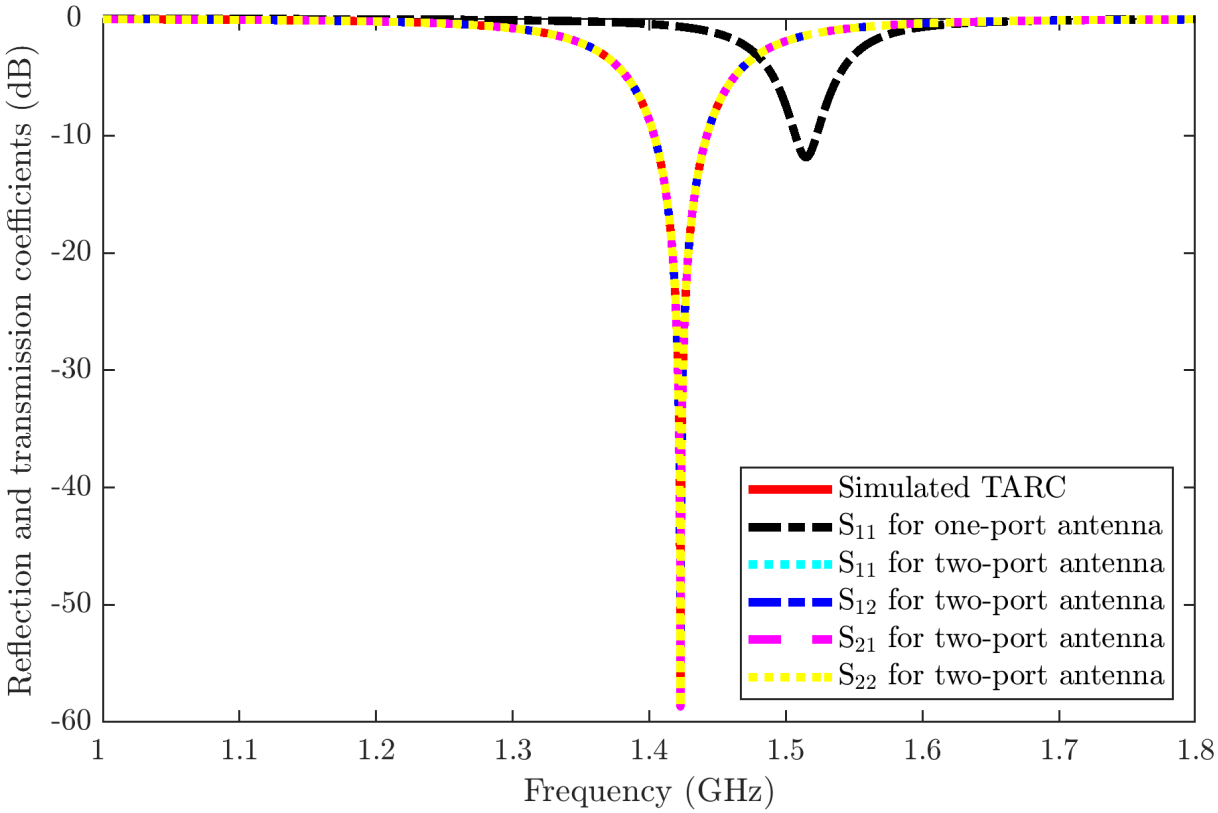


Figure 7.20. Simulated TARC, individual port reflection coefficients, and transmission coefficients between the two ports for the two-port injection matched ESA, and the S-parameter for the corresponding one-port ESA.

At the centre frequencies of the two antennas, the two-port ESA has a matching efficiency of 99.99%, whereas the corresponding one-port ESA has a matching efficiency of 93.4% as shown in Figure 7.21. The difference in matching efficiency observed at the centre frequencies of the two antennas is attributed to the difference in impedance matching attained by the two antennas, where the two-port ESA has an excellent impedance matching than the corresponding one-port ESA. On the other hand, at the centre frequency, the two-port injection matched ESA has a radiation efficiency of 93%. In contrast, the corresponding one-port ESA has a radiation efficiency of 91% at the centre frequency.

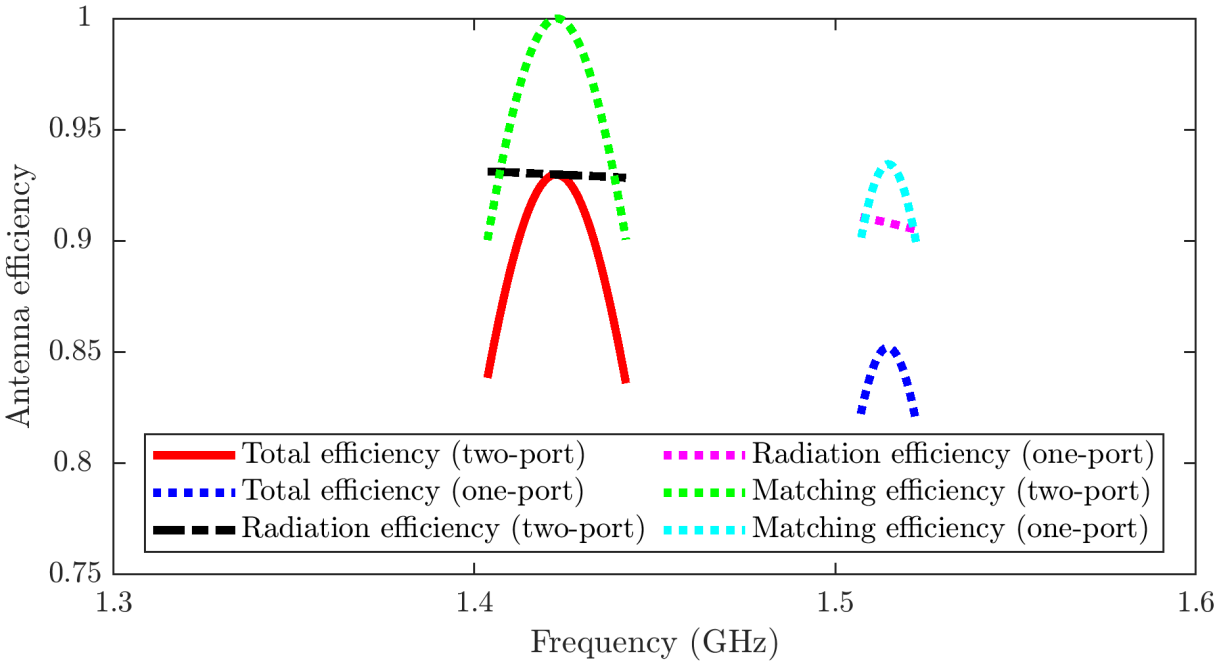
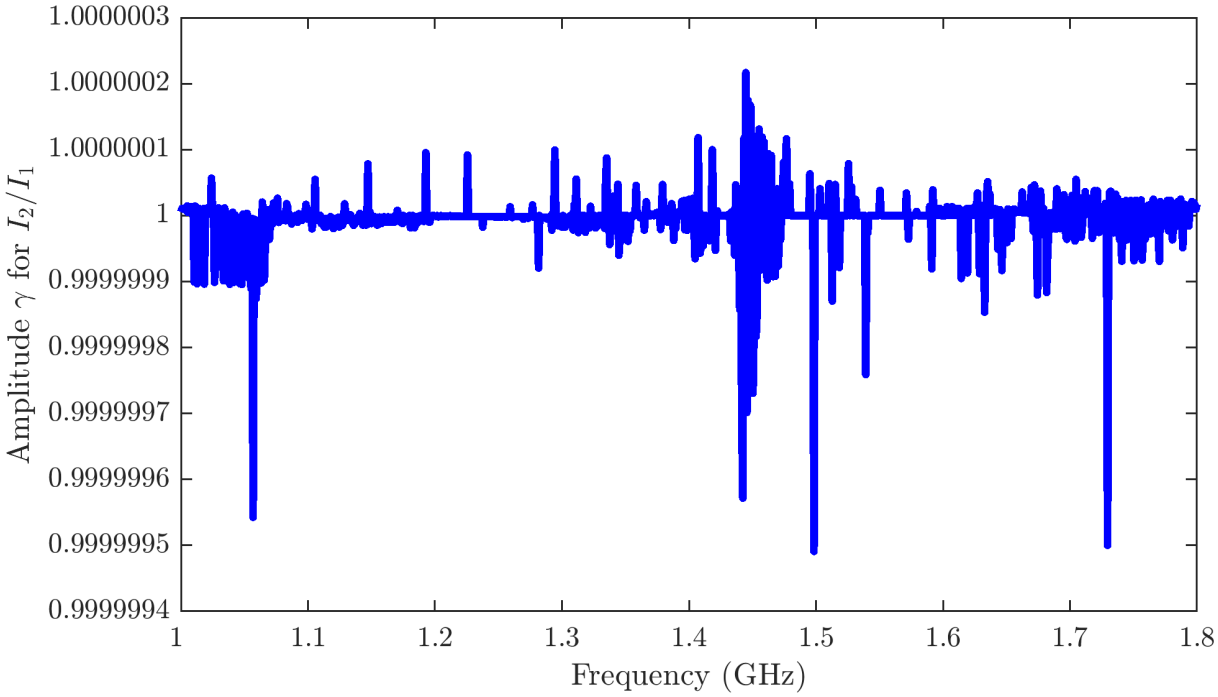


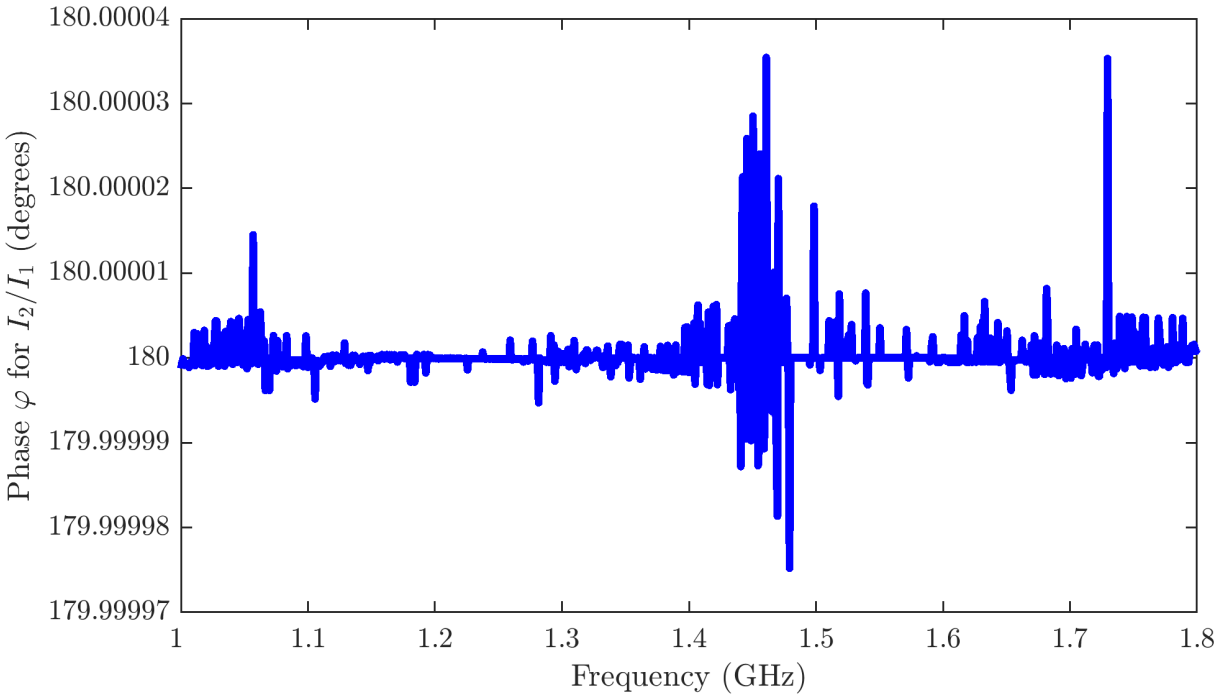
Figure 7.21. Simulated efficiencies for the two-port ESA and for the corresponding one-port antenna.

The difference in radiation efficiency between the two ESAs at the centre frequencies is attributed to the difference in Q values at these frequencies where the two-port ESA has a low Q value at its centre frequency compared to the corresponding one-port ESA. The high radiation efficiency attained by the two antennas is also attributed to the low loss tangent ($\tan\delta = 0.0009$) and low dielectric constant ($\varepsilon_r = 2.2$) substrate material used in the design. As a result, both the two-port ESA and the corresponding one-port ESA attained a total efficiency higher than 82% across the antennas' passbands.

It is shown in Figure 7.22 that after the injection matching operation on the modified antenna of Figure 7.15, the applied γ and φ responses remained approximately constant across the entire frequency range of investigation. This observation shows that the injection matching operation was successful in comparison to the observation in Figure 7.14a and 7.14b where the injection matching operation could not be achieved with constant applied relative amplitude γ and phase shift φ to the antenna across the entire frequency

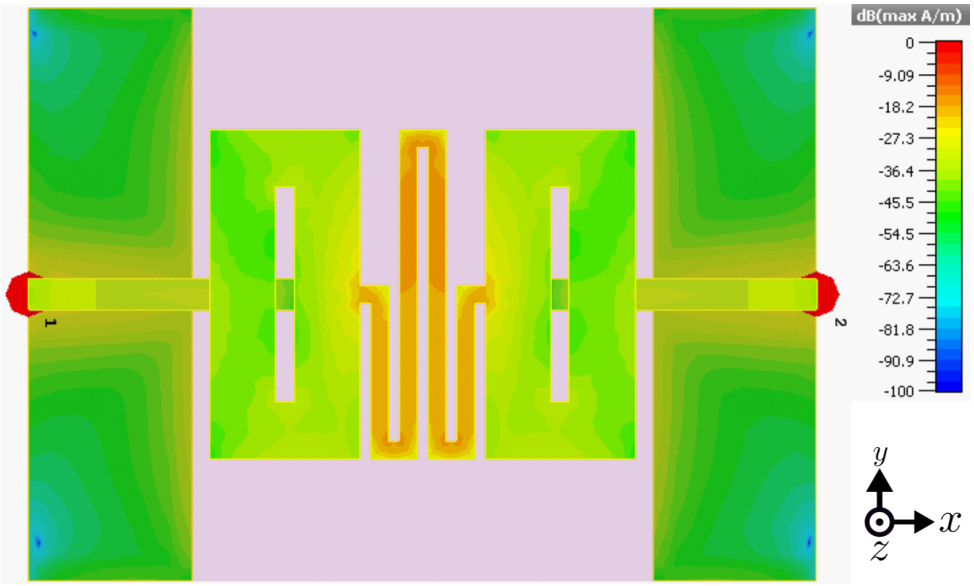


(a)



(b)

Figure 7.22. Simulated response of the applied (a) relative amplitude γ between the currents I_1 and I_2 (b) phase shift φ between the currents I_1 and I_2 when the two-port ESA was injection matched at $\gamma = 1$ and $\varphi = 180°$.



(a)



(b)

Figure 7.23. Surface current on the (a) two-port injection matched ESA at around 1.423 GHz frequency (b) corresponding one-port ESA at around 1.514 GHz frequency.

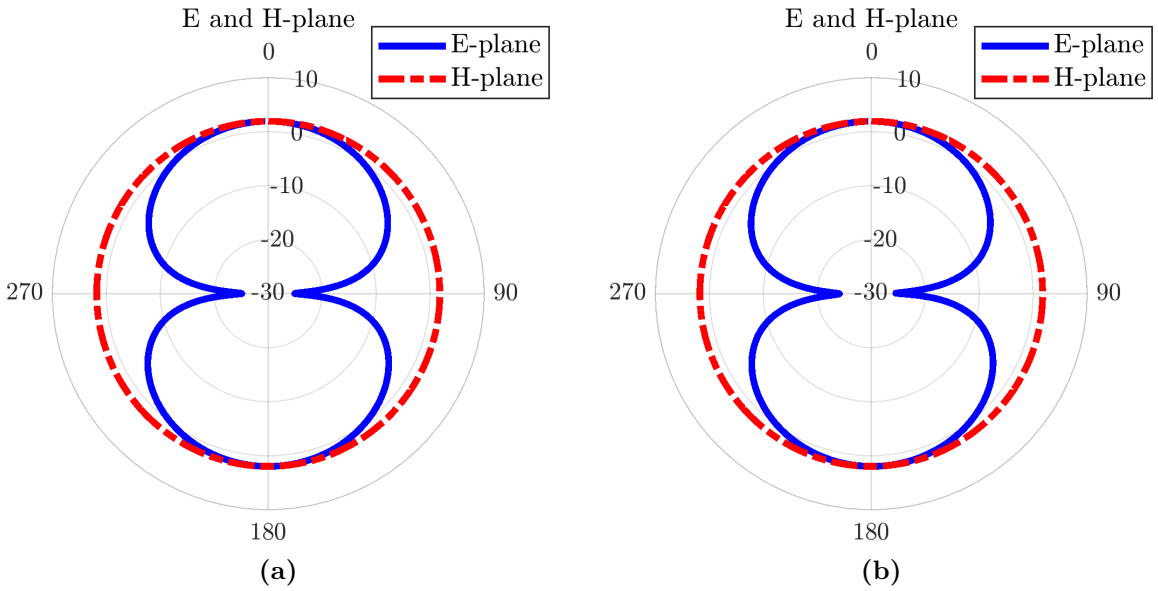


Figure 7.24. Simulated directive (a) radiation patterns for the two-port ESA at 1.423 GHz frequency (b) radiation patterns for the corresponding one-port ESA at 1.514 GHz frequency.

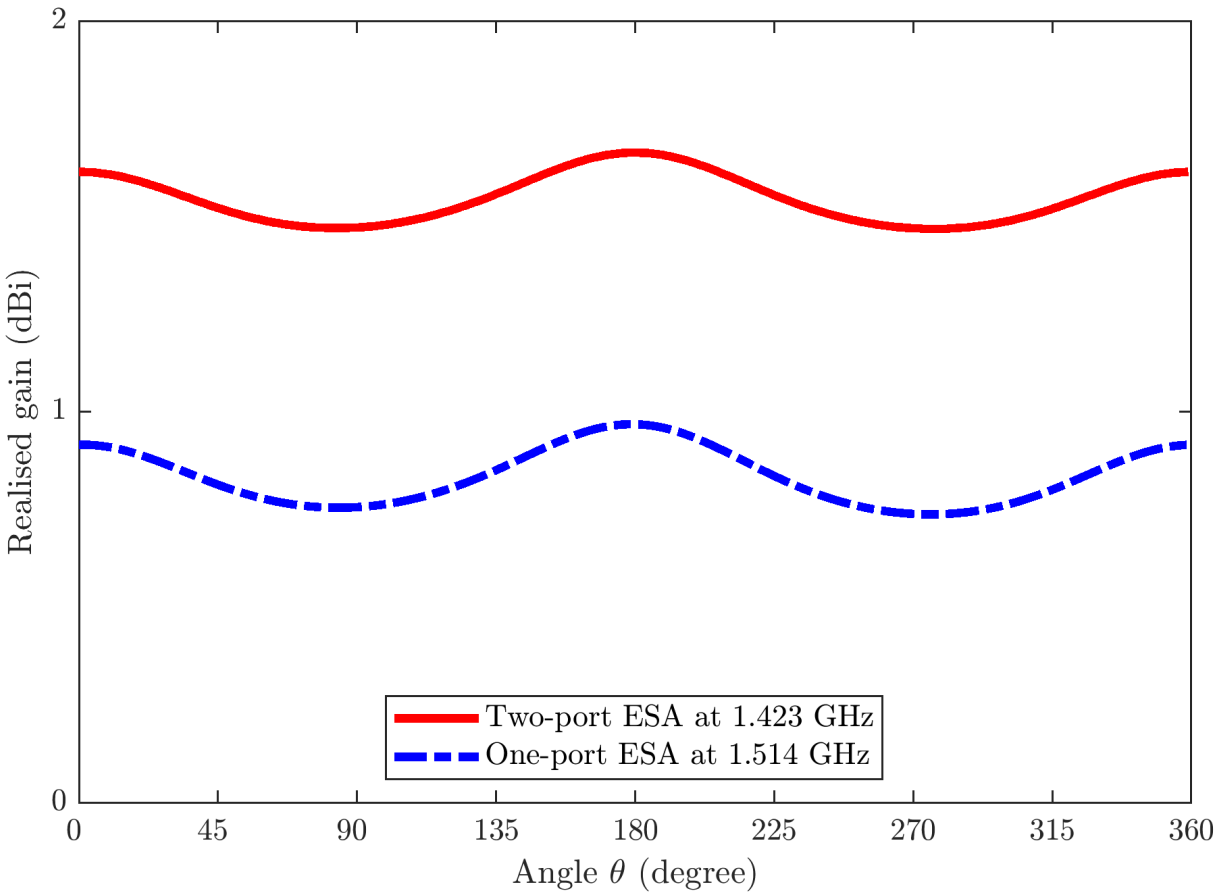


Figure 7.25. Simulated realised gain in the H-plane ($\phi = 90°$) for the two ESAs at their resonant frequencies.

range of investigation because of the narrowband matching behaviour of the lumped elements.

Both the two-port ESA and the corresponding one-port ESA have almost similar surface current distributions and radiation patterns as depicted in Figure 7.23 and 7.24, where the patterns are omnidirectional in the H-plane.

At the centre frequencies, the two-port ESA has the highest realised gain than the corresponding one-port ESA, as shown in Figure 7.25, because of driving the two-port ESA from two ports. The maximum gain at the centre frequency of the two-port ESA is around 1.66 dBi oriented in the $\theta = 180°$, where the minimum gain is around 1.47 dBi in the directions $\theta = 90°$ and $\theta = 270°$. For the corresponding one-port ESA, the maximum gain at the centre frequency is around 1.0 dBi oriented in the $\theta = 180°$. In contrast, the minimum gain for the one-port ESA is around 0.74 dBi in the $\theta = 270°$. Generally, the realised gain at the centre frequencies for the two antennas is stable in all θ angles.

7.4 Summary

The simultaneous or mutual injection matching at the two ports is not possible at electrically small dimensions of the two-port patch antenna because of the absence of the resonant characteristic modes of the antenna at ESA frequencies. This is also shown by the non-constant behaviour of the theoretical γ and φ variations with frequency across the antenna at the electrically small frequencies. Because of these factors, the injection matching technique cannot achieve ESA operation on its own, but it can enhance ESA operation.

Also, the use of lumped elements to tune the injection matched antenna to an electrically small operation mode is not feasible because of the narrowband matching behaviour of the lumped elements, which causes significant variations in the applied γ and φ.

An enhanced electrically small operation by injection matching technique can typically be obtained by modifying the radiating element for the two-port patch antenna to create a slow wave on the antenna. In particular, an electrically small operation was achieved in this investigation with $ka = 0.81$ by use of the slow-wave structure. The attained Q-factor for the realised two-port ESA was about $12Q_{Chu}$, which resulted in the -10 dB FBW of around 2.7%, and radiation and total efficiencies of about 93% at a 1.423 GHz resonant frequency. However, the achieved bandwidth is still bounded by the theoretical limit of 5% for the electrically small patch antennas. Because of the marginal bandwidth attained by the two-port ESA, there was no need of pursuing the experiment.

Chapter 8

Conclusions and future work

8.1 Conclusions

The injection matching technique provides an effective way of exciting the characteristic modes of a patch antenna by changing the phase shift φ between the two excitation signals applied at the two ports of the antenna between two combinations of 0° and 180°, respectively. At the same time, the relative amplitude is maintained at $\gamma = 1$. In each case, wide bandwidth is attained through excitation of the multiple correlated characteristic modes of the antenna. The remaining φ values between 0° and 180° can only affect the impedance matching of the resonances obtained through the common mode ($\varphi = 0°$) or differential ($\varphi = 180°$) excitations. Because of this limitation, it is impossible to have a progressive frequency-tuning of the injection matched antenna across its entire operating frequency band.

Also, the excitation of multiple modes in patch antennas attained in this thesis is attributed to the adoption of partial grounds, which reduces the stored EM energy at the boundary between the substrate and ground plane. This action reduces the Q-value of

the antenna to enhance the impedance matching of the modes, consequently increasing the operational bandwidth.

Besides, simultaneous or mutual injection matching at the two ports is not feasible in an electrically small two-port patch antenna. This infeasibility is caused by the antenna's absence of resonant characteristic modes at electrically small operating frequencies. Moreover, because of the narrowband matching behaviour of the lumped elements, which causes significant variations in the applied γ and φ, it is impossible to tune the injection matched antenna to an electrically small frequency of operation by using lumped matching elements.

Therefore, applying the injection matching technique in patch antennas enables the excitation of different characteristic modes of the antenna. Changing the phase shift between the two excitation signals at port two of the antenna improves the matching or antenna bandwidth. Typical -10 dB operational FBWs of around 64%, 69.5% and 67.8% validated in Chapter 4, 5, 6, and a theoretical FBW of around 85.2% in Chapter 5 with the radiation efficiencies higher than 98% and fairly stable approximately omnidirectional H-plane patterns, promote the realised antennas for use in the 5G and dynamically shared wireless services in the Sub-6 GHz high-band. However, these features are attained at the expense of complex driving circuitry, which is not always advantageous to realise.

Also, because the active modulation of the terminal impedances for the two-port injection matched antennas by modulating the relative amplitude γ is not feasible, as shown in Section 4.3.4, there is no need of having the amplifier in the driving circuitry. As such, the amplifier block can be removed from the block diagram for simulating the injection matched antennas provided in Figure 4.10.

8.2 Contributions to the research

8.2.1 Theory for the two-port injection matched antennas

A rigorous theory governing the design and operation of the injection matched antennas has been developed in Chapter 3 through 7. Also, the reflection and transmission coefficients, radiation, matching and total efficiencies, and the radiation patterns for the two-port injection matched antennas have been characterised.

8.2.2 Design methodology for injection matched antennas

The design methodology for the injection matched antennas has been formulated in Chapter 4, and the work was published in a conference paper [92]. The positions for the placement of the feed lines were also determined in Section 4.3.2.

8.2.3 Injection matched antenna reciprocity

The reciprocity analysis of the two-port injection matched antennas to verify an intuitive arrangement of the feeding network around the antenna to be fed by an injection matched antenna in the receive mode has been theoretically characterised in Chapter 3 and validated through simulations in Chapter 4. It has been shown that the same feeding network arrangement used by an injection matched antenna in the transmit mode can be used by the same antenna in the receive mode. Also, the two-port injection matched antennas can work reciprocally with any other antenna with similar radiation characteristics.

8.2.4 Bandwidth enhancement in patch antennas

Operational -10 dB FBWs higher than 64% with fairly stable and approximately omnidirectional H-plane radiation patterns have been attained by applying the injection matching technique to the two-port patch antenna. Also, FBWs of 67% and 19% have been achieved from a patch antenna through the frequency tuning of the modes through differential and common mode excitations, respectively, applied to the antenna. Some of these results have been published in [92, 93], while other results are being published as outlined in Appendix A.

8.2.5 Validation of injection matched antenna operation

Procedures to validate the TARC and radiation patterns for the two-port injection matched antennas have been formulated. The formulated procedures were applied in Section 4.4, 5.3 and 6.3 to validate the two-port injection matched antennas, which verified to an acceptable degree that the expected characteristic of an antenna operating under the injection matched operation have been observed experimentally.

8.2.6 Wideband, frequency tunability and electrically small operations

The three operation modes of the injection matched antenna, wideband, frequency tunability and electrically small operation, have been explored in some detail in Chapter 5, 6 and 7, respectively. It has been shown that the wideband operation can be attained by exciting the multiple correlated characteristic modes of the antenna. Also, frequency tunability can be attained by tuning the excitation modes applied to the antenna by

changing the phase shift φ from $\varphi = 0°$ to $\varphi = 180°$. On the other hand, the injection matching technique cannot achieve an electrically small operation on its own, but it can enhance the electrical length of the two-port patch antenna.

8.3 Future work

8.3.1 Bandwidth enhancement

The attractive feature of the injection matching technique in enhancing patch antennas' bandwidth can cater to the high demand for bandwidth in wireless communication. In particular, the -10 dB FBWs higher than 64% were achieved in this thesis. However, extending the injection matching theory to accommodate many ports, such as more than four ports, while at the same time increasing the antenna size, may allow more characteristic modes to be excited from patch antennas. It may also provide flexibility in controlling the frequency reconfigurability of the realised antenna. Besides, operational bandwidth can be enhanced because of the increase in simultaneously excited modes.

8.3.2 Leakage currents on partial grounds

Despite the wide bandwidth obtained from patch antennas through the injection matching technique, there is a performance degradation to the injection matched antennas caused by leakage currents on the partial grounds. Specifically, the observed leakage currents on partial grounds were proven to alter the resonance and, consequently, the radiation patterns of the antenna. Further investigation is needed to resolve this problem systematically.

8.3.3 Modulating and demodulating a carrier signal

Modulating a carrier onto and demodulating the received signal from the injection matched antennas is yet to be explored. Investigations in this area were beyond the scope of this thesis but are needed before establishing the potential of injection matched antennas in future communication systems.

8.3.4 Analysis of two-port monopole patch antennas

The theoretical analysis of the two-port injection matched monopole patch antennas through the cavity model is needed to provide the initial antenna dimensions for the design. This analysis will shorten the design process for injection matched antennas.

8.3.5 Experimental validation of reciprocity analysis of injection matched antennas

The reciprocity analysis of the two-port injection matched antennas to verify an intuitive arrangement of the feeding network around the antenna to be fed by an injection matched antenna in the receive mode was not experimentally validated because of the limitation of the equipment (R&S ZVA67 VNA) to allow coherence mode operation with all four ports and performing the injection matched operation in the receive mode. The 4-port R&S ZVA67 VNA has four internal signal sources. One of the sources is reserved for the main signal generation when the coherence mode is activated, leaving only three sources available for the coherence mode operation at the ports. So to have the coherence mode working in four ports, five signal sources are needed, a feature which the R&S ZVA67 VNA cannot provide. These issues require further investigations.

Appendices

A List of publications

Journal papers in preparation

- P. Kihogo, C. Constantinou, P. Gardner, "Frequency reconfigurable two-port injection matched antenna," *IEEE Transaction on Antennas and Propagation*, 2022.
- P. Kihogo, C. Constantinou, P. Gardner, "An efficient, wideband, two-port injection matched patch antenna," *IEEE Transaction on Antennas and Propagation*, 2022.

Published conference papers

- P. Kihogo, L. Shen, C. Constantinou, and P. Gardner, "A wideband injection matched patch antenna," in *Antennas and Propagation Conference 2019 (APC-2019)*, Birmingham, UK, 2019: IET.
- L. Shen, P. Kihogo, P. Gardner, and C. Constantinou, "Theory design and validation of a tunable injection-matched 2-port antenna," in *2020 14th European Conference on Antennas and Propagation (EuCAP)*, Copenhagen, Denmark, March 2020: IEEE.
- P. Gardner, Y. Wang, C. Constantinou, L. Shen, and P. Kihogo, "Circuit-antenna Interactions in Multi-port Active Antennas," in *2020 14th European Conference on Antennas and Propagation (EuCAP)*, Copenhagen, Denmark, March 2020.

B Further design information

B.1 Simulation of injection matched antennas

The 3D EM and circuit co-simulation are achieved in CST SS through the use of CST MWS and CST DS modules, which are integrated to work together. The simulation of two-port injection matched antennas in CST SS is accomplished through the following procedure:

(1) A two-port antenna (also a single-port antenna) is created in CST MWS and is passively simulated using a Time Domain Solver (TDS) as shown in Figure B.1. Hexahedral meshes (shown in Figure B.1) are used in the simulation while 25 mesh cells per wavelength (shown in Figure B.2) are configured. The TDS stopping criterion for the simulations is a -80 dB accuracy, as depicted in Figure B.1. Open boundary conditions were used for the simulation. Through this step, the passive S-parameters are obtained as shown in Figure B.1 and B.2.

(2) After the passive S-parameters for the two-port antenna are obtained, the schematic of Figure 4.10 in Section 4.3.3 is created in CST DS for the simultaneous excitation of the antenna as shown in Figure B.3.

(3) The relative amplitude γ and phase shift φ between the two excitations are configured in the phase shifter block, which has an internal attenuator.

(4) Using the AC combining tool in CST DS, the excitation voltage and current signals for the simultaneously excited two-port antenna are generated as shown in Figure B.4.

(5) The post-processing template in the CST DS shown in Figure B.5 is used to combine the voltage and current signals to generate the incident and reflected waves, active S-parameters, terminal impedances, and TARC using Equations (3.10) and (3.11), (3.26) through (3.29), Equation (C.3), and Equation (3.14) outlined in Section 3.3, 3.3.2, Appendix C, and Section 3.3.1, respectively.

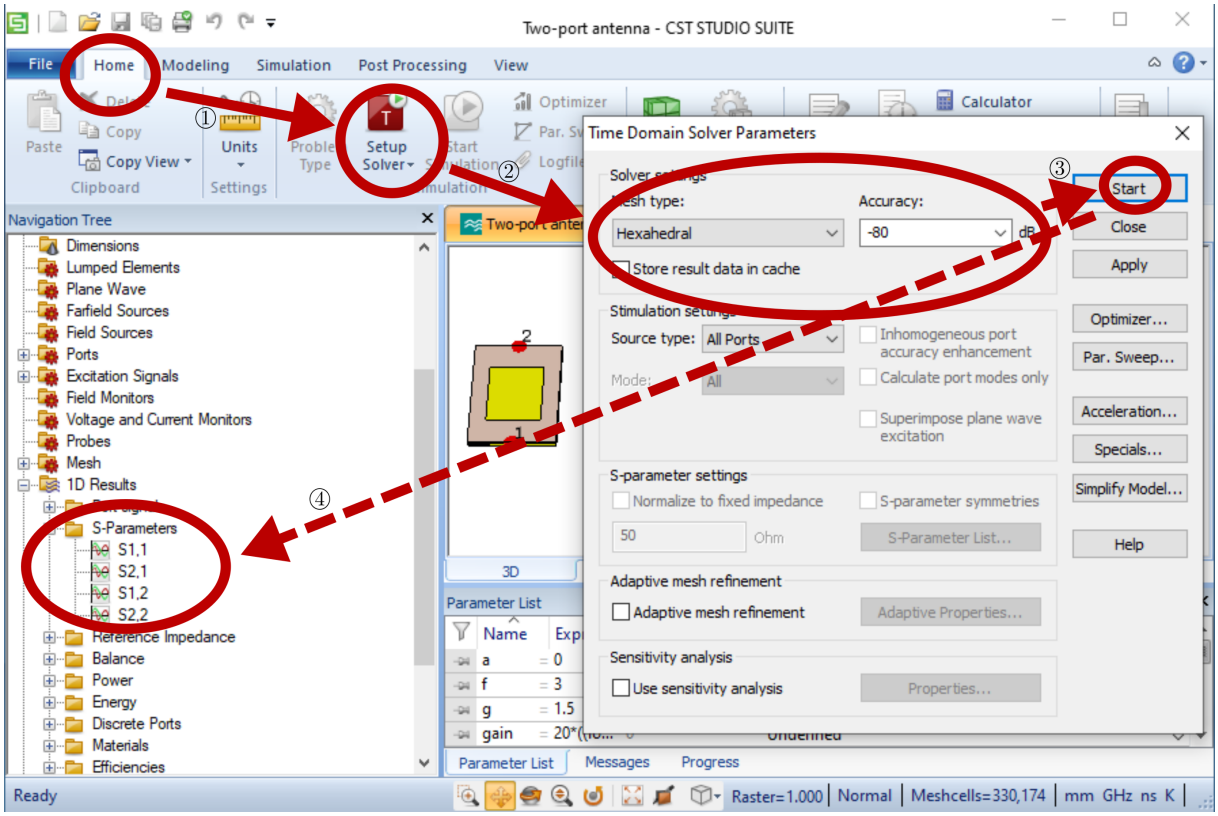


Figure B.1. The Time Domain Solver settings used in simulating the one-port antennas, and two-port injection matched patch antennas in CST MWS.

(6) The antenna optimisation is done using the Optimiser DS (design studio) or Parameter DS in CST DS.

(7) To simulate the antenna radiation patterns, the field monitors are first created in CST MWS, and the antenna is passively simulated. After the passive S-parameters are obtained, the field monitors are updated using the AC combine tool in CST DS,

and the simulation is updated as shown in Figure B.6. The resulting patterns from this simulation are then obtained in CST MWS at the navigation tree as indicated by the monitored frequencies with the suffix AC1.

(8) To obtain the antenna efficiency, the broadband field monitors are defined in the CST MWS across the antenna passband, and step (7) is followed. The antenna efficiency for the injection matched antenna is then obtained in CST MWS under 1D results in the navigation tree with the suffix AC1.

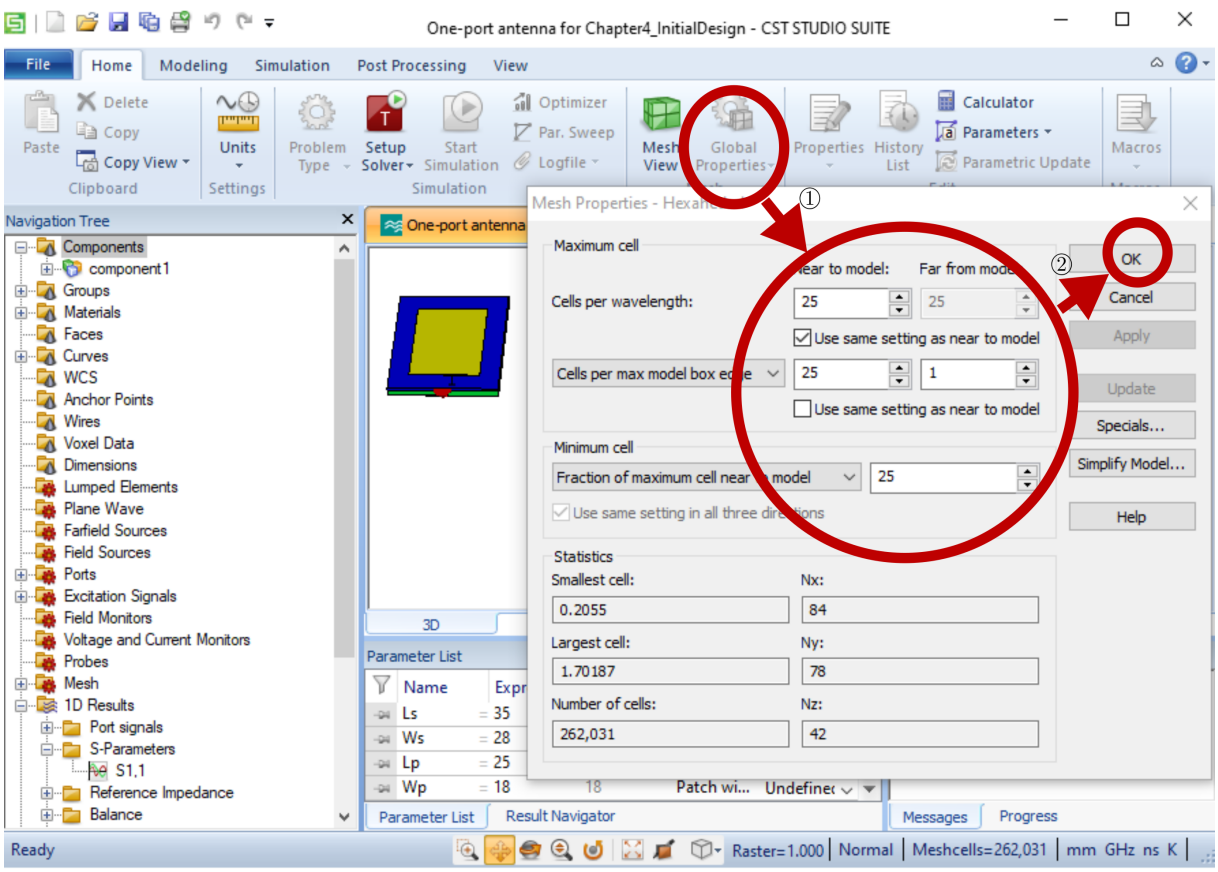


Figure B.2. Mesh settings used in simulating one-port antennas, and two-port injection matched patch antennas in CST MWS.

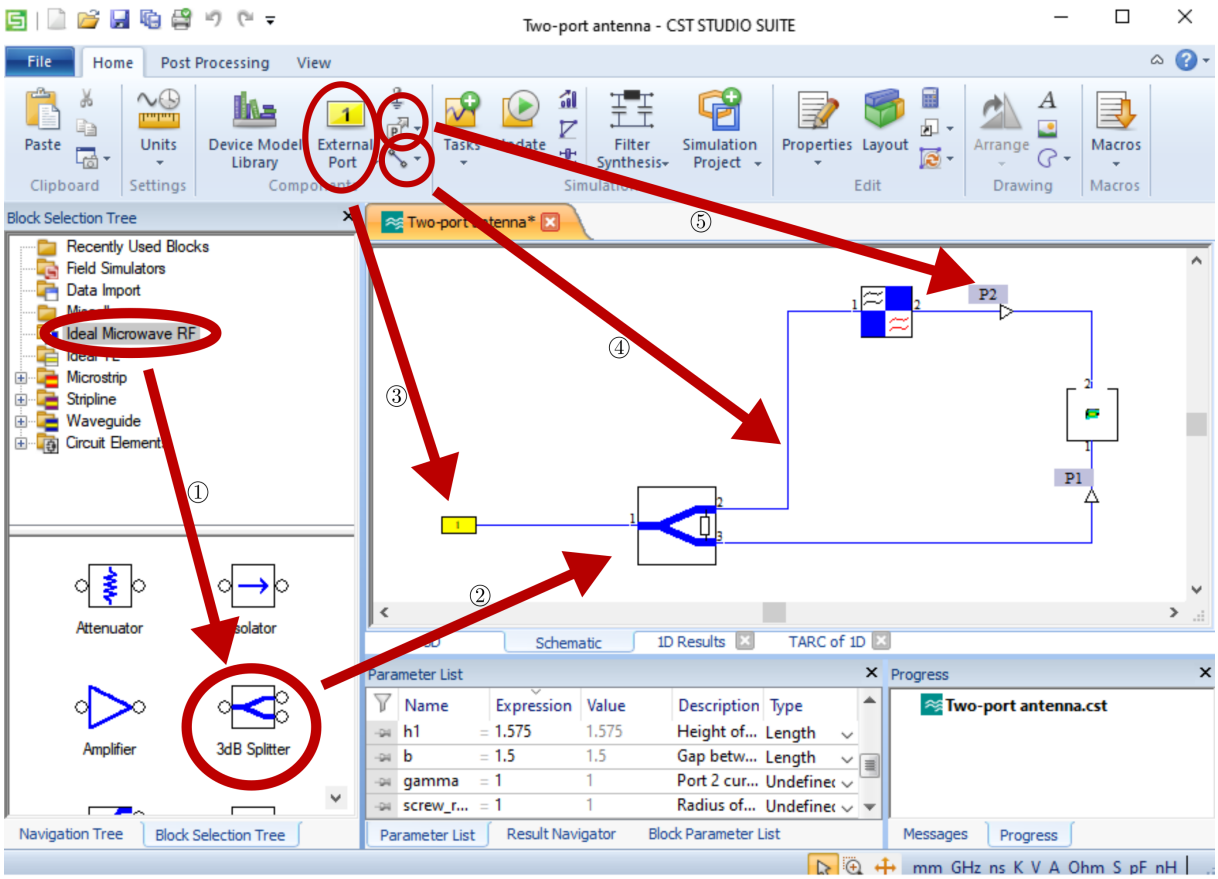


Figure B.3. The schematic for exciting the two-port injection matched patch antennas in CST DS.

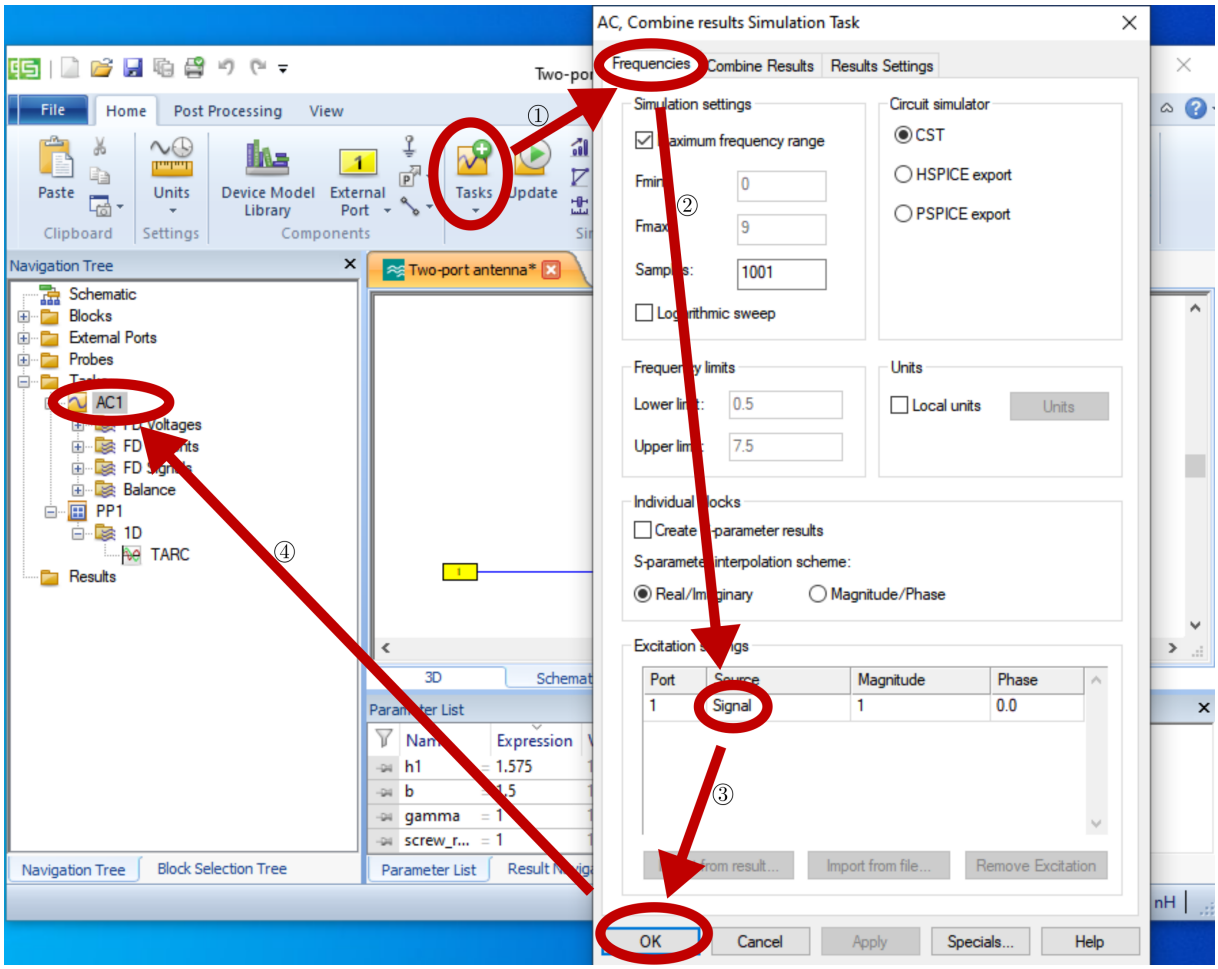


Figure B.4. Setting the signal source for exciting the two-port injection matched patch antennas in CST DS.

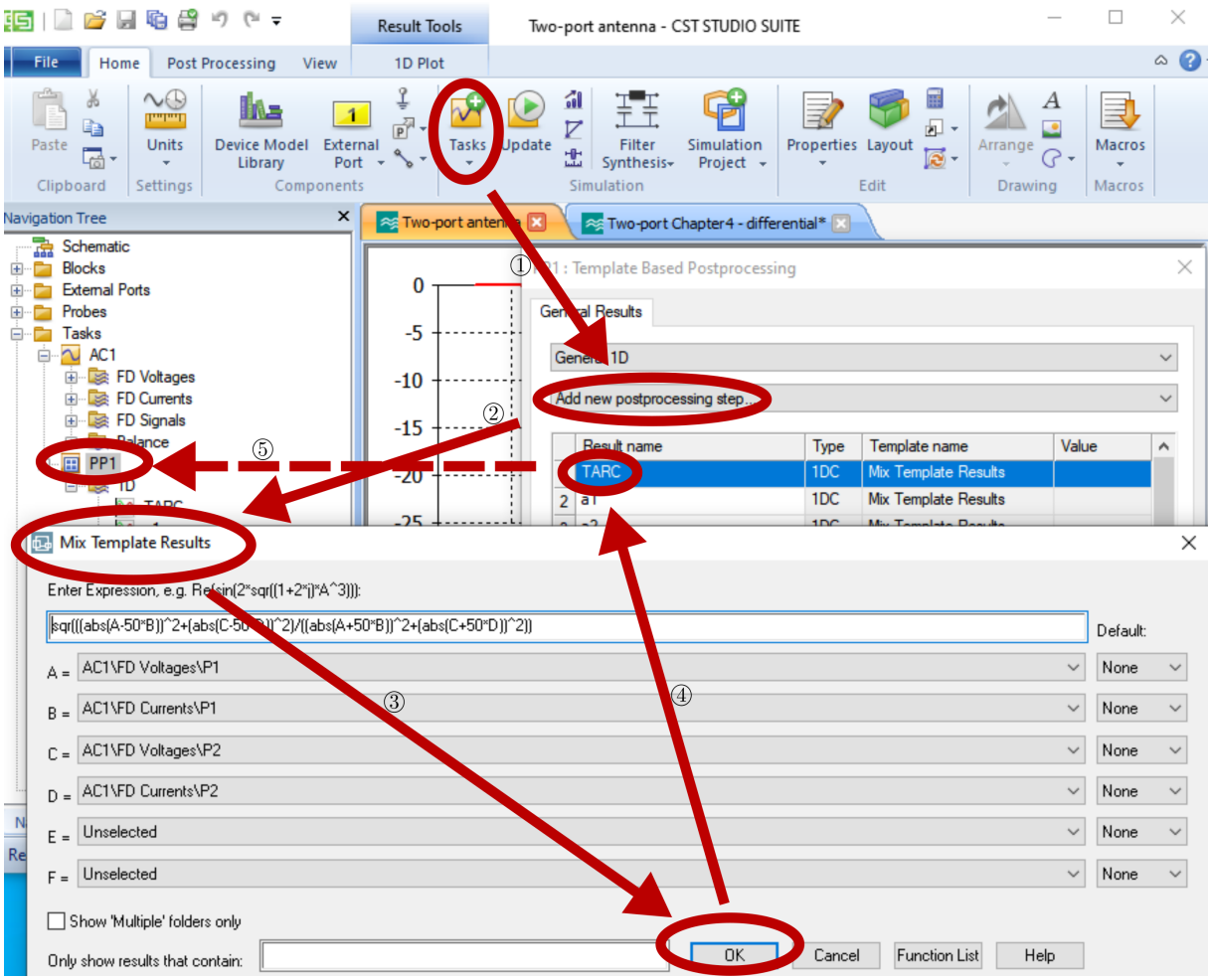


Figure B.5. Post-processing of the simulated TARC from the simulated current and voltage signals in CST DS.

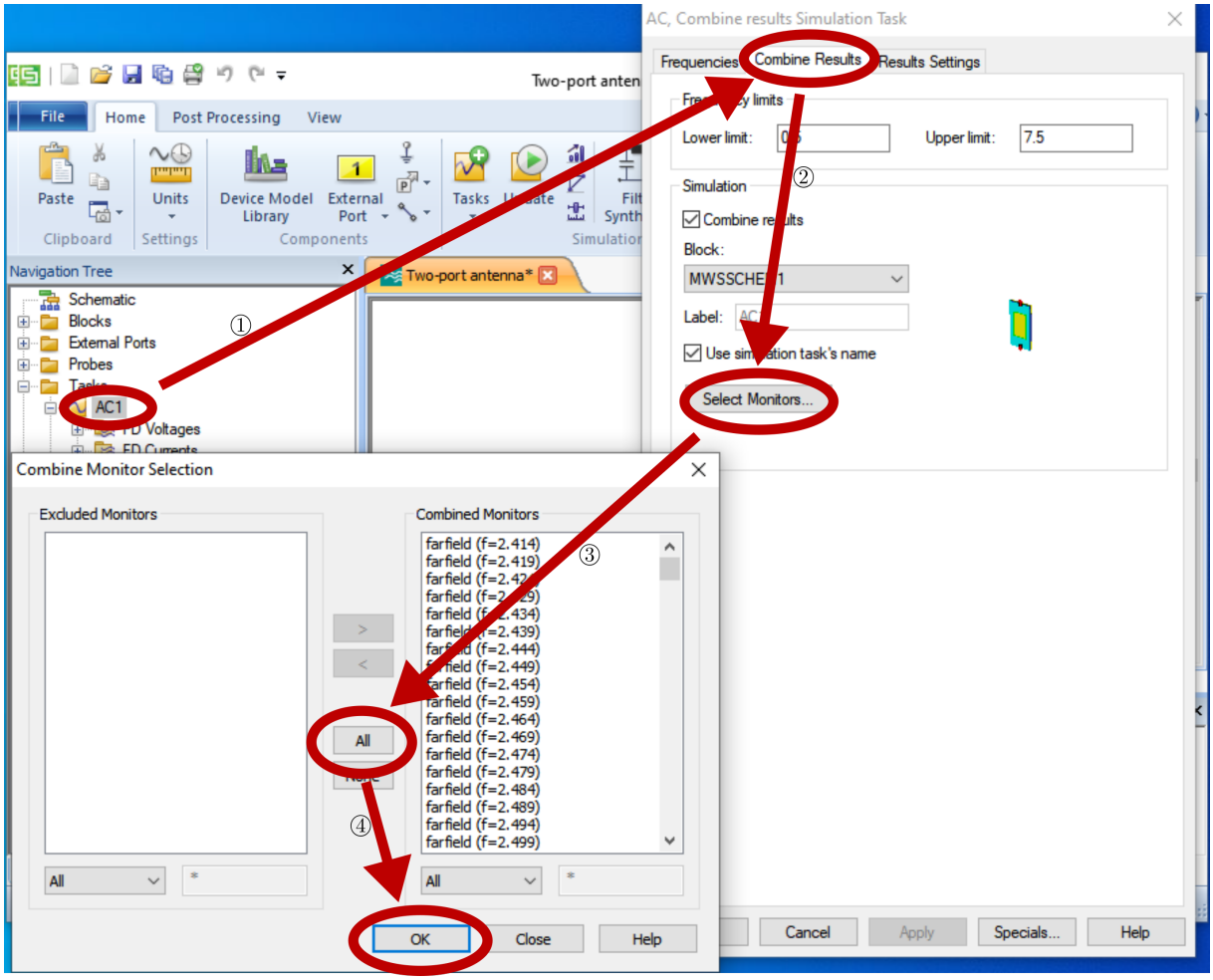


Figure B.6. Defining the field monitors for the simulation of the radiation patterns and efficiency of two-port injection matched antenna using the AC result combining tool in CST DS.

B.2 CMA of planar antennas in CST MWS

The CMA of all antennas in this thesis was accomplished in CST MWS using a Multilayer Solver. The mesh and solver settings for each antenna are summarised in Table B.1 and B.2.

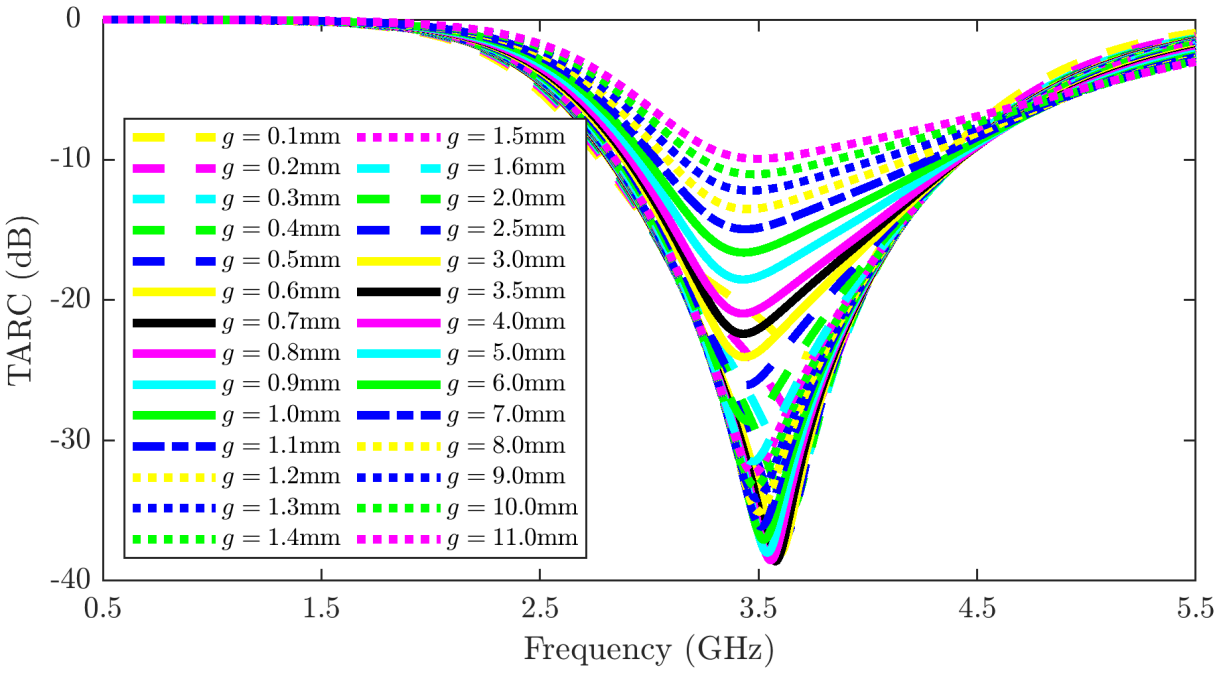
Table B.1. Multilayer mesh settings used in the CMA of proposed patch antennas in this thesis.

Antenna	**Multilayer Mesh Settings**					
	Meshing method	Cells per wavelength (model)	Cells per maximum model box edge (model)	Cells per wavelength (background)	Cells per maximum model box edge (background)	Minimum cells (absolute value)
Figure 4.5	Surface based	70	70	70	1	0
Figure 4.17	Surface based	60	60	60	1	0
Figure 5.7	Surface based	40	40	40	1	0
Figure 6.4a	Surface based	25	25	25	1	0
Figure 6.9	Surface based	25	25	25	1	0
Figure 6.19	Surface based	25	25	25	1	0
Figure 7.17	Surface based	50	50	50	1	0

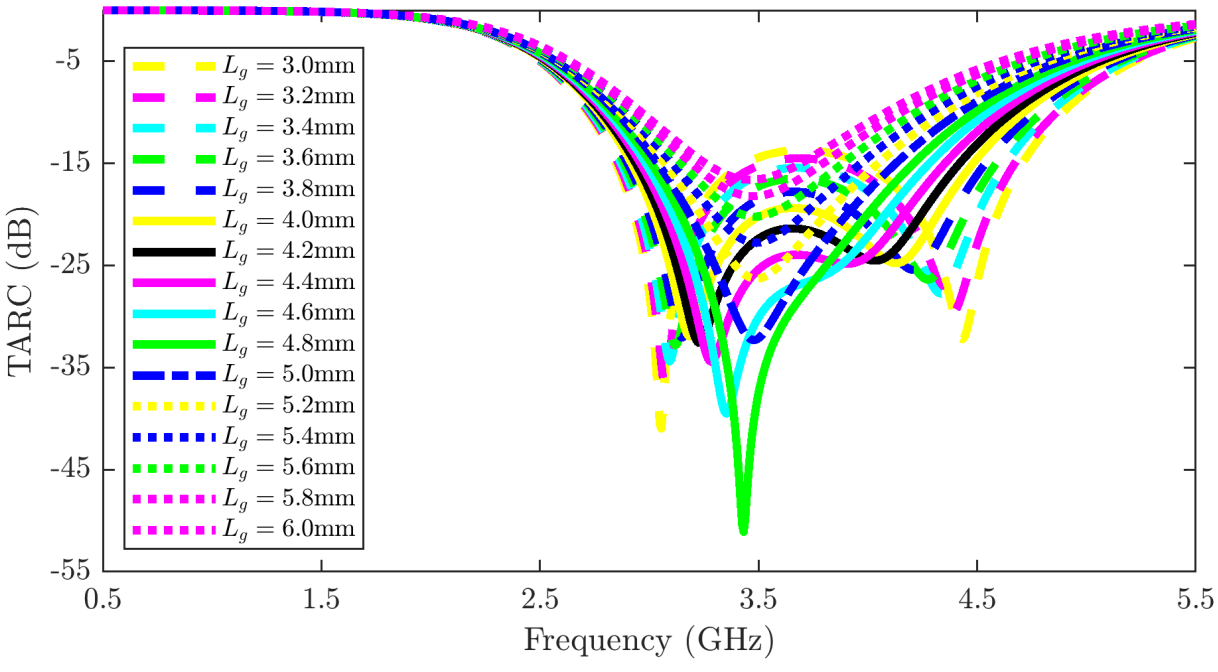
Table B.2. Multilayer Solver parameter settings used in the CMA of the proposed patch antennas in this thesis.

Antenna	**Multilayer Solver parameters**			
	Accuracy	Source type	Number of modes	Frequency for mode sorting GHz
Figure 4.5	1e-4	CMA	4	3.9
Figure 4.17	1e-4	CMA	3	4.2855
Figure 5.7	1e-4	CMA	4	3.5
Figure 6.4a	1e-4	CMA	3	2.75
Figure 6.9	1e-4	CMA	6	3.3, 5.7, 7.0
Figure 6.19	1e-4	CMA	5	2.5, 3.5, 4.5, 6.5, 7.5
Figure 7.17	1e-4	CMA	6	1.386

B.3 Further results



(a)



(b)

Figure B.7. Variation of (a) g on the two-port injection matched antenna when $L_p = 25$, $W_p = 18$, $L_s = 35$, $W_s = 28$, $L_g = 5$, and $w = 1.6$ mm (b) L_g on the two-port injection matched antenna when $L_p = 25$, $W_p = 18$, $L_s = 35$, $W_s = 28$, $w = 1.6$ and $g = 1.5$ mm.

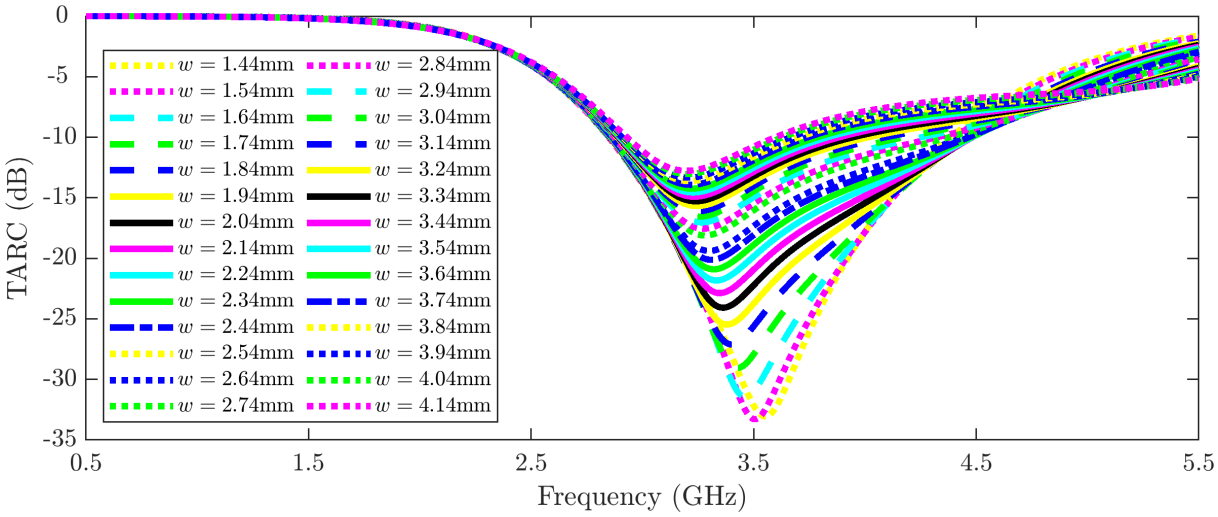
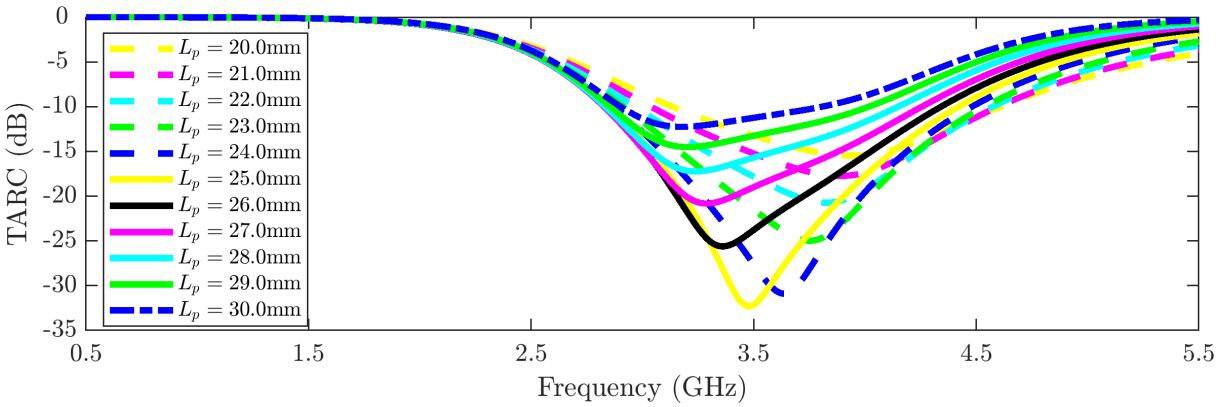
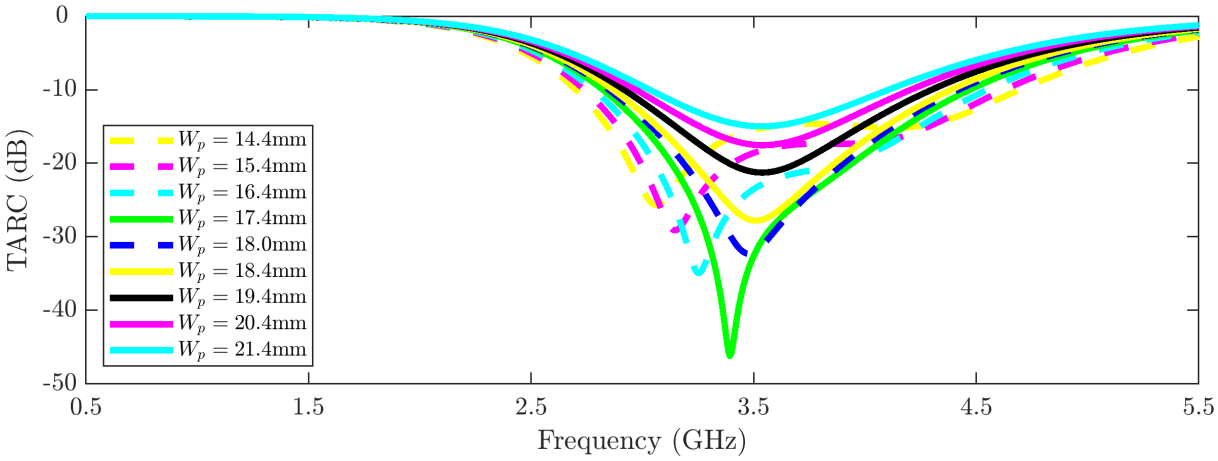


Figure B.8. Variation of w on the two-port injection matched antenna when $L_p = 25$, $W_p = 18$, $L_s = 35$, $W_s = 28$, $L_g = 5$, and $g = 1.5$ mm.



(a)



(b)

Figure B.9. Variation of (a) L_p on the two-port injection matched antenna when $W_p = 18$, $L_s = 35$, $W_s = 28$, $L_g = 5$, $w = 1.6$ and $g = 1.5$ mm (b) W_p on the two-port injection matched antenna when $L_p = 25$, $L_s = 35$, $W_s = 28$, $L_g = 5$, $w = 1.6$ and $g = 1.5$ mm.

Table B.3. Dimensions for the fine-tuned TARC resonances shown in Figure 4.15.

Simulation ID	Antenna dimensions (mm)						
	L_p	W_p	L_s	W_s	L_g	w	g
TARC1	29.0	20.9	44.0	30.8	5.4	2.3	0.2
TARC2	29.0	18.9	44.0	28.8	5.4	2.5	0.4
TARC3	29.0	18.9	46.0	30.8	5.4	2.5	0.4
TARC4	31	20.9	44.0	28.8	5.4	2.3	0.2
TARC5	31.0	18.9	46.0	29.8	5.4	2.4	0.2
TARC6	31.0	20.9	45.0	29.8	5.4	2.3	0.3
TARC7	30.0	19.9	45.0	29.8	5.4	2.4	0.3
TARC8	31.0	20.9	44.0	30.8	5.4	2.4	0.4
TARC9	30.0	20.9	44.0	29.8	5.4	2.4	0.4
TARC10	29.0	18.9	44.0	28.8	5.4	2.5	0.3
TARC11	29.0	19.9	45.0	29.8	5.4	2.4	0.4
TARC12	29.0	19.9	46.0	30.8	5.4	2.4	0.3
TARC13	31.0	18.9	45.0	28.8	5.4	2.4	0.4
TARC14	31.0	20.9	46.0	30.8	5.4	2.4	0.3
TARC15	31.0	20.9	46.0	28.8	5.4	2.4	0.2

B.4 Antenna bandwidth calculations

The FBW of the antenna is given by,

$$\text{FBW} = \frac{f_{\text{UB}} - f_{\text{LB}}}{f_{\text{c}}} \tag{B.1}$$

where, f_{LB} is the lower boundary frequency, f_{UB} is the upper boundary frequency at resonance, and f_{c} is the centre frequency given by,

$$f_{\text{c}} = \frac{f_{\text{LB}} + f_{\text{UB}}}{2} \tag{B.2}$$

For FBW $> 100\%$, the antenna BW is expressed as a ratio using the following equation,

$$\text{BW} = (f_{\text{UB}}/f_{\text{LB}}) : 1 \tag{B.3}$$

B.5 Design equations for electrically small antenna

The lower bounded Q-factor, Q_{Chu} for a linear polarised electrically small antenna is given by the following equation,

$$Q_{Chu} = \frac{1}{(ka)^3} + \frac{1}{ka} \tag{B.4}$$

where, $k = 2\pi/\lambda$ is the free space wavenumber, λ is the free space wavelength, and a is the radius of the Chu-sphere circumscribing the maximum dimension of the antenna. At resonant frequency f_0, the Q-factor is calculated by [1, p. 853-854],

$$Q = \frac{\text{VSWR} - 1}{\text{FBW}\sqrt{\text{VSWR}}} \tag{B.5}$$

where, VSWR is the voltage standing wave ratio at f_0 and FBW is the -10 dB fractional bandwidth of the antenna.

C Measurements with R&S ZVA67 VNA

The R&S ZVA67 VNA does not support direct measurements of the terminal currents, voltages and impedances, and active reflection coefficients. To measure these parameters, one has to configure their corresponding equations in the inbuilt user-defined template, from which they can be used in measurements when the two ports are configured in coherence mode. The terminal current at the i^{th} port of the antenna is given by,

$$I_i = \frac{1}{\sqrt{Z_0}}\Big(a_i - b_i\Big) \tag{C.1}$$

where a_i and b_i are the incident and reflected waves, respectively, at the i^{th} port of the antenna, and $Z_0 = 50\ \Omega$ is the characteristic impedance of the source. Also, the terminal voltage at the i^{th} port of the antenna is given by,

$$V_i = \sqrt{Z_0}\Big(a_i + b_i\Big) \tag{C.2}$$

On the other hand, the terminal impedance at the i^{th} port of the antenna is given by,

$$Z_i = \frac{V_i}{I_i} = Z_0\Big(\frac{a_i + b_i}{a_i - b_i}\Big) \tag{C.3}$$

Also, Equations (3.14), and (3.26) through (3.29) provided in Section 3.3.1 and 3.3.2 are used for measuring the total active reflection coefficient (TARC), active reflection

coefficients, as well as the transmission coefficients at the individual ports of the two-port injection matched antenna. However, the transmission and reflection coefficients from the individual ports are contained in the TARC.

D Reference antenna

The open boundary quad-ridged horn antenna model 3164-08 was used as a reference antenna during the characterisation of the far-field patterns for the two-port injection matched antennas. The data sheet for this antenna is provided on the next page.

ETS•LINDGREN
An ESCO Technologies Company

Wireless Antennas

Open Boundary Quad-Ridged Horn

Model 3164-08

FEATURES:

- **700 MHz - 10 GHz Frequency Range**
- **Excellent Gain Over Entire Range**
- **Low VSWR With Improved Gain**
- **Linear or Circular Polarization (With Hybrid)**
- **Compact Design**
- **Flexible Mounting Schemes**
  -- Standard Tripod Mounting Flange
  -- Optional Wall Mounting Plate
- **Maintains Shielding Integrity When Wall Mounted With Optional Mounting Plate**



ETS-Lindgren's Model 3164-08 Quad-Ridged Horn

The Model 3164-08 Open Boundary Quad-Ridged Horn "open boundary" design makes this antenna unique in both appearance and performance. Because of excellent gain and improved VSWR, the 3164-08 replaces former models 3164-04 and 3164-07.

FEATURES

Numerically modeled, the Model 3164's open boundary design is similar to two double-ridged waveguide antennas placed orthogonally to each other.

With its highest gain in the 5.8 GHz range, this antenna is ideal for WiMAX testing. Additional applications include UWB wireless testing (3 GHz - 10 GHz) and lower frequency testing (700 MHz - 3 GHz) for GSM, PCS, Wi-Fi, etc. applications.

The 3164-08's compact design makes it ideal for use as both a tripod mounted or wall mounted antenna.

Should a wall mount be desired, an optional wall mounting plate can be ordered, and helps to maintain shielding integrity in the chamber.

Calibrated at 10 m per ANSI C63.5, the Model 3164-08 has actual Antenna Factors and a signed Certificate of Conformance included with the antenna.

STANDARD CONFIGURATION

- Antenna Including Mounting Flange
- Individually Calibrated at 10 m per ANSI C63.5-1988. Actual antenna factors gain uncertainty values and a signed Certificate of Calibration Conformance included in manual.

OPTIONS

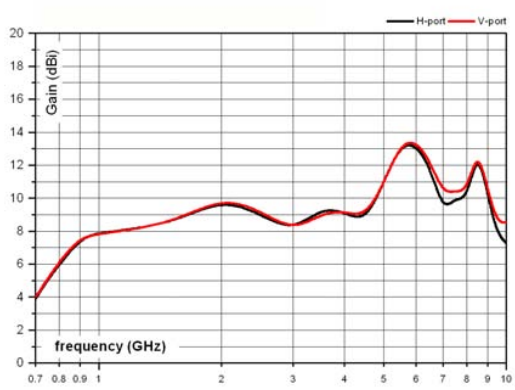
- Wall Mounting Plate

ETS-LINDGREN
An ESCO Technologies Company

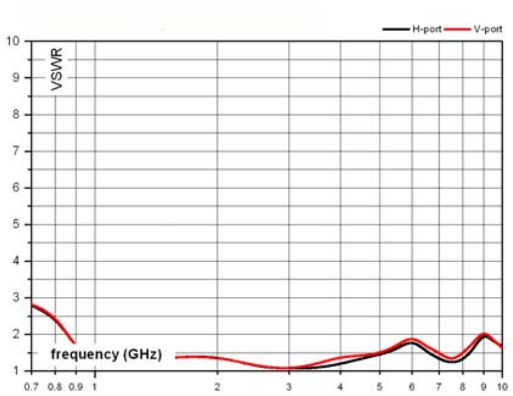
Wireless Antennas

Open Boundary Quad-Ridged Horn

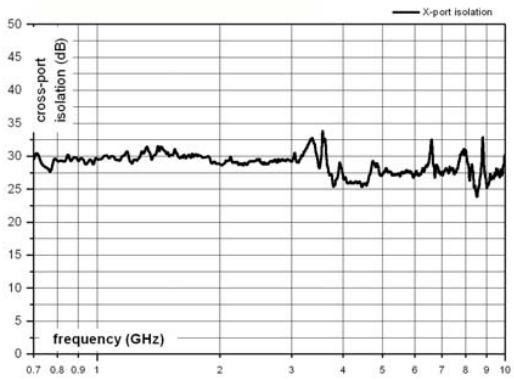
Model 3164-08



Model 3164-08 Typical Antenna Gain



Model 3164-08 Typical VSWR



Model 3164-08 Typical Cross Port Isolation

Electrical Specifications

MODEL #	FREQUENCY RANGE	CROSS-POLARIZATION ISOLATION	IMPEDENCE (NORMAL)	CONNECTOR INPUT POWER
3164-08	700 MHz - 10 GHz	> 20 dB	50 Ω	SMA Female (2)

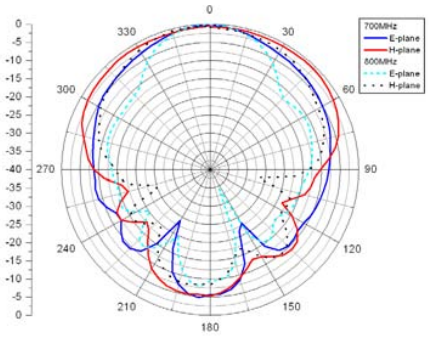
Physical Specifications

MODEL #	HEIGHT (OVERALL)	WIDTH (OVERALL)	DEPTH (OVERALL)	WEIGHT
3164-08	36.07 cm 14.20 in.	36.07 cm 14.20 in.	36.58 cm 14.40 in.	5.1 kg 11.4 lb.

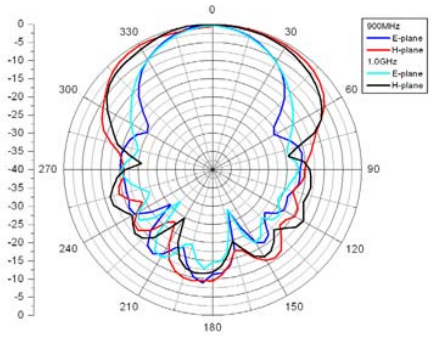
Wireless Antennas

Open Boundary Quad-Ridged Horn

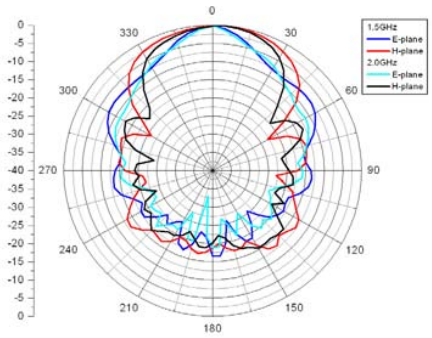
Model 3164-08



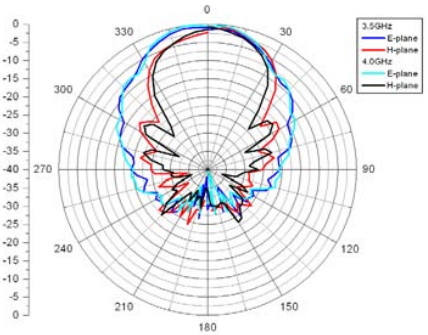
Model 3164-08 Typical 700 MHz to 800 MHz



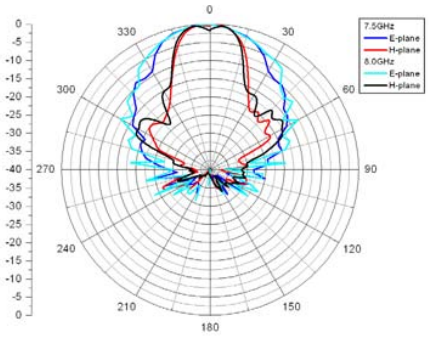
Model 3164-08 Typical 900 MHz to 1.0 GHz



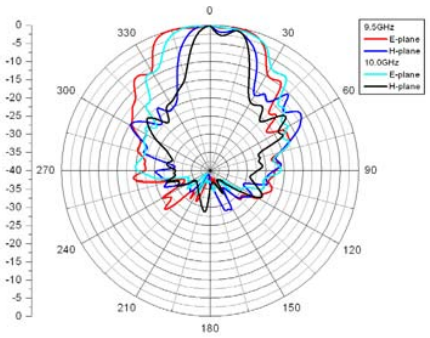
Model 3164-08 Typical 1.5 GHz to 2.0 GHz



Model 3164-08 Typical 3.5 GHz to 4.0 GHz



Model 3164-08 Typical 7.5 GHz to 8.0 GHz



Model 3164-08 Typical 9.5 GHz to 10 GHz

Information presented is subject to change as product enhancements are made. Contact ETS-Lindgren Sales Department for current specifications.

3/08 - PDF R © 2008 ETS-Lindgren REV B

References

[1] C. A. Balanis, *Antenna Theory Analysis and Design*, 3rd ed. New Jersey: John Wiley and Sons, Inc, 2005.

[2] C. Shannon, "Communication in the presence of noise," *Proceedings of the IRE*, vol. 37, no. 1, pp. 10–21, 1949.

[3] C. Smith and D. Collins, *3G Wireless Networks*, 2nd ed. India: Tata McGraw-Hill, 2008.

[4] R. F. Harrington, "Effect of antenna size on gain, bandwidth, and efficiency," *Journa l of Research of the National Bureau of Standards*, vol. 64D, no. 1, pp. 1–12, 1960.

[5] W. C. Y. Lee, *Wireless and Cellular Telecommunications*, 3rd ed. Singapore: McGraw-Hill, 2006.

[6] S. Kasera and N. Narang, *3G Networks Architecture, Protocols and Procedures.* New Delhi: McGraw-Hill, 2004.

[7] G. Casu, C. Moraru, and A. Kovacs, "Design and implementation of microstrip patch antenna array," in *2014 10th International Conference on Communications (COMM).* IEEE, 2014, Conference Proceedings.

[8] B. Kunooru, S. V. Nandigama, D. RamaKrishna, and R. Gugulothu, "Design and analysis of a microstrip antenna array for high gain applications at mm wave frequencies," in *2019 TEQIP III Sponsored International Conference on Microwave Integrated Circuits, Photonics and Wireless Networks (IMICPW)*. IEEE, 2019, Conference Proceedings.

[9] D. Jackson, "Phased array antenna handbook (third edition) [book review]," *IEEE Antennas and Propagation Magazine*, vol. 60, no. 6, pp. 124–128, 2018.

[10] 2013. [Online]. Available: https://www.3gpp.org/technologies/keywords-acronyms/101-carrier-aggregation-explained

[11] 2009. [Online]. Available: https://www.3gpp.org/specifications/releases/70-release-10

[12] L. Malviya and S. Chouhan, "Multi-cut four-port shared radiator with stepped ground and diversity effects for WLAN application," *International Journal of Microwave and Wireless Technologies*, vol. 11, no. 10, pp. 1044–1053, 2019.

[13] G. Byun and H. Choo, "New perspective on single-radiator multiple-port antennas for adaptive beamforming applications," *PLOS ONE*, vol. 12, pp. 1–15, 2017.

[14] Y. Kabiri, P. Gardner, and C. Constantinou, "Injection matched approach for wideband tunable electrically small antennas," *IET Microwaves, Antennas and Propagation*, vol. 8, no. 11, pp. 878–886, 2014.

[15] ——, "A novel approach for wideband tunable electrically small antennas," in *The 8th European Conference on Antennas and Propagation (EuCAP 2014)*. IEEE, 2014, Conference Proceedings, pp. 3633–3637.

[16] ——, "Wideband two-port injection matched antenna," in *2015 IEEE International Symposium on Antennas and Propagation and USNC/URSI National Radio Science Meeting*. IEEE, 2015, Conference Proceedings, pp. 1384–1385.

[17] E. Lee, K. M. Chan, P. Gardner, and T. E. Dodgson, "Active integrated antenna design using a contact-less, proximity coupled, differentially fed technique," *IEEE Transactions on Antennas and Propagation*, vol. 55, no. 2, pp. 267–276, 2007.

[18] J. Lee, D. Kim, and J. Lee, "Design of multi-port one-radiator antenna for octa-band mobile terminals," *Microwave and Optical Technology Letters*, vol. 59, no. 10, pp. 2692–2695, 2017.

[19] R. Heath and A. Paulraj, "Multiple antenna arrays for transmitter diversity and space-time coding," in *1999 IEEE International Conference on Communications*. IEEE, 1999, Conference Proceedings.

[20] W. Duan, S. Liao, X. Y. Zhang, Y. C. Li, and Q. Xue, "Multi-port patch antennas for flexible power combining and feeding choice," *IEEE Access*, vol. 6, pp. 79 094–79 104, 2018.

[21] S. M. Bowers and A. Hajimiri, "Multi-port driven radiators," *IEEE Transactions on Microwave Theory and Techniques*, vol. 61, no. 12, pp. 4428–4441, 2013.

[22] R. Wang, B.-Z. Wang, Z.-S. Gong, and X. Ding, "Compact multiport antenna with radiator-sharing approach and its performance evaluation of time reversal in an intra-car environment," *IEEE Transactions on Antennas and Propagation*, vol. 63, no. 9, pp. 4213–4219, 2015.

[23] W. Duan, X. Y. Zhang, S. Liao, K. X. Wang, and Q. Xue, "Multiport power combining patch antenna with stable reflection coefficient and radiation pattern in six polarization states," *IEEE Transactions on Antennas and Propagation*, vol. 67, no. 2, pp. 719–729, February 2019.

[24] N. Peitzmeier and D. Manteuffel, "Selective excitation of characteristic modes on an electrically large antenna for MIMO applications," in *12th European Conference on Antennas and Propagation (EuCAP 2018)*. IET, 2018, Conference Proceedings.

[25] N. L. Johannsen and P. A. Hoeher, "Single-element beamforming using multi-mode antenna patterns," *IEEE Wireless Communications Letters*, vol. 9, no. 7, pp. 1120–1123, 2020.

[26] S. A. Almasri, R. Pöhlmann, N. Doose, P. A. Hoeher, and A. Dammann, "Modeling aspects of planar multi-mode antennas for direction-of-arrival estimation," *IEEE Sensors Journal*, vol. 19, no. 12, pp. 4585–4597, 2019.

[27] N. Peitzmeier and D. Manteuffel, "Upper bounds and design guidelines for realizing uncorrelated ports on multimode antennas based on symmetry analysis of characteristic modes," *IEEE Transactions on Antennas and Propagation*, vol. 67, no. 6, pp. 3902–3914, 2019.

[28] E. Ebrahimi and P. S. Hall, "A dual port wide-narrowband antenna for cognitive radio," in *2009 3rd European Conference on Antennas and Propagation*. IEEE, 2009, Conference Proceedings.

[29] G. Augustin, B. P. Chacko, and T. A. Denidni, *Dual Port Ultra Wideband Antennas for Cognitive Radio and Diversity Applications.* www.intechopen.com: Intechopen, 2013, pp. 203–226.

[30] F. Albarracín-Vargas, E. Ugarte-Muñoz, V. Gonzalez-Posadas, and D. Segovia-Vargas, "A design strategy of active matched small antennas with non-Foster elements," in *9th European Conference on Antennas and Propagation (EuCAP).* IEEE, 2015, Conference Proceedings.

[31] F. Albarracín-Vargas, V. Gonzalez-Posadas, F. J. Herraíz-Martinez, and D. Segovia-Vargas, "Design method for actively matched antennas with non-Foster elements," *IEEE Transactions on Antennas and Propagation*, vol. 64, no. 9, pp. 4118–4123, 2016.

[32] J. T. Aberle, "Two-port representation of an antenna with application to non-Foster matching networks," *IEEE Transactions on Antennas and Propagation*, vol. 56, no. 5, pp. 1218–1222, 2008.

[33] S. Soltani, P. Lotfi, and R. D. Murch, "Design of compact dual-band dual-port WLAN MIMO antennas using slots," in *2015 IEEE International Symposium on Antennas and Propagation and USNC/URSI National Radio Science Meeting.* IEEE, 2015, Conference Proceedings.

[34] W.-W. Lee and B. Jang, "A tunable MIMO antenna with dual-port structure for mobile phones," *IEEE Access*, vol. 7, pp. 34 113–34 120, 2019.

[35] R. N. Simons, *Coplanar waveguide circuits, components, and systems.* John Wiley and Sons, Inc., 2001.

[36] B. C. Wadell, *Trasmission line design handbook*. Artech House, Inc., 1991.

[37] M. Gopikrishna, D. D. Krishna, C. K. Anandan, P. Mohanan, and K. Vasudevan, "Design of a compact semi-elliptic monopole slot antenna for UWB systems," *IEEE Transactions on Antennas and Propagation*, vol. 57, no. 6, pp. 1834–1837, 2009.

[38] I. Carrasquillo-Rivera, R. Solis, and J. Colom-Ustariz, "Tunable and dual-band rectangular slot-ring antenna," in *IEEE Antennas and Propagation Society Symposium, 2004.* IEEE, 2004, Conference Proceedings, pp. 4308–4311.

[39] S. Jia, W. Chen, and D. Schreurs, "A novel Doherty transmitter based on antenna active load modulation," *IEEE Microwave and Wireless Components Letters*, vol. 25, no. 4, pp. 271–273, 2015.

[40] T. M. Hone, S. Bensmida, K. A. Morris, M. A. Beach, J. P. McGeehan, J. Lees, J. Benedikt, and P. J. Tasker, "Controlling active load–pull in a dual-input inverse load modulated Doherty architecture," *IEEE Transactions on Microwave Theory and Techniques*, vol. 60, no. 6, pp. 1797–1804, 2012.

[41] L. J. Chu, "Physical limitations of omni-directional antennas," Research Laboratory of Electronics: Massachusetts Institute of Technology, Report, 1948.

[42] M. R. Chaurasia, P. R. Pimpalgaonkar, B. Raval, and T. K. Upadhyaya, "Electrically small antennas: The art of miniaturization," *International Journal of Advanced Research in Computer Engineering and Technology (IJARCET)*, vol. 5, no. 2, pp. 229–234, 2016.

[43] S. R. Best, *Small antennas*, 4th ed. New York: McGraw-Hill, 2007.

[44] H. A. Wheeler, "Fundamental limitations of a small VLF antenna for submarines," *IEEE Transactions on Antennas and Propagation*, vol. 6, pp. 123–125, 1958.

[45] G. A. Thiele, P. L. D. weiler, and R. P. Peno, "On the lower bound of the radiation Q for electrically small antennas," *IEEE Transactions on Antennas and Propagation*, vol. 51, pp. 1263–1269, 2003.

[46] A. D. Yaghjian and S. R. Best, "Impedance, bandwidth, and Q of antennas," *IEEE Transactions on Antennas and Propagation*, vol. 53, no. 4, pp. 1298–1324, 2005.

[47] M. N. Abdallah, W. Dyab, and T. K. Sarkar, "Electrically small antennas design challenges," in *2015 IEEE International Symposium on Antennas and Propagation and USNC/URSI National Radio Science Meeting*, 2015, Conference Proceedings.

[48] O. S. Kim, "Low-q electrically small spherical magnetic dipole antennas," *IEEE Transactions on Antennas and Propagation*, vol. 58, no. 7, 2010.

[49] G. Breed, "Basic principles of electrically small antennas," High Frequency Electronics, Summit Technical Media, LLC, Report, 2007.

[50] R. W. Ziolkowski, "An efficient, electrically small antenna designed for VHF and UHF applications," *IEEE Antennas and Wireless Propagation Letters*, vol. 7, 2008.

[51] S. Lim, R. L. Rogers, and H. Ling, "Frequency tuning of an electrically small antenna for HF ground wave transmission," in *2005 IEEE Antennas and Propagation Society International Symposium.* IEEE, 2005, Conference Proceedings.

[52] M.-D. Chiou and S.-Y. Chen, "An electrically small planar antenna using complementary split-ring resonators," in *2012 International Symposium on Antennas and Propagation (ISAP)*, 2012, Conference Proceedings.

[53] K. S. Song, "Non-foster impedance matching and loading networks for electrically small antennas," PhD thesis, The Ohio State University, 2011.

[54] Y. Kabiri, P. Gardner, and C. Constantinou, "Simultaneous two-port injection matched antenna," in *2015 9th European Conference on Antennas and Propagation (EuCAP)*. IEEE, 2015, Conference Proceedings.

[55] M. S. Shakhirul, M. Jusoh, Y. S. Lee, and C. R. N. Husna, "A review of reconfigurable frequency switching technique on micostrip antenna," *Journal of Physics: Conference Series*, 2018.

[56] F. Ghanem, P. Hall, and J. Kelly, "Two port frequency reconfigurable antenna for cognitive radios," *Electronics Letters*, vol. 45, no. 11, 2009.

[57] G. Jin, H. Liao, and D. Liu, "A dual-port frequency reconfigurable antenna for cognitive radio applications," in *2016 IEEE International Conference on Computational Electromagnetics (ICCEM)*. IEEE, 2016, Conference Proceedings.

[58] C.-X. Mao, S. Gao, Y. Wang, Y. Liu, X.-X. Yang, Z.-Q. Cheng, and Y.-L. Geng, "Integrated dual-band filtering/duplexing antennas," *IEEE Access*, vol. 6, pp. 8403–8411, 2018.

[59] Z. Zhang, *Antenna design for mobile devices*. IEEE Press, 2011.

[60] G. A. Mavridis, D. E. Anagnostou, and M. T. Chryssomallis, "Evaluation of the quality factor, Q, of electrically small microstrip-patch antennas," *IEEE Antennas and Propagation Magazine*, vol. 53, no. 4, pp. 216–224, 2011.

[61] K. Fujimoto and H. Morishita, *Modern Small Antennas*. Cambridge: Cambridge University Press, 2013.

[62] A. Camps, F. Torres, I. Corbella, J. Bara, and P. d. Paco, "Mutual coupling effects on antenna radiation pattern: An experimental study applied to interferometric radiometers," *Radio Science*, vol. 33, no. 6, pp. 1543–1552, 1998.

[63] W. Su, Q. Zhang, S. Alkaraki, Y. Zhang, X.-Y. Zhang, and Y. Gao, "Radiation energy and mutual coupling evaluation for multimode MIMO antenna based on the theory of characteristic mode," *IEEE Transactions on Antennas and Propagation*, vol. 67, no. 1, pp. 74–84, 2019.

[64] S. K. Garakoui, E. A. M. Klumperink, B. Nauta, and F. E. v. Vliet, "Phased-array antenna beam squinting related to frequency dependency of delay circuits," in *2011 41st European Microwave Conference*. IEEE, 2011, Conference Proceedings.

[65] R. Stuhlfauth and C. Rowell, "Over the air testing for antenna arrays: Challenges and solutions," *Microwave Product Digest*, 2017. [Online]. Available: https://www.mpdigest.com/2017/09/25/over-the-air-testing-for-antenna-arrays-challenges-and-solutions/

[66] N. Bošković, B. Jokanović, and V. Marković, "Frequency scanning antenna arrays with metamaterial based phased shifters," *Electronics and Energetics*, vol. 32, no. 3, pp. 449–461, 2019.

[67] O. Bakr and M. Johnson, "Impact of phase and amplitude errors on array performance," University of California at Berkeley, Report, 2009.

[68] D. Sikri and R. M. Jayasuriya, "Multi-beam phased array with full digital beamforming for SATCOM and 5G," *Microwave Journal*, 2019.

[69] G. Coviello, G. Avitabile, G. Piccinni, G. D'Amato, and C. Talarico, "Effects on phased arrays radiation pattern due to phase error distribution in the phase shifter operation," in *MATEC Web of Conferences*, vol. 76. MATEC Web of Conferences, 2016, Conference Proceedings.

[70] Y. Kabiri, "Injection matching of antenna," PhD thesis, University of Birmingham, 2016.

[71] F. Yang, X.-X. Zhang, X. Ye, and Y. Rahmat-Samii, "Wide-band e-shaped patch antennas for wireless communications," *IEEE Transactions on Antennas and Propagation*, vol. 49, no. 7, pp. 1094–1100, 2001.

[72] S. Xiao, B.-Z. Wang, W. Shao, and Y. Zhang, "Bandwidth-enhancing ultralow-profile compact patch antenna," *IEEE Transactions on Antennas and Propagation*, vol. 53, no. 11, pp. 3443–3447, 2005.

[73] J. Liang, C. Chiau, X. Chen, and C. Parini, "Study of a printed circular disc monopole antenna for uwb systems," *IEEE Transactions on Antennas and Propagation*, vol. 53, no. 11, pp. 3500–3504, 2005.

[74] R. Singh, "Broadband planar monopole antennas," *Semantic Scholar*, pp. 1–24, 2004.

[75] Y. Kabiri, P. Gardner, and C. Constantinou, "A novel approach for wideband tunable electrically small antennas," in *The 8th European Conference on Antennas and Propagation*. IEEE, 2014, Conference Proceedings, pp. 3633–3637.

[76] S. J. Orfanidis, *Electromagnetic waves and antennas*. Rutgers University, 2016.

[77] M. Manteghi and Y. Rahmat-Samii, "Multiport characteristics of a wide-band cavity backed annular patch antenna for multipolarization operations," *IEEE Transactions on Antennas and Propagation*, vol. 53, no. 1, pp. 466 – 474, 2005.

[78] K. Kurokawa, "Power waves and the scattering matrix," *IEEE Transactions on Microwave Theory and Techniques*, vol. 13, no. 2, pp. 194–202, 1965.

[79] F. Caspers, "RF engineering basic concepts: S-parameters," 2010, lecture notes. [Online]. Available: https://cds.cern.ch/record/1415639/files/p67.pdf

[80] J.-M. Hannula, J. Holopainen, and V. Viikari, "Concept for frequency-reconfigurable antenna based on distributed transceivers," *IEEE Antennas and wireless propagation letters*, vol. 16, pp. 764–768, 2017.

[81] T. S. Maclean, *Principles of antennas: wire and aperture*. Cambridge: Cambridge University Press, 1986.

[82] P. Russer, *Electromagnetics, Microwave Circuit and Antenna Design for Communications Engineering*, 2nd ed. Artech House, 2006.

[83] L. Cohen, "Elements of electromagnetic theory," 2018, lecture notes. [Online]. Available: https://nanopdf.com/download/1-elements-of-electromagnetic-theory_pdf

[84] K. T. McDonald, "An antenna reciprocity theorem," 2010, lecture notes. [Online]. Available: https://physics.princeton.edu/~mcdonald/examples/reciprocity.pdf

[85] R. Garg, P. Bartia, I. Bahl, and A. Ittipiboon, *Microstrip Antenna Design Handbook*. London, UK: Artech House, 2001.

[86] M. B. Perotoni, F. A. A. d. Silva, and L. A. d. Silva, "Characteristic mode analysis applied to antennas," *Revista Brasileira de Ensino de Física*, vol. 42, no. e20200119, pp. 1–6, 2020.

[87] M. Cabedo-Fabres, E. Antonino-Daviu, A. Valero-Nogueira, and M. F. Bataller, "The theory of characteristic modes revisited - a contribution to the design of antennas for modern applications," *IEEE Antennas and Propagation Magazine*, vol. 49, no. 5, pp. 52–68, 2007.

[88] Y. Huang, *Antennas: from theory to practice*, 2nd ed. Willey, 2021.

[89] Z. Zhang, *Antenna design for mobile devices*. IEEE Press, 2011.

[90] T. L. Wilson, K. Rohlfs, and S. Huttemeister, *Tools of Radio Astronomy*. Springer, 2009, vol. Fifth Edition.

[91] Q. U. Khan, M. B. Ihsan, D. Fazal, F. M. Malik, S. A. Sheikh, and M. Salman, "Higher order modes: A solution for high gain, wide band patch antennas for different vehicular applications," *IEEE Transactions on Vehicular Technology*, vol. 66, no. 5, pp. 3548–3554, 2017.

[92] L. Shen, P. Kihogo, P. Gardner, and C. Constantinou, "Theory design and validation of a tunable injection-matched 2-port antenna," in *2020 14th European Conference on Antennas and Propagation (EuCAP)*. EuCAP, 2020, Conference Proceedings.

[93] P. Kihogo, L. Shen, C. Constantinou, and P. Gardner, "A wideband injection matched patch antenna," in *Antennas and Propagation Conference 2019 (APC-2019)*. IET, 2019, Conference Proceedings.